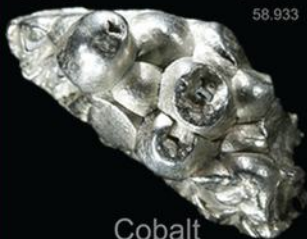

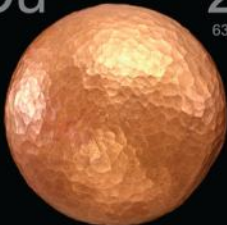




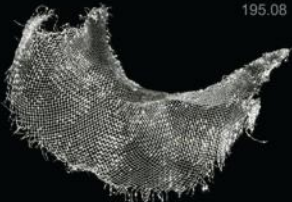



# КОНДЕНСИРОВАННЫЕ СРЕДЫ И МЕЖФАЗНЫЕ ГРАНИЦЫ

# CONDENSED MATTER AND INTERPHASES

Том Vol. 22, No. 2  
2020

<p>Co 27 58.933</p>  <p>Cobalt</p>	<p>Ni 28 58.693</p>  <p>Nickel</p>	<p>Cu 29 63.546</p>  <p>Copper</p>
<p>Rh 45 102.91</p>  <p>Rhodium</p>	<p>Pd 46 106.42</p>  <p>Palladium</p>	<p>Ag 47 107.87</p>  <p>Silver</p>
<p>Ir 77 192.22</p>  <p>Iridium</p>	<p>Pt 78 195.08</p>  <p>Platinum</p>	<p>Au 79 196.97</p>  <p>Gold</p>

# Condensed Matter and Interphases (Kondensirovannye sredy i mezhfaznye granitsy)

Peer-reviewed scientific journal

Issued 4 times a year

**Volume 22, No. 2 (2020)**

Full-text version is available in the Russian language

on the website: <https://journals.vsu.ru/kcmf/about>

ISSN 1606-867X

eISSN 2687-0711

## FOUNDER

Voronezh State University  
Belgorod State University

## PUBLISHER

Voronezh State University

The journal was founded in 1999 by Professor A. M. Khoviv, DSc in Chemistry, with the support of Kurnakov Institute of General and Inorganic Chemistry of the Russian Academy of Sciences

The journal is registered by the Russian Federal Supervision Service for Compliance with the Law in the Field of Mass Media and Cultural Heritage Protection, Certificate of Registration ПИ No. ФС 77-28318 dated 15.06.2007

The journal is included in the List of Leading Peer-reviewed Scientific Journals and Publications Recommended by the State Commission for Academic Degrees and Titles, where the main scientific results of dissertations for DSc and PhD degrees in Chemistry, Physics and Mathematics should be published. Specialities: 02.00.01 – Inorganic Chemistry, 02.00.04 – Physical Chemistry, 02.00.05 – Electrochemistry, 02.00.21 – Solid State Chemistry, 01.04.07 – Condensed Matter Physics

Indexed and archived by the Russian Science Citation Index, RSCI, Scopus, Chemical Abstract, EBSCO, DOAJ, CrossRef

Editorial Board and Publisher Office  
1 Universitetskaya pl., Voronezh 394018

Tel.: +7 (432) 2208445

<https://journals.vsu.ru/kcmf/about>

E-mail: [kcmf@main.vsu.ru](mailto:kcmf@main.vsu.ru)

Date of publication 30.06.2020

Price – not fixed

Subscription is available using the unified catalogue “Russian Press”, subscription index 80568

When reprinting the materials, a reference to the Condensed Matter and Interphases must be cited

Materials of the journal are available under the Creative Commons “Attribution” 4.0 International licence



© Voronezh State University, 2020

## EDITOR-IN-CHIEF

V. N. Semenov, DSc in Chemistry, Professor (Voronezh)

## VICE EDITORS-IN-CHIEF

V. A. Ketsko, DSc in Chemistry (Moscow)

E. P. Domashevskaya, DSc in Physics and Mathematics, Professor (Voronezh)

## EDITORIAL BOARD:

N. N. Afonin, DSc in Chemistry, Professor (Voronezh)

A. V. Vvedenskii, DSc in Chemistry, Professor (Voronezh)

V. V. Gusarov, DSc in Chemistry, Associate Member of the RAS (St. Petersburg)

V. E. Guterman, DSc in Chemistry, Professor (Rostov-on-Don)

B. M. Darinskii, DSc in Physics and Mathematics, Professor (Voronezh)

I. D. Zartsyn, DSc in Chemistry, Professor (Voronezh)

V. P. Zlomanov, DSc in Chemistry, Professor (Moscow)

V. M. Ievlev, DSc in Physics and Mathematics, Full Member of the RAS (Moscow)

A. D. Izotov, DSc in Chemistry, Associate Member of the RAS (Moscow)

A. N. Latyshev, DSc in Physics and Mathematics, Professor (Voronezh)

A. I. Marchakov, DSc in Chemistry, Professor (Moscow)

I. Ya. Mittova, DSc in Chemistry, Professor (Voronezh)

G. F. Novikov, DSc in Physics and Mathematics, Professor (Chernogolovka)

S. N. Saltykov, DSc in Chemistry (Lipetsk)

V. F. Selemenev, DSc in Chemistry, Professor (Voronezh)

V. A. Terekhov, DSc in Physics and Mathematics, Professor (Voronezh)

E. A. Tutov, DSc in Chemistry (Voronezh)

P. P. Fedorov, DSc in Chemistry, Professor (Moscow)

V. A. Khonik, DSc in Physics and Mathematics, Professor (Voronezh)

V. A. Shaposhnok, DSc in Chemistry, Professor (Voronezh)

A. B. Yaroslavtsev, DSc in Chemistry, Associate Member of the RAS (Moscow)

## INTERNATIONAL MEMBERS OF THE EDITORIAL BOARD

M. B. Babanly, DSc in Chemistry, Associate Member of the ANAS (Baku, Azerbaijan)

T. Bellezze, DSc (Ancona, Italy)

P. M. Volovitch, DSc, Professor (Paris, France)

V. B. Gorfinkel, DSc (Stony Brook, USA)

R. M. Mane, DSc (Kolhapur, India)

Nguyen Anh Tien, PhD in Chemistry, Associate Professor (Ho Chi Minh City, Vietnam)

V. V. Pan'kov, DSc in Chemistry, Professor (Minsk, Belarus)

F. Scholz, DSc, Professor (Greifswald, Germany)

M. S. Wickleder, DSc, Professor (Cologne, Germany)

V. Sivakov, DSc (Jena, Germany)

## Chief Secretary

V. A. Logacheva, PhD in Chemistry (Voronezh)

# CONTENTS

## BRIEF OVERVIEW

- Silaeva S. Yu., Belenova A. S., Slivkin A. I., Chupandina E. E., Naryshkin S. R., Krasnyuk (Jr.) I. I., Krasnyuk I. I.*  
Use of Solid Dispersion Systems in Pharmacy 173

## ORIGINAL ARTICLES

- Aliev O. M., Bayramova S. T., Azhdarova D. S., Mammadov Sh. H., Ragimova V. M., Maksudova T. F.*  
Synthesis and Properties of Synthetic Aikinite  $\text{PbCuBiS}_3$  182

- Atlukhanova L. B., Dolbin I. V., Kozlov G. V.*  
The Physics of Interfacial Adhesion between a Polymer Matrix and Carbon Nanotubes (Nanofibers) in Nanocomposites 190

- Bazarov B. G., Shendrik R. Yu., Tushinova Yu. L., Sofich D. O., Bazarova J. G.*  
Spectral-Luminescent Properties of Terbium-Containing Zirconomolybdates 197

- Bedova E. V., Tonkikh E. A., Kozaderov O. A.*  
Electrochemical Oxidation of Formic Acid on the Surface of an Anodically Modified  $\text{Ag}_{15}\text{Pd}$  Alloy 204

- Bedova E. V., Kolganova D. I., Kozaderov O. A.*  
Voltamperometry of a Kinetically Irreversible Electrochemical Process on a Rough Electrode 211

- Kovtunets E. V., Subanakov A. K., Bazarov B. G.*  
Synthesis, Structure, and Luminescent Properties of the New Double Borate  $\text{K}_3\text{Eu}_3\text{B}_4\text{O}_{12}$  219

- Kuznetsov S. V., Nizamutdinov A. S., Madirov E. I., Konyushkin V. A., Nakladov A. N., Voronov V. V., Yapyrintsev A. D., Ivanov V. K., Semashko V. V., Fedorov P. P.*

- The Study of the Luminescence of Solid Solutions Based on Yttrium Fluoride Doped with Ytterbium and Europium for Photonics 225

- Mammadov Sh. H.*

- The study of the quasi-triple system  $\text{FeS}-\text{Ga}_2\text{S}_3-\text{Ag}_2\text{S}$  by a  $\text{FeGa}_2\text{S}_4-\text{AgGaS}_2$  section 232

- Mashkina E. S.*

- Spectral analysis of heat fluctuations in KI transient premelting states 238

- Mittova I. Ya., Sladkopevtsev B. V., Ilyasova N. A., Tomina E. V., Dontsov A. I., Tarasova O. S.*

- The Effect of Certain Complex Chemostimulators and Modifiers on InP Thermal Oxidation 245

- Peregudov Yu. S., Mejri R., Gorbunova E. M., Niftaliev S. I.*

- Glauconite-Based Sorbents for Skimming Oil and Oil Products 257

- Rodina N. D., Morozova N. B., Vvedenskii A. V.*  
Kinetics of Atomic Hydrogen Evolution and Hydrogen Permeability of  $\text{Ag}-\text{Pd}$  Alloys in an Alkaline Medium 266



# Condensed Matter and Interphases (Kondensirovannye sredy i mezhfaznye granitsy)

## Brief overview

DOI <https://doi.org/10.17308/kcmf.2020.22/2820>

Received 5 February 2020

Accepted 15 April 2019

Published online 25 June 2020

ISSN 1606-867X

eISSN 2687-0711

## Use of Solid Dispersion Systems in Pharmacy

© 2020 S. Yu. Silaeva<sup>a</sup>, A. S. Belenova<sup>a</sup>, A. I. Slivkin<sup>a</sup>, E. E. Chupandina<sup>a</sup>, S. R. Naryshkin<sup>a</sup>,  
I. I. Krasnyuk (Jr.)<sup>b</sup>, I. I. Krasnyuk<sup>b</sup>

<sup>a</sup>Voronezh State University,

1 Universitetskaya pl., Voronezh 394018, Russian Federation

<sup>b</sup>I. M. Sechenov First Moscow State Medical University (Sechenov University),

8, ul. Trubetskaya, building 2, Moscow 119991, Russian Federation

### Abstract

An overview of the use of solid dispersion systems in pharmacy is presented. The main techniques of obtaining solid dispersions were considered. The simplest one is the solvent removal technique: the medicinal drug and the carrier are dissolved in the solvent that is then evaporated. The fusion method involves heating the mixture of the medicinal drug with the carrier above the fusion temperature with further hardening under quick cooling. The co-milling method is based on the co-use of compression, fracture, and friction energy for the transition of the solid-state drug and carrier into the amorphous state. The kneading method is a variation of the co-milling method. In this case, the solvent performs several functions at the same time: it dissolves one of the components and enters the micro-fissures of crystals of another component, producing a wedge effect and contributing to the milling and interpenetration of one substance into the pores of another. The method of using the agents stabilising the amorphous state of the medicinal drug involves mixing the following components: a sparingly soluble medicinal drug, an agent inducing the transition of the system into the amorphous state, and an agent stabilising its amorphous state. The obtained mixture is subjected to thermal or mechanochemical treatment. Combinations of these methods are also used to obtain solid dispersion systems. Examples of polymers and non-polymer substances used as carriers in solid dispersion systems are given. The works of authors were studied that are dedicated to the creation and study of solid dispersions of various active pharmaceutical ingredients as well as dosage forms produced from these solid dispersions.

**Keywords:** solid dispersion systems, carriers, medicinal drugs.

**For citation:** Silaeva S. Yu., Belenova A. S., Slivkin A. I., Chupandina E. E., Naryshkin S. R., Krasnyuk I. I. (Jr.), Krasnyuk I. I. Use of Solid Dispersion Systems in Pharmacy. *Kondensirovannye sredy i mezhfaznye granitsy = Condensed Matter and Interphases*. 2020;22(2): 173-181. DOI: <https://doi.org/10.17308/kcmf.2020.22/2820>

The term “solid dispersions” was suggested by Japanese scientists Sekiguchi and Obi in 1961. “Solid dispersions (SDs) are bi- or multicomponent systems consisting of a pharmaceutical substance and a carrier, which are highly dispersed solid phases of pharmaceutical substance or solid solutions that form complexes with the carrier material [1]”. The use of SDs allows solving a number of problems that occur while creating different medicinal drugs:

– regulation of release time of the medicinal drug from the dosage form;

✉ Sof'ya Yurievna Silaeva, e-mail: [sophiasilaeva@yandex.ru](mailto:sophiasilaeva@yandex.ru)



The content is available under Creative Commons Attribution 4.0 License.

– elimination of undesirable properties of the pharmaceutical substance (adverse reactions, unpleasant organoleptic properties);

– increasing the stability of medicinal drugs in storage and their resistance to environmental influences;

– optimisation of the production technology of the dosage form.

Various techniques are used to obtain SDs:

1) solvent removal technique. It is the simplest technique of obtaining SDs. The medicinal drug and the carrier are dissolved in the solvent that is further evaporated under low pressure.

Chloroform, dichloromethane, methanol, ethanol, acetone, methylene chloride, and others are used as solvents. The role of the solvent is to ensure the disintegration and homogenisation of the system components at the molecular level and better interaction between the medicinal drug and the carrier.

2) the fusion method involves heating the mixture of the medicinal drug with the carrier above the fusion temperature with further hardening under quick cooling.

3) the co-milling method (mechanochemical method) is based on the co-use of compression, fracture, and friction energy for transition of the solid-state medicinal drug and carrier into the amorphous state. The original substances are mixed and milled using special equipment: a ball mill, a planetary mill, pressure treatment, etc. This method ensures a higher quality of disperse distribution of the amorphous medicinal drug in the carrier.

4) the kneading method is a variation of the co-milling method. The components are placed in a mortar with ethanol and then the mixture is ground until the ethanol is completely removed. In this case, the solvent performs several functions at the same time: it dissolves one of the components; enters the micro-fissures of crystals of another component, producing a wedge effect and contributing to the milling and interpenetration of one substance into the pores of another.

5) the method using the agents stabilising the amorphous state of the medicinal drug. The idea of the method is based on mixing the following components: a sparingly soluble medicinal drug, an agent inducing the transition of the system into the amorphous state, and an agent stabilising its amorphous state. The agent inducing the transition into the amorphous state can be a crystalline compound that is able to lower the fusion temperature of the mixture with the medicinal drug. Such a compound can change the energy of the crystal lattice of the sparingly soluble medicinal drug decreasing it and increasing the vibrations of the crystal lattice at the same temperature in the presence of a source of thermal or mechanical energy. Examples of such substances are organic acids and their sodium and potassium salts, urea

derivatives, creatinin, aluminium hydroxide, nicotinamide, maltol, mannitol, methyl glucamine, sodium deoxycholate, phosphatidylcholine, etc. A thermally-stable compound containing a functional group interacting with the sparingly soluble medicinal drug acts as an agent stabilising the amorphous state. For this purpose the following are used: cellulose derivatives, polyvinylpyrrolidone (PVP), polyvinyl alcohol (PVA), polyvinyl acetate (PVAC), copolymer of vinyl alcohol and vinyl acetate, copolymer of ethylene and vinyl acetate, derivatives of polyethylene oxides (PEO), tweens, polysaccharides, cyclodextrins, derivatives of alginic acid, acrylic polymers, aerosil, aluminium hydroxide, and others. The process is completed with the thermal or mechanochemical treatment of the obtained mixture.

6) finally, combinations of the above-mentioned techniques can be used to obtain solid dispersion systems [2].

Various polymers, copolymers or their combinations as well as non-polymer substances are used as carriers for the formation of SDs. For example, polyvinylpyrrolidone (PVP) with different molecular weights and its derivatives, polymers of acrylic and metacrylic acid and their copolymers,  $\alpha$ -,  $\beta$ -,  $\gamma$ -cyclodextrins (CDs) and their derivatives, chitosan, cellulose and its derivatives, starch, alginic acid, polyethylene glycols (PEGs) or polyethylene oxides (PEOs) with different molecular weights, carbomers, trisamine, lactose, fructose, maltose, urea, saccharose, alkaline carbonates and other compounds [3].

Medicinal drugs of different pharmacotherapeutic groups are often used among active pharmaceutical ingredients introduced into dosage forms as SDs.

M.K. Sarangi and N. Singh obtained an SD based on aceclofenac using PEO 6000,  $\beta$ -cyclodextrin ( $\beta$ -CD), and carboxymethylcellulose sodium (Na-CMC) using the solvent removal technique. The results of their research showed that aceclofenac can exist in the amorphous state in solid dispersion. The SD produced with the ratio of 1:2 (aceclofenac: PEO 6000) showed the fastest dissolution among all solid dispersion systems. Basing on this SD, pills were formed that showed the best solution profiles as compared to dosage forms available on the market [4].

S. Muralidhar et al. obtained an SD of etoricoxib using the co-milling method, the kneading method, and solvent removal technique with PEO 6000 as the carrier with the ratios 1:1, 1:3, 1:6, 1:9. While studying the solution profile of solid dispersion system in 0.1 N HCl containing 1% of sodium lauryl sulphate, it was shown that the maximum dissolution rate is observed in the solid dispersion system of etoricoxib with PEO 6000 with the ratio of 1:6 produced by the solvent removal technique [5].

While studying the solid dispersion system of ibuprofen with hydroxypropylmethylcellulose (HPMC), hydroxypropylcellulose (HPC), powdered sugar, dextrose, mannitol, and lactose obtained by the fusion method, N. Saffoon et al. showed that the rate of ibuprofen dissolution was considerably improved when prepared in the solid dispersion system with HPMC and HPC. Solid dispersion systems with powdered sugar, dextrose, mannitol, and lactose release the drug considerably slower in the dissolution test [6].

A system was developed that includes indomethacin and a composition consisting of a hydrophilic hydroxypropylmethylcellulose polymer and stearyl macrogol-32 glycerides, Gelucire 50/13. The studies of this solid dispersion system using X-ray diffraction analysis, differential scanning calorimetry, and hot stage microscopy showed the presence of amorphous indomethacin in polymer/lipid matrices. Near-infrared spectroscopy allowed detecting the shifts of the peaks indicating possible interaction and formation of H-bonds between the drug and the polymer/lipid carrier. Studies of the dissolution in vitro showed a synergetic effect of the polymer/lipid carrier with the delay time of 2 hours in acid environment but with further increase of the rate of indomethacin dissolution at pH > 5.5 [7].

M. Ochi et al. developed an amorphous solid dispersion system of meloxicam with PVP K-30, hydroxypropylmethylcellulose SSL, and Eudragit EPO. The morphology, crystallinity, dissolution properties, stability, and interactions between meloxicam and polymers are described. The solid dispersion system of meloxicam with Eudragit EPO is characterised by physicochemical stability after being stored at 40 °C with a relative humidity of 75 % for 30 days. As for the solid dispersion system of meloxicam with PVP and HPC-SSL,

recrystallisation of meloxicam was observed at 40 °C with a relative humidity of 75 % for 30 days. IR spectroscopy and <sup>1</sup>H NMR analysis showed that Eudragit EPO interacts with meloxicam and reduces the intramolecular binding between its molecules, which may lead to inhibition of the growth of meloxicam crystals. The solid dispersion system of meloxicam with Eudragit EPO showed the highest improvement in dissolution among all the prepared SDs of meloxicam.

B. Karolewicz et al. developed a solid dispersion system for imatinib using the kneading method with Pluronic F127 from 10 to 90 % (copolymer of polyoxyethylene and polyoxypropylene). The studies were conducted using X-ray diffraction analysis, differential scanning calorimetry, FTIR spectroscopy, and scanning electron microscopy which showed that there was no chemical interaction between imatinib and Pluronic F127 in a solid state, and they form a simple eutectic phase diagram. When studying the dissolution of solid dispersion systems in 0.1 M HCl and phosphate buffer (pH 6.8), it was shown that the dynamics of release of the imatinib base from the solid dispersion system with Pluronic F127 depends on the pH of the dissolution medium. With pH 1.2, the presence of polymer in the solid dispersion causes a delay in the drug release due to the formation of a viscous gel layer, while with pH 6.8 a considerable increase in the dissolution rate of the drug from solid dispersions, as compared to a pure substance, is observed. In the view of solubility, solid dispersion systems containing 20 % and 30 % of the polymer were the most appropriate [9].

Pluronic F127 was also used for the formation of solid dispersion systems with fenofibrate using the fusion method. Studies of the obtained SD using FTIR spectroscopy, X-ray diffraction analysis, and differential scanning calorimetry did not identify any interaction between fenofibrate and Pluronic F127 but showed that these substances form a simple eutectic system. In this solid dispersion system the dissolution rate of fenofibrate was considerably higher as compared to the pure drug. The highest increase in the dissolution rate was observed in the solid dispersion system containing 30 % of fenofibrate and 70 % of Pluronic F127 [10].

The solid dispersion system of lovastatin obtained using the co-milling method is also described. Instead of a polymer, it uses a low-molecular substance, acetylsalicylic acid, as a carrier. Differential scanning calorimetry, FTIR spectroscopy, and X-ray diffraction (XRD) analysis showed that there is no interaction between the drugs. Lovastatin and acetylsalicylic acid form a simple eutectic phase diagram. Studies of the dissolution showed that the dissolution rate of lovastatin *in vitro* released from the solid dispersion systems, containing 10, 20, 40, and 60 % of lovastatin was improved, as compared to a separate medicinal drug [11].

C. C. C. Teixeira et al. developed an SD of curcumin containing Gelucire® 50/13-Aerosil® using the spray drying method. The solid dispersion system containing 40 % of curcumin was studied by DSC, IR spectroscopy, and XRD. Solubility and dissolution rate of curcumin in HCl or phosphate buffer improved by 3600 and 7.3 times respectively. The accelerated stability test showed that the SD was stable for 9 months [12].

An SD of glibenclamide with Neusilin® UFL2, an amorphous synthetic form of magnesium aluminum metasilicate, was developed in various proportions. Physicochemical and biopharmaceutical properties as well as the stability of four different batches were characterised. It was established that the complete dispersion of glibenclamide in the amorphous polymer was obtained with the ratio of the medicinal drug to Neusilin being 1:2.5. Completely amorphous dispersion was tested by thermal and X-ray diffraction analysis. Amorphous batches were physically and chemically stable for the duration of experiments. Physicochemical properties of four batches were compared to the properties of the original materials and physical mixtures Neusilin® UFL2 and glibenclamide. Studies of the solubility of four solid dispersion systems showed the very high dissolution rate of completely amorphous batches due to amorphous characteristics of these SDs, the very small size of the particles, and the presence of polysorbate 80 that improved the wettability of the solid substance [13].

K. Punčochová et al. used magnetic resonance imaging, ATR-FTIR spectroscopic imaging,

and Raman mapping to study the mechanism of aprepitant release from multi-component amorphous solid dispersion systems. The SD was prepared on the basis of the combination of two polymers – Soluplus as a solubilising agent and PVP as a dissolution amplifier. The compositions were prepared with the ratio of Soluplus:PVP being 1:10, 1:5, 1:3, and 1:1. Crystallisation of aprepitant during the dissolution was observed to a variable extent with the polymer ratios of 1:10, 1:5, and 1:3, but the increase of the amount of Soluplus in the composition delayed the start of crystallisation. The best matrix for the SD was the composition of Soluplus:PVP (1:1). In this case, the dissolution rate of aprepitant was considerably increased [14].

An SD of valsartan was prepared and characterised using  $\beta$ -cyclodextrin with the ratios 1:1, 1:2, 1:3, 1:4 to improve its solubility in water and the dissolution rate using the solvent evaporation method. The compositions were studied using DSC, FTIR spectroscopy, and scanning electron microscopy. Solid dispersions showed a marked improvement of solubility characteristics and improved release of the drug. It was found that the composition valsartan: $\beta$ -cyclodextrin (1:4) is the most appropriate based on the study of solubility characteristics and dissolution rate. The obtained results showed that solubility in water and dissolution rate were considerably higher in solid dispersion as compared to the pure drug. The increase of dissolution rate depends on the nature and amount of the carrier and increase with the higher concentration of cyclodextrin [15].

D. Akiladevi et al. prepared an SD of paracetamol using the co-milling and fusion methods with PEO 4000, PEO 6000, and urea with the ratio of drug:polymer being 1:1, 1:4, and 1:5. The SD was studied by the following parameters: appearance, solubility, and dissolution *in vitro*. The method of FTIR spectroscopy showed that paracetamol is stable in the SD. It was established that the content of the drug is high. The prepared SD showed a notable increase in the dissolution rate of paracetamol as compared to the pure substance. The solid dispersion system with PEO 6000 (1:5) prepared using the fusion method showed higher dissolution rate (107.26 %) as compared to PEO 4000 and urea (1:4 and 1:5) [16].

I. I. Krasnyuk (Jr.) et al. developed solid dispersion systems of erythromycin, synthomycin, amoxicillin trihydrate, ampicillin trihydrate, protionamide, rifampin, nozepam, benzonal, parmidinum, and chloramphenicol. PEO1500, PVP 10000,  $\beta$ -CD were used to obtain the solid dispersion systems. The solvent removal technique, the co-milling method, and the kneading method were used to prepare the SDs.

It was found that the introduction of the medicinal drug into a solid dispersion system with PEO leads to the increase of solubility and the rate of drug dissolution in water. The highest increase of solubility was shown for the SD with benzonal (by 3.50 times), rifampin (by 2.49 times), ampicillin trihydrate (by 1.73 times), and synthomycin (by 1.47 times). On average, the studied solid dispersion systems with PEO are dissolved 4 times faster.

The solubility of solid dispersion systems with PVP increased by 2.50–3.00 times. Increased solubility was found for solid dispersion systems of benzonal (by 5.46 times), rifampin (by 2.68 times), chloramphenicol (by 3.54 times), protionamide (by 2.56 times), synthomycin, erythromycin, and nozepam (approximately by 2.00 times), and amoxicillin trihydrate (by 1.63 times). No changes in solubility were found for the solid dispersion system of ampicillin trihydrate with PVP. The dissolution rate of the studied medicinal drugs from the SDs with PVP increases by 4 times on average.

The obtaining of the solid dispersion system with  $\beta$ -CD has a less obvious effect on solubility and dissolution rate of the drug. The solubility of the drugs obtained in the SD with  $\beta$ -CD increased by 1.70 times on average. The increase of solubility was observed for SDs of: benzonal (by 3.57 times), rifampin (by 2.11 times), nozepam (by 1.90 times), chloramphenicol (approximately by 1.50 times), ampicillin trihydrate, erythromycin, and protionamide (not more than 1.35 times). The dissolution rate of the studied drugs from the SDs with  $\beta$ -CD increases on average by 2.80 times.

The mechanisms that cause changes in the solubility and dissolution rate of the medicinal drugs from SDs were identified. A complex of physicochemical methods (X-ray diffraction analysis, crystalline microchemical analysis, IR spectroscopy, thermal analysis) proved the

change in the crystal structure and amorphisation, formation of intramolecular complexes, products of interaction, and polymorphic modifications of the studied drugs in SDs.

Solid dosage forms (pills and capsules) with the solid dispersion systems of erythromycin, chloramphenicol, and rifampin were developed. PVP was used as a carrier for the SDs. The study of the medicinal drug release from model pills and capsules showed that the introduction of SDs of the studied medicinal drugs with PVP in pills and capsules increases the pharmaceutical availability of the medicinal drug.

L. P. Suntsova et al. obtained and studied the properties of the solid dispersion systems based on such flavonoids as genistein, dihydroquercetin, and rutin. Calcium and magnesium carbonates as well as natural polysaccharide arabinogalactan (AG) were used as carriers. The SDs were obtained using the mechanical treatment of the mixtures of powders. In mechanochemically treated mixtures the heat of fusion and intensity of XRD reflections are decreased while the crystallinity of solid phases of flavonoids is partially lost. The shift of equilibrium to ionised molecules through the use of substances of calcium and magnesium carbonates increases the general concentration of flavonoids in the solution. As a result of the mechanical treatment of flavonoids with AG, their molecules were dispersed into the matrix of water-soluble polysaccharide, which contributed to their accelerated release into the solution and formation of intramolecular complexes during hydration [31–33].

I. V. Kovalevskaya et al. studied the properties of the solid dispersion systems of thioctic acid with water-soluble high-molecular substances obtained using the solvent removal technique. SD samples with polyethylene glycol 6000, polyvinylpyrrolidone, shellac, carbomers 934, 980, Ultrez 21 were studied in terms of their form and size of particles, hygroscopy, values of dissolution of thioctic acid, and technological properties. It was established that the most promising carrier for the solid dispersion system of thioctic acid is PEG 6000 that ensures a 5 times better dissolution of the substance, has higher values of compressibility, flowability, and durability [34].

M. L. Tkachenko et al. studied the phase equilibria of the compositions of the solid primary



condensed system of ibuprofen with trisamine as well as the secondary system of the formed compound (ibutris) with trisamine. According to DSC and visual-polythermal analysis, a phase diagram was created. In terms of physicochemical interaction, this is a simple eutectic system which is achieved with the ibutris:trisamine ratio of 53:47 % by weight with a fusion temperature of 134°C. It has been shown that, as compared to the parameters of the pure substance, the extreme solubility (more than by 200 times) and dissolution rate (approximately by 8 times) of ibuprofen is typical for the eutectic composition of the ibutris – trisamine system.

Phase equilibria of the solid system of butadionum with trisamine was studied using DSC and visual-polythermal analysis. It was established that with the ratio of butadionum with trisamine being 71.8:28.2 % by weight, a compound butatris is formed that interacts with the original substances (butadionum and trisamine) similarly to simple eutectics. When studying the solubility of the prepared binary samples with trisamine, it was established that the solubility of butadionum from the butatris sample at the temperature of 37 °C is almost 100 times higher than typical solubility of butadionum substance in similar conditions, while for the eutectic composition butatris–trisamine it is 170 times higher, reaching the value of 1.2 g per 100 g of water expressed as butadionum. It is shown that the release rate of butadionum from the butatris samples is 10 times higher and 20 times higher from the butatris – trisamine eutectic sample, as compared to the release rate of butadionum from the sample of the pure substance [37, 38].

V. V. Grikh studied the effect of solid dispersion systems on the process of nifedipine dissolution. PVP 10000 with the ratio of 1:1–2 as well as PEG 400 and PEG 1500 with the ratio of 1:3 were used as polymer carriers. Solid dispersion systems were obtained using the solvent removal technique. Compositions of nifedipine ointments with hydrophilic and diphilic bases as well as hydrogels based on carbomer gelation agent were developed [39–49].

Therefore, the use of the drugs included in solid dispersion systems in pharmaceutical technology allows increasing the solubility

and dissolution rate of active pharmaceutical ingredients, optimise technological properties and improve biopharmaceutical parameters of a drug ensuring its optimal stability. The use of solid dispersions in medicine and pharmacy is driven by the possibility of optimising medicinal drug release from the dosage form, the increase of bioavailability and pharmacological activity of the medicinal drug due to the increase of its solubility, and the release rate from the dosage form.

### Conflict of interests

The authors declare that they have no known competing financial interests or personal relationships that could have appeared to influence the work reported in this paper.

### References

1. Sekiguchi K., Obi N. Studies on absorption of eutectic mixtures: a comparison of the behavior of eutectic mixture of sulfathiazole and that of ordinary sulfathiazole in man. *Chem. Pharm. Bull.* 1961;9: 866–872. DOI: <https://doi.org/10.1248/cpb.9.866>
2. Teslev A. A. K voprosu primeneniya tverdykh dispersnykh sistem dlya uluchsheniya biofarmatsevticheskikh kharakteristik lekarstvennykh sredstv [On the use of solid disperse systems to improve the biopharmaceutical characteristics of drugs] *Pharmaceutical Technologies and Packaging.* 2014;2: 18–21. (In Russ.)
3. Debjit Bhowmik, Harish G., Duraivel S., Pragathi Kumar B., Vinod Raghuvanshi, Sampath Kumar K. P. Solid dispersion – an approach to enhance the dissolution rate of poorly water soluble drugs. *The Pharma Innovation Journal.* 2013;1(12): 24–38.
4. Manoj Kumar Sarangi, Neha Singh. A comparative study of solubility enhancement of aceclofenac by solid dispersion technique using several polymers. *J. Appl. Pharm.* 2018;10(1): 1–11. DOI: <https://doi.org/10.4172/1920-4159.1000259> Available at: <https://www.longdom.org/abstract/a-comparative-study-of-solubility-enhancement-of-aceclofenac-by-solid-dispersion-technique-using-several-polymers-17207.html>
5. Muralidhar S., Devala Rao G., Krishna Murthy M., Kiran Kumar K., Kranthi Teja K., Syed Khaja Nawaj, Narayana T. V. Enhancement of dissolution rate of etoricoxib through solid dispersion technique. *J. Appl. Pharm. Sci.* 2011;1(5): 129–132.
6. Nadia Saffoon, Yeakuty Marzan Jhanker, Naz Hasan Huda. Dissolution profile of ibuprofen solid dispersion prepared with cellulosic polymers and sugar by fusion method. *S. J. Pharm. Sci.* 2011;4(1): 31–37. DOI: <https://doi.org/10.3329/sjps.v4i1.8864>

7. Maniruzzaman M., Islam M. T., Halsey S., Amin D., Douroumis D. Novel controlled release polymer-lipid formulations processed by hot melt extrusion. *AAPS PharmSciTech*. 2016;17(1): 191–199. DOI: <https://doi.org/10.1208/s12249-015-0470-2>
8. Ochi M., Kimura K., Kanda A., Kawachi T., Matsuda A., Yuminoki K., Hashimoto N. Physicochemical and pharmacokinetic characterization of amorphous solid dispersion of meloxicam with enhanced dissolution property and storage stability. *AAPS PharmSciTech*. 2016;17(4): 932–939. DOI: <https://doi.org/10.1208/s12249-015-0422-x>
9. Karolewicz B., Gajda M., Gorniak A., Owczarek A., Mucha I. Pluronic F127 as a suitable carrier for preparing the imatinib base solid dispersions and its potential in development of a modified release dosage forms. *J. Therm. Anal. Calorim.* 2017;130(1): 383–390. DOI: <https://doi.org/10.1007/s10973-017-6139-1>
10. Karolewicz B., Gajda M., Pluta J., Gorniak A. Dissolution study and thermal analysis of fenofibrate–Pluronic F127 solid dispersions. *J. Therm. Anal. Calorim.* 2016;125(2): 751–757. DOI: <https://doi.org/10.1007/s10973-015-5013-2>
11. Gorniak A., Gajda M., Pluta J., Czapor-Irzabek H., Karolewicz B. Thermal, spectroscopic, and dissolution studies of lovastatin solid dispersions with acetylsalicylic acid. *J. Therm. Anal. Calorim.* 2016;125(2): 777–784. DOI: <https://doi.org/10.1007/s10973-016-5279-z>
12. Teixeira C. C. C., Mendonça L. M., Bergamaschi M. M., Queiroz R. H. C., Souza G. E. P., Antunes L. M. G., Freitas L. A. P. Microparticles containing curcumin solid dispersion: stability, bioavailability, and anti-inflammatory activity. *AAPS PharmSciTech*. 2016;17(2): 252–261. DOI: <https://doi.org/10.1208/s12249-015-0337-6>
13. Censi R., Gigliobianco M. R., Dubbini A., Malaj L., Di Martino P. New nanometric solid dispersions of glibenclamide in neusilin® UFL2. *AAPS PharmSciTech*. 2016;17(5): 1204–1212. DOI: <https://doi.org/10.1208/s12249-015-0457-z>
14. Punčochová K., Ewing A. V., Gajdošová M., Pekárek T., Beránek J., Kazarian S. G., Štěpánek F. The combined use of imaging approaches to assess drug release from multicomponent solid dispersions. *Pharm. Res.* 2017;34(5): 990–1001. DOI: <https://doi.org/10.1007/s11095-016-2018-x>
15. Sapkal S. B., Shinde S. A., Darakhe R. A., Shrikhande V. N. Solid dispersion of valsartan for solubility improvement using  $\beta$ -cyclodextrin. *MOJ Bioequivalab.* 2018;5(6): 313–319. DOI: <https://doi.org/10.15406/mojbb.2018.05.00121>
16. Akiladevi D., Shanmugapandiyam P., Jebasingh D., Sachinandhan Basak. Preparation and evaluation of paracetamol by solid dispersion technique. *Int. J. Pharm.* 2011;3(1): 188–191. Available at: <https://innovareacademics.in/journal/ijpps/Vol3Issue1/1053.pdf>
17. Krasnyuk I. I. (Jr.), Arzamastsev A. P., Popkov V. A., Reshetnyak V. Yu., Krasnyuk I. I. *Patent No 2261087 RF*. 2005.
18. Krasnyuk Jr. I. I. (Jr.) Effects of solid dispersions on the solubility of antibiotics. *Pharmaceutical Chemistry Journal*. 2009;43(4): 226–229. DOI: <https://doi.org/10.1007/s11094-009-0267-2>
19. Krasnyuk I. I. (Jr.) Povyshenie biodostupnosti lekarstvennykh form s primeneniem tverdykh dispersii [Increasing the bioavailability of dosage forms using solid dispersions]. *Abstract Diss. DSc in pharm.* Moscow: 2010. 48 p. Available at: <https://dlib.rsl.ru/viewer/01004609020#?page=1> (in Russ.)
20. Krasnyuk I. I. (Jr.) Determining the solubility of synthomycin in solid dispersions. *Pharmaceutical Chemistry Journal*. 2010;44(1): 25–32. DOI: <https://doi.org/10.1007/s11094-010-0390-0>
21. Krasnyuk I. I. (Jr.), Lapshova A. S., Khabriev R. U., Popkov V. A., Reshetnyak V. Yu., Zvereva S. O., Krasnyuk O. I. Solubility of erythromycin from solid dispersions. *Pharmaceutical Chemistry Journal*. 2009;43(11): 625–631. DOI: <https://doi.org/10.1007/s11094-010-0367-z>
22. Krasnyuk I. I. (Jr.), Lapshova A. S., Khabriev R. U., Popkov V. A., Reshetnyak V. Yu., Zvereva S. O., Krasnyuk O. I. Increase of the solubility of Mezepam by forming its solid dispersions. *Pharmaceutical Chemistry Journal*. 2010;44(11): 611–615. DOI: <https://doi.org/10.1007/s11094-011-0529-7>
23. Krasnyuk I. I. (Jr.), Manakhova O. V., Khabriev R. U., Popkov V. A., Reshetnyak V. Yu., Krasnyuk O. I. Increasing the solubility of Phenazepam by forming its solid dispersions. *Pharmaceutical Chemistry Journal*. 2010;44(5): 274–277. DOI: <https://doi.org/10.1007/s11094-010-0448-z>
24. Krasnyuk I. I. (Jr.), Popkov V. A., Reshetnyak V. Yu., Skovpen' Yu. V. Povyshenie biodostupnosti malorastvorimykh lekarstvennykh veshchestv s ispol'zovaniem tverdykh dispersii [Increasing bioavailability of low-soluble drugs using solid dispersions]. *Russian Medical Journal*. 2005;6: 34–37. (In Russ.)
25. Krasnyuk I. I. (Jr.), Popkov V. A., Reshetnyak V. Yu., Skovpen' Yu. V. Vliyanie tverdykh dispersii na rastvorimost' lekarstvennykh veshchestv [Effect of solid dispersions on drug solubility]. *Pharmacy*. 2004;1: 17–21. (In Russ.)
26. Krasnyuk I. I. (Jr.), Tarkhanova V. V. Povyshenie rastvorimosti oksazepama s primeneniem vspomogatel'nykh veshchestv (polietilenglikolei) [Increasing the solubility of Oxazepam using adjuvants (Polyethylene Glycols)]. *Voенно-медицинский журнал*. 2009;330(3): 69–70. (In Russ.)
27. Krasnyuk I. I. (Jr.), Khabriev R. U., Popkov V. A., Reshetnyak V. Yu., Lapshova A. S. Primenenie tverdykh dispersii v lechenii i profilaktike infektsionnykh zabolevaniy [Use of solid dispersions in the treatment

- and prevention of infectious diseases]. *Russian Medical Journal*. 2009;2: 42–44. (In Russ.)
28. Popkov V. A., Reshetnyak V. Yu., Krasnyuk I. I., Skovpen' Yu. V. Tverdye dispersii s polietilenglikolyami v farmatsii [Solid dispersions with Polyethylene Glycols in pharmacy]. *Pharmacy*. 2005;3: 39–42. (In Russ.)
29. Khabriev R. U., Popkov V. A., Krasnyuk I. I., Krasnyuk I. I. (Jr.) Basic principles for the classification of medicinal forms. *Pharmaceutical Chemistry Journal*. 2009;43(2): 118–122.. DOI: <https://doi.org/10.1007/s11094-009-0244-9>
30. Khabriev R. U., Popkov V. A., Reshetnyak V. Yu., Krasnyuk I. I. (Jr.), Manakhova O. V. Increasing the solubility of angioprotector by the method of solid dispersions. *Pharmaceutical Chemistry Journal*. 2009;43(8): 472–476. DOI: <https://doi.org/10.1007/s11094-009-0326-8>
31. Dushkin A. V., Meteleva E. S., Chistyachenko Yu. S., Khalikov S. S. Mechanochemical obtaining of solid dispersions forming water soluble supramolecular systems. *Fundamental Research*. 2013;1: 741–749. (In Russ., abstract in Eng.)
32. Dushkin A. V., Suntsova L. P., Khalikov S. S. Mechanochemical technology for improving the solubility of drugs. *Fundamental Research*. 2013;1–2: 448–457. (In Russ., abstract in Eng.)
33. Suntsova L. P., Meteleva E. S., Dushkin A. V. Mechanochemical obtaining and study of water soluble compositions based on flavonoids – genistein, dihydroquercetin, rutin. *Fundamental Research*. 2014;11–10: 2174–2179. (In Russ., abstract in Eng.)
34. Kovalevskaya I. V., Ruban O. A., Kutovaya O. V. Research of properties of thioctic acid solid dispersions obtained by liquid phase method. *Vestnik Farmatsii*. 2018;1(79): 47–53. (In Russ., abstract in Eng.)
35. Tkachenko M. L., Zhnyakina L. E., Kosmynin A. S. Physicochemical investigation of paracetamol - caffeine solid mixtures. *Pharmaceutical Chemistry Journal*. 2003;37(8): 430–432. DOI: <https://doi.org/10.1023/A:1027312131095>
36. Tkachenko M. L., Zhnyakina L. E., Moshchenskii Yu. V., Smelova S. G. Issledovanie tverdykh dispersii ibuprofena s trisaminom v kachestve gidrofil'nogo nositelya [Study of ibuprofen solid dispersions with trisamine as hydrophilic carrier]. *Proceedings of Voronezh State University. Series: Chemistry. Biology. Pharmacy*. 2007;1: 53–60. Available at: <http://www.vestnik.vsu.ru/pdf/chembio/2007/01/2007-01-09.pdf> (In Russ.)
37. Tkachenko M. L., Zhnyakina L. E., Kosmynin A. S. Peculiarities of dissolution kinetics in the paracetamol – Aminocaproic acid system. *Pharmaceutical Chemistry Journal*. 2002;36(11): 634–636. DOI: <https://doi.org/10.1023/A:1022633819427>
38. Tkachenko M. L., Smelova S. G., Zhnyakina L. E., Pavlova L. V. Solid dispersions of butadionum and trisamine as a hydrophilic carrier. *Pharmacy*. 2006;3: 31–35. (In Russ.)
39. Belyatskaya A. V., Krasnyuk I. I., Krasnyuk I. I. (Jr.), Stepanova O. I., Grikh V. V., Rastopchina O. V., Yankova V. G. Use of ready-made drugs in extemporaneous compounding of soft formulations. *Pharmacy*. 2017;4: 28–32. (In Russ., abstract in Eng.)
40. Grikh V. V. Razrabotka lekarstvennykh form nifedipina s primeneniem tverdykh dispersii [Development of dosage forms of nifedipine using solid dispersions]. *Abstract Diss. PhD in Farm*. Moscow: 2018. 24 p. (In Russ.)
41. Grikh V. V., Belyatskaya A. V., Krasnyuk I. I. (Jr.), Stepanova O. I., Krasnyuk I. I. Izuchenie rastvorimosti proizvodnogo 1,4-digidropiridina v prisutstvii polivinilpirrolidona-10000 v tverdykh dispersiyakh [Study of solubility of 1,4-dihydropyridine derivative in the presence of polyvinylpyrrolidone-10000 in solid dispersions]. In: «*Perspektivy razvitiya biologii, meditsiny i farmatsii*», *Materials of the V International Scientific Conference of Young Scientists and Students, December 8–9, 2017*. Shymkent: 2017. p. 157. (In Russ.)
42. Grikh V. V., Krasnyuk I. I. (Jr.), Belyatskaya A. V., Stepanova O. I. Izuchenie rastvorimosti nifedipina v prisutstvii polietilenglikolya v tverdykh dispersiyakh [Study of solubility of nifedipine in the presence of polyethylene glycol in solid dispersions]. In: «*Aktual'nye problemy sovremennoi meditsiny i farmatsii*», *Materials of the LXXI International Scientific and Practical Conference of Students and Young Scientists. Minsk: 2017*. p. 1531. (In Russ.)
43. Grikh V. V., Krasnyuk I. I. (Jr.), Krasnyuk I. I., Stepanova O. I., Kosheleva T. M., Ovsyannikova L. V., Plakhotnaya O. N., Korol' L. A., Galaiko A. N. Prospects for using solid methyluracil dispersions in medicine and pharmacy. *Pharmacy*. 2016;5: 9–13. (In Russ., abstract in Eng.)
44. Grikh V. V., Krasnyuk I. I. (Jr.), Belyatskaya A. V., Stepanova O. I., Krasnyuk I. I., Ovsyanikova L. V., Kosheleva T. M. Izuchenie opticheskikh svoystv rastvorov proizvodnogo 1,4-digidropiridina i ego tverdykh dispersii s polimerom [Study of optical properties of solutions of 1,4-dihydropyridine derivative and its solid dispersions with polymer. In: «*Farmobrazovanie*», *Materials of the VII International Scientific and Methodological Conference, March, 28-30, 2018, Voronezh*. Voronezh: 2018. p. 423–425. (In Russ.)
45. Grikh V. V., Krasnyuk I. I. (Jr.), Stepanova O. I., Belyatskaya A. V., Krasnyuk I. I., Krasnyuk O. V. *Patent No 2629843 RF*. 2017.
46. Grikh V. V., Krasnyuk I. I. (Jr.), Stepanova O. I., Belyatskaya A. V., Krasnyuk I. I., Atyakshin D. A. *Zayavka RF na izobretenie No 2017139594*. 2017. (In Russ.)
47. Grikh V. V., Krasnyuk I. I. (Jr.), Stepanova O. I., Belyatskaya A. V., Krasnyuk I. I., Tarasov V. V.,

Kozin D. A., Nesterenko E. Razrabotka myagkikh lekarstvennykh form, soderzhashchikh tverdye dispersii [Development of producing soft medicinal forms containing solid dispersion]. *Razrabotka i registratsiya lekarstvennykh sredstv*. 2018;1(22): 36–38. (In Russ.)

48. Krasnyuk I. I. (Jr.), Belyatskaya A. V., Krasnyuk I. I., Stepanova O. I., Ovsyannikova L. V., Grikh V. V., Allenova T. M., Odintsova E. B. Prospects for the use of solid polyvinylpyrrolidone dispersions in medicine and pharmacy. *Pharmacy*. 2016;6: 7–11. (In Russ., abstract in Eng.)

49. Krasnyuk I. I. (Jr.), Belyatskaya A. V., Nikulina O. I., Krasnyuk I. I., Kharitonov Yu. Ya., Grikh V. V. Biofarmatsevticheskie aspekty primeneniya tverdykh dispersii [Biopharmaceutical aspects of solid dispersion application]. In: *Epokha v farmatsii* [The era in pharmacy]. A. I. Tentsova (ed.). Moscow, Pero Publ., 2014, pp. 62–66.

### Information about the authors

*Sof'ya Yu. Silaeva*, postgraduate student, Department of Pharmacy Management and Economics and Pharmacognosy, Voronezh State University, Voronezh, Russian Federation; e-mail: sophiasilaeva@yandex.ru. ORCID iD: <https://orcid.org/0000-0002-3007-6271>.

*Alena S. Belenova*, PhD in biology, Assistant of the Department of Pharmaceutical Chemistry and Pharmaceutical Technology, Voronezh State University, Voronezh, Russian Federation; e-mail: alenca198322@mail.ru. ORCID iD: <https://orcid.org/0000-0002-9036-7302>.

*Aleksey I. Slivkin*, DSc in Pharmacy, Professor, Head of the Department of Pharmaceutical Chemistry and Pharmaceutical Technology, Voronezh State University, Voronezh, Russian Federation; e-mail: slivkin@pharm.vsu.ru.

*Elena E. Chupandina*, DSc in Pharmacy, Professor, Head of the Department of Pharmacy Management and Economics and Pharmacognosy, Voronezh State University, Voronezh, Russian Federation; e-mail: chupandina@vsu.ru.

*Savva R. Naryshkin*, postgraduate student, Department of Analytical, Physical and Colloid Chemistry, A. P. Nelyubin Institute of Pharmacy, I. M. Sechenov First Moscow State Medical University (Sechenov University), Moscow, Russian Federation; e-mail: lonely.sloka@yandex.ru.

*Ivan I. Krasnyuk (Jr.)*, DSc in Pharmacy, Professor, Head of the Department of Analytical, Physical and Colloid Chemistry, A. P. Nelyubin Institute of Pharmacy, I. M. Sechenov First Moscow State Medical University (Sechenov University), Moscow, Russian Federation; e-mail: krasnyuk.79@mail.ru. ORCID iD: <https://orcid.org/0000-0002-7242-2988>.

*Ivan I. Krasnyuk*, DSc in Pharmacy, Professor, Head of the Department of Pharmaceutical Technology, A. P. Nelyubin Institute of Pharmacy, I. M. Sechenov First Moscow State Medical University (Sechenov University), Moscow, Russian Federation; e-mail: krasnyuki@mail.ru.

All authors have read and approved the final manuscript.

*Translated by Marina Strepetova*

*Edited and proofread by Simon Cox*



# Condensed Matter and Interphases (Kondensirovannye sredy i mezhfaznye granitsy)

## Original articles

DOI: <https://doi.org/10.17308/kcmf.2020.22/2821>

Received 12 March 2020

Accepted April 2020

Published online 25 June 2020

ISSN 1606-867X

eISSN 2687-0711

## Synthesis and Properties of Synthetic Aikinite $\text{PbCuBiS}_3$

© 2020 O. M. Aliev<sup>a</sup>, S. T. Bayramova<sup>b</sup>, D. S. Azhdarova<sup>a</sup>, Sh. H. Mammadov<sup>a✉</sup>, V. M. Ragimova<sup>a</sup>, T. F. Maksudova<sup>b</sup>

<sup>a</sup>M. Nagiyev Institute of Catalysis and Inorganic Chemistry of National Academy of Sciences of Azerbaijan, 113 G. Javid ave., Baku AZ 1143, Azerbaijan

<sup>b</sup>Baku European Lyceum, 37 Rostrupovich str., Baku AZ 1001, Azerbaijan

### Abstract

The goal of this study was the synthesis and study of the properties of synthetic aikinite,  $\text{PbCuBiS}_3$ .

The synthesis was carried out in evacuated quartz ampoules for 7–8 h; the maximum temperature was 1250–1325 K. Next, the samples were cooled and kept at 600 K for a week. Then the ampoules were opened, the samples were carefully ground, and after melting, annealed at 600–800 K, depending on the composition, for at least two weeks to bring the samples into equilibrium. The annealed samples were studied by differential thermal (DTA), X-ray diffraction (XRD), microstructural (MSA) analyses, as well as microhardness measurements and density determination. XRD was performed using D 2 PHASER with  $\text{CuK}_\alpha$  radiation and a Ni filter.

$\text{CuBiS}_2$ – $\text{PbS}$ ,  $\text{Cu}_2\text{S}$ – $\text{PbCuBiS}_3$ ,  $\text{Bi}_2\text{S}_3$ – $\text{PbCuBiS}_3$ ,  $\text{PbBi}_2\text{S}_4$ – $\text{PbCuBiS}_3$ ,  $\text{PbBi}_4\text{S}_7$ – $\text{PbCuBiS}_3$  sections of quasi-triple system  $\text{Cu}_2\text{S}$ – $\text{Bi}_2\text{S}_3$ – $\text{PbS}$  were studied using the complex of physical and chemical analysis methods and their phase diagrams were plotted. It was found that in addition to the  $\text{PbBi}_2\text{S}_4$ – $\text{PbCuBiS}_3$  section, all sections are quasi-binary and they were characterized by the presence of limited solubility regions based on the initial components. The study of the  $\text{CuBiS}_2$ – $\text{PbS}$  section revealed the formation of a quaternary compound  $\text{PbCuBiS}_3$  occurring in nature as the mineral aikinite, congruently melting at 980 K. We established that  $\text{PbCuBiS}_3$  crystallizes in a rhombic syngony with lattice parameters  $a = 1.1632$ ,  $b = 1.166$ ,  $c = 0.401$  nm,  $\text{Pnma}$  space group,  $Z = 4$ . Using DTA and XRD methods we established that  $\text{PbCuBiS}_3$  compound is a phase of variable composition with a homogeneity range from 45 to 52 mol%  $\text{PbS}$ . The  $\text{PbCuBiS}_3$  compound is a  $p$ -type semiconductor with a band gap energy of  $\Delta E = 0.84$  eV.

**Keywords:** aikinite, compound, single crystal, structure, thermodynamic function, band gap energy.

**For citation:** Aliev O. M., Bayramova S. T., Azhdarova D. S., Mammadov Sh. H., Ragimova V. M., Maksudova T. F. Synthesis and Properties of Synthetic Aikinite  $\text{PbCuBiS}_3$ . *Kondensirovannye sredy i mezhfaznye granitsy = Condensed Matter and Interphases*. 2020; 22(2): 182–189. DOI: <https://doi.org/10.17308/kcmf.2020.22/2821>

## 1. Introduction

Minerals possess specific semiconductor, optical, and electro-optical properties, allowing them to be used as semiconductors in special devices. All this determines the attention paid to the synthesis of aikinite and the growth of aikinite single crystals.

Now one of the most promising materials of modern electronics are chalcogenide phases of the  $\text{A}_2\text{B}_3$  type. Physicochemical and electrophysical parameters of these materials are easily

controllable and have a wide spectrum of action.  $\text{A}_2\text{B}_3$  type ( $\text{A} = \text{Sb, Bi}$ ;  $\text{B} = \text{S, Se, Te}$ ) chalcogenides possess thermoelectric and photoelectric properties. These features of the materials create favourable conditions for their widespread use in the electronics industry [1–7]

Compound  $\text{PbCuBiS}_3$  occurs in nature in the form of a mineral and crystallizes in rhombic syngony with a lattice period:  $a = 1.1632$ ,  $b = 1.166$ ,  $c = 0.401$  nm,  $\text{Pnma}$  space group,  $Z = 4$  [8–18]. The structure is similar to the structure of antimonite  $\text{K}_2\text{CuCl}_2$  and others [3] and similar to the structure of

✉ Sharafat H. Mammadov, e-mail: [azxim@mail.ru](mailto:azxim@mail.ru)



The content is available under Creative Commons Attribution 4.0 License.

bournonite  $\text{PbCuSbS}_3$  and zeligmannite  $\text{PbCuAsS}_3$ . The exact distribution of Pb and Bi atoms in the crystal lattice has not been elucidated. In comparison with  $\text{Bi}_2\text{S}_3$  in aikinite replacement of  $\text{Bi}^{+3}$  with  $\text{Pb}^{+2}$  compensated by the inclusion of a single  $\text{Cu}^+$  ion of such small size that it occupies the empty spaces of the lattice without distorting it.

The lead atoms in the aikinite structure are surrounded by five sulphur atoms with distances from 0.284 to 0.298 nm and two more sulphur atoms separated by 0.324 nm, and the coordination is close to octahedral (Fig. 1).

Extensive experimental studies of natural minerals showed that all the considered compounds are ordered, their compositions are limited to a certain stoichiometry and very narrow regions of solid solutions, as was previously assumed in [19]. According to available data, the structure of all these minerals is a derivative of the structure of bismuthine, obtained by substitution of Bi in the latter with Pb with the simultaneous addition of Cu atoms to the vacant tetrahedral sites  $\text{Cu} + \text{Pb} + \text{Bi}$  [8, 9]. There are three types of ribbons in the structures of these minerals [9], the combination of which can lead to the motives of all the minerals of this series: bismuthine  $\text{Bi}_4\text{S}_6$ , krupkaite  $\text{CuPbBi}_3\text{S}_6$ , and aikinite.

It should be noted that although the ratio between metal sulphides is  $\text{Cu}_2\text{S}:\text{PbS}$  in the aikinite–bismuthine series is constant and equal to 1:2, in a selenium-containing mineral of a similar composition  $\text{Cu}_2\text{Pb}_3\text{Bi}_8(\text{S}, \text{Se})_{16}$  it is 1:3, which also exhibited as slightly altered arrangement of atoms. The basis of the structural motif is composed by zigzag ribbons of Pb and Bi octahedra connected along the edges, linked together by pairs of other octahedrons also with an edge bonds. In the voids of this structure, additional Pb and Bi atoms are located in seven-dimensional coordination. The environment of Cu atoms is intermediate between tetrahedral and plane triangular, the Cu–S distances are 232 nm (3 S) and 252 nm (1 S) [13, 17].

Earlier, we [20, 25] synthesized and studied the physicochemical and physical properties of complex sulfosalts based on the  $\text{PbCuSbS}_3$  bournonite mineral.

The purpose of this work was the synthesis and study of the properties of synthetic aikinite  $\text{PbCuBiS}_3$ .

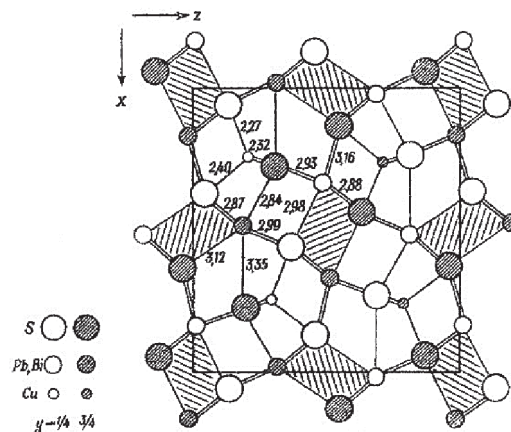


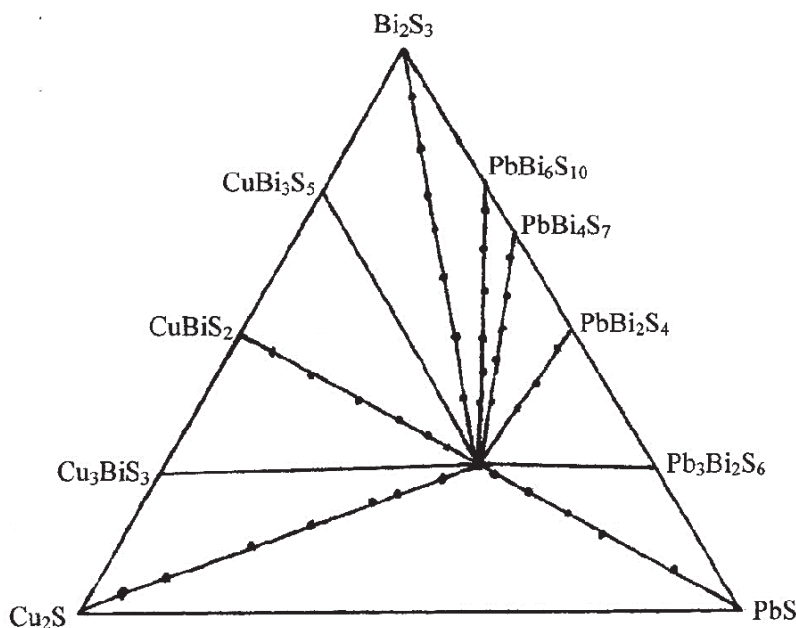
Fig. 1. The crystal structure of the aikinite mineral  $\text{PbCuBiS}_3$  [1]

## 2. Experimental

Quaternary sulfosalt  $\text{PbCuBiS}_3$  was revealed while studying the  $\text{CuBiS}_2\text{–PbS}$  section of the quasi-triple  $\text{Cu}_2\text{S–Bi}_2\text{S}_3\text{–PbS}$  system. The quasi-triple system, except for  $\text{CuBiS}_2\text{–PbS}$ , was studied by based on  $\text{Cu}_3\text{BiS}_3\text{–PbCuBiS}_3$ ,  $\text{CuBi}_3\text{S}_5\text{–PbCuBiS}_3$ ,  $\text{Cu}_2\text{S–PbCuBiS}_3$ ,  $\text{PbBi}_2\text{S}_4\text{–PbCuBiS}_3$ ,  $\text{PbBi}_4\text{S}_7\text{–PbCuBiS}_3$  and  $\text{Bi}_2\text{S}_3\text{–PbCuBiS}_3$  sections. The position of the connodes in the  $\text{Cu}_2\text{S–Bi}_2\text{S}_3\text{–PbS}$  system is shown in Fig. 2.

The quaternary alloys for the study were obtained by the vacuum-thermal method from the source alloys ( $\text{CuBiS}_2$ ,  $\text{PbS}$ ,  $\text{CuBi}_2\text{S}_4$  etc.), previously synthesized from ultra-pure elements ( $\text{Cu} - 99.997\%$ ,  $\text{Pb} - 99.994\text{ wt}\%$ ,  $\text{Bi} - 99.999\text{ wt}\%$ ,  $\text{S} - 99.9999\text{ wt}\%$ ). The maximum temperature was 1250–1325 K. The synthesis was carried out in evacuated quartz ampoules for 7–8 h; then, the samples were cooled and kept at 600 K for a week [26]. Then the ampoules were opened, the samples were carefully ground, and after melting, annealed at 600–800 K, depending on the composition, for at least two weeks to bring the samples into equilibrium, Table 1.

Annealed samples were studied by physicochemical analysis: thermal analysis was carried out using Kurnakov pyrometer NTR-73 (heating rate  $10^\circ/\text{min}$ , standard  $\text{Al}_2\text{O}_3$ , chromel–alumel thermocouple); XRD patterns were obtained using D 2 PHASER Brucker diffractometer ( $\text{CuK}_\alpha$ -radiation, Ni-filter); the microhardness of the samples was measured using PMT-3 microhardness tester (optimal load of 0.02 kg), the microstructure of the alloys



**Fig. 2.** The position of the connodes in the  $\text{PbS-Cu}_2\text{S-Bi}_2\text{S}_3$  system. The compositions of the synthesized samples are indicated by black dots

**Table 1.** Results of physicochemical analysis of alloys of the  $\text{CuSbS}_2\text{-PbS}$  system

Composition, mol% PbS	Thermal effects, K		Microhardness ( $\times 10^7$ Pa)	Density, g/cm <sup>3</sup>	Phase composition
	solidus	liquidus			
0.0	-	780	2200	7.40	$\text{CuBiS}_2$ (single phase)
5.0	715	765	2250	7.38	$\alpha$
10	650	730	2300	7.32	$\alpha+\beta$
15	650	690	2300	7.30	$\alpha+\beta$
20	650	700	eutectic	7.28	$\alpha+\beta$
25	650	765	-	7.28	$\alpha+\beta$
30	650	830	1980	7.26	$\alpha+\beta$
40	650	925	1980	7.24	$\alpha+\beta$
45	-	970	1970	7.22	$\beta$
50	-	980	1980	7.20	$\beta$
52	-	970	1990	-	$\beta$
55	815	930	1990	-	$\beta + \text{PbS}$
60	810	865	-	7.12	$\beta + \text{PbS}$
65	815	-	eutectic	7.06	$\beta + \text{PbS}$
70	815	920	720	6.90	$\beta + \text{PbS}$
80	815	1070	720	6.82	$\beta + \text{PbS}$
90	815	1240	720	6.70	$\beta + \text{PbS}$
100	-	1400	720	6.11	Pbs (single phase)

was studied using a MIM-7 microscope, and the density was determined by the pycnometer.

### 3. Results and discussion

We will discuss in details the  $\text{CuSbS}_2\text{-PbS}$  system, in which the sulfosalt  $\text{PbCuBiS}_3$  was found.

As can be seen from Table 1, the microhardness value related to the  $\text{PbCuBiS}_3$  quaternary compound, increased on both sides from 50 mol% PbS, but it decreased with stoichiometric composition. This shows that a range of homogeneity exists based on the  $\text{PbCuBiS}_3$  compound. According to the results of XRD and microstructural analysis, it

was found that  $\text{PbCuBiS}_3$  is a phase of variable composition and that solubility at a eutectic temperature (650 K) was 10 mol%, while with decreasing temperature it sharply narrows, not exceeding 7 mol% PbS at 300 K.

The MSA analysis showed that with the exception of compositions 0–7 and 45–52 mol% PbS, all alloys were biphasic.

According to the physicochemical analysis, a phase diagram of the  $\text{CuBiS}_2$ –PbS system was plotted and it is shown in Fig. 3. As can be seen from the figure, the system is characterized by the presence of  $\text{PbCuBiS}_3$  sulfosalt melting at 980 K congruently. Coordinates of eutectic points: 20 mol% PbS 650 K, and 65 mol% PbS 815 K. XRD demonstrated that in the range of concentrations of 0–7 mol% PbS, only reflections related to  $\text{CuBiS}_2$  were observed on diffractograms. These solutions crystallize in rhombic syngony, and with an increase in the concentration of PbS, the lattice parameters increase ( $a = 0.614 \div 0.620$ ,  $b = 0.391 \div 0.395$ ,  $c = 1.493 \div 1.502$  nm,  $\text{Pnma}$  space group,  $Z = 4$ ).

In the range of concentration 7–45 mol% PbS  $\alpha$ -solid solutions based on  $\text{CuBiS}_2$  and  $\beta$ -solid solutions based on quaternary sulfosalt  $\text{PbCuBiS}_3$  co-crystallize and in the 52–100 mol% PbS two phases ( $\beta + \text{PbS}$ ) co-crystallize. Composition 50 mol% PbS in terms of interplanar spacing and intensity differed from the source sulphides. Calculation of XRD patterns of the quaternary compound  $\text{PbCuBiS}_3$ , as well as XRD patterns of the initial sulphides for comparison are presented in Table 2.

X-ray analysis confirmed the formation of quaternary sulfosalts  $\text{PbCuBiS}_3$  found in nature in the form of the mineral aikinite in  $\text{CuBiS}_2$ –PbS system. It was found that sulfosalt crystallizes in rhombic syngony with unit cell parameters  $a = 1.1632$ ,  $b = 1.166$ ,  $c = 0.4017$  nm,  $\text{Pnma}$  space group,  $Z = 4$ .

The  $\text{Bi}_2\text{S}_3$ – $\text{PbCuBiS}_3$  section is of eutectic type. The composition of the eutectic point determined by the plotting of the Tamman's triangle was 50 mol%  $\text{Bi}_2\text{S}_3$  at 800 K. Solubility based on  $\text{Bi}_2\text{S}_3$  was 5 mol%, based on  $\text{PbCuBiS}_3$  – 7 mol% (Fig. 4a).

The  $\text{Cu}_2\text{S}$  –  $\text{PbCuBiS}_3$  section was quasi-binary and eutectic with limited solubility based on the starting sulphides (Fig. 4b).

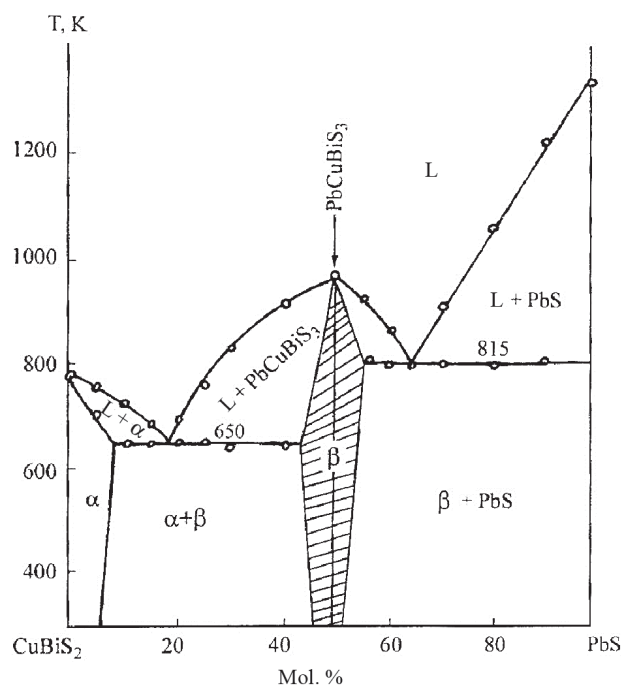


Fig. 3. Phase diagram of the  $\text{CuBiS}_2$ –PbS system

Conclusion on the formation of solid solutions based on  $\alpha$ -,  $\beta$ - and  $\gamma$ - $\text{Cu}_2\text{S}$  was based on the results of the DTA and MSA methods. On thermograms of samples containing 7 and 8 mol %  $\text{PbCuBiS}_3$ , thermal effects below the solidus temperature were revealed. These effects were associated with the formation and decomposition of a solid solution based on  $\gamma$ - $\text{Cu}_2\text{S}$ . This was also confirmed by the MSA data. In samples containing from 2 to 5.5 mol%  $\text{PbCuBiS}_3$ , the second phase was present in the form of needle insertions, and eutectic was not revealed. In the  $\text{Cu}_2\text{S}$ – $\text{PbCuBiS}_3$  system in the range of concentrations of 2.0–90 mol%  $\text{PbCuBiS}_3$  in a condensed state, two phases were in equilibrium:  $\alpha$ - $\text{Cu}_2\text{S}$ -based solid solution and  $\beta$ - $\text{PbCuBiS}_3$  based solid solution. They were clearly distinguishable by MSA and formed a eutectic of the composition 40 mol %  $\text{Cu}_2\text{S}$  and  $T = 850$  K. Eutectic in the indicated concentration range was present on the sections of all section samples and it was represented by the alternation of needle crystals of the  $\text{PbCuBiS}_3$  phase and oval  $\text{Cu}_2\text{S}$  crystals. Based on  $\alpha$ - $\text{Cu}_2\text{S}$  a limited solution was formed, which at 300 K reached 2 mol%  $\text{PbCuBiS}_3$ .

The phase transitions  $\alpha$ - $\text{Cu}_2\text{S} \leftrightarrow \beta$ - $\text{Cu}_2\text{S} \leftrightarrow \gamma$ - $\text{Cu}_2\text{S}$  had a eutectic nature and occurred at 375 and 580 K, respectively. Thermal effects related to  $\beta$ - $\text{Cu}_2\text{S} \leftrightarrow \gamma$ - $\text{Cu}_2\text{S}$  were revealed only for alloys



**Table 2.** Interplanar distances and intensities of the  $\text{CuBiS}_2$ ,  $\text{PbCuBiS}_3$  and  $\text{PbS}$  lines for comparison

$\text{CuBiS}_2$		$\text{PbCuBiS}_3$			$\text{PbS}$	
$d_{\text{exp}}, \text{\AA}$	$I/I_0$	$d_{\text{exp}}, \text{\AA}$	$I/I_0$	$hkl$	$d_{\text{exp}}, \text{\AA}$	$I/I_0$
4.700	8	4.070	4	220	3.790	2
3.200	10	3.770	1	011	3.442	9
3.100	8	3.670	10	130	3.283	3
3.020	10	3.580	7	111, 310	2.965	10
2.810	2	3.180	9	121	2.311	2
2.340	9	2.880	8	040, 221	2.693	10
2.290	4	2.740	2	410	1.780	9
2.160	9	2.680	3	131, 330	1.707	8
1.960	5	2.620	6	311	1.480	5
1.880	7	2.580	1	240	1.359	6
1.800	8	2.560	1	420	1.324	10
1.780	3	2.510	3	231	1.209	8
1.755	3	2.570	2	150	1.141	7
1.655	8	2.170	3	241	1.048	3
1.560	5	2.150	3	250, 421		
1.475	2	2.020	5	440, 051		
1.450	4	1.984	4	431, 151		
1.365	3	1.974	3	530, 112		
1.320	4	1.883	1	202, 600		
1.260	2	1.805	4	441		
1.125	5	1.766	1	351, 133		
1.208	5	1.648	4	042, 170		
1.190	5	1.593	4	270		
1.168	7	1.514	1	370		
1.112	3	1.475	2	171		
1.100	3	1.406	4	740		
		1.380	2	561		
		1.354	2	612		
		1.330	3	003		
		1.278	2	661		
		1.158	1	770		

containing 10÷20 mol%  $\text{PbCuBiS}_3$ , therefore, this transition in Fig. 4b was marked with a dotted line.

The  $\text{PbBi}_2\text{S}_4$ – $\text{PbCuBiS}_3$  section was partially quasi-binary due to the incongruent nature of the melting of sulphide  $\text{PbBi}_2\text{S}_4$ . The solubility based on  $\text{PbCuBiS}_3$  sulfosalt was 8 mol% at 300 K, and at a eutectic temperature of 15 mol% Coordinates of the eutectic point were 40 mol%  $\text{PbCuBiS}_3$  and  $T = 825$  K.

The  $\text{PbBi}_4\text{S}_7$ – $\text{PbCuBiS}_3$  section was quasi-binary and eutectic with limited solid solutions. The eutectic corresponds to 55 mol%  $\text{PbBi}_4\text{S}_7$  and 800 K. The solubility of  $\text{PbCuBiS}_3$  in  $\text{PbBi}_4\text{S}_7$  at eutectic temperature was 10 mol%, at 300 K it

decreased to 5 mol%  $\text{PbCuBiS}_3$  ( $\alpha$ -solid solution), and the solubility of  $\text{PbBi}_4\text{S}_7$  in quaternary sulphide was 18 mol% at eutectic temperature and decreased to 10 mol%  $\text{PbBi}_4\text{S}_7$  at 300 K ( $\beta$ -solid solution).

$\text{PbCuBiS}_3$  single crystals were obtained by targeted crystallization of a stoichiometric melt in vertical quartz ampoules. An ampoule with a cone-shaped bottom was placed in a furnace with a small temperature gradient in height. After the formation of the melt, directed cooling was carried out at a speed of 4 °/h for 48 h until the entire melt solidified, then the furnace was cooled at a speed of 60 °/h. Thus, polycrystalline ingots with a large number of cracks were obtained.

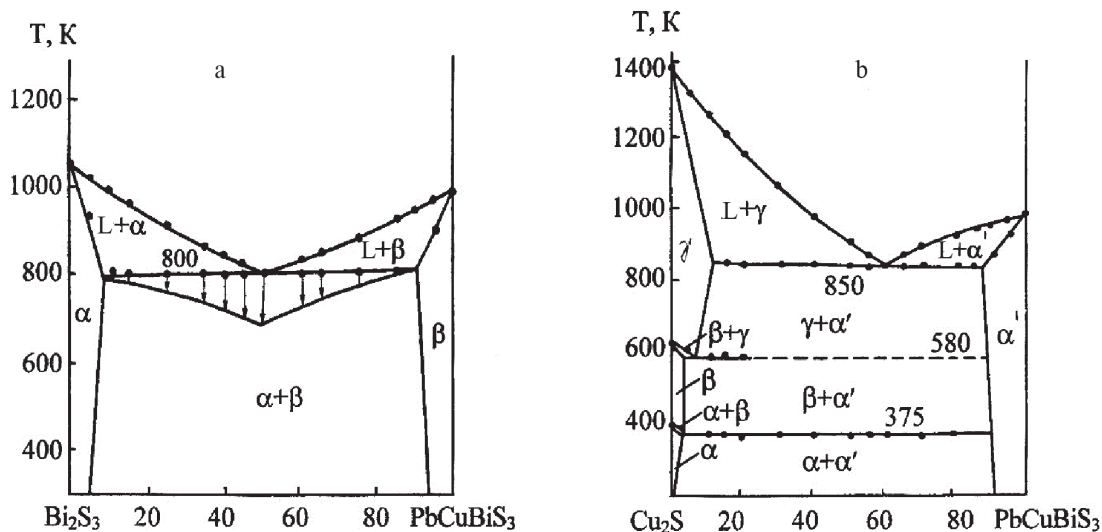


Fig. 4. Phase diagram of the  $\text{Bi}_2\text{S}_3$ – $\text{PbCuBiS}_3$  (a) and  $\text{Cu}_2\text{S}$ – $\text{PbCuBiS}_3$  (b) systems

However, it was possible to cut single crystal sections with a length of 1 mm, free of visible defects from these ingots (Fig. 5).

Significantly larger single crystals of the  $\text{PbCuBiS}_3$  compound were obtained by the similar method in quartz ampoules with a diameter of 5 mm. The single crystals reached a length of 8–12 mm with a diameter of 5 mm. One feature of the  $\text{PbCuBiS}_3$  compound should be noted: directional crystallization of stoichiometric composition without special additives always provided ingots characterized mainly by p-type conductivity. It is possible that this was the result of a deviation from stoichiometry due to the combination of volatile components (sulphur and bismuth). The ingot always contained an excess of copper, which in significant quantities dissolves in the compound and provides p-type conductivity. Therefore, any doping of the  $\text{PbCuBiS}_3$  compound (obtained  $\text{PbCuBiS}_3$  crystals were doped with erbium) during crystal growth by directed

cooling will occur against the background of this phenomenon.

The standard thermodynamic functions of the  $\text{PbCuBiS}_3$  compound were calculated:  $S_{298}^0 = 253.1 \pm 5 \text{ J}/(\text{mol}\%)$ ,  $\Delta S_{298}^0 = -14.1 \pm 3 \text{ J}/\text{mol}$ ,  $\Delta H_{298}^0 = -270.2 \pm 10 \text{ kJ}/\text{mol}$  and  $\Delta G_{298}^0 = -266.3 \pm 10 \text{ kJ}/\text{mol}$

The photoconductivity spectra of pure  $\text{PbCuBiS}_3$  crystals and crystals doped with erbium grown by the directed crystallization method from the melt were studied. The spectral dependences of these sulfosalts are shown in Fig. 6. As can be seen, crystals grown by directional crystallization had approximately the same photosensitivity, which at 293 K was  $I_{sc}/I_t = 10^5$  when illuminated by natural light, and when the temperature decreased, it grew and reached  $10^5$  at 100 K. In



Fig. 5. Single crystals of the  $\text{PbCuBiS}_3$  compound

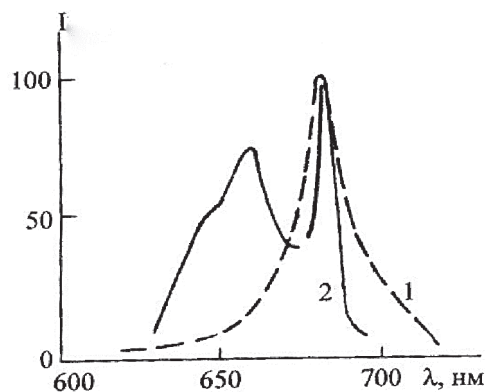


Fig. 6. The spectral dependence of the photoconductivity of  $\text{PbCuBiS}_3$  (1) and  $\text{PbCuBiS}_3$ –Er (2) grown by the directed crystallization method

crystals of both types, bands of shallow levels – traps with an activation energy of 0.25–0.35 eV, as well as trap levels with an activation energy  $\Delta E = 0.50$ –0.60 eV, were observed. The band gap energy calculated from photoconductivity was  $\Delta E = 0.84$ –0.91 eV.

Thus, the nature of the formation of  $\text{PbCuBiS}_3$  sulfosalt was revealed based on studying the quasi-triple  $\text{Cu}_2\text{S}$ – $\text{Bi}_2\text{S}_3$ – $\text{PbS}$  system based on  $\text{CuBiS}_2$ – $\text{PbS}$ ,  $\text{Cu}_2\text{S}$ – $\text{PbCuBiS}_3$ ,  $\text{PbBi}_2\text{S}_4$ – $\text{PbCuBiS}_3$ ,  $\text{PbBi}_4\text{S}_7$ – $\text{PbCuBiS}_3$  and  $\text{Bi}_2\text{S}_3$ – $\text{PbCuBiS}_3$  sections. The single crystals of synthetic aikinite  $\text{PbCuBiS}_3$  were grown and some of its properties were studied.

#### 4. Conclusions

1. The  $\text{CuBiS}_2$ – $\text{PbS}$ ,  $\text{Cu}_2\text{S}$ – $\text{PbCuBiS}_3$ ,  $\text{Bi}_2\text{S}_3$ – $\text{PbCuBiS}_3$ ,  $\text{PbBi}_2\text{S}_4$ – $\text{PbCuBiS}_3$ ,  $\text{PbBi}_4\text{S}_7$ – $\text{PbCuBiS}_3$  sections of quasi-triple  $\text{Cu}_2\text{S}$ – $\text{Bi}_2\text{S}_3$ – $\text{PbS}$  system were studied by a set of physicochemical analysis methods and their phase diagrams were plotted. It was established that in addition to the  $\text{PbBi}_2\text{S}_4$ – $\text{PbCuBiS}_3$  section, all sections were quasi-binary and they were characterized by the presence of limited solubility regions based on the source components.

2. The study of  $\text{CuBiS}_2$ – $\text{PbS}$  section revealed the formation of a quaternary compound of the  $\text{PbCuBiS}_3$  composition, found in nature in the form of the mineral aikinite, melting congruently at 980 K. It was established that  $\text{PbCuBiS}_3$  crystallizes in rhombic syngony with lattice parameters  $a = 1.1632$ ,  $b = 1.166$ ,  $c = 0.401$  nm,  $\text{Pnma}$  space group,  $Z = 4$ .

3.  $\text{PbCuBiS}_3$  single crystals were grown by directional crystallization and the spectral dependence of photoconductivity was studied. It was established that  $\text{PbCuBiS}_3$  possesses photosensitivity in the visible region of the spectrum.

#### Conflict of interests

The authors declare that they have no known competing financial interests or personal relationships that could have influenced the work reported in this paper.

#### References

- Zhang Y-X., Ge Z-H., Feng J. Enhanced thermoelectric properties of  $\text{Cu}_{1.8}\text{S}$  via introducing  $\text{Bi}_2\text{S}_3$  and  $\text{Bi}_2\text{S}_3/\text{Bi}$  core-shell nanorods. *Journal of Alloys and Compounds*. 2017;727: 1076–1082. DOI: <https://doi.org/10.1016/j.jallcom.2017.08.224>
- Mahuli N., Saha D., Sarkar S. K. Atomic layer deposition of p-type  $\text{Bi}_2\text{S}_3$ . *Journal of Physical Chemistry C*. 2017;121(14): 8136–8144. DOI: <https://doi.org/10.1021/acs.jpcc.6b12629>
- Ge Z-H, Qin P., He D, Chong X., Feng D., Ji Y-H., Feng J., He J. Highly enhanced thermoelectric

properties of  $\text{Bi}/\text{Bi}_2\text{S}_3$  nano composites. *ACS Applied Materials & Interfaces*. 2017;9(5): 4828–4834. DOI: <https://doi.org/10.1021/acsami.6b14803>

4. Savory C. N., Ganose A. M., Scanlon D. O. Exploring the  $\text{PbS}$ – $\text{Bi}_2\text{S}_3$  series for next generation energy conversion materials. *Chemistry of Materials*. 2017;29(12): 5156–5167. DOI: <https://doi.org/10.1021/acs.chemmater.7b00628>

5. Li X., Wu Y, Ying H., Xu M., Jin C., He Z., Zhang Q., Su W., Zhao S. In situ physical examination of  $\text{Bi}_2\text{S}_3$  nanowires with a microscope. *Journal of Alloys and Compounds*. 2019;798: 628–634. DOI: <https://doi.org/10.1016/j.jallcom.2019.05.319>

6. Patila S. A., Hwanga Y-T., Jadhav V. V., Kim K. H., Kim H-S. Solution processed growth and photoelectrochemistry of  $\text{Bi}_2\text{S}_3$  nanorods thin film. *Journal of Photochemistry & Photobiology, A: Chemistry*. 2017;332: 174–181. DOI: <https://doi.org/10.1016/j.jphotochem.2016.07.037>

7. Yang M., Luo Y. Z., Zeng M. G., Shen L., Lu Y. H., Zhou J., Wang S. J., Souf I. K., Feng Y. P. Pressure induced topological phase transition in layered  $\text{Bi}_2\text{S}_3$ . *Physical Chemistry Chemical Physics*. 2017;19(43): 29372–29380. DOI: <https://doi.org/10.1039/C7CP04583B>

8. Kohatsu I., Wuensch B. J. The crystal structure of aikinite,  $\text{PbCuBiS}_3$ . *Acta Crystallogr*. 1971;27(6): 1245–1252. DOI: <https://doi.org/10.1107/s0567740871003819>

9. Ohmasa M., Nowacki W. A redetermination on the crystal structure of aikinite ( $\text{BiS}_2/\text{S}/\text{Cu}^{\text{IV}}\text{Pb}^{\text{VII}}$ ). *Z. Kristallogr*. 1970;132(1–6): 71–86. DOI: <https://doi.org/10.1524/zkri.1970.132.1-6.71>

10. Strobel S., Sohleid T. Three structures for strontium copper (I) lanthanidid (III) selinides  $\text{SrCuMeSe}_3$  ( $\text{M}=\text{La}$ ,  $\text{Gd}$ ,  $\text{Lu}$ ). *J. Alloys and Compounds*. 2006;418(1–2): 80–85. DOI: <https://doi.org/10.1016/j.jallcom.2005.09.090>

11. Sikerina N. V., Andreev O. V. Kristallicheskaya struktura soedinenii  $\text{SrLnCuS}_3$  ( $\text{Ln}=\text{Gd}$ ,  $\text{Lu}$ ) [Crystal structure of  $\text{SrLnCuS}_3$  compounds ( $\text{Ln} = \text{Gd}$ ,  $\text{Lu}$ )]. *Russian Journal of Inorganic Chemistry*. 2007;52(4): 641–644. Available at: <https://www.elibrary.ru/item.asp?id=9594111> (In Russ.)

12. Edenharter A., Nowacki W., Takeuchi Y. Verfeinerung der kristallstruktur von Bournonit [ $(\text{SbS}_3)_1/\text{Cu}_2^{\text{IV}}\text{Pb}^{\text{VII}}\text{Pb}^{\text{VIII}}$ ] und von seligmannit [ $(\text{AsS}_3)_2/\text{Cu}_2^{\text{IV}}\text{Pb}^{\text{VII}}\text{Pb}^{\text{VIII}}$ ]. *Z. Kristallogr*. 1970;131(1): 397–417. DOI: <https://doi.org/10.1524/zkri.1970.131.1-6.397>

13. Kaplunnik L. N. Kristallicheskie struktury mineralov velikita, aktashita, shvatsita, tennantita, galkhaita, lindstremita-krupkaita i sinteticheskoi  $\text{Pb}$ ,  $\text{Sn}$  sul'fosoli [The crystal structures of the minerals are granite, actashite, schwa-cit, tennantite, galhaite, lindstromite-krupkaite and synthetic  $\text{Pb}$ ,  $\text{Sn}$  sulphosols]. *Abstract. diss. cand. geol.-miner. sciences*. Moscow: MSU Publ.; 1978. 25 p. Available

at: <https://search.rsl.ru/ru/record/01007805415> (In Russ.)

14. Gasymov V. A., Mamedov H. S. On the crystal chemistry of the intermediate phases of the vis-mutin-aikinite system ( $\text{Bi}_2\text{S}_3\text{-CuPbBiS}_3$ ). *Azerb. khim. zhurn.* [Azerbaijan Chemical Journal]. 1976;(1): 121–125. Available at: <https://cyberleninka.ru/article/n/fazovye-ravnovesiya-v-sisteme-pbla2s4-pbbi2s4> (In Russ., abstract in Eng.)

15. Christuk A. E., Wu P., Ibers J. A. New quaternary chalcogenides  $\text{BaLnMQ}_3$  (Ln – Rare Earth; M = Cu, Ag; Q = S, Se). *J. Solid State Chem.* 1994;110(2): 330–336. DOI: <https://doi.org/10.1006/jssc.1994.1176>

16. Wu P., Ibers J. A. Synthesis of the new quaternary sulfides  $\text{K}_2\text{Y}_4\text{Sn}_2\text{S}_{11}$  and  $\text{BaLnAgS}_3$  (Ln = Er, Y, Gd) and the Structures of  $\text{K}_2\text{Y}_4\text{Sn}_2\text{S}_{11}$  and  $\text{BaErAgS}_3$ . *J. Solid State Chem.* 1994;110(1): 156–161. DOI: <https://doi.org/10.1006/jssc.1994.1150>

17. Pobedimskaya E. A., Kaplunnik L. N., Petrova I. V. *Crystal chemistry of sulfides. Results of Science and Technology. Series crystal chemistry.* Moscow: Publishing House of the Academy of Sciences of the USSR; 1983. 17: 164 p. (In Russ.)

18. Gulay L. D., Shemet V. Ya., Olekseyuk I. D. Investigation of the  $\text{R}_2\text{S}_3\text{-Cu}_2\text{S-PbS}$  (R = Y, Dy, Ho and Er) systems. *J. Alloys and Compounds.* 2007;43(1–2): 77–84. DOI: <https://doi.org/10.1016/j.jallcom.2006.05.029>

19. Kostov I., Mincheva-Stefanova I. *Sulfide minerals.* Moscow: Mir, 1984. 281 p.

20. Alieva R. A., Bayrмова S. T., Aliev O. M. Phase diagrams of the  $\text{CuSbS}_2\text{-MS}$  (M = Pb, Eu, Yb) systems. *Inorganic Materials.* 2010;46(7): 703–706. DOI: <https://doi.org/10.1134/S0020168510070022>

21. Bayramova S. T., Bagieva M. R., Aliev O. M., Ragimova V. M. Synthesis and properties of structural analogs of the mineral bournonite. *Inorganic Materials.* 2011;47(4): 345–348. DOI: <https://doi.org/10.1134/S0020168511040054>

22. Bayramova S. T., Bagieva M. R., Aliev O. M. Phase relations in the  $\text{CuAsS}_2\text{-MS}$  (M = Pb, Eu, Yb) systems. *Inorganic Materials.* 2011; 47 (3): 231–234. DOI: <https://doi.org/10.1134/S0020168511030046>

23. Aliev O. M., Ajdarova D. S., Bayramova S. T., Ragimova V. M. Nonstoichiometry in  $\text{PbCuSbS}_3$ . *Azerb. chem. journal.* 2016;(2): 51–54. Available at: <https://cyberleninka.ru/article/n/nonstoichiometry-in-pbcusbs3-compound>

24. Aliev O. M., Ajdarova D. S., Agayeva R. M., Ragimova V. M. Phase formation in quaternary system  $\text{Cu}_2\text{S-PbS-Sb}_2\text{S}_3$ . *Intern Journal of Application and Fundamental Research.* 2016;(12): 1482–1488. Available at: [https://applied-research.ru/pdf/2016/2016\\_12\\_8.pdf](https://applied-research.ru/pdf/2016/2016_12_8.pdf) (In Russ., abstract in Eng.)

25. Aliev O. M., Azhdarova D. S., Agayeva R. M., Maksudova T. F. Phase relations along the  $\text{Cu}_2\text{S}(\text{Sb}_2\text{S}_3, \text{PbSb}_2\text{S}_4, \text{Pb}_5\text{Sb}_4\text{S}_{11})\text{-PbCuSbS}_3$  joins in the pseudoternary system  $\text{Cu}_2\text{S-PbS-Sb}_2\text{S}_3$  and physical properties of  $(\text{Sb}_2\text{S}_3)_{1-x}(\text{PbCuSbS}_3)_x$  solid solutions. *Inorganic Materials.* 2018;54(12): 1199–1204. DOI: <https://doi.org/10.1134/S0020168518120014>

26. Rzaguluev V. A., Kerimli O. Sh., Azhdarova D. S., Mammadov Sh. H., Aliev O. M. Phase equilibria in the  $\text{Ag}_8\text{SnS}_6\text{-Cu}_2\text{SnS}_3$  and  $\text{Ag}_2\text{SnS}_3\text{-Cu}_2\text{Sn}_4\text{S}_9$  systems. *Kondensirovannye sredy i mezhfaznye granitsy = Condensed Matter and Interphases.* 2019;21 (4): 544–551. DOI: <https://doi.org/10.17308/kcmf.2019.21/2365> (In Russ., abstract in Eng.)

### Information about the authors

*Ozbek M. Aliev*, DSc in Chemistry, Professor, M. Nagiyev Institute of Catalysis and Inorganic Chemistry of National Academy of Sciences of Azerbaijan, Baku, Azerbaijan; e-mail: [azxim@mail.ru](mailto:azxim@mail.ru).

*Sabina T. Bayramova*, PhD in Chemistry, Baku European Lyceum, Baku, Azerbaijan; e-mail: [azxim@mail.ru](mailto:azxim@mail.ru).

*Dilbar S. Ajdarova*, DSc in Chemistry, Chief Researcher, M. Nagiyev Institute of Catalysis and Inorganic Chemistry of National Academy of Sciences of Azerbaijan, Baku, Azerbaijan; e-mail: [azxim@mail.ru](mailto:azxim@mail.ru).

*Valida M. Ragimova*, PhD in Chemistry, Assistant Professor, Leading Researcher, M. Nagiyev Institute of Catalysis and Inorganic Chemistry of National Academy of Sciences of Azerbaijan, Baku, Azerbaijan; e-mail: [azxim@mail.ru](mailto:azxim@mail.ru).

*Sharafat H. Mammadov*, PhD in Chemistry, Assistant Professor, M. Nagiyev Institute of Catalysis and Inorganic Chemistry of National Academy of Sciences of Azerbaijan, Baku, Azerbaijan; e-mail: [azxim@mail.ru](mailto:azxim@mail.ru). ORCID ID: <https://orcid.org/0000-0002-1624-7345>.

All authors have read and approved the final manuscript.

*Translated by Valentina Mittova*

*Edited and proofread by Simon Cox*



# Condensed Matter and Interphases (Kondensirovannye sredy i mezhfaznye granitsy)

## Original articles

DOI: <https://doi.org/10.17308/kcmf.2020.22/2822>

Received 30 January 2020

Accepted 15 April 2020

Published online 25 June 2020

ISSN 1606-867X

eISSN 2687-0711

## The Physics of Interfacial Adhesion between a Polymer Matrix and Carbon Nanotubes (Nanofibers) in Nanocomposites

©2019 L. B. Atlukhanova<sup>a</sup>, I. V. Dolbin<sup>✉,b</sup>, G. V. Kozlov<sup>b</sup>

<sup>a</sup>Dagestan State Medical University,  
1 Lenina pl., Makhachkala 367000, Russian Federation

<sup>b</sup>Kh. M. Berbekov Kabardino-Balkarian State University,  
173 Chernyshevskogo ul., Nalchik 360004, Russian Federation

### Abstract

The aim of this study was to investigate the physics of interfacial adhesion in polymer/carbon nanotube systems. The study was carried out on polypropylene/carbon nanotube (nanofiber) nanocomposites employing fractal analysis.

Due to a high degree of anisotropy and low bending stiffness, carbon nanotubes (nanofibers) form ring-like structures in the polymer matrix of the nanocomposite, which are structural analogue of macromolecular coils of branched polymers. This allowed us to simulate the structure of polymer/carbon nanotube (nanofiber) nanocomposites as a polymer solution, using the methods of fractal physical chemistry. Using this approach we assume that macromolecular coils are represented by the ring-like structures of carbon nanotubes and the solvent is represented by the polymer matrix. The suggested model can be used to perform structural analysis of the level of interfacial interaction between the polymer matrix and the nanofiller, i.e. the level of interfacial adhesion. The analysis demonstrated that most contacts between carbon nanotubes and the polymer matrix, which determine the adhesion level, take place inside the ring-like structures. The fractal analysis showed that a decrease in the radius of the ring-like structures or their compactization increases the fractal dimension, which makes it difficult for the matrix polymer to penetrate into these structures. This results in a decrease in the number of contacts between the polymer and the nanofiller and a significant reduction of the level of interfacial adhesion. This effect can also be described as the consequence of compactization of the ring-like structures, demonstrated by the increased density. The article shows a direct correlation between the value of interfacial adhesion (dimensionless parameter  $b_{\sigma}$ ), the number of contacts between the polymer and carbon nanotubes, and the volume of the ring-like structures, accessible for penetration by the polymer. The quantitative analysis demonstrated, that the number of interactions occurring on the surface of ring-like structures of carbon nanotubes (nanofibers) is only ~ 7–10 %. The suggested model allowed us to determine the correlation between the structure of the nanofiller in the polymer matrix and the level of interfacial adhesion for this class of nanocomposites.

The results of our study can be used to define the structure of carbon nanotubes (nanofibers) necessary to obtain the highest level of interfacial adhesion.

**Keywords:** nanocomposite, carbon nanotubes (nanofibers), interfacial adhesion, ring-like structures, fractal analysis.

**For citation:** Atlukhanova L. B., Dolbin I. V., Kozlov G. V. The physics of interfacial adhesion between a polymer matrix and carbon nanotubes (nanofibers) in nanocomposites. *Kondensirovannye sredy i mezhfaznye granitsy = Condensed Matter and Interphases*. 2020;22(2): 190-196. DOI: <https://doi.org/10.17308/kcmf.2020.22/2822>

### 1. Introduction

The level of interfacial adhesion between the polymer matrix and the filler (nanofiller) is the key factor determining the properties of polymer composites (nanocomposites). The

authors [1–4] demonstrated that a high level of interfacial adhesion reinforces polymer nanocomposites, while the absence of adhesion may result in a decrease in the elastic modulus of a nanocomposite below the corresponding parameter of the matrix polymer. Today, carbon

✉ Igor V. Dolbin, e-mail: [i\\_dolbin@mail.ru](mailto:i_dolbin@mail.ru)



The content is available under Creative Commons Attribution 4.0 License.

nanotubes (nanofibers) are considered to be among the most promising nanofillers used in polymers [5–10]. It is known [11–13], that the said nanofillers form ring-like structures in the polymer matrix which are similar to macromolecular coils due to their high degree of anisotropy and low bending stiffness. In work [13] demonstrated that the characteristics of these ring-like structures have a significant effect on both the level of interfacial adhesion and the properties of polymer nanocomposites filled with carbon nanotubes (nanofibers). Therefore, the purpose of this study was to investigate the physics of interfacial adhesion in polypropylene/carbon nanotube (nanofiber) nanocomposites.

## 2. Experimental

Kaplen 01030 polypropylene (PP) was used as the matrix. This type of PP is characterised by the melt flow rate of 2.3–3.6 g/10 min (the mass of polymer, in grams, flowing in 10 minutes through a standard capillary rheometer (viscometer) under specific conditions), with the weight-average molecular weight being  $\sim (2-3) \times 10^5$  and the polydispersity index being 4.5.

The nanofillers were Taunite carbon nanotubes (CNTs) with 20–70 nm outer diameter, 5–10 nm inner diameter, and 2  $\mu\text{m}$  length. The concentration of taunite in PP/CNT nanocomposites varied within the range of 0.25–3.0 wt%. We also used 20–30 layer carbon nanofibers (CNFs) with a diameter of 20–30 nm and a length of about 2  $\mu\text{m}$ . The concentration of CNFs in PP/CNF nanocomposites varied within the range of 0.15–3.0 wt%.

PP/CNT and PP/CNF nanocomposites were prepared by mixing the components in melt on a twin screw extruder Thermo Haake, model Reomex RTW 25/42 (Germany). The mixing was performed at a temperature of 463–503 K and a screw speed of 50 rpm for 5 minutes. The testing samples were obtained by injection moulding on a Ray-Ran casting machine Test Sample Molding Apparate RR/TS MP (Taiwan) at a temperature of 503 K and a pressure of 43 MPa.

Uniaxial tension testing was performed on the samples in the shape of a two-sided spade with the size conforming to GOST 112 62-80. The tests were conducted on a universal testing machine

Gotech Testing Machine CT-TCS 2000 (Germany), at the temperature of 293 K and the strain rate of  $\sim 2 \times 10^{-3} \text{ sec}^{-1}$ .

## 3. Results and discussion

As stated above, carbon nanotubes (nanofibers) form ring-like structures in the polymer matrix of the nanocomposite, which are similar to macromolecular coils [11–15]. We can therefore describe them using established theoretical methods of both classic [6] and fractal [16] physical chemistry of polymer solutions. In the latter case, carbon nanotubes (nanofibers) are modelled as macromolecular coils, and the polymer matrix is modelled as the solvent. The fractal analysis demonstrated [16], that the number of interactions between CNTs (CNFs) and the polymer matrix  $n$  can be determined the same way as the one used for polymer solutions:

$$n \sim R_{\text{CNT}}^{D_f^{\text{PP}}}, \quad (1)$$

where  $R_{\text{CNT}}$  is the radius of the ring-like structures of CNTs (CNFs) and  $D_f^{\text{PP}}$  is the fractal dimension of the macromolecular coils of the matrix polymer (in our study, PP), which in this case represent the molecules of the solvent.  $R_{\text{CNT}}$  can be determined within the percolative model using the following equation [17]:

$$\varphi_n = \frac{\pi L_{\text{CNT}} r_{\text{CNT}}^2}{(2R_{\text{CNT}})^3}, \quad (2)$$

where  $\varphi_n$  is the volume fraction of the nanofiller,  $L_{\text{CNT}}$  and  $r_{\text{CNT}}$  are the length and the radius of the carbon nanotube (nanofiber) respectively.

The value of  $\varphi_n$  can be determined using a well-known formula [1]:

$$\varphi_n = \frac{W_n}{\rho_n}, \quad (3)$$

where  $W_n$  is the weight fraction of the nanofiller and  $\rho_n$  is its density, evaluated for the nanoparticles using [1]:

$$\rho_n = 188(D_{\text{CNT}})^{1/3}, \text{ kg/m}^3, \quad (4)$$

where  $D_{\text{CNT}}$  is the diameter of the carbon nanotube (nanofiber) in nm.

The dimension  $D_f^{\text{PP}}$  are determined for linear polymers using [19]:

$$D_f^{\text{PP}} = \frac{2d_f}{3}, \quad (5)$$

where  $d_f$  is the fractal dimension of the structure of the nanocomposite (namely, its polymer matrix) determined according to [18]:

$$d_f = (d - 1)(1 + \nu), \tag{6}$$

where  $d$  is the dimension of the Euclidean space in which the fractal is considered (apparently, in our study  $d = 3$ ),  $\nu$  is Poisson's ratio determined as a result of mechanical testing using the following [18–20]:

$$\frac{\sigma_Y}{E_n} = \frac{1 - 2\nu}{6(1 + \nu)}, \tag{7}$$

where  $\sigma_Y$  and  $E_n$  are the yield stress and the elastic modulus of the nanocomposite respectively.

It is known [16] that in polymer solutions the solvent penetrates into the macromolecular coil, with the process regulated by the volume of the coil accessible for penetration. Since both the macromolecular coil [16] and the ring-like structures of CNTs (CNFs) [13, 21, 22] are fractal objects, the volume of the latter structures  $V_{CNT}$  can be determined as follows [23]:

$$V_{CNT} = R_{CNT}^{D_f^{CNT}} \eta^{d - D_f^{CNT}}, \tag{8}$$

where  $D_f^{CNT}$  is the fractal dimension of the ring-like structures of CNTs (CNFs) and  $\eta$  is the linear scale of measurement further considered to be equal to the mean diameter of the CNTs, i.e. 45 nm.

To evaluate the dimensionality of  $D_f^{CNT}$  the following method was used [14, 15]. The calculation of  $R_{CNT}$  using equation (2) demonstrated its decrease with the growth of  $\phi_n$ . At the maximum used values of  $\phi_n$ , corresponding to  $W_n = 3.0$  wt%, the said dependencies tend to be in the asymptotic branch, which means that the ring-like structures of CNTs or CNFs reach their minimum values  $R_{CNT}$ . Similar to the case of macromolecular coils, this means that the maximum density of the ring-like structure is reached at the maximum value of its fractal dimension  $D_f^{CNT}$  ( $D_f^{lim}$ ), which is determined using the equation [24, 25]:

$$D_f^{lim} = \frac{4(d + 1)}{7}. \tag{9}$$

For  $d = 3$  the value  $D_f^{lim} = 2.286$ .

Then, in order to estimate  $D_f^{CNT}$  an irreversible aggregation model can be used which describes the polymerization process (macromolecular

coil formation) and yields the following ratio for determining the radius of the particle aggregate  $R_{ag}$  [26–29]:

$$R_{ag} \sim c_0^{-1/(d - D_f)}, \tag{10}$$

where  $c_0$  is the initial concentration of the aggregated particles and  $D_f$  is the fractal dimension of the aggregate.

The coefficient in ratio (10) can be determined under the following conditions:  $R_{ag} = R_{CNT}$ ,  $c_0 = \phi_n$ , and  $D_f = D_f^{lim}$ . Values  $R_{CNT}$  and  $\phi_n$  are applicable, when  $W_n = 3.0$  wt%. The estimate obtained using this ratio demonstrated that the value  $D_f^{CNT}$  increases with the growth of  $\phi_n$  (and a decrease in  $R_{CNT}$ ) from 1.91 to 2.29 for PP/CNT nanocomposites and from 1.76 to 2.21 for PP/CNF nanocomposites.

However, due to the excluded volume effect, the polymer can not occupy the whole volume  $V_{CNT}$ , but rather occupies the available space determined by the available volume of the ring-like structures  $V_{CNT}^{av}$ , which is calculated as follows [23]:

$$V_{CNT}^{av} = V_{CNT} (3 - D_f^{CNT}). \tag{11}$$

Fig. 1 shows the ratio of the number of contacts in the studied nanocomposites between the CNTs (CNFs) and the polymer matrix  $n$  to the volume of the ring-like structures of CNTs (CNFs)  $V_{CNT}^{av}$  that can be occupied by the matrix polymer. We can see that there is a linear correlation between the said parameters which goes through the origin of the coordinates and can be described by the empirical equation

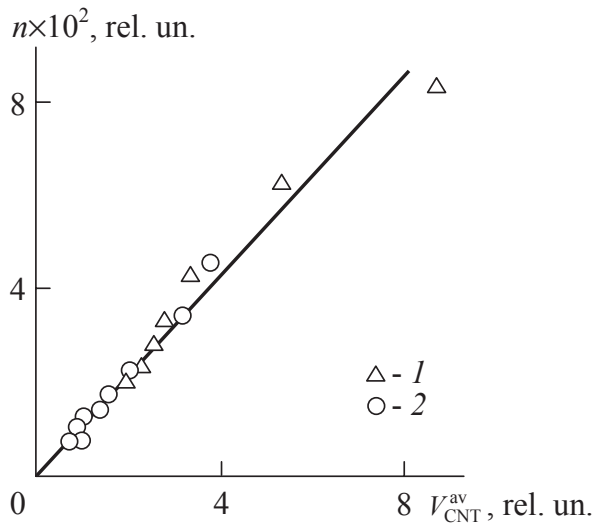
$$n = 12,1 V_{CNT}^{av}, \tag{12}$$

provided that the linear dimensions in ratios (1) and (8) are given in  $\mu\text{m}$ .

Thus, the number of interactions between the nanofiller and the polymer matrix  $n$  is, as expected, determined by the volume of the ring-like structures  $V_{CNT}^{av}$ , available to be occupied by the polymer which in our study is considered to be the solvent.

It is known [1] that the density of a fractal object (in our study, the density of the ring-like structures of CNTs (CNFs))  $\rho_{CNT}$  is determined by the equation:

$$\rho_{CNT} = \rho_{dens} \left( \frac{R_{CNT}}{O} \right)^{D_f^{CNT} - d}, \tag{13}$$



**Fig. 1.** The ratio of the number of contacts between the nanofiller and the polymer matrix  $n$  to the accessible volume of the ring-like structures of CNT (CNF)  $V_{\text{CNT}}^{\text{av}}$  for PP/CNT (1) and PP/CNF (2) nanocomposites

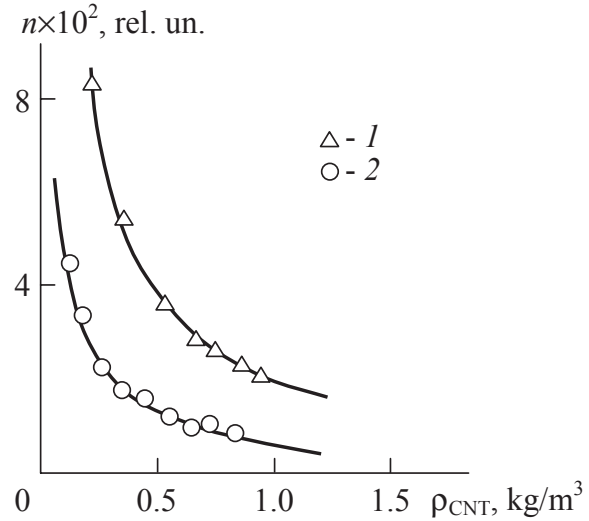
where  $\rho_{\text{dens}}$  is the density of the material of the fractal object in the compact state (i.e. when  $D_f^{\text{CNT}} = d$ ), which in our case was  $2700 \text{ kg/m}^3$  [1], and  $a$  is the lower scaling limit of fractal behaviour assumed to be equal to  $D_{\text{CNT}}^*$ .

Fig. 2 shows the dependencies of  $n(\rho_{\text{CNT}})$  for the studied nanocomposites, which demonstrate that with equal  $\rho_{\text{CNT}}$  the value of  $n$  is lower for CNFs than for CNTs. This difference is accounted for by the smaller diameter of the CNFs as compared to CNTs, which results in smaller spaces between CNFs and makes it more difficult for the macromolecular coils of PP to penetrate into the ring-like structures, since the diameter of the coils is compatible with the diameter of the CNFs.

The level of interfacial adhesion in the polymer nanocomposites can be evaluated using the dimensionless parameter  $b_\alpha$ , which is determined according to the following ratio [1]:

$$\frac{E_n}{E_m} = 1 + 11(c\varphi_n b_\alpha)^{1.7}, \quad (14)$$

where  $E_n$  and  $E_m$  are the elastic moduli of the nanocomposite and the matrix polymer respectively (ratio  $E_n/E_m$  is usually called the reinforcement degree of the nanocomposite),  $c$  is a constant coefficient, which for the CNTs is approximately 2.86 [1].

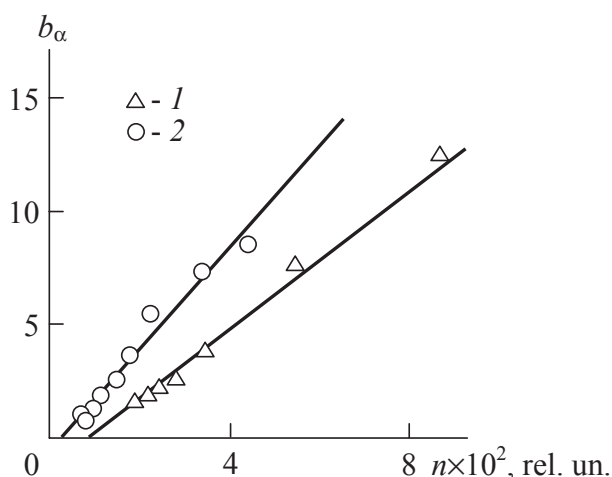


**Fig. 2.** Dependencies of the number of contacts between the nanofiller and the polymer matrix  $n$  on the density of the ring-like structures of CNT (CNF)  $\rho_{\text{CNT}}$  for PP/CNT (1) and PP/CNF (2) nanocomposites

Parameter  $b_\alpha$  allows both a quantitative and qualitative gradation of the level of interfacial adhesion. Thus, when  $b_\alpha = 0$ , no interfacial adhesion is present;  $b_\alpha = 1.0$  corresponds to perfect adhesion by Kerner; and the condition  $b_\alpha > 1.0$  defines the nanoadhesion effect [1].

Fig. 3 demonstrates the dependency of the parameter  $b_\alpha$  on the value  $n$  for PP/CNT and PP/CNF nanocomposites. As expected, the level of interfacial adhesion characterised by parameter  $b_\alpha$  increases with a larger number of contacts between the polymer matrix and the nanofiller. The graphs in Fig. 3 have two specific features. First, the slope of the line graph  $b_\alpha(n)$  is greater for CNFs as compared to CNTs. It is known [1,30] that the value  $b_\alpha$  is the function of both the structure factor, i.e.  $n$ , and the degree of physical and/or chemical interaction between the polymer matrix and the nanofiller. The higher slope of graph  $b_\alpha(n)$  for CNFs, meaning higher values of  $b_\alpha$  for CNFs as compared to CNTs, demonstrates that physical and/or chemical interaction between PP and CNFs is stronger than the interaction between PP and CNTs. Second, graphs of  $b_\alpha(n)$  are extrapolated to  $b_\alpha = 0$ , when  $n$  is not equal to zero. This means that for the condition  $b_\alpha > 0$  (i.e. interfacial adhesion) to be implemented, we need to obtain a finite number of interactions between the polymer matrix and the nanofiller which has to be above zero.

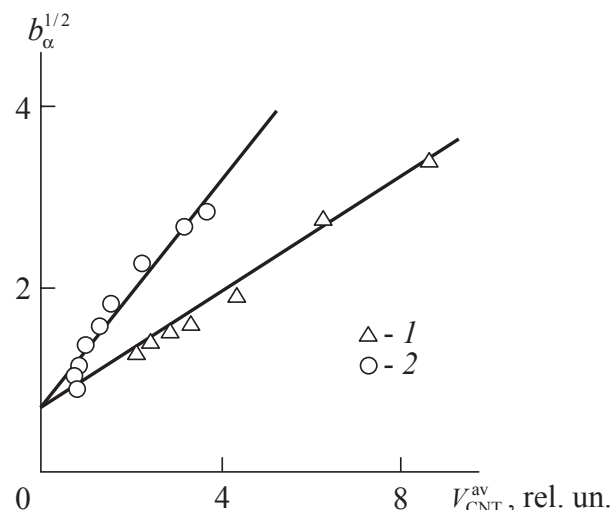




**Fig. 3.** Dependencies of parameter  $b_\alpha$  on the number of contacts between the nanofiller and the polymer matrix  $n$  for PP/CNT (1) and PP/CNF (2) nanocomposites

Finally, Fig. 4 shows the dependency  $b_\alpha^{1/2}(V_{\text{CNT}}^{\text{av}})$  for the studied nanocomposites (the form of the dependency was chosen so that it would allow its linearization). The figure demonstrates the growth of  $b_\alpha$  with the increase in  $V_{\text{CNT}}^{\text{av}}$ , which was what we expected (Fig. 1 and 3). Once again the value of  $b_\alpha$  with comparable  $V_{\text{CNT}}^{\text{av}}$  is higher for CNFs than for CNTs, which is explained by the factors described above. The most interesting feature of the dependencies  $b_\alpha^{1/2}(V_{\text{CNT}}^{\text{av}})$  is the fact that they are extrapolated to zero  $b_\alpha^{1/2} \approx 0.7$  ( $b_\alpha \approx 0.5$ ) when  $V_{\text{CNT}}^{\text{av}} = 0$ . Therefore, the interaction between the polymer matrix and carbon nanotubes (nanofibers) on the surface of the ring-like structures of the nanotubes (nanofibers) constitute only a comparatively small portion ( $\sim 7\text{--}10\%$ ) of the total number. The level of interfacial adhesion is mostly determined by the interaction with the polymer penetrating into the ring-like structures of CNTs (CNFs). Therefore, the smaller radius of the said structures  $R_{\text{CNT}}$  and their corresponding compactization result in a decrease in the parameter  $b_\alpha$ . The nano-adhesion effect ( $b_\alpha > 1.0$ ) is observed only when the polymer penetrates into the ring-like structures of CNTs (CNFs).

It should be noted that the curvature of carbon nanotubes and their influence on the properties of nanocomposites has always been a subject of scientific studies [31–39].



**Fig. 4.** Dependencies of parameter  $b_\alpha$  on the accessible volume of the ring-like structures of CNT (CNF)  $V_{\text{CNT}}^{\text{av}}$  for PP/CNT (1) and PP/CNF (2) nanocomposites

#### 4. Conclusions

The paper suggests a structural model of creation of interfacial adhesion in polymer/carbon nanotubes (nanofibers) nanocomposites, which considers the nanofillers to be analogous to macromolecular coils and the polymer matrix to be analogous to the solvent. This model allowed us to demonstrate that most contacts between the polymer matrix and the nanofiller, determining the level of interfacial adhesion, occur within the ring-like structures of carbon nanotubes (nanofibers) when they are penetrated by the polymer. The smaller radius of the said structures makes them more compact, reduces the concentration of the polymer, and therefore reduces the level of interfacial adhesion.

#### Conflict of interests

The authors declare that they have no known competing financial interests or personal relationships that could have influenced the work reported in this paper.

#### References

1. Mikitaev A. K., Kozlov G. V., Zaikov G. E. *Polymer Nanocomposites: Variety of structural forms and applications*. New York: Nova Science Publishers, Inc., 2008. 319 p.
2. Kozlov G. V., Dolbin I. V. Transfer of mechanical stress from polymer matrix to nanofiller in dispersion-

filled nanocomposites. *Inorganic Mater.: Appl. Res.* 2019;10(1): 226–230. DOI: <https://doi.org/10.1134/S2075113319010167>

3. Dolbin I. V., Karnet Yu. N., Kozlov G. V., Vlasov A. N. Mechanism of growth of interfacial regions in polymer/carbon nanotube nanocomposites. *Composites: Mechanics, Computations, Applications: An Intern. J.* 2018;10(3): 213–220. DOI: <https://doi.org/10.1615/CompMechComputApplIntJ.2018029234>

4. Kozlov G. V., Dolbin I. V. The effect of uniaxial extrusion of the degree of reinforcement of nanocomposites polyvinyl chloride/boron nitride. *Inorganic Mater.: Appl. Res.* 2019;10(3): 642–646. DOI: <https://doi.org/10.1134/S2075113319030183>

5. Moniruzzaman M., Winey K. I. Polymer nanocomposites containing carbon nanotubes. *Macromolecules.* 2006;39(16): 5194–5206. DOI: <https://doi.org/10.1021/ma060733p>

6. Thostenson E. T., Li C., Chou T.-W. Nanocomposites in context. *Composites Sci. Techn.* 2005;65(2): 491–516. DOI: <https://doi.org/10.1016/j.compscitech.2004.11.003>

7. Kozlov G. V., Dolbin I. V. The description of elastic modulus of nanocomposites polyurethane/graphene within the framework of modified blends rule. *Materials Physics and Mechanics.* 2018;40(2): 152–157. DOI: [https://doi.org/10.18720/MPM.4022018\\_3](https://doi.org/10.18720/MPM.4022018_3)

8. Kozlov G. V., Dolbin I. V. The fractal model of mechanical stress transfer in nanocomposites polyurethane/carbon nanotubes. *Letters on Materials.* 2018;8(1): 77–80. DOI: <https://doi.org/10.22226/2410-3535-2018-1-77-80>(In Russ., abstract in Eng.)

9. Kozlov G. V., Dolbin I. V., Koifman O. I. A fractal model of reinforcement of carbon polymer–nanotube composites with ultralow concentrations of nanofiller. *Doklady Physics.* 2019;64(5): 225–228. DOI: <https://doi.org/10.1134/S1028335819050021>

10. Kozlov G. V., Dolbin I. V. Structural model of efficiency of covalent functionalization of carbon nanotubes. *Izvestiya Vysshikh Uchebnykh Zavedenii, Seriya Khimiya i Khimicheskaya Tekhnologiya.* 2019;62(10): 118–123. DOI: <https://doi.org/10.6060/ivkkt.20196210.5962>(In Russ., abstract in Eng.)

11. Schaefer D. W., Justice R. S. How nano are nanocomposites? *Macromolecules.* 2007;40(24): 8501–8517. DOI: <https://doi.org/10.1021/ma070356w>

12. Atlukhanova L. B., Kozlov G. V., Dolbin I. V. Structural model of frictional processes for polymer/carbon nanotube nanocomposites. *Journal of Friction and Wear.* 2019;40(5): 475–479. DOI: <https://doi.org/10.3103/S1068366619050027>

13. Yanovsky Yu. G., Kozlov G. V., Zhirikova Z. M., Alov V. Z., Karnet Yu. N. Special features of the structure of carbon nanotubes in polymer composite media. *Nanomechanics. Sci. Technol.: An Intern. J.*

2012;3(2). 99–124. DOI: [10.1615/NanomechanicsSciTechnolIntJ.v3.i2.10](https://doi.org/10.1615/NanomechanicsSciTechnolIntJ.v3.i2.10)

14. Kozlov G. V., Dolbin I. V. Influence of the nanofiller interactions on the reinforcement degree of the nanocomposites of polymer/carbon nanotubes. *Nano- i mikrosistemnaya tekhnika = Nano- and Microsystems Technology.* 2018;20(5): 259–266. DOI: <https://doi.org/10.17587/nmst.20.259-266>(In Russ., abstract in Eng.)

15. Kozlov G. V., Dolbin I. V. Interrelation between elastic moduli of filler and polymethyl methacrylate–carbon nanotube nanocomposites. *Glass Physics and Chemistry.* 2019;45(4): 277–280. DOI: <https://doi.org/10.1134/S1087659619040060>

16. Kozlov G. V., Dolbin I. V., Zaikov G. E. *The Fractal Physical Chemistry of Polymer Solutions and Melts.* Toronto, New Jersey: Apple Academic Press, 2014; 316 p.

17. Bridge B. Theoretical modeling of the critical volume fraction for percolation conductivity of fibre-loaded conductive polymer composites. *J. Mater. Sci. Lett.* 1989;8(2): 102–103. DOI: <https://doi.org/10.1007/BF00720265>

18. Kozlov G. V., Zaikov G. E. *Structure of the Polymer Amorphous State.* Utrecht, Boston: Brill Academic Publishers; 2004. 465 p.

19. Puertolas J. A., Castro M., Morris J. A., Rios R., Anson-Casaos A. Tribological and mechanical properties of graphene nanoplatelet/PEEK composites. *Carbon.* 2019;141(1): 107–122. DOI: <https://doi.org/10.1016/j.carbon.2018.09.036>

20. Zhang M., Zhang W., Jiang N., Futaba D. N., Xu M. A general strategy for optimizing composite properties by evaluating the interfacial surface area of dispersed carbon nanotubes by fractal dimension. *Carbon.* 2019;154(2): 457–465. DOI: <https://doi.org/10.1016/j.carbon.2019.08.017>

21. Kozlov G. V., Dolbin I. V. Effect of a nanofiller structure on the degree of reinforcement of polymer–carbon nanotube nanocomposites with the use of a percolation model. *Journal of Applied Mechanics and Technical Physics.* 2018;59(4): 765–769. DOI: <https://doi.org/10.1134/S0021894418040259>

22. Kozlov G. V., Dolbin I. V. Structural interpretation of variation in properties of polymer/carbon nanotube nanocomposites near the nanofiller percolation threshold. *Technical Physics.* 2019;64(10): 1501–1505. DOI: <https://doi.org/10.1134/S1063784219100128>

23. Kozlov G. V., Zaikov G. E. *The structural stabilization of polymers: Fractal Models.* Leiden, Boston: Brill Academic Publishers; 2006. 345 p.

24. Kozlov G. V., Dolbin I. V. Modeling of carbon nanotubes as macromolecular coils. Melt viscosity. *High Temperature.* 2018;56(5): 830–832. DOI: <https://doi.org/10.1134/S0018151X18050176>

25. Kozlov G. V., Dolbin I. V. Viscosity of a melt of polymer/carbon nanotube nanocomposites. An

analogy with a polymer solution. *High Temperature*. 2019;57(3): 441–443. DOI: <https://doi.org/10.1134/S0018151X19030088>

26. Kozlov G. V., Dolbin I. V. The simulation of carbon nanotubes as macromolecular coils: Interfacial adhesion. *Materials Physics and Mechanics*. 2017;32(2): 103–107. DOI: 10.18720/MPM.3222017-1

27. Kozlov G. V., Dolbin I. V. Fractal model of the nanofiller structure affecting the degree of reinforcement of polyurethane–carbon nanotube nanocomposites. *Journal of Applied Mechanics and Technical Physics*. 2018;59(3): 508–510. DOI: <https://doi.org/10.1134/S002189441803015X>

28. Dolbin I. V., Kozlov G. V. Structural version of Ostwald-de Waele equation: Fractal treatment. *Fluid Dynamics*. 2019;54(2): 288–292. DOI: <https://doi.org/10.1134/S0015462819010051>

29. Atlukhanova L. B., Kozlov G. V., Dolbin I. V. The correlation between the nanofiller structure and the properties of polymer nanocomposites: fractal model. *Inorganic Mater.: Appl. Res.* 2020;11(1): 188–191. DOI: <https://doi.org/10.1134/S2075113320010049>

30. Kozlov G. V., Yanovskii Yu. G., Zaikov G. E. *Structure and properties of particulate-filled polymer composites: the fractal analysis*. New York: Nova Science Publishers, Inc.; 2010. 282 p.

31. Shaffer M. S. P., Windle A. H. Analogies between polymer solutions and carbon nanotube dispersions. *Macromolecules*. 1999;32(2): 6864–6866. DOI: <https://doi.org/10.1021/ma990095t>

32. Yi Y. B., Berhan L., Sastry A. M. Statistical geometry of random fibrous networks revisited: waviness, dimensionality and percolation. *Journal of Applied Physics*. 2004;96(7): 1318–1327. DOI: <https://doi.org/10.1063/1.1763240>

33. Berhan L., Sastry A. M. Modeling percolation in high-aspect-ratio fiber systems. I. Soft-core versus hard-core models. *Physical Review E – Statistical, Nonlinear, and Soft Matter Physics*. 2007;75(23): 041120. DOI: <https://doi.org/10.1103/PhysRevE.75.041120>

34. Shi D.-L., Feng X.-Q., Huang Y.Y., Hwang K.-C., Gao H. The effect of nanotube waviness and agglomeration on the elastic property of carbon nanotube-reinforced composites. *Journal of Engineering Materials and Technology, Transactions of the ASME*. 2004;126(2): 250–257. DOI: <https://doi.org/10.1115/1.1751182>

35. Lau K.-T., Lu M., Liao K. Improved mechanical properties of coiled carbon nanotubes reinforced epoxy nanocomposites. *Composites. Part A*. 2006;37(6): 1837–1840. DOI: <https://doi.org/10.1016/j.compositesa.2005.09.019>

36. Martone A., Faiella G., Antonucci V., Giordano M., Zarrelli M. The effect of the aspect ratio of carbon nanotubes of their effective reinforcement modulus in an epoxy matrix. *Composites Sci. Techn.* 2011;71(8): 1117–1123. DOI: <https://doi.org/10.1016/j.compscitech.2011.04.002>

37. Shao L. H., Luo R. Y., Bai S. L., Wang J. Prediction of effective moduli of carbon nanotube – reinforced composites with waviness and debonding. *Composite Struct.* 2009;87(3): 274–281. DOI: <https://doi.org/10.1016/j.compstruct.2008.02.011>

38. Omidi M., Hossein Kokni D. T., Milani A. S., Seethaller R. J., Arasteh R. Prediction of the mechanical characteristics of multi-walled carbon nanotube/epoxy composites using a new form of the rule of mixtures. *Carbon*. 2010;48(11): 3218–3228. DOI: <https://doi.org/10.1016/j.carbon.2010.05.007>

39. Shady E., Gowayed Y. Effect of nanotube geometry on the elastic properties of nanocomposites. *Composites Sci. Techn.* 2010;70(10): 1476–1481. DOI: <https://doi.org/10.1016/j.compscitech.2010.04.027>

### Information about the authors

Luiza B. Atlukhanova, PhD in Pedagogics, Associate Professor, Department of Biophysics, Informatics and Medical Devices, Dagestan State Medical University, Makhachkala, Russian Federation; e-mail: [bremovna77@mail.ru](mailto:bremovna77@mail.ru). ORCID iD: <https://orcid.org/0000-0002-5341-3349>.

Igor V. Dolbin, PhD in Chemistry, Associate Professor, Department of Organic Chemistry and High-Molecular Compounds, Kh. M. Berbekov Kabardino-Balkarian State University, Nalchik, Russian Federation; e-mail: [i\\_dolbin@mail.ru](mailto:i_dolbin@mail.ru). ORCID iD: <https://orcid.org/0000-0001-9148-2831>.

Georgii V. Kozlov, senior research fellow, Kh. M. Berbekov Kabardino-Balkarian State University, Nalchik, Russian Federation; e-mail: [i\\_dolbin@mail.ru](mailto:i_dolbin@mail.ru). ORCID iD: <https://orcid.org/0000-0002-9503-9113>.

All authors have read and approved the final manuscript.

*Translated by Yulia Dymant*

*Edited and proofread by Simon Cox*



# Condensed Matter and Interphases (Kondensirovannye sredy i mezhfaznye granitsy)

## Original articles

DOI: <https://doi.org/10.17308/kcmf.2020.22/2831>

Received 28 April 2020

Accepted 15 May 2020

Published online 25 June 2020

ISSN 1606-867X

eISSN 2687-0711

## Spectral-Luminescent Properties of Terbium-Containing Zirconomolybdates

©2020 B. G. Bazarov<sup>✉,a,b</sup>, R. Yu. Shendrik<sup>c,d</sup>, Yu. L. Tushinova<sup>a,b</sup>, D. O. Sofich<sup>c</sup>, J. G. Bazarova<sup>a</sup>

<sup>a</sup>Baikal Institute of Nature Management, Siberian Branch of the Russian Academy of Sciences, 6 ul. Sakhyanovoy, Ulan-Ude 670047, Republic of Buryatia, Russian Federation

<sup>b</sup>Banzarov Buryat State University, 24a ul. Smolina, Ulan-Ude 670000, Republic of Buryatia, Russian Federation

<sup>c</sup>Vinogradov Institute of Geochemistry, Siberian Branch of the Russian Academy of Sciences, 1a ul. Favorskogo, Irkutsk 664033, Russian Federation

<sup>d</sup>Irkutsk State University, 20 bulvar Gagarina, Irkutsk 664003, Russian Federation

### Abstract

To date, double molybdates of mono- and tetravalent elements have been comprehensively studied, and systems with molybdates of mono- and trivalent elements have been studied quite thoroughly. Some materials based on double molybdates, for example, those containing lanthanides, are considered promising for laser technology and electronics. Meanwhile, there is limited information on the properties, especially optical ones, of the molybdates containing rare-earth elements and zirconium. The aim of this work was to study the luminescent properties of self-activated terbium-containing zirconomolybdates with the compositions  $Tb_2Zr_3(MoO_4)_9$  (1:3) and  $Tb_2Zr(MoO_4)_5$  (1:1), crystallising in two different structural types.

Powder samples of the studied molybdates were synthesised by ceramic technology. The absorption, excitation, and emission spectra were measured using a Perkin Elmer Lambda 950 spectrophotometer. Luminescence was excited by a 250 W DKSSh-250 xenon lamp through an MDR-2 monochromator and recorded using an SDL-1 double monochromator with a grating of 600 lines/mm. The optical properties of new zirconium molybdates containing  $Tb^{3+}$  ions were studied. They revealed bright luminescence in the green spectral region due to the transitions inside the 4f shell of the rare-earth  $Tb^{3+}$  ion, excited both in the bands associated with the 4f-4f transitions and in the band with a charge transfer. The observed spectral lines as well as luminescence and excitation bands were identified.

It was shown that the position of the wide excitation band associated with the “charge transfer” transitions from  $O^{2-}$  in  $MoO_4^{2-}$  groups via Mo–O bonds to luminescent centres ( $Tb^{3+}$ ) does not depend on the matrix structure. The structure and intensity of the observed spectral lines, indicating a low symmetry of the  $Tb^{3+}$  crystalline environment, correlate with the structural analysis data. The results obtained in this work can be used when creating promising phosphors in the green spectral region under ultraviolet excitation.

**Keywords:** solid-phase synthesis, luminescence, terbium-containing zirconomolybdate.

**Funding:** The study was conducted within the framework of the state order by the Baikal Institute of Nature Management, Siberian Branch of the Russian Academy of Sciences, and partially funded by the Russian Foundation for Basic Research (project No. 18-08-799a).

**For citation:** Bazarov B. G., Shendrik R. Yu., Tushinova Yu. L., Sofich D. O., Bazarova J. G. Spectral-luminescent properties of terbium-containing zirconomolybdates. *Kondensirovannye sredy i mezhfaznye granitsy = Condensed Matter and Interphases*. 2020;22(2): 197–203. DOI: <https://doi.org/10.17308/kcmf.2020.22/2831>

✉ Bair G. Bazarov, e-mail: bazbg@rambler.ru



The content is available under Creative Commons Attribution 4.0 License.

**1. Introduction**

Since lanthanoids luminesce in the UV and in visible and near-infrared regions, they can be used in various fields: laser and fibre optics technology, medical diagnostics, and the creation of scintillators and luminophores.

The electrons in lanthanoids, located on the 4f shell, are screened by the outer 5s<sup>2</sup> and 5p<sup>6</sup> shells. As a result, the position of the energy levels is weakly dependent on the environment. In this case, the energetic states of the sublevels are completely determined by the immediate

environment of rare-earth ions due to the Stark splitting effect.

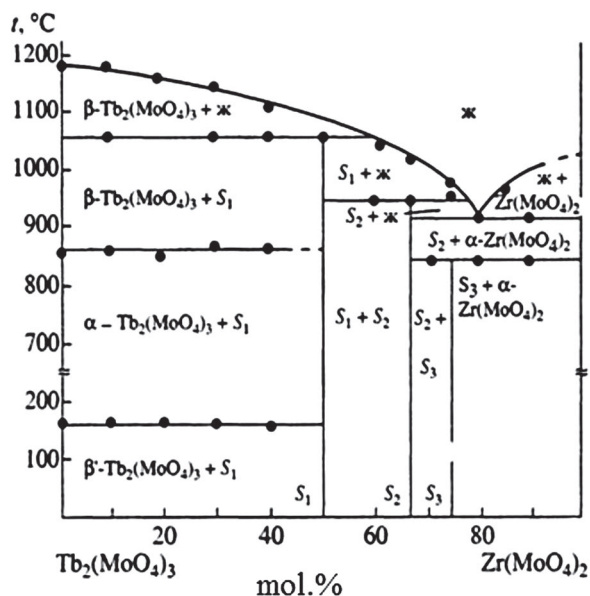
The studies aimed at the search for new materials for matrices activated by rare-earth ions are considered relevant. There are works of Russian and foreign scientists [1–6] dedicated to the study of luminescent properties of double zirconium molybdates and lanthanoids, although the luminescent properties of zirconomolybdates with Tb<sup>3+</sup> of the Tb<sub>2</sub>Zr(MoO<sub>4</sub>)<sub>5</sub> composition were not studied.

Our study of the Tb<sub>2</sub>(MoO<sub>4</sub>)<sub>3</sub>-Zr(MoO<sub>4</sub>)<sub>2</sub> system allowed establishing for the first time the formation of three new molybdates with the following compositions: Tb<sub>2</sub>Zr<sub>3</sub>(MoO<sub>4</sub>)<sub>9</sub> (1:3), Tb<sub>2</sub>Zr<sub>2</sub>(MoO<sub>4</sub>)<sub>7</sub> (1:2), and Tb<sub>2</sub>Zr(MoO<sub>4</sub>)<sub>5</sub> (1:1) (Fig. 1) [7].

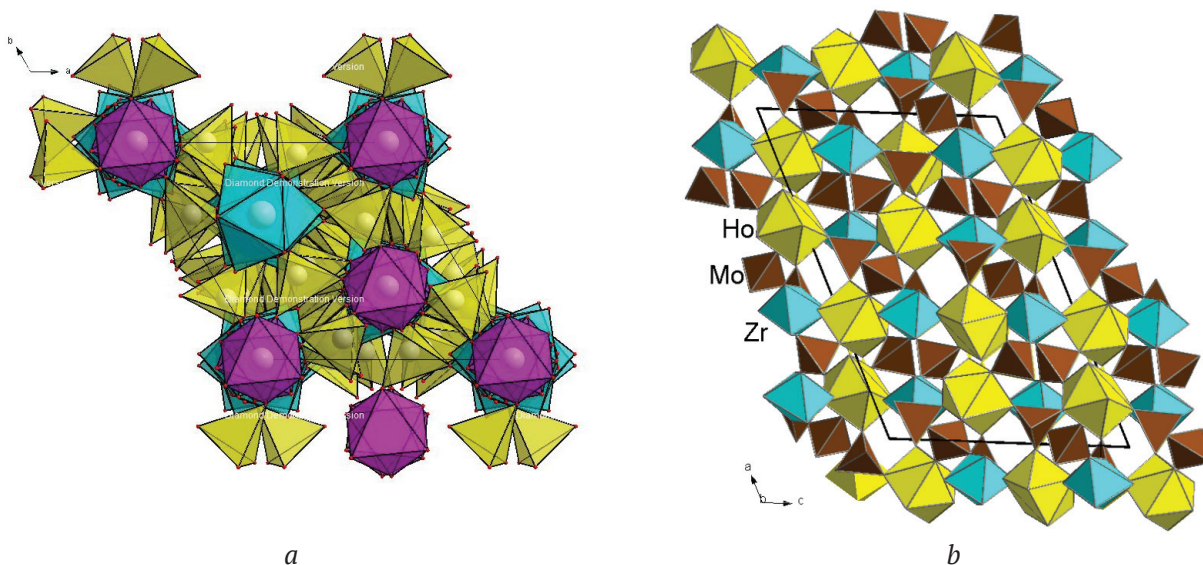
The structures of the first two molybdates, 1:3 (space group R $\bar{3}c$ , Z = 6) and 1:2 (space group C2/c, Z = 4), were determined for monocrystals (Fig. 2a, b) [8–10].

The structure of the 1:1 molybdate was determined through the use of isostructural Er<sub>2</sub>Zr(MoO<sub>4</sub>)<sub>5</sub>, the Rietveld refinement method, and principles of derivative difference minimisation (Fig. 3) [11].

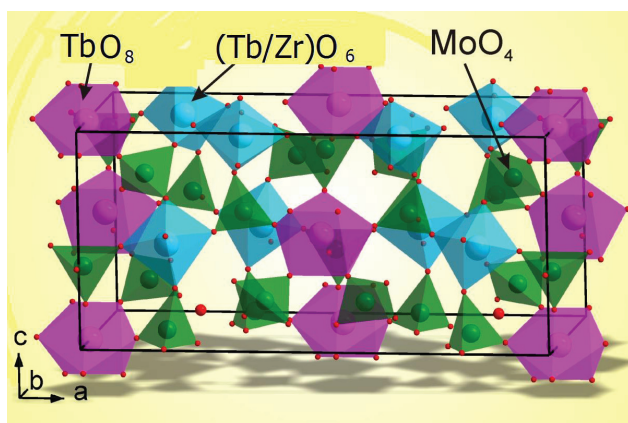
The aim of this work was to study the luminescent properties of self-activated terbium-containing zirconomolybdates with the 1:3 and 1:1 compositions, crystallising in two different structural types.



**Fig. 1.** Phase diagram of the system Tb<sub>2</sub>(MoO<sub>4</sub>)<sub>3</sub> – Zr(MoO<sub>4</sub>)<sub>2</sub>



**Fig. 2.** Part of the structure Ln<sub>2</sub>Zr<sub>3</sub>(MoO<sub>4</sub>)<sub>9</sub> (space group R $\bar{3}c$ , Z = 6) (Ln = Nd) (a); Part of the structure Ln<sub>2</sub>Zr<sub>2</sub>(MoO<sub>4</sub>)<sub>7</sub> (space group C2/c, Z = 4) (b)



**Fig. 3.** Part of the structure  $\text{Ln}_2\text{Zr}(\text{MoO}_4)_5$  (space group  $\text{Cmc}2_1$ ,  $Z = 2$ )

## 2. Experimental

The absorption, excitation, and emission spectra of  $\text{Tb}^{3+}$  were measured in two terbium-containing matrices  $\text{Tb}_2\text{Zr}(\text{MoO}_4)_5$  (space group  $\text{Cmc}2_1$ ,  $Z = 4$ ) and  $\text{Tb}_2\text{Zr}_5(\text{MoO}_4)_9$  (space group  $\text{R}\bar{3}\text{c}$ ,  $Z = 6$ ). The molybdates were obtained by ceramic technology [7].

In order to study the optical properties of the investigated samples, the absorption, emission, and excitation spectra were recorded in the integrating sphere at various temperatures.

The absorption spectra were recorded using a Perkin Elmer Lambda 950 spectrophotometer with an integrating sphere. When recording the absorption spectra, the studied sample

was poured into a KU-1 quartz-glass ampoule and placed inside the integrating sphere. The absorption of the test glass was subtracted from the absorption spectra.

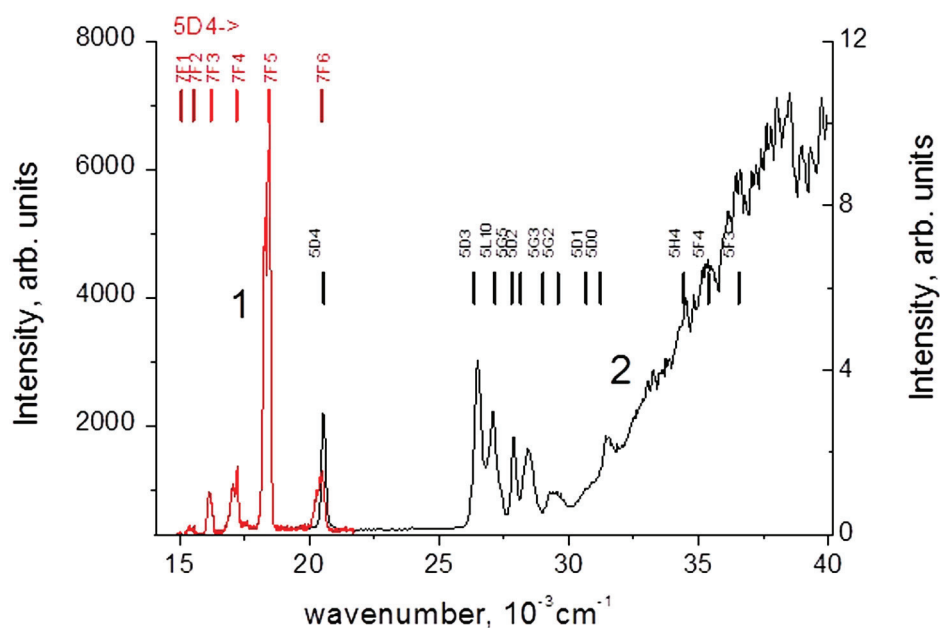
Luminescence was excited in the spectral interval of 200–500 nm by a 250 W DKSSh-250 xenon lamp through an MDR-2 monochromator with a ruled grating of 1200 lines/mm. The emissions were recorded using an SDL-1 double monochromator with a grating of 600 lines/mm. The spectral dimension of the monochromator slits varied from 1.2 nm to 0.3 nm. The measurements at temperature 77 K were conducted in the evacuated cryostat. The excitation spectra were corrected by the lumogen excitation spectra.

## 3. Results and discussion

Two types of bands were observed in the excitation spectra of the studied samples: narrow bands, corresponding to the transitions inside the 4f shell of the rare-earth ion, and wide bands, associated with the bands of charge transfer in the  $\text{MoO}_4^{2-}$  complexes to the rare-earth element.

Intensive luminescence was observed in the green spectral region in  $\text{Tb}_2\text{Zr}(\text{MoO}_4)_5$  upon the excitation in the UV region (Fig. 4).

The emission spectrum upon the excitation in the band with the energy  $26500 \text{ cm}^{-1}$  ( $\lambda = 377 \text{ nm}$ ), measured at a temperature of 77 K, is presented in Fig. 4 (curve 1). The bands observed in the



**Fig. 4.** Emission (curve 1) and excitation (curve 2) spectra of the  $\text{Tb}_2\text{Zr}(\text{MoO}_4)_5$  sample measured at temperature 77 K

spectrum are related to the electronic transitions inside the  $4f$  shell from the  ${}^5D_4$  term to the  ${}^7F_J$  ( $J = 1-6$ ) terms. The greatest intensity in the emission spectrum was found in the band with the maximum in the  $18500\text{ cm}^{-1}$  region ( $\lambda = 540\text{ nm}$ ). The band is related to the magnetic dipole transition of  ${}^5D_4-{}^7F_5$ . The intensity of this transition changes only slightly depending on the value of the crystalline field. The observed band is split into three lines with the energies of  $18280$ ,  $18405$ , and  $18460\text{ cm}^{-1}$ .

The luminescence band with the  $20500\text{ cm}^{-1}$  maximum ( $\lambda = 488\text{ nm}$ ) is associated with the electronic dipole transition of  ${}^5D_4-{}^7F_6$  in the  $\text{Tb}^{3+}$  ion, which is environment-sensitive (but not hypersensitive) and depends on the symmetry of the crystalline field. Transitions of  ${}^5D_4-{}^7F_1$  in the emission of the  $\text{Tb}^{3+}$  ion have low intensity. Band intensities related to the  $f-f$  transitions diminish with a decreasing value of  $J$  in the following way:  ${}^5D_4 \rightarrow {}^7F_6 > {}^7F_4 > {}^7F_5 > {}^7F_2$ . The presence of the thin structure in the emission spectra of the  ${}^5D_4-{}^7F_J$  transitions in terbium ions is associated with their sensitivity to the ligand environment.

The  ${}^5D_4-{}^7F_6$  band is more intense as compared to the intensities of other bands (except for  ${}^5D_4-{}^7F_5$ ) and is split into three peaks, which can be indicative of spacial distortion of the nine-peak  $\text{TbO}_9$  with symmetry decreased to  $C_{2v}$  [12], which correlates with the data of the structure. The presence of intensive lines of magnetic dipole and

electronic dipole transitions in the spectrum is also indicative of the presence of several various types of ligands [13].

The emission was excited in the band with energy of  $26500\text{ cm}^{-1}$  ( $\lambda = 377\text{ nm}$ ), corresponding to the  ${}^4F_0-{}^5D_3$  transition, and the excitation spectrum was measured for the band with energy of  $18500\text{ cm}^{-1}$  ( $\lambda = 540\text{ nm}$ ), corresponding to the  ${}^5D_4-{}^4F_5$  transition. Vertical lines show the energies of the term of the  $\text{Tb}^{3+}$  free ion. A row of thin bands was observed in the excitation spectrum (Fig. 4, curve 2) that are related to the transitions from the ground state  ${}^7F_0$  to the states split by spin-orbital interaction of the  $4f^8$  term. The band in the  $37000\text{ cm}^{-1}$  region ( $\lambda = 270\text{ nm}$ ) is associated with the charge transfer transition in the  $(\text{MoO}_4)^{2-}$  complexes. The emission spectrum excited in this band is almost the same as the spectrum excited in the region of  $4f-4f$  transitions.

The absorption spectrum of  $\text{Tb}_2\text{Zr}_3(\text{MoO}_4)_9$  is presented in Fig. 5 [2]; it consists of a wide absorption band in the ultraviolet region and one narrow low-intensity peak, related to the  $4f-4f$  transition from the ground state of terbium ions  ${}^7F_6$  to the lower excited state  ${}^5D_4$ . The  $\text{Tb}^{3+}$  transitions are characterised by the low force of the oscillator. As a result, most of the bands of intracentre transitions in the absorption spectrum are not visible as compared to other absorption bands.

Fig. 6 [2] shows the excitation and luminescence spectra  $\text{Tb}_2\text{Zr}_3(\text{MoO}_4)_9$ . Intensive narrow emission

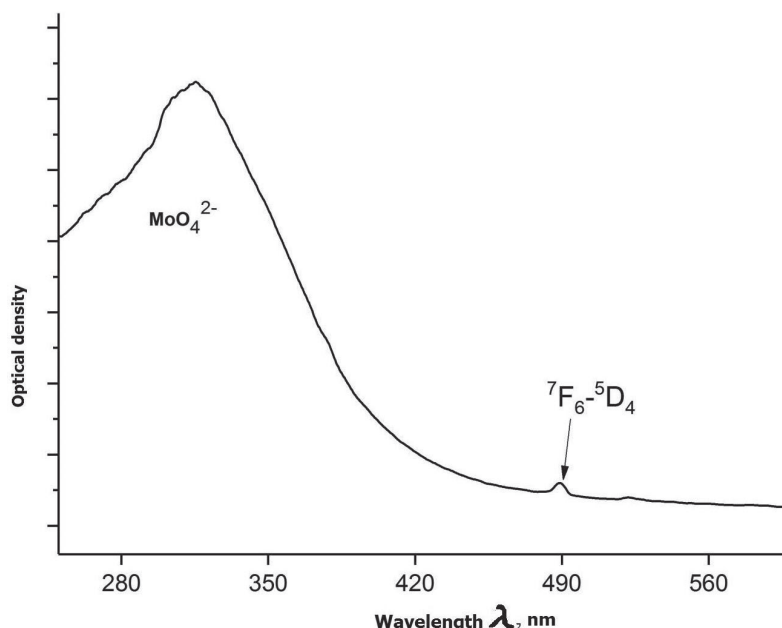
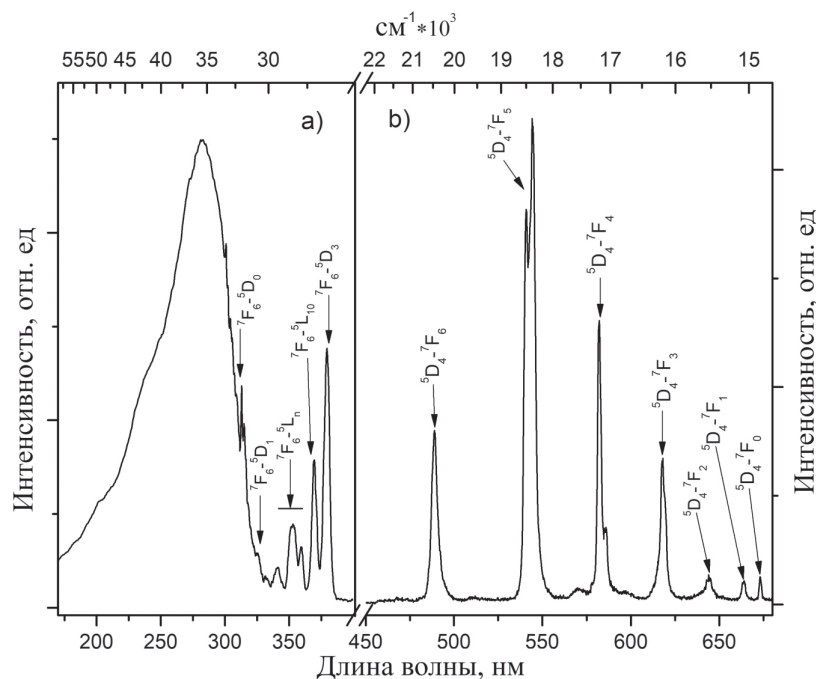


Fig. 5. Absorption spectrum of  $\text{Tb}_2\text{Zr}_3(\text{MoO}_4)_9$



**Fig. 6.** Excitation (a) and emission spectra (b) of  $\text{Tb}_2\text{Zr}_3(\text{MoO}_4)_9$  at liquid nitrogen temperature

bands were observed in the region of 480–680 nm (20800–14700  $\text{cm}^{-1}$ ), which is typical for the  $\text{Tb}^{3+}$  transitions from the  $\text{D}_4$  level to the lower  ${}^7\text{F}_J$  levels ( $J = 0, 1, 2, 3, 4, 5$ ). Transitions from the  ${}^7\text{F}_6$  ground state were observed in the excitation spectrum. Upon the excitation in the  $4f-4f$  bands, the greatest intensity of luminescence was achieved with the excitation wavelength of 380 nm ( ${}^7\text{F}_6-{}^5\text{D}_3$  transition). In the region of 300 nm (33300  $\text{cm}^{-1}$ ) a wide intensive excitation band was observed. Seven narrow lines in the emission spectrum belong to the transitions  $\text{Tb}^{3+}: {}^5\text{D}_4-{}^7\text{F}_J$  (electronic dipole transition, 488 nm (20500  $\text{cm}^{-1}$ )),  ${}^5\text{D}_4-{}^7\text{F}_5$  (magnetic dipole transition, 540 nm (18500  $\text{cm}^{-1}$ )),  ${}^5\text{D}_4-{}^7\text{F}_4$  (582 nm (17180  $\text{cm}^{-1}$ )),  ${}^5\text{D}_4-{}^7\text{F}_3$  (618 nm (16180  $\text{cm}^{-1}$ )),  ${}^5\text{D}_4-{}^7\text{F}_2$  (644 nm (15530  $\text{cm}^{-1}$ )),  ${}^5\text{D}_4-{}^7\text{F}_1$  (663 nm (15080  $\text{cm}^{-1}$ )), and  ${}^5\text{D}_4-{}^7\text{F}_0$  (673 nm (14860  $\text{cm}^{-1}$ )). The most intensive line reaching the peak at 540 nm (18500  $\text{cm}^{-1}$ ) is responsible for the green colour of  $\text{Tb}_2\text{Zr}_3(\text{MoO}_4)_9$ .

Decay times of luminescence, corresponding to different transitions inside the  $f$  shell with different lengths of the excitation waves, were measured at temperatures 297 K and 77 K (Table).

#### 4. Conclusions

As a result of the conducted studies, we can draw the following conclusions:

**Table.** Decay times of principal transitions of  $\text{Tb}^{3+}$  at 297 and 77 K

$({}^5\text{D}_4-{}^7\text{F}_J)$	Wave length (nm)		Decay time ( $\mu\text{s}$ )	
	Emis-sion	Exci-tation	297 K	77 K
6	488	270	420	400
		352	390	360
		370	430	400
		380	430	390
5	540	270	420	400
		352	460	410
		370	450	400
		380	450	420
4	582	290	420	400
		352	500	390
		370	420	370
		380	420	410

1. Spectral-luminescent properties of terbium-containing zirconium molybdates of two compositions (1:3 and 1:1) and structures ( $R\bar{3}c$ ,  $Z = 6$  and  $\text{Cmc}2_1$ ,  $Z = 4$ ) were studied. The observed spectral lines as well as luminescence and excitation bands were identified. Specific features of the matrix structure determine the spectral-luminescent properties of  $\text{Tb}^{3+}$  ions.

2. The comparison of the excitation spectra of terbium-containing molybdates with different



structures showed that the position of the wide excitation band associated with the “charge transfer” transitions from  $O^{2-}$  in  $MoO_4^{2-}$  groups via Mo–O bonds to luminescent centres ( $Tb^{3+}$ ) does not depend on the matrix structure and the nature of REE.

3. The structure of the band associated with the electronic dipole transition  ${}^5D_4 \rightarrow {}^7F_6$  in the  $Tb^{3+}$  ion is indicative of spacial distortion of  $TbO_9$  with decreasing symmetry. The presence of intensive lines of magnetic dipole ( ${}^5D_4 \rightarrow {}^7F_5$ ) and electronic dipole ( ${}^5D_4 \rightarrow {}^7F_6$ ) transitions is also indicative of the presence of low symmetry. All this data correlates with the data of the structural analysis.

4. The results obtained in this work can be used when creating promising phosphors in the green spectral region under ultraviolet excitation.

### Acknowledgements

The studies were carried out using the scientific equipment of the Centre for Collective Use of Equipment “Isotope-geochemical research of the Institute of Geochemistry, Siberian Branch of the Russian Academy of Sciences” and of the Centre for Collective Use of Equipment of the Baikal Institute of Nature Management, Siberian Branch of the Russian Academy of Sciences.

### Conflict of interests

The authors declare that they have no known competing financial interests or personal relationships that could have appeared to influence the work reported in this paper.

### References

1. Sofich D. O., Dorzhieva S. G., Chimitova O. D., Bazarov B. G., Tushinova Y. L., Bazarova Zh. G., Shendrik R. Yu. Hypersensitive  ${}^5D_0 \rightarrow {}^7F_2$  Transition of Trivalent Europium in Double Molybdates. *Bull. Russ. Acad. Sci.: Phys.* 2019;83(3): 321–323. DOI: <https://doi.org/10.1134/S0367676519030220>
2. Sofich D., Tushinova Yu. L., Shendrik R., Bazarov B. G., Dorzhieva S. G., Chimitova O. D., Bazarova J. G. Optical spectroscopy of molybdates with composition  $Ln_2Zr_3(MoO_4)_9$  (Ln: Eu, Tb). *Opt. Mater.* 2018;81: 71–77. DOI: <https://doi.org/10.1016/j.optmat.2018.05.028>
3. Sofich D., Dorzhieva S. G., Chimitova O. D., Bazarov B. G., Tushinova Yu. L., Bazarova Zh. G., Shendrik R. Yu. Luminescence of  $Pr^{3+}$  and  $Nd^{3+}$  Ions in Double Molybdates. *Phys. Solid State.* 2019;61(5): 844–846. DOI: <https://doi.org/10.21883/FTT.2019.05.47598.35F>

4. Dorzhieva S. G., Tushinova Y. L., Bazarov B. G., Nepomniashchikh A. I., Shendrik R. Y. Luminescence of Ln-Zr molybdates. *Bull. Russ. Acad. Sci.: Phys.* 2015;79(2): 276–279. DOI: <https://doi.org/10.7868/S0367676515020076>

5. Baur F., Justel Th. New red-emitting phosphor  $La_2Zr_3(MoO_4)_9:Eu^{3+}$  and the influence of host absorption on its luminescence efficiency. *Aust. J. Chem.* 2015;68(11): 1727–1734. DOI: <https://doi.org/10.1071/CH15268>

6. Qi S., Huang Y., Cheng H., Seo H. J. Luminescence and application of red-emitting phosphors of  $Eu^{3+}$ -activated  $R_2Zr_3(MoO_4)_9$  (R = La, Sm, Gd). *Electron. Mater. Lett.* 2016;12(1): 171–177. DOI: <https://doi.org/10.1007/s13391-015-5244-1>

7. Bazarova J. G., Tushinova Yu. L., Bazarov B. G., Dorzhieva S. G. Double molybdates of rare earth elements and zirconium. *Rus. Chem. Bull.* 2017; 66(4): 587–592. DOI: <https://doi.org/10.1007/s11172-017-1777-9>

8. Klevtsova R. F., Solodovnikov S. F., Tushinova Y. L., Bazarov B. G., Glinskaya L. A., Bazarova Z. G. A new type of mixed framework in the crystal structure of binary molybdate  $Nd_2Zr_3(MoO_4)_9$ . *J. Struct. Chem.* 2000;41(2): 280–284. DOI: <https://link.springer.com/article/10.1007/BF02741593>

9. Bazarov B. G., Grossman V. G., Tushinova Y. L., Fedorov K. N., Bazarova Z. G., Klevtsova R. F., Glinskaya L. A., Anshits A. G., Vereshchagina T. A. Crystal structure of binary molybdate  $Pr_2Hf_3(MoO_4)_9$ . *J. Struct. Chem.* 2009;50(3): 566–569. DOI: <https://doi.org/10.1007/s10947-009-0086-z>

10. Grossman V. G., Bazarov B. G., Bazarova T. T., Bazarova J. G., Glinskaya L. A., Temuujiin J. Phase equilibria in the  $Tl_2MoO_4 - Ho_2(MoO_4)_3 - Zr(MoO_4)_2$  system and the crystal structure of  $Ho_2Zr_2(MoO_4)_7$  and  $TlHoZr_{0.5}(MoO_4)_4$ . *J. Ceram. Process. Research.* 2017;18(12): 875–881.

11. Bazarov B. G., Bazarova J. G., Tushinova Y. L., Solovyov L. A., Dorzhieva S. G., Surenjav E., Temuujiin J. A new double molybdate of erbium and zirconium, its crystalline structure and properties. *J. Alloys Compd.* 2017;701: 750–753. DOI: <https://doi.org/10.1016/j.jallcom.2017.01.173>

12. Bunuel M. A., Lozano L., Chaminade J. P., Moine B., Jacquier B. Optical properties of  $Tb^{3+}$ -doped  $Rb_2KInF_6$  elpasolite. *Opt. Mater.* 1999;13(2): 211–223. DOI: [https://doi.org/10.1016/S0925-3467\(98\)00085-8](https://doi.org/10.1016/S0925-3467(98)00085-8)

13. Gupta S. K., Ghosh P. S., Yadav A. K., Pathak N., Arya A., Jha S. N., Bhattacharyya D., Kadam R. M. Luminescence properties of  $SrZrO_3/Tb^{3+}$  perovskite: host-dopant energy transfer dynamics and local structure of  $Tb^{3+}$ . *Inorg. Chem.* 2016;55(4): 1728–1740. DOI: <https://doi.org/10.1021/acs.inorgchem.5b02639>

### Information about the authors

*Bair G. Bazarov*, DSc in Physics and Mathematics, Leading Researcher, Laboratory of Oxide Systems Baikal Institute of Nature Management, Siberian Branch of the Russian Academy of Sciences (BINM SB RAS), Associate Professor at the Department of Inorganic and Organic chemistry, Banzarov Buryat State University, Ulan-Ude, Russian Federation; e-mail: bazbg@rambler.ru. ORCID iD: <https://orcid.org/0000-0003-1712-6964>.

*Roman Yu. Shendrik*, PhD, Senior Researcher of Single Crystal Lab, A. P. Vinogradov Institute of Geochemistry Siberian Branch of the Russian Academy of Sciences, Irkutsk, Russian Federation, e-mail r.shendrik@gmail.com. ORCID iD: <https://orcid.org/0000-0001-6810-8649>.

*Yunna L. Tushinova*, PhD in Chemistry, Researcher Fellow, Laboratory of Oxide Systems, Baikal Institute

of Nature Management, Siberian Branch of the Russian Academy of Sciences, Associate Professor at the Department of Inorganic and Organic Chemistry, Banzarov Buryat State University, Ulan-Ude, Russian Federation; e-mail: tushinova@binm.ru. ORCID iD: <https://orcid.org/0000-0003-1032-8854>.

*Dmitriy O. Sofich*, Junior Researcher of Single Crystal lab, A. P. Vinogradov Institute of Geochemistry, Siberian Branch of the Russian Academy of Sciences, Irkutsk, Russia Federation, e-mailsofich-dmitriy@live.com. ORCID iD: <https://orcid.org/0000-0002-2836-3597>.

*Jibzema G. Bazarova*, DSc in Chemistry, Chief Scientist, Laboratory of Oxide Systems, Baikal Institute of Nature Management, Siberian Branch of the Russian Academy of Sciences, Ulan-Ude,, Russian Federation; e-mail jbaz@binm.ru.. ORCID iD: <https://orcid.org/0000-0002-1231-0116>.

All authors have read and approved the final manuscript.

*Translated by Marina Strepetova*

*Edited and proofread by Simon Cox*



# Condensed Matter and Interphases (Kondensirovannye sredy i mezhfaznye granitsy)

## Original articles

DOI: <https://doi.org/10.17308/kcmf.2020.22/2832>

Received 11 April 2020

Accepted 15 May 2020

Published online 25 June 2020

ISSN 1606-867X

eISSN 2687-0711

## Electrochemical Oxidation of Formic Acid on the Surface of an Anodically Modified Ag15Pd Alloy

© 2020 E. V. Bedova, E. A. Tonkikh, O. A. Kozaderov✉

Voronezh State University,  
1 Universitetskaya pl., Voronezh 394018, Russian Federation

### Abstract

It was shown that the phase transformation of palladium into its own phase during the selective dissolution of the Ag15Pd alloy proceeds in the instantaneous nucleation mode and is limited by the surface diffusion of Pd ad-atoms to the growing three-dimensional nucleus of the new phase. The kinetic regularities of the electrooxidation of formic acid on an Ag15Pd alloy subjected to preliminary selective dissolution were established using transient electrochemical methods. It was found that the process of anodic destruction of HCOOH in an acidic sulphate solution proceeds at a higher rate on the anodically modified Ag15Pd alloy, the surface of which is morphologically developed and enriched with palladium as a result of potentiostatic selective dissolution under overcritical polarization conditions. The process of electrooxidation of HCOOH is non-stationary, proceeds in a mixed-kinetic mode and accelerates with increasing anodic potential. Kinetic currents of anodic oxidation of formic acid were determined by the chronoamperometry. A correlation between the value of the electric charge transferred during preliminary anodic modification of the Ag15Pd alloy and the rate of the kinetic stage of the electrooxidation of HCOOH was revealed.

**Keywords:** alloy, silver, palladium, selective dissolution, phase transformation, formic acid, electrooxidation.

**For citation:** Bedova E. V., Tonkikh E. A., Kozaderov O. A. Electrochemical Oxidation of Formic Acid on the Surface of an Anodically Modified Ag15Pd Alloy. *Kondensirovannye sredy i mezhfaznye granitsy = Condensed Matter and Interphases*. 2020; 22(2): 204–210. DOI: <https://doi.org/10.17308/kcmf.2020.22/2832>

### 1. Introduction

The anodic behaviour of metal alloy is often selective. During the selective dissolution of a binary homogeneous A,B-alloy, the electrochemically negative component A undergoes preferential ionization. This process is a source of defects (including vacancies) in its surface layer [1], which under certain conditions of anodic selective dissolution of the alloy or under the influence of corrosion environment [2–7] is morphologically destabilized and passes into a highly developed, dispersed state. This transition is based on irreversible processes of phase regrouping of an electropositive metal [8–10], which is thermodynamically possible

✉ Kozaderov Oleg Alexandrovich, e-mail: [ok@chem.vsu.ru](mailto:ok@chem.vsu.ru)

with overcritical anodic potentials and charges. With subcritical potentials, only the dissolution of the electronegative component occurs, the alloy surface is morphologically stable, and the concentration of the noble component increases when approaching the interphase boundary with the electrolyte. In the overcritical region of potentials and charges along with the ionization of component A in the highly defective surface layer of the alloy, component B recrystallizes from metastable structurally disordered state in its own highly developed phase [11]. As a result, the selective dissolution of alloys in the region of overcritical potentials can be used to obtain electrode materials with a micro- and nanoporous structure. Such materials can be used for the



The content is available under Creative Commons Attribution 4.0 License.

manufacture of electrodes in electrochemical power sources in electrochemical energetics. An important advantage of the electrochemical method for producing highly developed electrode materials by selective dissolution of alloys is the possibility of optimization of their morphological and electrocatalytic properties by controlling the process of the preliminary anodic modification of the alloy [12–15].

Considering that palladium effectively accelerates the anodic oxidation of formic acid [16–18], it seems promising to use the process of selective dissolution of homogeneous Ag,Pd-alloys for the synthesis of the electrocatalyst of the anodic process in low-temperature fuel cells operating on the direct oxidation of HCOOH [19]. During anodic polarization in an acidified non-complexing medium solid solutions of the Ag-Pd system based on silver undergo selective dissolution of silver, accompanied by a phase transformation of palladium [7, 11]. It is possible to form an electrode material with various degrees of morphological development of the surface layer and its enrichment with palladium and, as a result, with different electrocatalytic activity with respect to the electrooxidation reaction of formic acid by regulating the conditions of the anodic dissolution of solid solutions, i.e. the electrode potential and the electric charge transferred through the electrode.

The purpose of this study was the identification of the kinetic regularities of electrooxidation of formic acid on the surface of an Ag15Pd alloy (atomic fraction of palladium 15 %) subjected to selective dissolution of silver, and determination of the role of the conditions of preliminary anodic modification of the alloy in the kinetics of anodic destruction of HCOOH.

The objectives of study were as follows:

1. To find conditions and identify the kinetic regime of the process of recrystallization of palladium upon anodic selective dissolution of the Ag15Pd alloy in an acidic nitrate medium.

2. To determine the kinetic regularities of the electrooxidation process of formic acid on the surface of the anodically modified alloy Ag15Pd in an acidic sulphate medium.

3. To identify the influence of the conditions of the selective dissolution of the Ag15Pd alloy on the electrooxidation rate of formic acid on

the anodically modified surface of the alloy in an acidic sulphate medium.

## 2. Experimental

The studies were carried out on an alloy of the Ag-Pd system with atomic fraction of palladium 15 %. The alloy was prepared by direct melting in a tungsten induction furnace preliminarily evacuated and filled with argon (1.2 atm.) in  $A_2O_3$  crucibles. The metals were kept in a molten state at 1723 K, then cooled to 1373 K at a rate of 600 K/h, after which they were quench hardened in water. According to the phase diagram and quench hardening mode, the obtained alloy was a statistically disordered solid solution [20].

In order to make the electrode, the alloy was cut, polished, and placed in a frame of polymerized epoxy resin. Standard preparation of the electrode surface included striping on sanding paper with decreasing grain size, polishing on chamois with an aqueous MgO suspension to a mirror finish, washing with distilled water, degreasing with ethyl alcohol, followed by washing with twice distilled water, and drying with filter paper.

Working solutions of 0.1 M  $KNO_3 + 10^{-5}$  M  $HNO_3 + 10^{-5}$  M  $AgNO_3$  and 0.05 M  $H_2SO_4 + 1$  M HCOOH were prepared using twice distilled water from analytical grade reagents and sulphuric and nitric acid fixanals. Deaeration of the working solutions with chemically pure argon was carried out directly in the electrochemical cell for at least 2 h. The experiments were conducted in non-mixed solutions.

In studies, a standard three-electrode cell was used, without separation of the spaces of the working and auxiliary electrodes. The auxiliary electrode was platinum. The silver chloride reference electrode was located in a separate vessel and connected to the cell by an electrolytic bridge filled with a saturated solution of ammonium nitrate, with a Luggin capillary. The potentials in the study are presented relative to the standard hydrogen electrode scale.

The change and maintenance of the electrode potential, as well as the registration of polarization curves and curves corresponding to the current decay, were performed using an IPC-Compact universal computerized potentiostatic set. The electrode prepared for the experiment was placed in a cell filled with a deaerated working

solution and kept for some time until the quasi-stationary value of the open-circuit potential was established. For potentiodynamic measurements, the potential scan rate was set  $V = dE/dt$  and the polarization of the  $I, E$ -curve was recorded. For chronoamperometric measurements the potential  $E = \text{const}$  was set and  $I, t$ -dependence of the current decay was recorded for some time. Current density  $i$  was calculated by dividing the current strength per unit geometric area of the electrode.

### 3. Results and discussion

Bilogarithmic curves corresponding to the current decay obtained at different anodic potentials are shown in Fig. 1. Linear sections, probably corresponding to the process of selective dissolution in the regime of non-stationary diffusion [11], proceeding with rate  $i_{\text{diff}}(t)$  can be distinguished on these curves. When reaching a certain time point  $t_{\text{cr}}$  the current decay slowed down, and the linearity of the current dependence was impaired. With the increase of the anodic potential, the deviation from linearity increased, and the length of the linear section and  $t_{\text{cr}}$  parameter noticeably reduced.

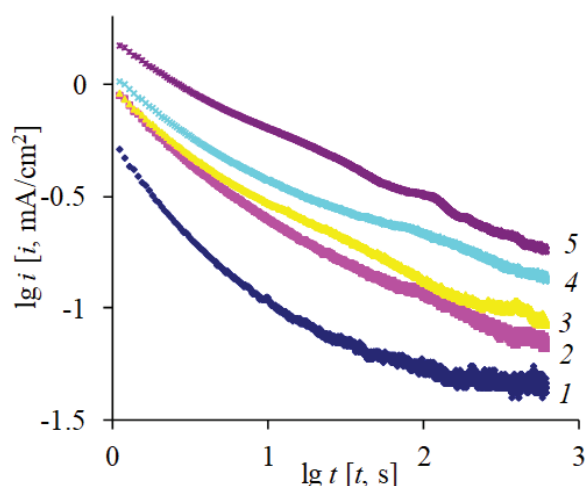
The curvature of the bilogarithmic chronoamperograms was probably caused by the acceleration of silver ionization due to the phase regrouping of palladium [7, 11], accompanied by

the displacement of palladium ad-atoms over the alloy surface to the nucleation sites of the new Pd phase. During this process new underlying layers of the alloy, which were in contact with the electrolyte solution, were released and as a result, the total ionization flux increased. Assuming the additivity of the rates of two parallel non-stationary processes, the selective dissolution of silver in the delayed diffusion mass-transfer mode and the phase transformation of palladium in the heterogeneous nucleation mode, the current transient of the nucleation process can be determined using the formula [11]:

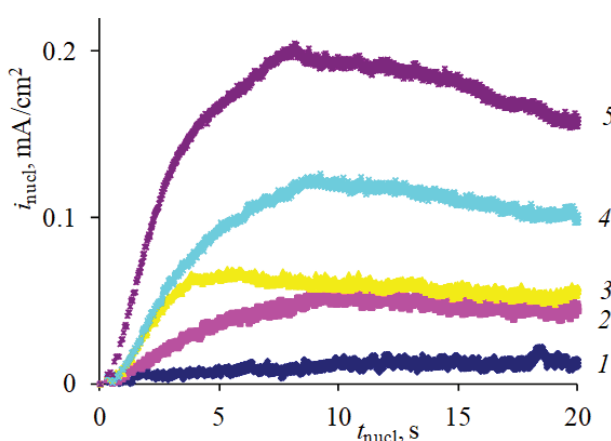
$$i_{\text{nucl}}(t) = i_{\text{SD}}(t) - i_{\text{diff}}(t)$$

as the difference of the total ( $i_{\text{SD}}$ ) and diffusion ( $i_{\text{diff}}$ ) currents. Current density transients of phase formation obtained using such calculations and plotted as nucleation current density dependencies  $i_{\text{nucl}}$  from nucleation time  $t_{\text{nucl}} = t - t_{\text{cr}}$  are shown in Fig. 2. It can be seen that with an increase in the potential, the process rate increased, and the current dependences had a curve shape with a maximum or reaching a plateau characteristic for nucleation processes.

The determined current transients of the phase formation process were re-plotted in coordinates, criterion for various models of heterogeneous nucleation [21], which allowed revealing the nature of the kinetic limitations of the formation



**Fig. 1.** Anodic chronoamperograms of Ag15Pd alloy in  $0.1 \text{ M KNO}_3 + 10^{-3} \text{ M HNO}_3 + 10^{-3} \text{ M AgNO}_3$  solution at potentials of 835 (1), 840 (2), 850 (3), 860 (4), 870 (5) mV and replotted in logarithmic coordinates

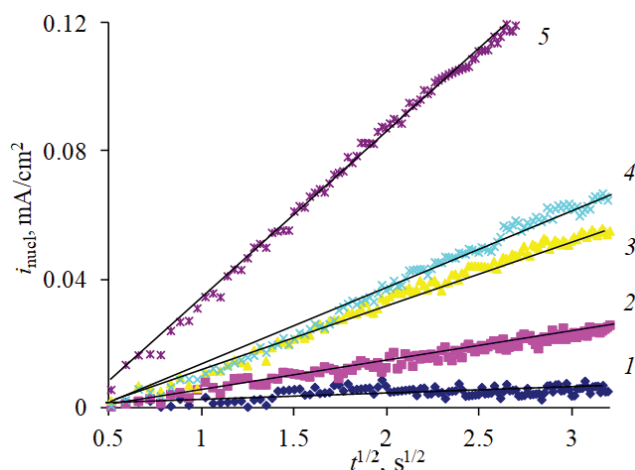


**Fig. 2.** Current transients of the phase regrouping of palladium upon selective dissolution of the Ag15Pd alloy in  $0.1 \text{ M KNO}_3 + 10^{-3} \text{ M HNO}_3 + 10^{-3} \text{ M AgNO}_3$  solution at potentials of 835 (1), 840 (2), 850 (3), 860 (4), 870 (5) mV

of the palladium phase. Linearisation was possible only in  $i_{\text{nucl}}, t_{\text{nucl}}^{1/2}$ -coordinates, criterion for instantaneous nucleation in the diffusion mode of a 3D-nucleus (Fig. 3). An increase in the slope of the linear initial parts of the chronoamperograms during the ennoblement of the electrode potential indicated an increase in the effective rate constant of the formation of the palladium phase  $k_{\text{eff}} = di_{\text{nucl}}/dt_{\text{nucl}}^{1/2}$ .

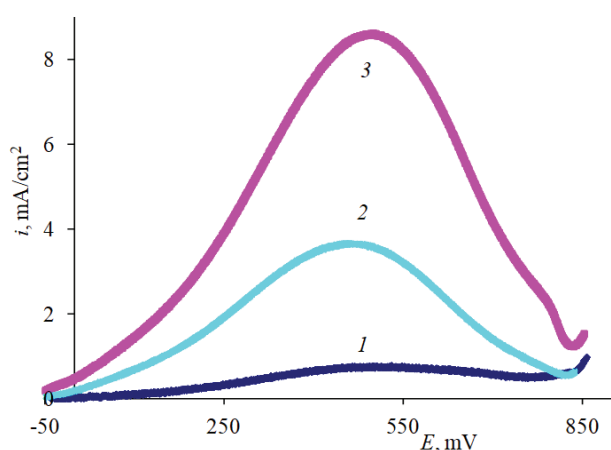
Polarization curves of the electrooxidation of formic acid on the surface of an Ag15Pd alloy subjected to anodic modification at various values of the applied electrode potential  $E_{\text{mod}}$  and transferred electric charge  $q_{\text{mod}}$ , respectively are shown in Figs. 4 and 5. It can be seen that the rate of electrochemical destruction of the HCOOH increased both with a positive shift of  $E_{\text{mod}}$  and with an increase in  $q_{\text{mod}}$ . It turned out that on the surface of the modified alloy, the electrooxidation of formic acid proceeds with a noticeable rate only under the condition  $E_{\text{mod}} \geq 830$  mV.

For the establishment of the kinetic regularities of the anodic destruction of HCOOH on the surface of the anodically modified Ag15Pd alloy, the process was carried out under potentiostatic conditions in the region of the voltammetric maximum, varying the values of the anodic modification potential of the  $E_{\text{mod}}$  and electric charge  $q_{\text{mod}}$  transferred through the electrode at the stage of selective dissolution. The analysis showed that chronoamperograms of electrooxidation of formic acid (not provided in the

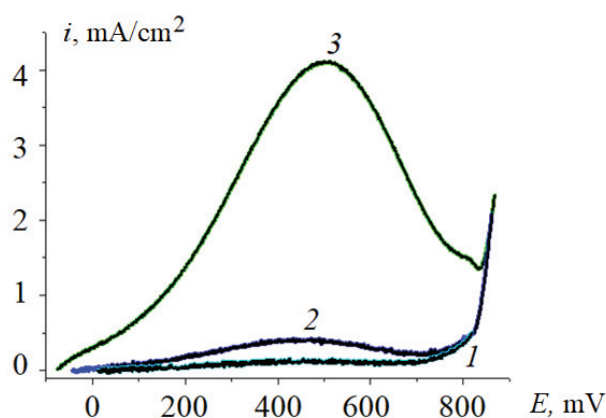


**Fig. 3.** Chronoamperograms of the formation of the palladium intrinsic phase, replotted in coordinates, criterion for instantaneous nucleation in the diffusion mode of growth of a three-dimensional nucleus on the surface of an Ag15Pd alloy upon its selective dissolution in 0.1 M  $\text{KNO}_3 + 10^{-3}$  M  $\text{HNO}_3 + 10^{-3}$  M  $\text{AgNO}_3$  at potentials of 835 (1), 840 (2), 850 (3), 860 (4), 870 (5) mV

article), regardless of the values  $E_{\text{mod}}$  and  $q_{\text{mod}}$  were non-linear in the Cottrell coordinates, criterion for diffusion kinetics, but they were characterized by a smooth current decay to almost zero. Such shape of the curves corresponding to the current decay indicates a non-stationary process and the implementation of mixed-kinetic control, when the diffusion of an electroactive substance to the electrode is accompanied by a kinetic stage. According to [22], we found the partial rate of this



**Fig. 4.** Voltammograms of electrooxidation of formic acid in 0.05 M  $\text{H}_2\text{SO}_4 + 1$  M  $\text{HCOOH}$  on an anodically modified Ag15Pd alloy subjected to selective dissolution in an acidic nitrate solution for 10 min at potentials of 830 (1), 840 (2), 850 (3) mV



**Fig. 5.** Voltammograms of electrooxidation of formic acid in 0.05 M  $\text{H}_2\text{SO}_4 + 1$  M  $\text{HCOOH}$  on the surface of an Ag15Pd alloy subjected to anodic modification at  $E_{\text{mod}} = 850$  mV and  $q_{\text{mod}} = 15$  (a), 25 (b), 46 (c)  $\text{mC}/\text{cm}^2$

stage (“kinetic current”), re-plotting the initial sections of the curve corresponding to the current decay in coordinates  $i-t^{1/2}$  (Fig. 6). We took into account that if the electrode process includes successive stages of volume diffusion and some kinetic stage, for example, a stage of charge transfer or a chemical reaction, characterized respectively by a diffusion coefficient  $D$  and rate constant  $k$ , then  $i,t$ -curve corresponding to the current decay in such a mixed-kinetic mode is described by the equation:

$$i(t) = i(0) \cdot \exp(k^2Dt) \cdot \operatorname{erfc}(kD^{1/2}t^{1/2}).$$

Partial rate of the kinetic stage  $i(0)$  was determined by extrapolating the linearized part of the chronoamperogram on the ordinate axis at  $t \rightarrow 0$ , taking into account that for  $k^2D \ll 1$  (“kinetic” electrooxidation mode) current transient obeys the ratio:

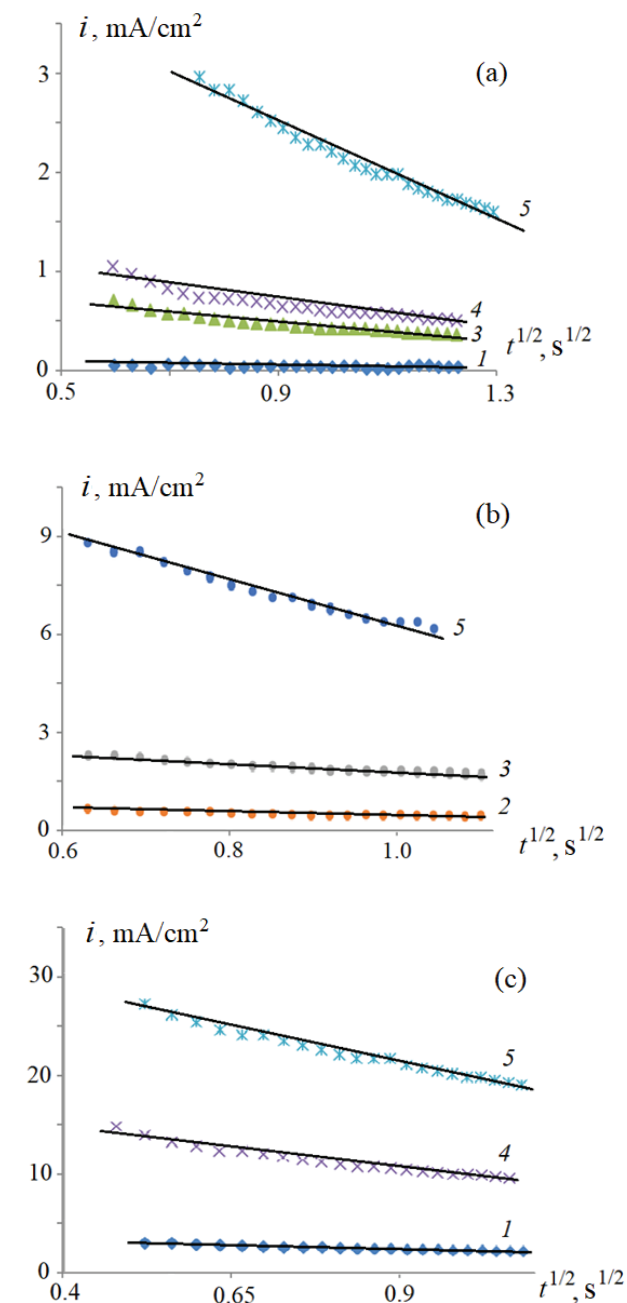
$$i(t) = i(0) \cdot \left(1 - \frac{2kD^{1/2}t^{1/2}}{\pi^{1/2}}\right).$$

It turned out that not only at the ennoblement of the electrode potential of selective dissolution of the alloy, but also with an increase in the electric charge passed during its anodic modification, the rate of the kinetic stage of the electrooxidation of HCOOH increases (Fig. 7). This can be explained by both the enrichment of the surface of the Ag15Pd alloy with palladium and the probable increase in its electrocatalytic activity due to the formation of a non-equilibrium, energetically metastable, and morphologically more highly developed phase during the recrystallization of Pd at the stage of selective dissolution of the Ag, Pd alloy. The revealed correlation between the parameters of the anodic modification of the silver-palladium alloy and the rate of electrochemical destruction of formic acid can be the basis for the development of optimal technological conditions for the formation of new effective electrode materials for low-temperature fuel cells operating on direct oxidation of HCOOH.

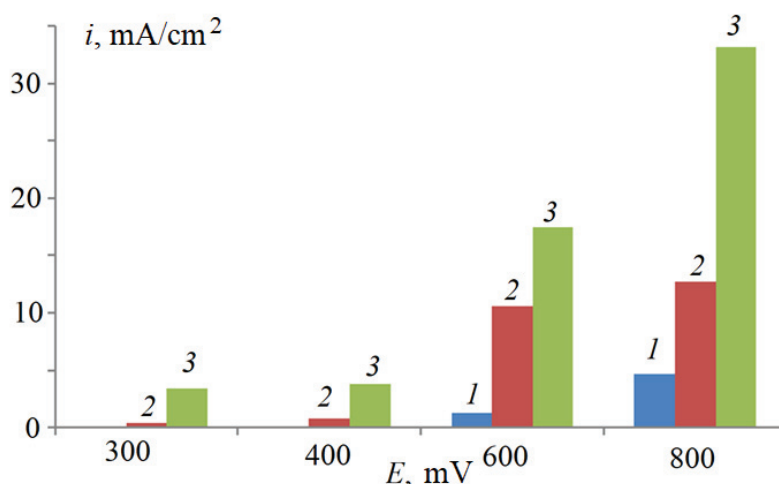
#### 4. Conclusions

The analysis of the partial current transients of the phase regrouping of palladium showed that the process of Pd recrystallization during the selective dissolution of the Ag15Pd alloy includes an instantaneous nucleation stage, while the

nucleus growth mode is diffusion-controlled. It was found that the rate of electrooxidation of formic acid in a sulphate medium on an anodically modified Ag15Pd alloy increases with an increase in the anodic destruction potential of HCOOH. The process is non-stationary and proceeds in a mixed-



**Fig. 6.** Criterion  $i,t^{1/2}$ -dependence of the process of electrooxidation of formic acid in  $0.05 \text{ M H}_2\text{SO}_4 + 1 \text{ M HCOOH}$  at potentials of 300 (1), 400 (2), 500 (3), 600 (4), 700 (5) mV on the surface of an Ag15Pd alloy subjected to anodic modification at  $E_{\text{mod}} = 850 \text{ mV}$  and  $q_{\text{mod}} = 15$  (a), 25 (b), 46 (c)  $\text{mC/cm}^2$



**Fig. 7.** Kinetic currents of electrooxidation of HCOOH on the surface of an Ag15Pd alloy subjected to anodic modification at  $E_{\text{mod}} = 850$  mV and  $q_{\text{mod}} = 15$  (1), 25 (2), 46 (3) mC/cm<sup>2</sup>

kinetic mode. The kinetic currents of the process were determined based on the chronoamperometry of the anodic oxidation of HCOOH in an acidic sulphate solution. It was shown that the rate of kinetic stage increases with an increase in both the electrode potential of selective dissolution and the electric charge transferred during anodic modification of the alloy.

### Conflict of interests

The authors declare that they have no known competing financial interests or personal relationships that could have influenced the work reported in this paper.

### References

1. Bedova E. V., Kozaderov O. A. Electrooxidation Kinetics of formic acid on anodically modified silver-palladium alloys. *Electrochemical Energetics*, 2018;18(3): 141–154. DOI: <https://doi.org/10.18500/1608-4039-2018-18-3-141-154> (In Russ., abstract in Eng.)

2. Marshakov I. K., Vvedensky A. V., Kondrashin V. Yu., Bokov G. A. *Anodnoye rastvoreniye i selektivnaya korroziya splavov* [Anodic dissolution and selective corrosion of alloys]. Voronezh: Voronezh University Press; 1988. 208 p. (In Russ.).

3. *Encyclopedia of electrochemistry. Vol. 4. Corrosion and oxide films*. Eds. A. J. Bard, M. Stratmann, G. S. Frankel. Weinheim (Germany): Wiley-VCH; 2003. 755 p.

4. Landolt D. *Corrosion and Surface Chemistry of Metals*. EPFL Press; 2007. 632 p. DOI: <https://doi.org/10.1201/9781439807880>

5. Keshe G. *Korroziya metallov. Fiziko-himicheskie principy i aktualnye problem* [Corrosion of metals.

Physiochemical principles and actual problems]. Moscow: Metallurgy Publ.; 1984. 400 p. (In Russ.)

6. Marshakov I. K. *Termodinamika i korroziya splavov* [Thermodynamics and corrosion of alloys]. Voronezh: Voronezh University Press; 1983. 168 p. (In Russ.)

7. Kozaderov O. A. *Massoperenos, fazoobrazovaniye i morfologicheskaya nestabilnost poverkhnostnogo sloya pri selektivnom rastvorenii gomogennykh metallicheskikh splavov*. Dis. dr. him. nauk [Mass transfer, phase formation and morphological instability of the surface layer during the selective dissolution of homogeneous metal alloys]. *Diss. DSc in chemistry*. Voronezh: 2016. 361 p. (In Russ.). Available at: <http://www.science.vsu.ru/dissinfo&cand=2897>

8. Zartsyn I. D., Vvedensky A. V., Marshakov I. K. Nonequilibrium behavior of the surface-layer in anodic-dissolution of homogeneous alloys. *Russian Journal of Electrochemistry*. 1994;30(4): 492–512. Available at: <https://www.elibrary.ru/item.asp?id=29204402>

9. Zartsyn I. D., Vvedensky A. V., Marshakov I. K. Conversions of the noble component during selective dissolution of anhomogeneous alloy in the active state. *Protection of Metals*. 1991;27(1): 1–9. Available at: <https://www.elibrary.ru/item.asp?id=23951443>

10. Zartsyn I. D., Vvedensky A. V., Marshakov I. K. Termodinamika neravnovesnykh fazovykh prevrashcheniy pri selektivnom rastvorenii gomogennykh binarnykh splavov [Thermodynamics of non-equilibrium phase conversion under selective dissolution of homogeneous binary alloys]. *Protection of Metals*. 1991;27(6): 883–891. Available at: <https://www.elibrary.ru/item.asp?id=12712615> (In Russ.)

11. Kozaderov O. A., Vvedensky A. V. *Massoperenos i fazoobrazovanie pri anodnom selektivnom rastvorenii gomogennykh splavov* [Mass transfer and phase



formation during anodic selective dissolution of homogeneous alloys]. Voronezh: Nauchnaya kniga Publ.; 2014. 288 p.

12. Liu W. B., Zhang S. C., Li N., Zheng J. W., An S. S., Xing Y. L. A general dealloying strategy to nanoporous intermetallics, nanoporous metals with bimodal, and unimodal pore size distributions *Corrosion Science*. 2012;58: 133–138. DOI: <https://doi.org/10.1016/j.corsci.2012.01.023>

13. Hakamada M., Chino Y., Mabuchi M. Nanoporous surface fabricated on metal sheets by alloying/dealloying technique. *Materials Letters*. 2010;64(21): 2341–2343. DOI: <https://doi.org/10.1016/j.matlet.2010.07.046>

14. Weissmüller J., Newman R. C., Jin Hai-Jun, Hodge A. M. Nanoporous metals by alloy corrosion: Formation and mechanical properties. *MRS Bull.* 2009;34(8): 577–586. DOI: <https://doi.org/10.1557/mrs2009.157>

15. Erlebacher J., Aziz M. J., Karma A., Dimitrov N., Sieradzki K. Evolution of nanoporosity in dealloying. *Nature*. 2001;410(6827): 450–453. DOI: <https://doi.org/10.1038/35068529>

16. Wang Y., Wu B., Gao Y., Tang Y., Lu T., Xing W., Liu Ch. Kinetic study of formic acid oxidation on carbon supported Pd electrocatalyst. *Journal of Power Sources*. 2009;192(2): 372–375. DOI: <https://doi.org/10.1016/j.jpowsour.2009.03.029>

17. Rice C., Ha S., Masel R. I., Waszczuk P., Wieckowski A., Barnard T. Direct formic acid fuel cells. *J. Power Sources*. 2002;111(1): 83–89. DOI: [https://doi.org/10.1016/S0378-7753\(02\)00271-9](https://doi.org/10.1016/S0378-7753(02)00271-9)

18. Rice C. A., Wieckowski A. Electrocatalysis of formic acid oxidation. In: Shao M. (eds.) *Electrocatalysis in Fuel Cells. Lecture Notes in Energy*. London: Springer; 2013:9. 43–67. DOI: <https://doi.org/10.1007/978-1-4471-4911-8>

19. Jiang K., Zhang H., Zou Sh., Cai W. Electrocatalysis of formic acid on palladium and platinum surfaces : from fundamental mechanisms to fuel cell applications. *Phys. Chem. Chem. Phys.* 2014;16. 20360–20376. DOI: <https://doi.org/10.1039/C4CP03151B>

20. Hansen M., Anderko K. P. *Constitution of binary alloys*. New York: McGraw-Hill; 1958. 1305 p.

21. Isaev V.A. *Jelectrohimicheskoe fazoobrazovanie* [Electrochemical phase formation] Ekaterinburg Publ.; 2007. 123 p. (In Russ.).

22. MacDonald D.D. *Transient techniques in electrochemistry*. New York; London: Plenum Press.; 1977. 329 p. DOI: <https://doi.org/10.1007/978-1-4613-4145-1>

### Information about the authors

*Evgeniya V. Bedova*, postgraduate student, Department of Physical Chemistry, Faculty of Chemistry, Voronezh State University, Voronezh, Russian Federation; e-mail: [iev.vsu@mail.ru](mailto:iev.vsu@mail.ru). ORCID iD: <https://orcid.org/0000-0002-1284-7909>.

*Evgeniya A. Tonkih*, MSc student, Department of Physical Chemistry, Faculty of Chemistry, Voronezh State University, Voronezh, Russian Federation; e-mail: [ok@chem.vsu.ru](mailto:ok@chem.vsu.ru). ORCID iD: <https://orcid.org/0000-0002-5243-1895>.

*Oleg A. Kozaderov*, DSc in Chemistry, Associate Professor, Head of the Department of Physical Chemistry, Faculty of Chemistry, Voronezh State University, Voronezh, Russian Federation; e-mail: [ok@chem.vsu.ru](mailto:ok@chem.vsu.ru). ORCID iD: <https://orcid.org/0000-0002-0249-9517>.

All authors have read and approved the final manuscript.

*Translated by Valentina Mittova*

*Edited and proofread by Simon Cox*



# Condensed Matter and Interphases (Kondensirovannye sredy i mezhfaznye granitsy)

## Original articles

DOI: <https://doi.org/10.17308/kcmf.2020.22/2833>

Received 14 May 2020

Accepted 15 June 2020

Published online 25 June 2020

ISSN 1606-867X

eISSN 2687-0711

## Voltamperometry of a Kinetically Irreversible Electrochemical Process on a Rough Electrode

© 2020 E. V. Bedova, D. I. Kolganova, O. A. Kozaderov\*

Voronezh State University,  
1 Universitetskaya pl., Voronezh 394018, Russian Federation

### Abstract

We investigated the role of the effect of morphological inhomogeneity of the electrode surface in the voltammetric response of the irreversible electrochemical process in the mixed-kinetic mode. An algorithm was developed using the Comsol Multiphysics computer package for the numerical simulation of the electrode reaction, including successive stages of irreversible charge transfer and diffusion mass-transfer, using the finite element method. By numerical solution of the diffusion-kinetic problem, polarization curves of the irreversible electrochemical process on electrodes with a rough surface formed by the irregularities of various geometric types (sinusoidal surface, surface with protrusions, trapezoidal surface, sawtooth surface, and “random” surface) were obtained. We established the usage conditions for the voltammetric method of studying the kinetics of electrochemical processes under which the roughness of the electrode should be considered. It was found that at relatively high potential scan rates, the voltammetric maximum on the polarization curve was formed under conditions of a very small thickness of the diffusion layer, repeating the profile of the rough surface, therefore the peak current strength was proportional to the roughness factor. If the scanning rate was relatively low, then by the time the peak on the voltammogram was reached, the diffusion front was completely smoothed out, and the surface roughness of the electrode no longer affected the maximum current. At the same time, the shape of the irregularities responsible for the roughness did not significantly affect the voltammetric response of the irreversible electrochemical process.

**Keywords:** voltammetry, irreversible process, diffusion, roughness.

**For citation:** Bedova E. V., Kolganova D. I., Kozaderov O. A. Voltamperometry of a kinetically irreversible electrochemical process on a rough electrode. *Kondensirovannye sredy i mezhfaznye granitsy = Condensed Matter and Interphases*. 2020;22(2): 211–000. DOI: <https://doi.org/10.17308/kcmf.2020.22/2833>

### 1. Introduction

Voltammetry is one of the most informative transient methods for studying the kinetics and mechanism of electrochemical processes [1–5]. At the same time, the theoretical basis of this method was developed mainly for perfectly smooth flat electrodes, while the vast majority of electrochemical processes occur on the surface of solid electrodes, which are characterized by a noticeable geometric heterogeneity. The roughness effect in the voltammetric response was previously studied

for a diffusion-controlled electrode process [6–10], while the stage of charge transfer was considered reversible or quasi-reversible. At the same time, the electrochemical process, which is complicated by non-stationary diffusion mass-transfer, is often irreversible [1, 11–17]. The solution to the corresponding diffusion-kinetic problem can be obtained by computer simulation of the electrode process on the surface of a solid electrode with varying degree of geometric heterogeneity.

The purpose of this study was the quantitative description of the effect of morphological heterogeneity of the electrode surface in

✉ Kozaderov Oleg Alexandrovich, e-mail: [ok@chem.vsu.ru](mailto:ok@chem.vsu.ru)



The content is available under Creative Commons Attribution 4.0 License.

the voltammetric response to an irreversible electrochemical process.

The objectives of the study were as follows:

1. The calculation of voltammograms of an irreversible electrochemical process on electrodes with a rough surface formed by irregularities of various harmonic types (sinusoidal surface, surface with protrusions, trapezoidal surface, sawtooth surface and “random” surface).

2. The establishment of the roles of potential scan rate, roughness factor, and geometric shape of roughness in the value of the criterion parameters of the voltammetric signal of an irreversible electrochemical process - current and overpotential maximum.

## 2. Formulation of the Problem

Consider the process of electrochemical transformation, described by the first-order reaction equation:



in which  $n$  – the number of electrons,  $\vec{k}$  and  $\bar{k}$  – heterogeneous rate constants of the anodic and cathodic reactions, respectively, depending on the electrode potential  $E$  (overpotential  $\eta$ ) [20]. Assuming that  $\vec{k} \gg \bar{k}$ , i.e. reverse transformation  $\text{Ox}$  in  $\text{Red}$  is neglected. This assumption is valid for sufficiently high overpotentials, several times higher than  $RT/F \approx 25$  mV ( $R$  – universal gas constant,  $T$  – temperature,  $F$  – Faraday constant), or in cases where the oxidized form of a substance  $\text{Ox}$  is insoluble or has a very high diffusion mobility in the solution.

We suppose that the electrochemically active substance  $\text{Red}$  is delivered to the electrode by semi-infinite diffusion, and the spatio-temporal profile of its concentration  $c$  is described by the equation of Fick's second law [4]. For a perfectly smooth flat surface, the diffusion problem will be one-dimensional:

$$\frac{\partial c}{\partial t} = D \frac{\partial^2 c}{\partial z^2}. \quad (2)$$

Where  $D$  – volume diffusion coefficient,  $t$  – time; coordinate axis  $z$  directed deep into the solution perpendicular to the plane of the electrode. As model surfaces, we will consider corrugated profiles (Fig. 1) with the distance between adjacent irregularities  $\lambda$ , the height of

the irregularities  $\varepsilon$  and roughness factor  $f_r = S/S_g$ , equal to the ratio of real  $S$  and geometric  $S_g$  electrode area. In this case, for the calculation of the concentration profile, it is necessary to solve a two-dimensional differential equation:

$$\frac{\partial c}{\partial t} = D \left( \frac{\partial^2 c}{\partial x^2} + \frac{\partial^2 c}{\partial z^2} \right). \quad (3)$$

Coordinate axis  $x$  directed perpendicular to the axis  $z$ .

The moment the polarization is turned on ( $t = 0$ ) the concentration of substance  $\text{Red}$  in all points of the solution is the same and equal to its volumetric value (the initial condition of the diffusion-kinetic problem):

$$c|_{t=0} = c^0. \quad (4)$$

According to the first boundary condition, the concentration of the substance  $\text{Red}$  approaches the value  $c^0$  the further from the surface of the electrode.

$$c|_{z \rightarrow \infty} = c^0. \quad (5)$$

The second boundary condition connects the diffusion flux of the substance to the electrode surface along the normal vector  $\vec{n}$  and its consumption rate during the electrode reaction:

$$D \frac{\partial c}{\partial \vec{n}} \Big|_s = \vec{k} c. \quad (6)$$

The rate constant  $\vec{k}$  exponentially depends on the overpotential  $\eta = Vt$  which in the potentiodynamic polarization mode varies linearly with time at a rate equal to the potential scan rate  $V = dE/dt$ :

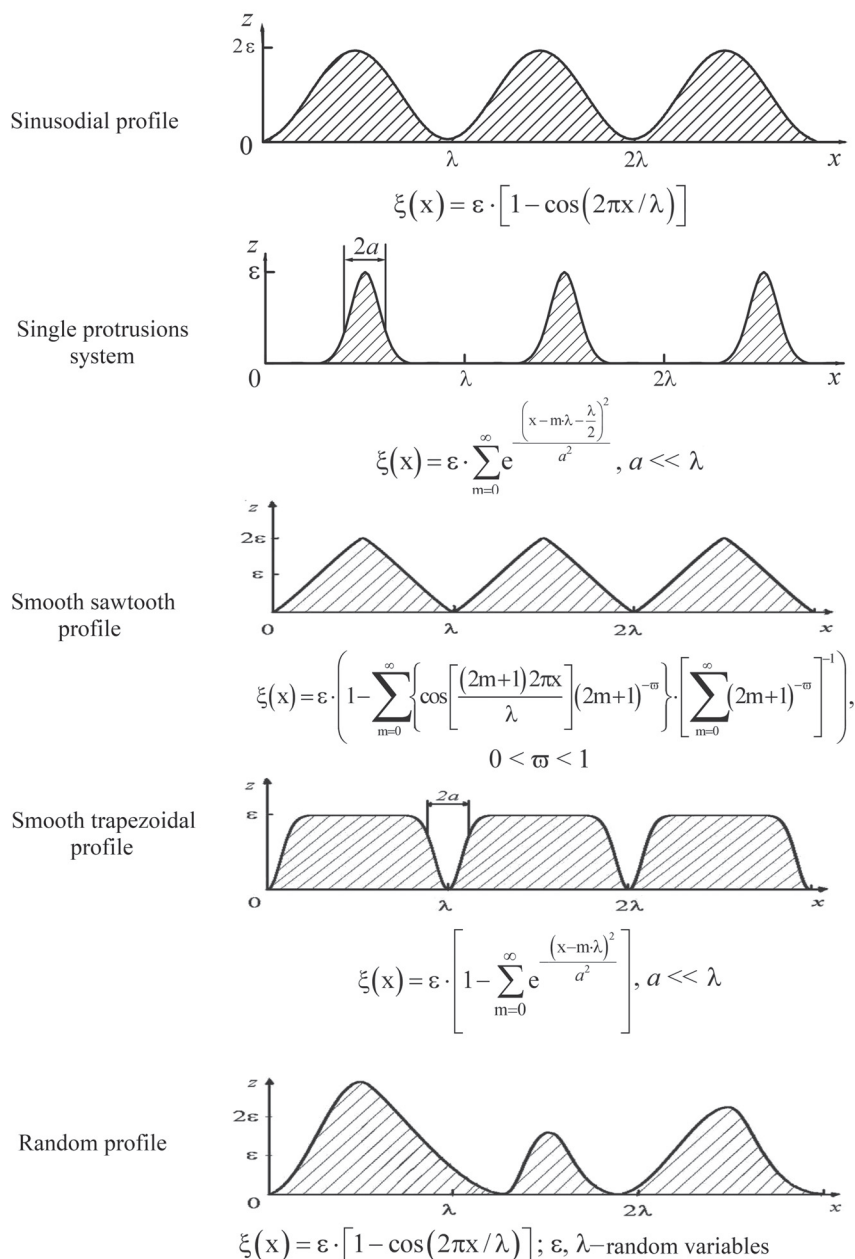
$$\vec{k} = \frac{i^0}{nFc^0} \exp\left(\frac{\alpha nF}{RT} Vt\right). \quad (7)$$

Here  $i^0$  – exchange current density,  $\alpha$  – charge transfer coefficient.

The voltammogram of the process was calculated as a dependence of the current density  $i$  on overpotential  $\eta$ , taking into account the following ratio:

$$I = nFD \frac{\partial c}{\partial \vec{n}} \Big|_s. \quad (8)$$

Graphically, the potentiodynamic curves were presented in dimensionless  $H, Y$  coordinates where  $H = nF\eta/RT$  (dimensionless overpotential) and  $Y = I/nFc^0DS_g$  (dimensionless current).

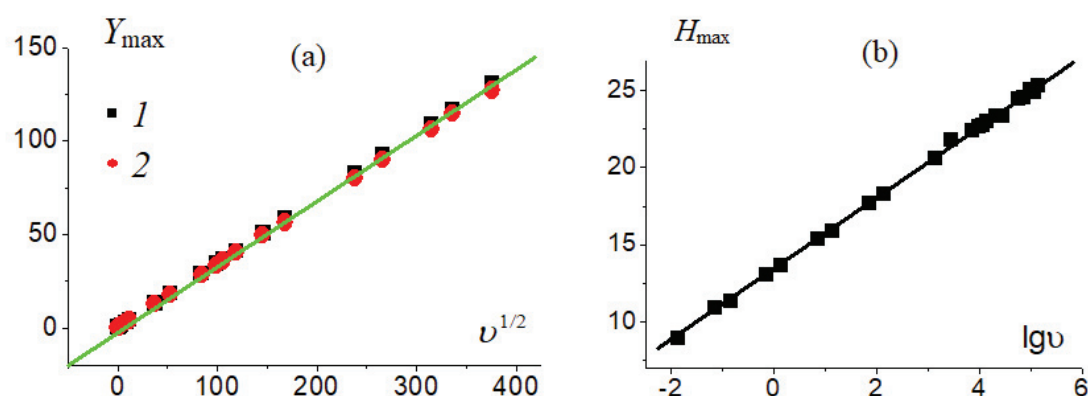


**Fig. 1.** Geometric profiles simulating the rough surface of the electrode

The system of equations (1)–(8) was solved numerically by the finite element method in the Comsol Multiphysics program [18, 19] for different values of the dimensionless potential scan rate  $v = \frac{nF\lambda^2}{RTD} V$ . The values of the estimated input parameters in Table 1 were selected so that they corresponded to the irreversible charge transfer stage on the electrode complicated by the non-stationary diffusion mass-transfer of *Red* in an electrolyte solution.

For checking the adequacy of the choice of input parameter values and the numerical solution

as a whole, during the first stage we compared the results obtained in Comsol Multiphysics for a perfectly smooth electrode with a flat surface (Fig. 2a) with an analytical solution known from the literature [19]. It turned out that the peak height  $Y_{\max}$  on the calculated curves was proportional to the square root of the dimensionless scan rate  $v^{1/2}$  (Fig. 2b). In the logarithmic  $H, \lg v$ -coordinates the maximum overpotential  $H_{\max} = nF\eta_{\max}/RT$  linearly increased. At the same time, the results of the numerical and analytical solutions completely coincided, which allowed using the developed algorithm for the rough surface of the electrode.



**Fig. 2.** Criterion dependences of current density (a) and overpotential (b) of the voltammogram maximum of an irreversible electrochemical process, obtained based the results of analytical (1) and numerical (2) solutions to the diffusion-kinetic problem and presented in dimensionless coordinates

**Table 1.** The values of the parameters of numerical calculation

Parameter	Value
Volume concentration of diffusant $c^0$	1 mol/m <sup>3</sup>
Exchange current density $i^0$	10 <sup>-3</sup> A/m <sup>2</sup>
The number of electrons $n$	1
Charge transfer coefficient $\alpha$	0.5
Faraday constant $F$	96485 C/mol
Universal gas constant $R$	8.314 J/K·mol
Temperature $T$	298 K
Diffusion coefficient $D$	10 <sup>-9</sup> m <sup>2</sup> /s
Roughness factor $f_r$	1 ÷ 5
The distance between adjacent irregularities $\lambda$	0.5 $\mu$ m
Potential scan rate $V$	10 <sup>-4</sup> ÷ 10 <sup>3</sup> V/s

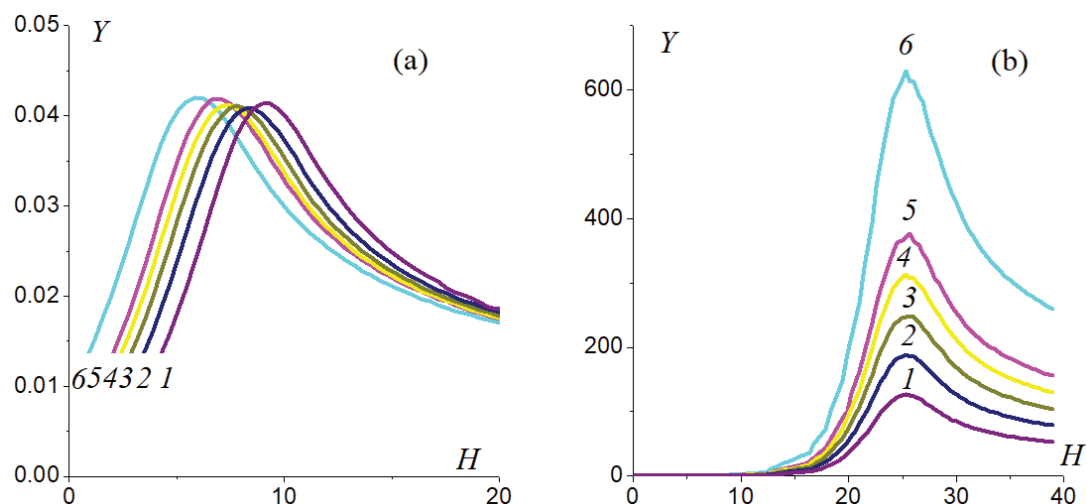
### 3. Results and discussion

Voltammograms of a kinetically irreversible electrochemical process calculated for two values of dimensionless potential scan rates  $\nu$ , which differ by 10<sup>7</sup> times, are shown in Fig. 3. As on a perfectly smooth electrode, the presented curves had a characteristic maximum of dimensionless current density  $Y$ . At the same time, if the scan rate was relatively low, then the maximum height did not depend on the roughness factor (Fig. 3a). With a high scan rate, on the contrary, a clear dependence of the peak height on  $f_r$  was revealed (Fig. 3b).

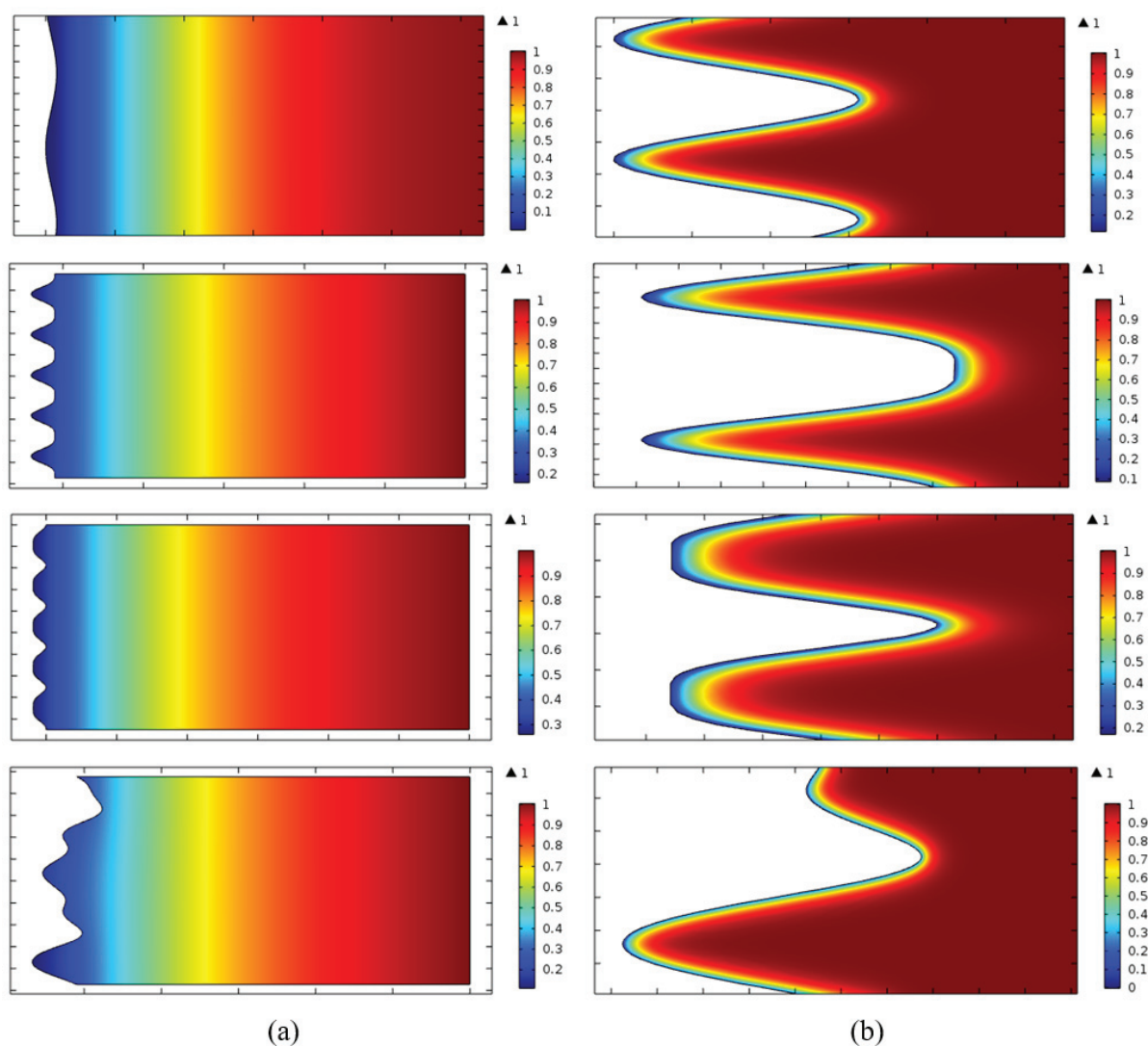
The observed difference in the potentiodynamic behaviour of the considered system can be explained by analysing the concentration field of the diffusant near the electrode (Fig. 4).

When the potential is scanned slowly, by the time the current peak is reached, the diffusion front propagates deep enough into the solution, acquiring a flat shape. The height of the electrode irregularities is much less than the thickness of the formed diffusion layer. As a result, the surface roughness factor does not affect the current strength (Fig. 4a). If the scan rate is high, then upon reaching the peak value of the current, the diffusion front propagates deep into the solution to a very small distance. In this case, the diffusion front repeats the profile of the rough surface, and the height of the irregularities is much higher than the thickness of the diffusion layer (Fig. 4b). That is why the diffusion flux of the electrochemically active substance, the electrochemical reaction rate, and the current strength are proportional to the roughness factor.

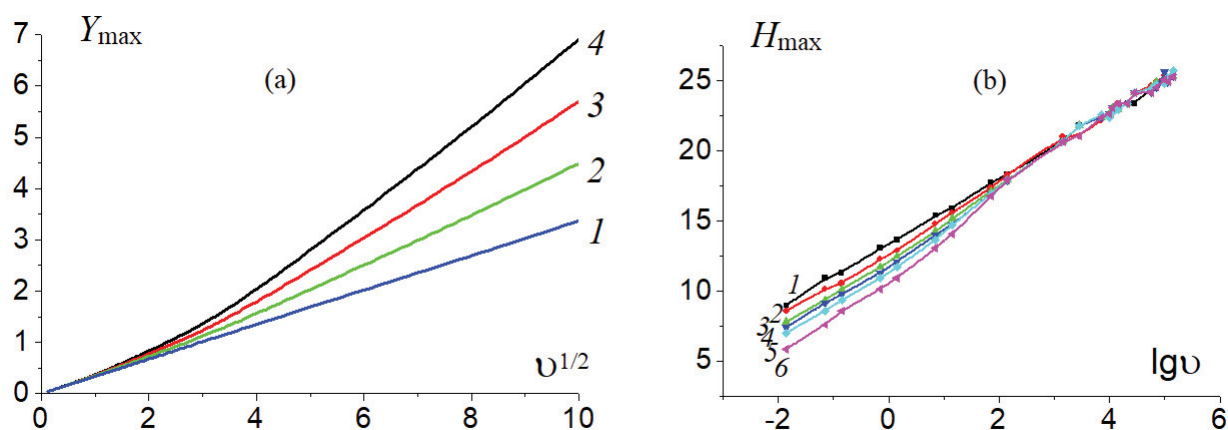
Consider the dependences of the maximum current strength and the maximum overpotential of the voltammogram on the scan rate, plotted in coordinates, criterion for voltammetry  $Y_{\max}, \nu^{1/2}$ - and  $H_{\max}, \lg \nu$  (Fig. 5). It can be seen that with  $\nu < 1$ , the calculated curves coincide, while for  $\nu > 2$  their divergence is observed. The analysis shows that for  $\nu \gg 1$  criterion  $Y_{\max}, \nu^{1/2}$ -dependencies are linearized and extrapolated to the origin of the coordinates. In turn, the maximum overpotential  $H_{\max}$  is linearly dependent on the logarithm of the scan rate over the entire range of values  $\nu$  only in the case of a perfectly smooth flat electrode surface. If the process occurs on a rough surface, then the dependence of  $H_{\max}$  on  $\lg \nu$  is linear only for  $\lg \nu < 0$  and  $\lg \nu > 3$ , i.e. in the region of very



**Fig. 3.** Voltammograms of a kinetically irreversible electrochemical process occurring on the surface of an electrode with a roughness factor  $f_r = 1$  (1), 1.5 (2), 2 (3), 2.5 (4), 3 (5), 5 (6), calculated for a corrugated electrode with a sinusoidal microroughness at the dimensionless potential scan rate  $\nu = 0.0141$  (a) and 141000 (b)



**Fig. 4.** The concentration field of the diffusant (in dimensionless  $c/c^0$  units) in a solution near a rough surface of various harmonic types by the time the current maximum was reached at  $f_r = 2$  and  $\nu = 0.0141$  (a) and 141000 (b)



**Fig. 5.** Criterion dependences of the voltammetric maximum parameters - peak current (a) and peak overpotential (b), calculated for a perfectly smooth plane (1) and sinusoidal (2) - (6) electrode surface at different values of the roughness factor  $f_r = 1.5$  (2), 2 (3), 2.5 (4), 3 (5), 5 (6)

low or very high values of the potential scan rate. Moreover, if  $v$  is low, then the maximum overpotential decreases with an increase in the roughness factor.

For electrodes with irregularities of various shapes the dependence of the ratio of currents on rough and flat electrodes  $\phi$ , which we will call the “roughness function” is shown in Fig. 5. In the case where the time to reach the maximum of the voltammogram was very short (i.e., at high potential scan rates), the roughness function is simply equal to the roughness factor  $\phi = f_r$ . Under such conditions of the voltammetric experiment, taking into account the roughness of the electrode surface is mandatory and is reduced to dividing the current strength by  $f_r$ . If the potential scan rate is low, then the roughness function is equal to one, and the correction of current at the maximum of the voltammogram for the electrode roughness is not required.

We come to the same conclusion, taking into account the behaviour of the roughness function  $\phi$  calculated over a wide range of dimensionless time to reach maximum current  $\tau_{\max} = Dt_{\max}/\lambda^2$ . The independence of the  $\phi$  function from the roughness factor  $f_r$  and from time is observed only over relatively large times  $\tau_{\max} > 50$  (Fig. 6), i.e. for the slow potential scan rate. If the maximum current is reached quickly, which corresponds to high scan rates and values  $\tau_{\max} < 10^{-2}$  then  $\phi = f_r$  since the diffusion front replicates the surface profile.

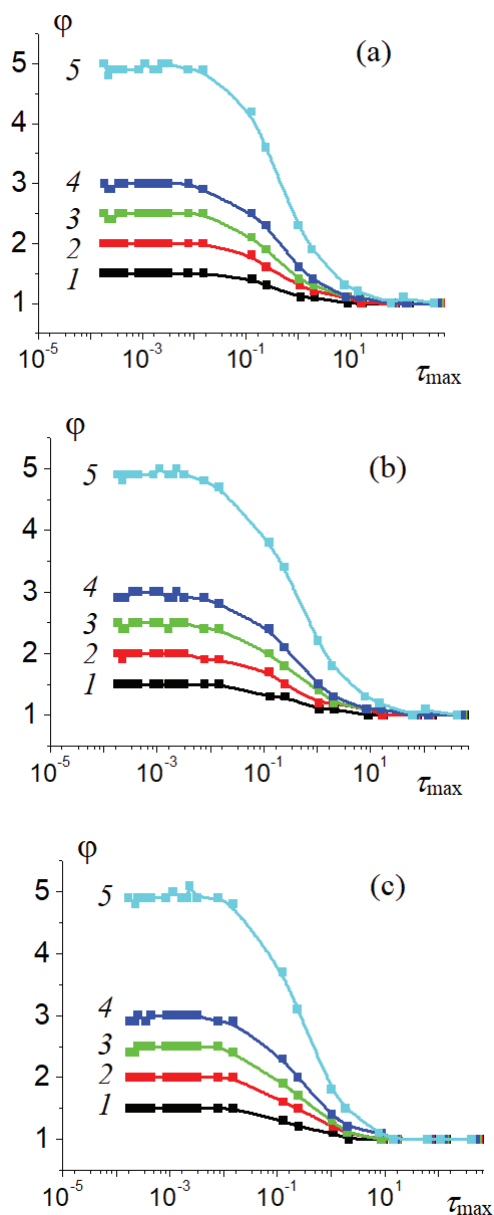
A comparison of the calculation results for rough surfaces of various harmonic types showed

that the geometric shape of the irregularities does not affect the shape of voltammograms irrespective of the potential scan rate value (Fig. 7).

It should be noted that under real conditions, the fact that at high scan potential rates electrochemical measurements can be complicated by the flow of a non-faradic capacitive current through the electrode should be also taken into account. The occurrence of non-faradic capacitive current is caused by the charging of a double electric layer, the electric capacity of which (especially with a highly developed surface) can reach very high values. The consideration of this effect was not included in the objectives of this study and requires additional research within the framework of the corresponding diffusion-kinetic problem.

#### 4. Conclusions

The numerical solution to the non-stationary diffusion-kinetic problem demonstrated that taking into account the roughness of the electrode surface in voltammetry of an irreversible electrochemical process, which is complicated by the non-stationary diffusion transfer of an electroactive substance, is mandatory if the potential scan rate is relatively high. Under these conditions, upon reaching the peak value of the current, the diffusion front propagates deep into the solution to a very small distance, and the diffusion layer completely replicates the profile of the rough surface, therefore, the diffusion flux density and current density should be normalized to the electrode roughness factor.

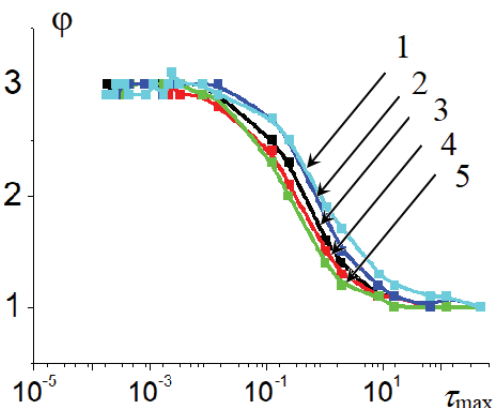


**Fig. 6.** Transients of roughness function calculated for sinusoidal (a), sawtooth (b), and consisting of single protrusion (c) surfaces with roughness factor  $f_r = 1.5$  (1), 2 (2), 2.5 (3), 3 (4), 5 (5)

If the potential scan rate is relatively low, then by the time the current peak is reached, the diffusion front propagates deep into the solution and is completely smoothed, therefore, the diffusion flux density and the current density are proportional not to the real, but to the geometric area of the electrode.

### Conflict of interests

The authors declare that they have no known competing financial interests or personal



**Рис. 7.** Транзиенты функции шероховатости, рассчитанные для случайной (1), трапецидальной (2), синусоидальной (3), пилообразной (4), состоящей из одиночных выступов (5) поверхностей при значении фактора шероховатости  $f_r = 3$

relationships that could have influenced the work reported in this paper.

### References

1. Compton R. G., Banks Craig E. *Understanding Voltammetry*. World Scientific; 2007. 371 p. DOI: <https://doi.org/10.1142/6430>
2. Vvedenskii A. V., Kozaderov O. A. Linear voltammetry of anodic selective dissolution of homogeneous metallic alloys. In: Saito Y., Kikuchi T. (eds.) *Voltammetry: theory, types and applications*. New York: Nova Science Publishers, Inc.; 2014. 349 p.
3. Bard A. J., Faulkner L. R. *Electrochemical methods. Fundamentals and applications. 2nd edition*. New York: Wiley; 2000. 856 p.
4. Galjus Z. *Teoreticheskie osnovy elektrohimicheskogo analiza* [Theoretical foundations of electrochemical analysis]. Moscow: Mir Publ.; 1974. 552 p. (In Russ.)
5. Matsuda H., Ayabe J. Z. Zur theorie der Randles-Sevcikschien kathodenstrahl-polarographie. *Z. Electrochem.* 1955;59(6): 494–503. Available at: DOI: <https://doi.org/10.1002/bbpc.19550590605>
6. Menshykau D., Streeter I., Compton R. G. Influence of electrode roughness on cyclic voltammetry. *J. Phys. Chem. C.* 2008;112(37): 14428–14438. DOI: <https://doi.org/10.1021/jp8047423>
7. Menshykau D., Compton R. G. Influence of electrode roughness on stripping voltammetry : mathematical modeling and numerical simulation. *J. Phys. Chem. C.* 2009;113(35): 15602–15620. DOI: <https://doi.org/10.1021/jp904187t>
8. Kozaderov O. A., Vvedenskij A. V. Vol'tamprometrija selektivnogo rastvorenija binarnogo gomogenennogo metallichesko splava v uslovijah tverdogaznogo massoperenosa [Voltammetry of selective dissolution of a binary homogeneous metal alloy under conditions of solid-phase mass transfer].



*Kondensirovannye sredy i mezhfaznye granitsy = Condensed Matter and Interphases*. 2011;13(4): 452–459. Available at: [http://www.kcmf.vsu.ru/resources/t\\_13\\_4\\_2011\\_010.pdf](http://www.kcmf.vsu.ru/resources/t_13_4_2011_010.pdf) (In Russ.)

9. Kozaderov O. A., Lozovskij V. V., Vvedenskij A. V. Chronovoltammetry of the anodic dissolution of Ag-Au alloys in a nitrate medium. *Protection of Metals*. 2008;44(4): 333–342. DOI: <https://doi.org/10.1134/S0033173208040036>

10. Kozaderov O. A., Vvedenskij A. V. Voltammetry of selective dissolution of Ag-Au alloys under conditions of solid phase liquid phase mass transfer. *Protection of Metals and Physical Chemistry of Surfaces*. 2013;49(6): 724–733. DOI: <https://doi.org/10.1134/S2070205113060099>

11. Arun Prasad M., Sangaranarayanan M. V. Formulation of a simple analytical expression for irreversible electron transfer processes in linear sweep voltammetry and its experimental verification. *Electrochimica Acta*. 2004;49(16): 2569–2579. DOI: <https://doi.org/10.1016/j.electacta.2004.01.028>

12. Singh T., Dutt J. Linear sweep voltammetry at the tubular graphite electrode: Part II. Totally irreversible processes. *J. of Electroanalytical Chem. and Interfacial Electrochemistr.* 1985;196(1): 35–42. DOI: [https://doi.org/10.1016/0022-0728\(85\)85078-6](https://doi.org/10.1016/0022-0728(85)85078-6)

13. Jin W., Cui H., Zhu L., Wang Sh. On the theory of the integer and half-integer integral and derivative linear potential sweep voltammetry for a totally irreversible interfacial reaction. *J. of Electroanalytical Chem. and Interfacial Electrochemistr.* 1991;309(1–2): 37–47. DOI: [https://doi.org/10.1016/0022-0728\(91\)87002-L](https://doi.org/10.1016/0022-0728(91)87002-L)

14. Aoki K., Tokuda K., Matsuda H. Theory of linear sweep voltammetry with finite diffusion space: Part II. Totally irreversible and quasi-reversible cases. *J. of Electroanalytical Chem. and Interfacial Electrochemistr.* 1984;160(1–2): 33–45. DOI: [https://doi.org/10.1016/S0022-0728\(84\)80113-8](https://doi.org/10.1016/S0022-0728(84)80113-8)

15. Andricacos P. C., Cheh H. Y. The application of linear sweep voltammetry to a rotating disk electrode for a first-order irreversible reaction. *J. of Electroanalytical Chem. and Interfacial Electrochemistr.* 1981;124(1–2): 95–101. DOI: [https://doi.org/10.1016/S0022-0728\(81\)80287-2](https://doi.org/10.1016/S0022-0728(81)80287-2)

16. Kohler H., Piron D. L., Belanger G. A linear sweep voltammetry theory for irreversible electrode reactions with an order of one or higher: I. Mathematical formulation. *J. of the Electrochemical Society*. 1987;134(1): 120–126. DOI: <https://doi.org/10.1149/1.2100388>

17. Nahir T. M., Clark R. A. Bowden E. F. Linear-sweep voltammetry of irreversible electron transfer in surface-confined species using the Marcus theory. *Anal. Chem.* 1994;66(15): 2595–2598. DOI: <https://doi.org/10.1021/ac00087a027>

18. Truhan S. N., Derevshnikov V. S. *Komp'yuternoe modelirovanie processov i javlenij fizicheskoy himii* [Computer modeling of processes and phenomena of physical chemistry]. Novosibirsk: NSU Publ.; 2012. 75 p. (In Russ.)

19. Krasnikov G. E., Nagornov O. V., Starostin N. V. *Modelirovanie fizicheskikh processov s ispol'zovaniem paketa Comsol Multiphysics* [Modeling of physical processes using the Comsol Multiphysics package]. Moscow: NRNU MEPhI Publ.; 2012. 184 p. (In Russ.)

20. Damaskin B. B., Petrij O. A., Cirlina G. A. *Jelektrohimiya: Uchebnik dlja vuzov* [Electrochemistry: a textbook for universities]. Moscow: Khimiya Publ.; 2001. 624 p. (In Russ.)

### Information about the authors

*Evgeniya V. Bedova*, postgraduate student, Department of Physical Chemistry, Faculty of Chemistry, Voronezh State University, Voronezh, Russian Federation; e-mail: [iev.vsu@mail.ru](mailto:iev.vsu@mail.ru). ORCID iD: <https://orcid.org/0000-0002-1284-7909>.

*Darya I. Kolganova*, student, Department of Physical Chemistry, Faculty of Chemistry, Voronezh State University, Voronezh, Russian Federation; e-mail: [kolganovadi@mail.ru](mailto:kolganovadi@mail.ru). ORCID iD: <https://orcid.org/0000-0001-9660-0761>.

*Oleg A. Kozaderov*, DSc in Chemistry, Associate Professor, Head of the Department of Physical Chemistry, Faculty of Chemistry, Voronezh State University, Voronezh, Russian Federation; e-mail: [ok@chem.vsu.ru](mailto:ok@chem.vsu.ru). ORCID iD: <https://orcid.org/0000-0002-0249-9517>.

All authors have read and approved the final manuscript.

*Translated by Valentina Mittova*

*Edited and proofread by Simon Cox*



# Condensed Matter and Interphases (Kondensirovannyye sredy i mezhfaznyye granitsy)

## Original articles

DOI: <https://doi.org/10.17308/kcmf.2020.22/2823>

Received 28 April 2020

Accepted 15 May 2020

Published online 25 June 2020

ISSN 1606-867X

eISSN 2687-0711

## Synthesis, Structure, and Luminescent Properties of the New Double Borate $K_3Eu_3B_4O_{12}$

© 2020 E. V. Kovtunets<sup>✉</sup>, A. K. Subanakov, B. G. Bazarov

Baikal Institute of Nature Management, Siberian Branch of the Russian Academy of Sciences,  
6, Sakhyanova str., 670047 Ulan-Ude, Republic of Buryatia, Russian Federation

### Abstract

The study established the formation of the new double borate  $K_3Eu_3B_4O_{12}$ . The Rietveld refinement of the crystal structure revealed that  $K_3Eu_3B_4O_{12}$  crystallises in the monoclinic syngony with unit cell parameters  $a = 10.6727(7) \text{ \AA}$ ,  $b = 8.9086(6) \text{ \AA}$ ,  $c = 13.9684(9) \text{ \AA}$ ,  $\beta = 110.388(2)^\circ$  (space group  $P2_1/c$ ).  $K_3Eu_3B_4O_{12}$  has a layered structure with  $[Eu_8(BO_3)_8]^\infty$  sheets which are almost parallel to the  $ab$  plane. These sheets are formed by pentagonal  $EuO_7$  bipyramids,  $EuO_6$  octahedras, and  $BO_3$  triangles attached to them through common vertices. Neighbouring layers are interconnected via pentagonal  $EuO_7$  bipyramids,  $BO_3$  triangles, and potassium cations. The luminescence spectrum demonstrates a noticeable emission band at 611 nm, resulting from the  ${}^5D_0 \rightarrow {}^7F_2$  transition of  $Eu^{3+}$  ions.

**Keywords:** double borates of potassium and rare-earth elements, ceramic technology, Rietveld method, luminescent properties.

**Funding:** The study received financing within the framework of state order No. 0339-2019-0007 to the Baikal Institute of Nature Management, Siberian Branch of the Russian Academy of Sciences. It was partially funded by the Russian Foundation for Basic Research (project No. 18-08-00985 a).

**For citation:** Kovtunets E. V., Subanakov A. K., Bazarov B. G. Synthesis, structure and luminescent properties of the new double borate  $K_3Eu_3B_4O_{12}$ . *Kondensirovannyye sredy i mezhfaznyye granitsy = Condensed Matter and Interphases*. 2020; 22(2): 219–224. DOI: <https://doi.org/10.17308/kcmf.2020.22/2823>

## 1. Introduction

Over recent years, a lot of attention has been paid to the synthesis of binary and ternary compounds with boron-oxygen groups. They include a great number of phases with functionally relevant (luminescence, nonlinear-optical, etc.) properties [1, 2].

The study of phase equilibria in systems  $Rb_2O - RE_2O_3 - B_2O_3$  ( $RE = Nd, Eu, Ho$ ) revealed two families of isostructural double borates:  $Rb_3REB_6O_{12}$  [3, 4] and  $Rb_3RE_2B_3O_9$  [5]. The present paper continues our systematic research aimed at the identification, preparation, and comprehensive characterisation of double borates

with an alkali metal cation and a rare-earth element in their composition.

The study of the phase formation in  $K_2O - Eu_2O_3 - B_2O_3$  resulted in obtaining the  $K_3Eu_3B_4O_{12}$  compound, isostructural  $K_3Gd_3B_4O_{12}$ , for the first time [6].

## 2. Experimental

Ultra pure  $K_2CO_3$ ,  $Eu_2O_3$ , and  $H_3BO_3$  were used for the synthesis. High temperature annealing was conducted in a Naberthern L3/11/P320 programmable laboratory furnace, cooling was carried out inertially in the furnace.

XRD patterns for the synthesised sample were obtained at room temperature using

✉ Evgeniy V. Kovtunets, e-mail: [kovtunets@binm.ru](mailto:kovtunets@binm.ru)



The content is available under Creative Commons Attribution 4.0 License.

a D8 ADVANCE Bruker AXS powder X-ray diffractometer with a Vantec-1 detector ( $CuK_{\alpha}$  radiation recording interval  $2\theta = 5-100^\circ$ , scanning step  $0.02076^\circ$ ).

The TOPAS 4.2 software suite was used to analyse the experimental data and to conduct the Rietveld refinement of the obtained compound [7]. All peaks in the  $K_3Eu_3B_4O_{12}$  X-ray powder diffraction patterns were indexed satisfactorily by a monoclinic cell (space group  $P2_1/c$ ).

The luminescence spectra were recorded with a SDL-1 (LOMO) double monochromator with  $600 \text{ lines/mm}^{-1}$  grating and a FEU-106 photoelectron multiplier, excitation was carried out using a high-pressure 150 WDKSH-150 xenon arc lamp through a MDR-2 monochromator with a diffraction grating of  $1200 \text{ lines/mm}^{-1}$ . A transparent undoped LiF crystal, used as a substrate for the sample, was fixed in a holder.

The  $K_3Eu_3B_4O_{12}$  synthesis was conducted using ceramic technology by stepped annealing of stoichiometric proportions of reagent mixtures.

Calcium carbonate and europium oxide were annealed at  $800^\circ\text{C}$  for 24 hours to remove water. The reaction mixture was carefully ground in an agate mortar for better homogenisation, gradually heated to  $200$  and  $600^\circ\text{C}$  at  $1^\circ\text{C/min}$ , and incubated for 5 hours at those temperatures. Then, the sample was homogenised and further annealed at  $750-850^\circ\text{C}$  for 48 hours (with intermediate grinding every 8 hours of the heat treatment).

### 3. Results and discussion

The synthesised sample of double borate is a dry white powder.

The powder X-ray diffraction patterns were used for the Rietveld refinement of the crystal structure of  $K_3Eu_3B_4O_{12}$ . The  $K_3Gd_3B_4O_{12}$  structure was used to define the positions of atoms for the initial model. They were refined by isotropic approximation with "soft" limitations of the B–O distance and the B–O–B bond angles. The refinement was carried out by gradually adding refined parameters with the constant graphical simulation of the background. The Pearson VII Function was used to describe the shape of peaks. Isotropic displacement parameters ( $B_{iso}$ ) for the Eu and K atoms were refined separately, while for the O and B atoms they were taken as equivalent.

The refinement process included corrections for the sample preferred orientation and anisotropy broadening of peaks within the model of spherical harmonics [8]. Occupancy refinement of the positions of the disordered oxygen atoms O1, O9, and O9p was not conducted, as the attempts to refine occupancy of the disordered atoms did not contribute to a better description of the x-ray diffraction patterns.

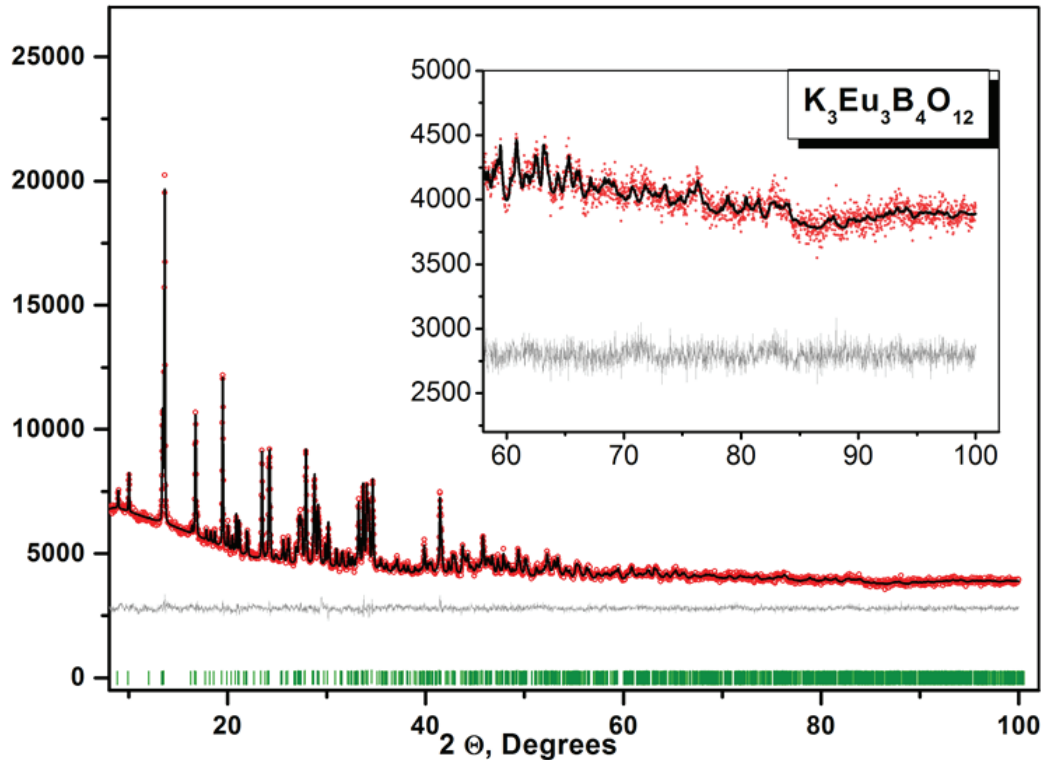
The refinement results for  $K_3Eu_3B_4O_{12}$  are shown in Table 1, coordinates of atoms and isotropic displacement parameters are given in Table 2, and calculated and experimental x-ray diffraction patterns with difference curves are shown in Fig. 1.

The structure of the synthesised compound is characterised by the  $[Eu_8(BO_3)_8]_\infty$  sheets which are almost parallel to the  $ab$  plane. These sheets are formed by pentagonal  $EuO_7$  bipyramids,  $EuO_6$  octahedras, and  $BO_3$  triangles attached to them through common vertices (see Fig. 2). Neighbouring layers are interconnected via pentagonal  $EuO_7$  bipyramids,  $BO_3$  triangles, and potassium cations.

The luminescence centres in the studied phases are the  $Eu^{3+}$  [9] ions with intensive red luminescence. All the spectra have the five bands characteristic of transitions in the  $4f$ -configuration of the  $Eu^{3+}$  ion from the excited metastable

**Table 1.**  $K_3Eu_3B_4O_{12}$  crystallographic characteristics and structure refinement parameters

Space group:	$P2_1/c$
$a, \text{Å}$	10.6727(7)
$b, \text{Å}$	8.9086(6)
$c, \text{Å}$	13.9684(9)
$\beta, ^\circ$	110.388(2)
$V, \text{Å}^3$	1244.90(14)
Z	4
$2\theta$ -interval, $^\circ$	8–100
No. of reflections	1295
No. of refined parameters	120
$R_{wp}, \%$	1.77
$R_p, \%$	1.39
$R_{exp}, \%$	1.45
$\chi^2$	1.22
$R_B, \%$	0.55



**Fig. 1.** The measured (circles) and calculated (line), differential, and stroke x-ray diffraction patterns of  $K_3Eu_3B_4O_{12}$

**Table 2.** Fractional atomic coordinates and isotropic displacement parameters ( $E^2$ ) of  $K_3Eu_3B_4O_{12}$

Atom	$x$	$y$	$z$	Occupancy	$B_{iso}, \text{\AA}^2$
Eu1	1/2	0.6925 (8)	1/4	1	0.2 (4)
Eu2	0.7884 (6)	1.3014 (5)	0.2502 (4)	1	1.0 (3)
Eu3	0.6643 (6)	0.9684 (7)	0.1195 (4)	1	1.0 (3)
Eu4	1	0.7648 (8)	1/4	1	1.3 (4)
K1	0.418 (2)	0.357 (2)	0.095 (1)	1	1.5 (6)
K2	0.887 (2)	1.431 (2)	0.042 (1)	1	1.4 (7)
K3	0.798 (2)	0.935 (2)	0.402 (1)	1	1.5 (7)
B1	1/2	1.111 (3)	1/4	1	2.0 (15)
B2	0.737 (2)	0.594 (2)	0.228 (2)	1	2.0 (15)
B3	0.877 (3)	0.758 (3)	0.016 (2)	1	2.0 (15)
B4	0.626 (2)	1.221 (2)	-0.008 (2)	1	2.0 (15)
B5	1	1.101 (3)	1/4	1	2.0 (15)
O1	0.517 (3)	0.960 (2)	0.233 (2)	0.5	0.9 (5)
O2	0.392 (3)	1.156 (2)	0.274 (3)	1	0.9 (5)
O3	0.641 (2)	0.499 (3)	0.236 (2)	1	0.9 (5)
O4	0.854 (2)	0.539 (3)	0.220 (3)	1	0.9 (5)
O5	0.713 (3)	0.751 (4)	0.230 (3)	1	0.9 (5)
O6	0.847 (3)	0.712 (4)	-0.086 (2)	1	0.9 (5)
O7	0.999 (2)	0.721 (4)	0.088 (2)	1	0.9 (5)
O8	0.784 (2)	0.840 (4)	0.042 (2)	1	0.9 (5)
O9	0.502 (6)	1.154 (6)	-0.027 (3)	0.537	0.9 (5)
O9p	0.567 (5)	1.089 (3)	-0.058 (1)	0.463	0.9 (5)
O10	0.628 (3)	1.348 (2)	-0.067 (1)	1	0.9 (5)
O11	0.722 (3)	1.214 (2)	0.089 (2)	1	0.9 (5)
O12	0.891 (2)	1.025 (3)	0.253 (2)	1	0.9 (5)
O13	1	1.254 (2)	1/4	1	0.9 (5)

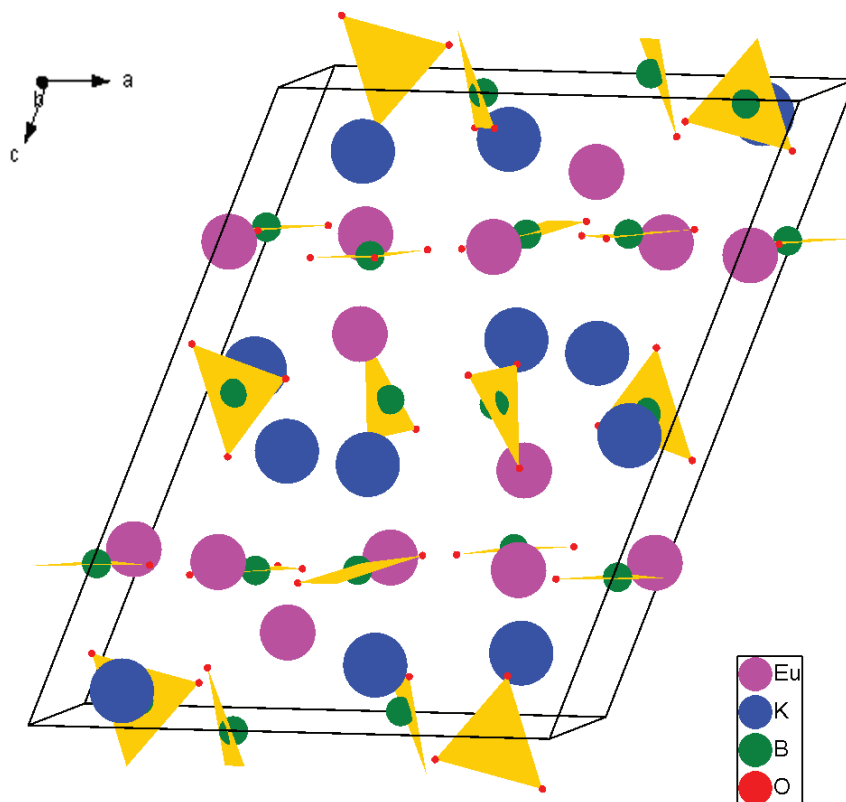


Fig. 2. The crystal structure of  $K_3Eu_3B_4O_{12}$

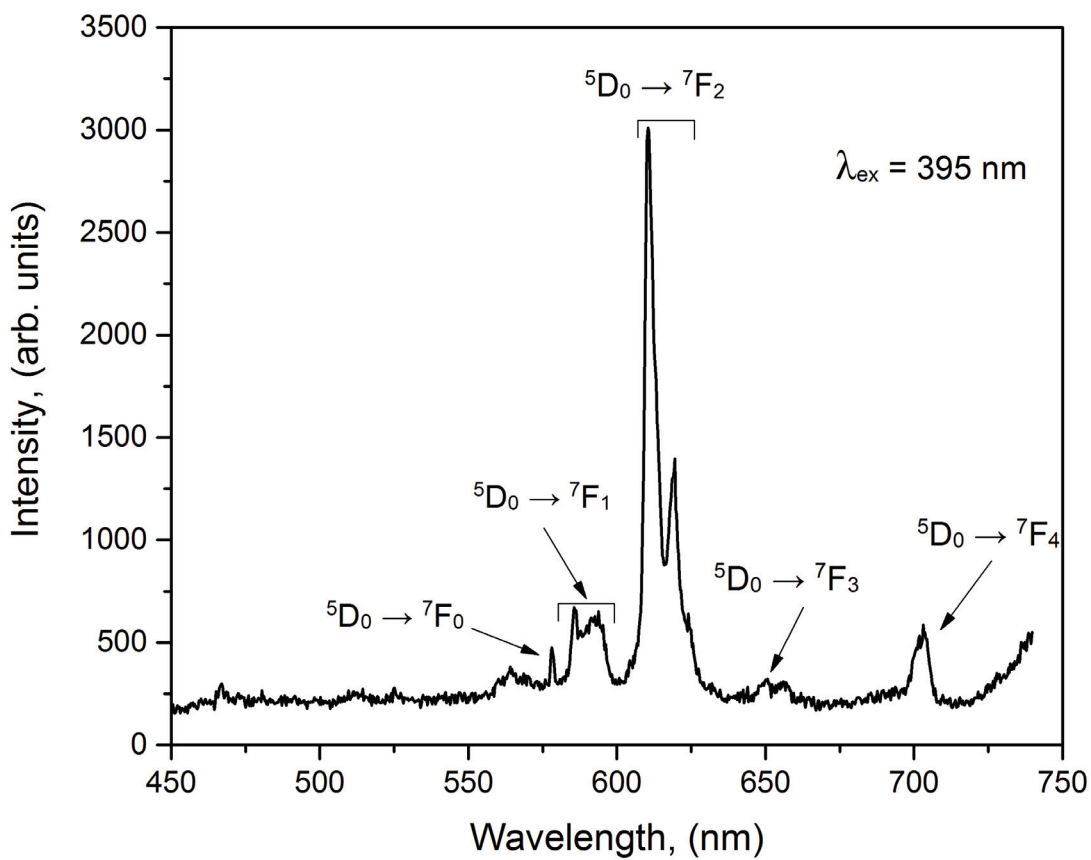


Fig. 3. Luminescence spectra of  $K_3Eu_3B_4O_{12}$ , excitation wavelength of 395 nm

state  $^5D_0$  to the  $^7F_1$  multiplet components ( $J = 0, 1, 2, 3, 4$ ). Fig. 3 shows the emission spectrum  $K_3Eu_3B_4O_{12}$ , and Table 3 provides wavelengths of the  $Eu^{3+}$  constituent spectra.

When studying the structure of luminescent materials, the  $^5D_0 \rightarrow ^7F_2$  transition of  $4f$ -configuration of the  $Eu^{3+}$  ion is of great interest. The fact that there is only one peak within the range of this transition which is characterised by an insignificant broadening indicates close resemblance of the crystallochemical environment of the four sites of the  $Eu^{3+}$  ion in a unit cell. The ratio of maximum intensities of the bands corresponding to the transitions  $(^5D_0 \rightarrow ^7F_2)/(^5D_0 \rightarrow ^7F_1)$  is 4.482, which

**Table 3.** Wavelengths (nm) of the  $Eu^{3+}$  constituent spectra of  $K_3Eu_3B_4O_{12}$

$^5D_0 \rightarrow ^7F_0$	$^5D_0 \rightarrow ^7F_1$	$^5D_0 \rightarrow ^7F_2$	$^5D_0 \rightarrow ^7F_3$	$^5D_0 \rightarrow ^7F_4$
578.1	585.6	610.4	650.7	701.9
	586.5			
	590.2			
	592.6			
	593.8			
	596.2			
	619.8	656.5	703.0	

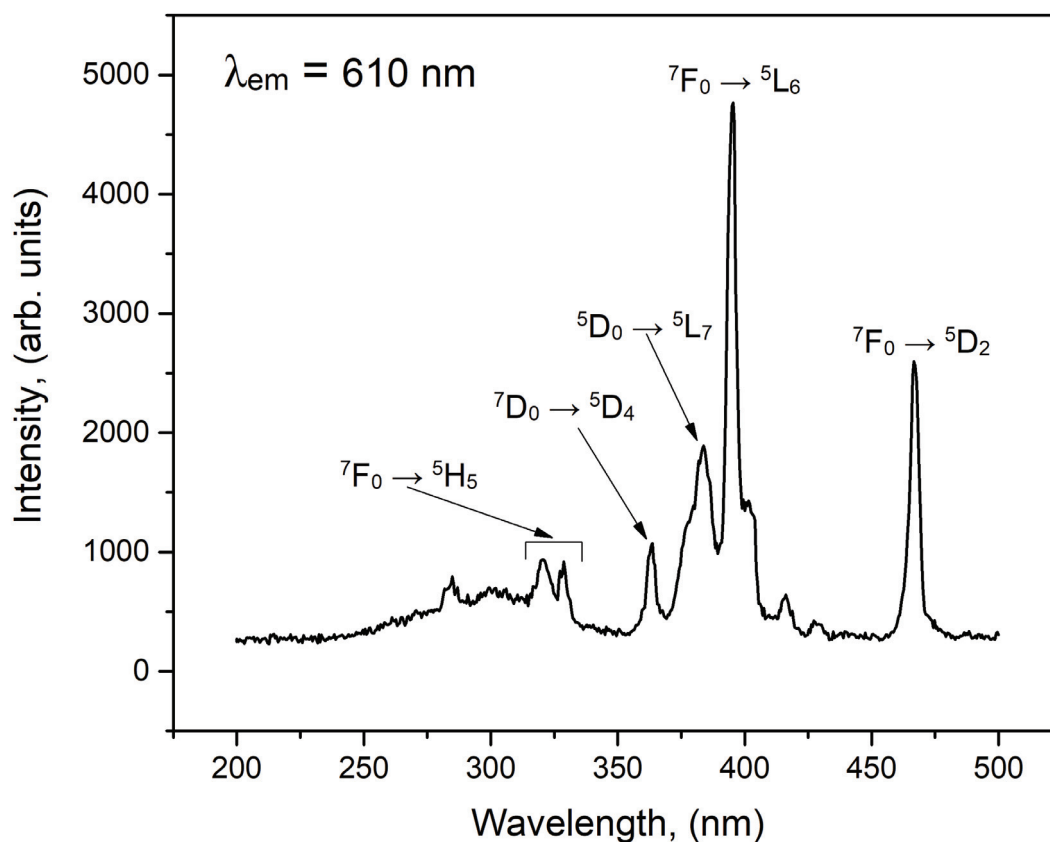
indicates a low symmetry of the  $Eu^{3+}$  ion sites in the crystalline structure of  $K_3Eu_3B_4O_{12}$  [10]. This agrees with the results of the structural study.

The excitation spectra (see Fig. 4) have bands of europium  $4f^6-4f^6$ -transitions from the ground state to the upper levels:  $^7F_0 \rightarrow ^5H_5$  (320.0 nm),  $^7D_0 \rightarrow ^5D_4$  (363.6 nm),  $^5D_0 \rightarrow ^5L_7$  (383.8 nm),  $^7F_0 \rightarrow ^5L_6$  (395.5 nm),  $^7F_0 \rightarrow ^5D_2$  (466.7 nm). The two narrow resonance bands corresponding to the  $^7F_0 \rightarrow ^5L_6$  и  $^7F_0 \rightarrow ^5D_2$  transitions are the most intensive.

#### 4. Conclusions

Thus, a ceramic technology and stepped annealing were used to synthesise a new double borate of potassium-europium  $K_3Eu_3B_4O_{12}$ . According to the results of the Rietveld refinement of the crystal structure, the synthesised phase is isostructural to the  $K_3Gd_3B_4O_{12}$  compound and crystallises in the monoclinic syngony with unit cell parameters  $a = 10.6727(7)$  Å,  $b = 8.9086(6)$  Å,  $c = 13.9684(9)$  Å,  $\beta = 110.388(2)^\circ$  (space group P2/c).

Luminescent properties of  $K_3Eu_3B_4O_{12}$  were studied. Luminescence is due to optical



**Fig. 4.** The excitation spectra of  $K_3Eu_3B_4O_{12}$ , emission wavelength of 610 nm

transitions in the 4f-configuration of the  $Eu^{3+}$  ion. The brightest luminescence of a bright red monochromatic colour is seen in the  ${}^5D_0 \rightarrow {}^7F_2$  electric dipole transition band, which is convenient for the production of screen luminophores with colours of high contrast.

### Acknowledgements

XRD data were obtained using the equipment of the Centre for Collective Use of Buryat Scientific Centre of Siberian Branch of Russian Academy of Sciences. Luminescence spectra were obtained using the equipment of the Centre for Collective Use of Vinogradov Institute of Geochemistry of Siberian Branch of Russian Academy of Sciences.

### Conflict of interests

The authors declare that they have no known competing financial interests or personal relationships that could have influenced the work reported in this paper.

### References

1. Xie Z., Mutailipu M., He G., Han G., Wang Y., Yang Z., Zhang M., Pan S. A series of rare-earth borates  $K_7MRE_2B_{15}O_{30}$  (M = Zn, Cd, Pb; RE = Sc, Y, Gd, Lu) with large second harmonic generation responses. *Chemistry of Materials*. 2018;30 (7): 2414–2423. DOI: <https://doi.org/10.1021/acs.chemmater.8b00491>
2. Mutailipu M., Xie Z., Su X., Zhang M., Wang Y., Yang Z., Janjua M. R. S. A., Pan S. Chemical cosubstitution-oriented design of rare-earth borates as potential ultraviolet nonlinear optical materials. *Journal of the American Chemical Society*. 2017;139(50): 18397–18405. DOI: <https://doi.org/10.1021/jacs.7b11263>
3. Atuchin V. V., Subanakov A. K., Aleksandrovsky A. S., Bazarov B. G., Bazarova J. G., Dorzhieva S. G., Gavrilova T. A., Krylov A. S., Molokeev M. S., Oreshonkov A. S., Pugachev A. M., Tushinova Yu. L., Yelissev A. P. Exploration of structural, thermal, vibrational and spectroscopic properties of new noncentrosymmetric double borate  $Rb_3NdB_6O_{12}$ . *Advanced Powder Technology*. 2017;28 (5): 1309–1315. DOI: <https://doi.org/10.1016/j.apt.2017.02.019>
4. Atuchin V. V., Subanakov A. K., Aleksandrovsky A. S., Bazarov B. G., Bazarova J. G., Gavrilova T. A., Krylov A. S., Molokeev M. S., Oreshonkov A. S., Stefanovich S. Yu. Structural and spectroscopic properties of new noncentrosymmetric selfactivated borate  $Rb_3EuB_6O_{12}$  with  $B_5O_{10}$  units. *Materials & Design*. 2018;140: 488–494. DOI: <https://doi.org/10.1016/j.matdes.2017.12.004>

5. Subanakov A. K., Kovtunets E. V., Bazarov B. G., Dorzhieva S. G., Bazarova J. G. New double holmium borates:  $Rb_3HoB_6O_{12}$  and  $Rb_3Ho_2B_3O_9$ . *Solid State Sciences*. 2020;105: 106231. DOI: <https://doi.org/10.1016/j.solidstatesciences.2020.106231>

6. Zhao J., Zhao D., Liu B.-Z., Xue Y.-L., Fan Y.-P., Zhang S.-R., Zong Q.  $K_3Gd_3B_4O_{12}$ : a new member of rare-earth orthoborate for luminescent host matrix. *Journal of Materials Science: Materials in Electronics*. 2018;29(24): 20808–20819. DOI: <https://doi.org/10.1007/s10854-018-0223-6>

7. Bruker AXS TOPAS V4: General profile and structure analysis software for powder diffraction data. *User's Manual*. Bruker AXS, Karlsruhe, Germany, 2008. 68 p.

8. Järvinen M. Application of symmetrized harmonics expansion to correction of the preferred orientation effect. *Journal of Applied Crystallography*. 1993;26(4): 525–531. DOI: <https://doi.org/10.1107/S0021889893001219>

9. Tanner P. A. Some misconceptions concerning the electronic spectra of tri-positive europium and cerium. *Chemical Society Reviews*. 2013;12: 5090 DOI: <https://doi.org/10.1039/c3cs60033e>

10. Zhao D., Ma F.-X., Wu Z.-Q., Zhang L., Wei W., Yang J., Zhang R.-H., Chen P.-F., Wu S.-X. Synthesis, crystal structure and characterizations of a new red phosphor  $K_3EuB_6O_{12}$ . *Materials Chemistry and Physics*. 2016;182: 231–236. DOI: <https://doi.org/10.1016/j.matchemphys.2016.07.027>

### Information about the authors

*Evgeniy V. Kovtunets*, Postgraduate Student, Laboratory of Oxide Systems, Baikal Institute of Nature Management, Siberian Branch of the Russian Academy of Sciences, Ulan-Ude, Russian Federation; e-mail: [kovtunets@binm.ru](mailto:kovtunets@binm.ru). ORCID iD: <https://orcid.org/0000-0003-1301-1983>.

*Alexey K. Subanakov*, PhD in Chemistry, Senior Researcher, Laboratory of Oxide Systems, Baikal Institute of Nature Management, Siberian Branch of the Russian Academy of Sciences, Ulan-Ude, Russian Federation; e-mail: [subanakov@binm.bscnet.ru](mailto:subanakov@binm.bscnet.ru). ORCID iD: <https://orcid.org/0000-0002-1674-283X>.

*Bair G. Bazarov*, DSc in Chemistry, Leading Researcher, Laboratory of Oxide Systems, Baikal Institute of Nature Management, Siberian Branch of the Russian Academy of Sciences, Ulan-Ude, Russian Federation; e-mail: [bazbg@rambler.ru](mailto:bazbg@rambler.ru). ORCID iD: <https://orcid.org/0000-0003-1712-6964>.

All authors have read and approved the final manuscript.

*Translated by Irina Charychanskaya*  
*Edited and proofread by Simon Cox*



# Condensed Matter and Interphases (Kondensirovannyye sredy i mezhfaznyye granitsy)

## Original article

DOI: <https://doi.org/10.17308/kcmf.2020.22/2834>

Received 19 February 2020

Accepted 15 April 2020

Published online 25 June 2020

ISSN 1606-867X

eISSN 2687-0711

## The Study of the Luminescence of Solid Solutions Based on Yttrium Fluoride Doped with Ytterbium and Europium for Photonics

© 2020 S. V. Kuznetsov<sup>✉a</sup>, A. S. Nizamutdinov<sup>b</sup>, E. I. Madirov<sup>b</sup>, V. A. Konyushkin<sup>a</sup>, A. N. Nakladov<sup>a</sup>, V. V. Voronov<sup>a</sup>, A. D. Yapryntsev<sup>c</sup>, V. K. Ivanov<sup>c</sup>, V. V. Semashko<sup>b</sup>, P. P. Fedorov<sup>a</sup>

<sup>a</sup>Prokhorov General Physics Institute of the Russian Academy of Sciences,  
38 Vavilov str., Moscow 119991, Russian Federation

<sup>b</sup>Kazan Federal University,  
18 Kremlyovskaya str., Kazan 420008, Russian Federation

<sup>c</sup>Kurnakov Institute of General and Inorganic Chemistry of the Russian Academy of Sciences,  
31 Leninsky pr., Moscow, 119991 Russian Federation

### Abstract

The majority of the global market for solar photovoltaic devices is based on silicon technology. It is very important to increase their efficiency through the use of luminescent coatings, including those converting radiation from the UV-blue region of the spectrum into the near-infrared range, where silicon absorbs radiation most efficiently (Stokes or down-conversion luminescence), or from the infrared region of the spectrum in the near-infrared range (up-conversion luminescence). The aim of this research was to synthesize and study the spectral-kinetic characteristics of single-phase solid solutions of  $Y_{1-x-y}Eu_xYb_yF_3$  and to determine the quantum yield of down-conversion luminescence.

Using the method of high-temperature melting, single-phase samples of solid solutions of  $Y_{1-x-y}Eu_xYb_yF_3$  with orthorhombic system were synthesized. For the series of samples with different  $Eu^{3+}/Yb^{3+}$  ratios, upon double doping with these ions, the formation of the corresponding solid solutions with a crystal lattice of the  $\beta$ - $YF_3$  phase was confirmed. Their chemical composition was determined using the energy dispersion analysis, and it was established that it corresponds to the nominal one. It was shown that both  $Eu^{3+}$  and  $Yb^{3+}$  ions become luminescent upon excitation at wavelengths of 266 nm and 296 nm. This indicates these compounds as promising sensitizers of UV radiation. In this case, upon excitation at a wavelength of 266 nm, luminescence of  $Eu^{2+}$  ions was recorded. The maximum quantum yield values (2.2 %) of the ytterbium down-conversion luminescence in the near-infrared wavelength range upon excitation at a wavelength of 266 nm were recorded for  $YF_3:Eu:Yb$  with the  $Eu^{3+}:Yb^{3+}$  ratios of 0.1:10.0 and 0.05:5.00.

**Keywords:** rare earth fluorides, phosphors, solar panels, down-conversion luminescence.

**Funding:** This study was supported by Russian Science Foundation grant No. 17-73-20352.

**For citation:** Kuznetsov S. V., Nizamutdinov A. S., Madirov E. I., Konyushkin V. A., Nakladov A. N., Voronov V. V., Yapryntsev A. D., Ivanov V. K., Semashko V. V., Fedorov P. P. The study of the luminescence of solid solutions based on yttrium fluoride doped with ytterbium and europium for photonics. *Kondensirovannyye sredy i mezhfaznyye granitsy = Condensed Matter and Interphases*. 2020; 22(2): 225–231. DOI: <https://doi.org/10.17308/kcmf.2020.22/2834>

✉ Sergey V. Kuznetsov, e-mail: [kouznetsovsv@gmail.com](mailto:kouznetsovsv@gmail.com)



The content is available under Creative Commons Attribution 4.0 License.



## 1. Introduction

The majority of the global market for solar photovoltaic devices is based on silicon technology. According to a report by the Fraunhofer Institute for Solar Energy (Fraunhofer ISE) in 2017, the widespread use of silicon is based on its availability and low cost of raw materials, the perfection of the technology for producing silicon of the required purity, and its non-toxicity to humans and the environment [1]. This is due to a significant simplification of the technology for purifying cheap silicon to an acceptable level [2]. From 2008 to 2017, there was a significant decrease in the cost of solar electricity from 3 US dollars / W to 0.3 US dollars / W [1]. It should be pointed out that failed solar panels can now be recycled as waste electronic components (*e-waste*). This strongly distinguishes them from new intensively developed organohalide materials with a perovskite structure of the  $\text{RPbX}$  type (R is an organic radical, X is Br or I, or their solid solution) [3–5]. It should be noted that most of these substances are less chemically stable and decompose over several years, and the recycling of heavy elements requires specific industries and significant investments.

One of the significant disadvantages of silicon is its low efficiency (less than 25 % even for the best samples [6,7]) of converting sunlight into electricity. In reality, the 22.5 % efficiency of solar energy conversion was achieved in devices produced at one of the largest silicon solar panel production plants located in Novocheboksarsk, Russia. There are various options for increasing the efficiency of silicon solar cells with multilayer structures, structures with different surface architecture types, and luminescent coatings [8, 9]. The photosensitivity spectrum and the maximum generation of electricity by silicon do not coincide with the spectrum of the Sun [6]. The maximum photosensitivity of silicon is in the range of 900–1100 nm, which coincides with the spectral range of radiation of trivalent ytterbium ions. As a result, the efficiency of solar-silicon photovoltaic cells may be increased by using luminescent coatings.

Phosphors are suggested to be used for this purpose. They transform radiation from the UV-blue spectrum region (down-conversion luminescence) [6–11] or from the IR spectrum region (up-conversion luminescence) [12–14] to the near-infrared range due to a number of various

processes, including step transitions between the states of the corresponding ions, energy transfer, or cooperative processes. In this range, silicon absorbs radiation most efficiently [6].

The quantum yield of up-conversion luminescence in the visible range or near-infrared range upon excitation in the range of 1.5–2.0  $\mu\text{m}$  is very low [15–17], as two low-energy IR photons should be converted to one photon with higher energy in the near-infrared spectral range (NIR). The quantum efficiency of down-conversion luminescence is higher than that for up-conversion, because one ultraviolet or visible high-energy photon is converted to one or two NIR photons. The quantum efficiency of down-conversion luminescence in fluoride phosphors has been studied a lot for various matrices [18, 19], but the quantum yield, which is important for practical applications, has not been estimated.

The aim of this research was to synthesize and study the spectral-kinetic characteristics of solid solutions of  $\text{Y}_{1-x-y}\text{Eu}_x\text{Yb}_y\text{F}_3$  and to determine the quantum efficiency and quantum yield of down-conversion luminescence of ytterbium in the near-infrared range.

## 2. Experimental

Samples of yttrium fluoride-based solid solutions doped with ytterbium and europium were synthesized using the method of high-temperature melting. Yttrium fluoride, europium fluoride, and ytterbium fluoride had a purity degree of 99.99 % (*LANHIT*, Russia). The samples of  $\text{Y}_{1-x-y}\text{Eu}_x\text{Yb}_y\text{F}_3$  solid solutions were synthesized in a vacuum oven at a temperature of 1155 °C. The mixture was placed in the vacuum oven in a graphite crucible and was gradually heated to 940 °C, then the vacuum pumping was turned off, a mixture of gases ( $\text{CF}_4$  and Ar) was introduced, and then it was smoothly heated to the melting temperature. The obtained melt was fluorinated and held at the process temperature for 30 minutes and then it was cooled to room temperature for 3 hours. The obtained samples were ground in an agate mortar.

All the samples were studied by X-ray diffraction analysis using a Bruker D8 Advanced diffractometer (CuK $\alpha$  radiation), their unit cell parameters were calculated in Powder 2.0 software (DQ < 10). Their chemical composition was evaluated using a Carl

Zeiss NVision 40 scanning electron microscope with an energy dispersion spectrometer. Diffuse reflection spectra were recorded using a Lambda 950 Perkin Elmer spectrophotometer. The luminescence spectra were recorded on a Stellarnet EPP2000 spectrometer with a spectral resolution of 0.5 nm. A tunable wavelength laser system based on an  $\text{Al}_2\text{O}_3:\text{Ti}$  laser with second and third harmonic generators (LOTIS TII, 10 Hz, 10 ns) and a wavelength converter based on stimulated Raman scattering in gaseous  $\text{H}_2$  were used as an impulse excitation source. The luminescence kinetics were recorded using MDR-23 and MDR-3 monochromators, a photomultiplier FEU-100 was used as a photodetector in the visible region of the spectrum, and a photomultiplier FEU-62 was used in the IR region of the spectrum. The time scan of the luminescence kinetics signals was carried out by a BORDO digital oscilloscope with a bandwidth of 200 MHz and a dynamic range of 10 bits. The direct measurement of the quantum yield of Stokes luminescence was carried out using a Thorlabs IS200 integrating sphere and a SOLAR S100 spectrometer, calibrated using a wide-range temperature lamp TRSh-2850 and a yellow glass optical filter ZhS-16. When measuring the quantum yield of luminescence, we used the technique from [20], which involves correcting the spectral characteristics of the luminescence recording system and calibrating the optical system using light sources with a given intensity.

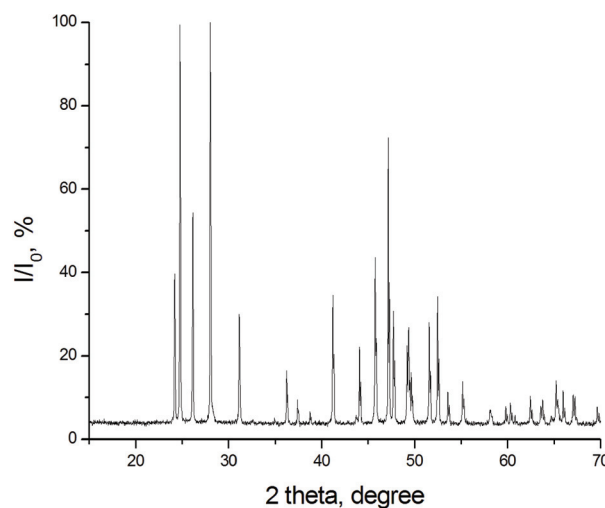
### 3. Results

The X-ray diffraction pattern of the  $\text{Y}_{0.949}\text{Eu}_{0.001}\text{Yb}_{0.05}\text{F}_3$  solution single-phase sample is provided in Fig. 1. It is typical for the whole

series of samples. The results of indexing in orthorhombic system (structural type  $\beta\text{-YF}_3$ ) are summarized in Table 1. The formation of a solid solution is confirmed by the absence of additional peaks compared to the corresponding JCPDS data and a change in the unit cell parameters of an undoped sample:  $\text{YF}_3$  ( $a = 6.353 \text{ \AA}$ ,  $b = 6.850 \text{ \AA}$ ,  $c = 4.393 \text{ \AA}$ , JCPDS card # 74-0911).

The chemical composition was analysed based on energy dispersion analysis (Table 1), the results showed that the real composition corresponded to the nominal composition within the limits of the determination error of  $\pm 0.5 \text{ mol}\%$ .

Luminescence of  $\text{Eu}^{3+}$  ions was recorded in the  $\text{YF}_3$  samples doped with Eu and Yb ions, both upon excitation in the 399 nm region, characteristic of europium, and upon excitation in the UV region of the spectrum (296 and 266 nm). In the



**Fig. 1.** The X-ray diffraction pattern of the  $\text{Y}_{0.949}\text{Eu}_{0.001}\text{Yb}_{0.05}\text{F}_3$  solid solution sample

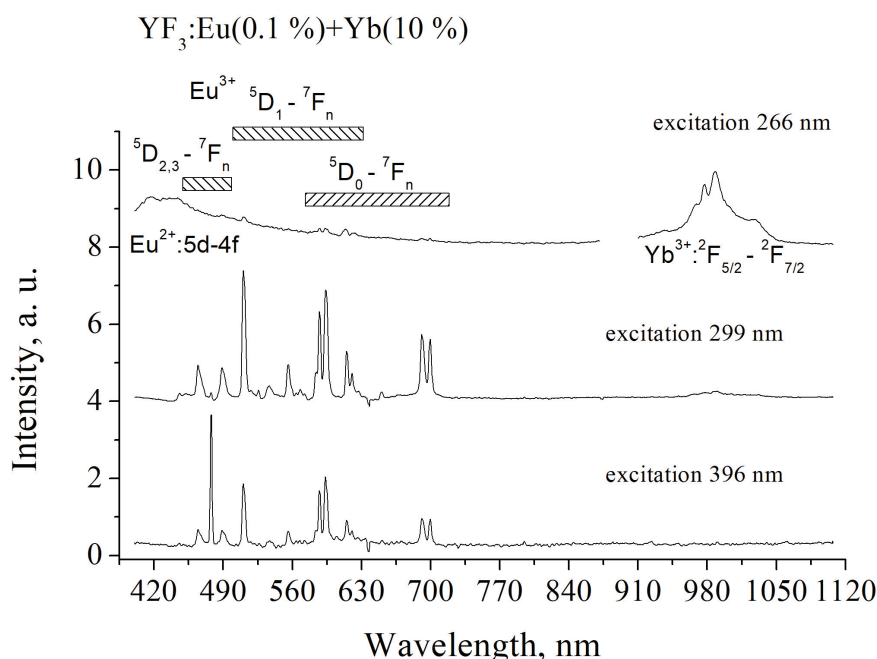
**Table 1.** The unit cell parameters and results of energy dispersion analysis of the  $\text{Y}_{1-x-y}\text{Eu}_x\text{Yb}_y\text{F}_3$  solid solutions

Nominal composition	$\text{Y}_{1-x-y}\text{Eu}_x\text{Yb}_y\text{F}_3$			Composition according to EDX
	Unit cell parameters, $\text{\AA}$			
	<i>a</i>	<i>b</i>	<i>c</i>	
$\text{YF}_3:\text{Eu}(0.05 \text{ мол.}\%):\text{Yb}(1.0 \text{ мол.}\%)$	6.365(1)	6.859(2)	4.3909(7)	$\text{YF}_3:\text{Eu}(0.2 \text{ мол.}\%):\text{Yb}(2.1 \text{ мол.}\%)$
$\text{YF}_3:\text{Eu}(0.1 \text{ мол.}\%):\text{Yb}(5.0 \text{ мол.}\%)$	6.345(2)	6.839(3)	4.384(1)	$\text{YF}_3:\text{Eu}(0.4 \text{ мол.}\%):\text{Yb}(6.4 \text{ мол.}\%)$
$\text{YF}_3:\text{Eu}(0.1 \text{ мол.}\%):\text{Yb}(1.0 \text{ мол.}\%)$	6.342(2)	6.838(2)	4.3862(9)	$\text{YF}_3:\text{Eu}(0.2 \text{ мол.}\%):\text{Yb}(1.9 \text{ мол.}\%)$
$\text{YF}_3:\text{Eu}(0.05 \text{ мол.}\%):\text{Yb}(10.0 \text{ мол.}\%)$	6.339(2)	6.834(2)	4.384(1)	$\text{YF}_3:\text{Eu}(*):\text{Yb}(12.9 \text{ мол.}\%)$
$\text{YF}_3:\text{Eu}(0.05 \text{ мол.}\%):\text{Yb}(5.0 \text{ мол.}\%)$	6.348(1)	6.842(2)	4.3859(9)	$\text{YF}_3:\text{Eu}(0.1 \text{ мол.}\%):\text{Yb}(7.1 \text{ мол.}\%)$
$\text{YF}_3:\text{Eu}(0.1 \text{ мол.}\%):\text{Yb}(10.0 \text{ мол.}\%)$	6.3597(8)	6.851(1)	43891(6)	$\text{YF}_3:\text{Eu}(0.1 \text{ мол.}\%):\text{Yb}(13.7 \text{ мол.}\%)$

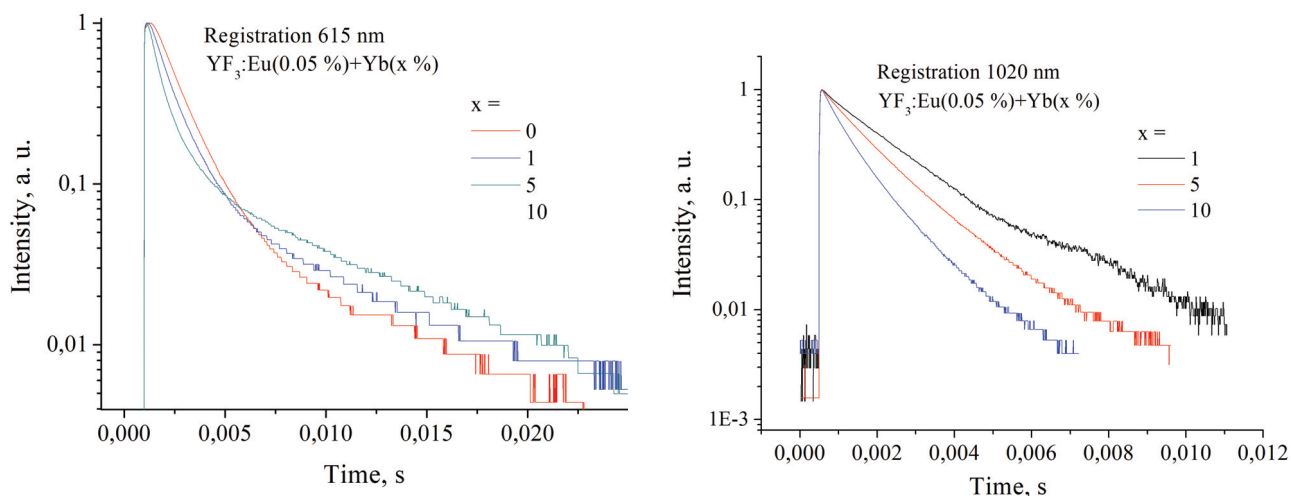
\* - the europium concentration was not determined, since it is below the detection limit of the energy dispersion analysis.

corresponding spectra provided in Fig. 2, we can see the  ${}^5D_0-{}^7F_n$  (691, 650, 615, 590 nm),  ${}^5D_1-{}^7F_n$  (568, 556, 537, 526 nm),  ${}^5D_2-{}^7F_n$  (511, 489, 464 nm) transitions, typical for  $\text{Eu}^{3+}$  [21]. Moreover, upon 266 nm excitation, a rather intense and wide luminescence band with a maximum in the region of 430 nm was recorded, which may correspond to the  $5d-4f$  interconfigurational transitions of  $\text{Eu}^{2+}$  ions [22]. It is important that the luminescence of  $\text{Yb}^{3+}$  ions was recorded only upon excitation at 266 nm and 296 nm (Fig. 2), and in the first case, it appeared to be more intense.

The luminescence kinetics of  $\text{Eu}^{3+}$  at a wavelength of 615 nm and  $\text{Yb}^{3+}$  at a wavelength of 1020 nm upon excitation at a wavelength of 266 nm for the  $\text{YF}_3$  matrix are provided in Fig. 3. The luminescence decay is non-exponential, for  $\text{Yb}^{3+}$  ions also with an increasing the concentration of  $\text{Eu}^{3+}$ . In our case, the luminescence decay kinetics of  $\text{Eu}^{3+}$  ions can be divided into the fast component, which shortens with an increasing concentration of  $\text{Yb}^{3+}$ , and the slow component, which becomes longer. Apparently, the fast component corresponds to the radiative lifetime of  $\text{Eu}^{3+}$  luminescence,



**Fig. 2.** The luminescence spectra of the  $\text{YF}_3:\text{Eu}:\text{Yb}$  samples upon excitation at wavelengths of 399, 296, and 266 nm



**Fig. 3.** The luminescence kinetics of  $\text{Eu}^{3+}$  and  $\text{Yb}^{3+}$  ions in the  $\text{YF}_3$  samples upon excitation at a wavelength of 266 nm

which undergoes quenching due to energy transfer to  $\text{Yb}^{3+}$  ions. Meanwhile, the slow component is determined some kind of channel for refilling of the  $^5\text{D}_0$  state population of  $\text{Eu}^{3+}$  ions. To evaluate the luminescence lifetime the mean lifetime was used, which was calculated using formula (1) [23]:

$$t_{\text{avg}} = \frac{\int t \cdot I(t) dt}{\int I(t) dt}, \quad (1)$$

where  $I(t)$  is the dependence of the luminescence intensity over time,  $t$  is time.

The estimated mean luminescence lifetime values show that concentration quenching is mostly manifested for  $\text{Yb}^{3+}$  ions (Table 2). In this case, the decrease in the luminescence lifetime in the IR region with an increase in the number of  $\text{Eu}^{3+}$  ions is insignificant, which indicates an insignificant effect of energy transfer back to the  $\text{Eu}^{3+}$  ions for the  $\text{YF}_3$  matrix. This mechanism was described in [24].

Using the integrating sphere, we determined the quantum yield of luminescence of  $\text{Yb}^{3+}$  ions (QY) upon excitation of the samples in the region of 266 nm (Table 3). The maximum values were recorded for the Eu and Yb ratios of 0.1:10.0 and 0.05:5.00 for the  $\text{YF}_3$  (QY = 2.2 %).

#### 4. Conclusions

Using the method of high-temperature melting, single-phase samples of solid solutions of  $\text{Y}_{1-x-y}\text{Eu}_x\text{Yb}_y\text{F}_3$  with different amounts of  $\text{Eu}^{3+}$  and  $\text{Yb}^{3+}$  cations were synthesized. The powder samples of these crystals were described using of X-ray diffraction, energy dispersion analysis, and

optical luminescent spectroscopy. Compliance with the  $\beta\text{-YF}_3$  structural type was confirmed for all samples. A monotonic change in the unit cell parameters indicates the formation of solid solutions of the same phase, while the deviation of the real composition from the nominal did not exceed  $\pm 0.5$  mol%. The study of luminescence of the samples doped with both  $\text{Eu}^{3+}$  and  $\text{Yb}^{3+}$  ions showed the luminescence spectra of  $\text{Eu}^{3+}$  and  $\text{Yb}^{3+}$  ions, which are characteristic of these compounds. Both ions became luminescent upon excitation at wavelengths of 266 and 296 nm. It was also shown that, upon excitation at a wavelength of 266 nm, a wide luminescence band with a centre of approximately 430 nm appears. It may be due to the  $5d-4f$  transition of  $\text{Eu}^{2+}$  ions. This leads to the fact that the kinetics of the luminescence decay of  $\text{Eu}^{3+}$  ions significantly differs from the exponential. In the luminescence kinetics, a short component can be distinguished, with the lifetime decreasing when the number of  $\text{Yb}^{3+}$  ions increases, and a long component, whose lifetime increases. Most likely, there is an energy transfer from  $\text{Eu}^{3+}$  ions to  $\text{Yb}^{3+}$  ions. Using the integrating sphere, we measured the quantum yield of luminescence of  $\text{Yb}^{3+}$  ions upon excitation at a wavelength of 266 nm. The quantum yield values of down-conversion luminescence were recorded for the Eu and Yb ratios of 0.1:10.0 and 0.05:5.00 for the  $\text{YF}_3$  (QY = 2.2 %).

#### Conflict of interests

The authors declare that they have no known competing financial interests or personal

**Table 2.** The mean luminescence lifetime, recorded at wavelengths of 615 nm and 1020 nm in the  $\text{YF}_3$ :Eu:Yb samples upon excitation at a wavelength of 266 nm

$\text{YF}_3$							
Recording wavelength	615 nm	615 nm	1020 nm	615 nm	1020 nm	615 nm	1020 nm
Composition	Yb 1.0 mol%		Yb 5.0 mol%		Yb 10.0 mol%		
Eu 0.05 mol%	2.6±0.1 ms	2.3±0.1 ms	1.7±0.1 ms	3.0±0.1 ms	1.3±0.1 ms	3.7±0.1 ms	1.0±0.1 ms
Eu 0.1 mol%	2.8±0.1 ms	2.1±0.1 ms	1.6±0.1 ms	2.7±0.1 ms	1.3±0.1 ms	3.5±0.1 ms	1.1±0.1 ms

**Table 3.** The quantum yield of the  $\text{Yb}^{3+}$  luminescence in the  $\text{YF}_3$ :Eu:Yb samples upon 266 nm excitation

$\text{YF}_3$ :Yb:Eu			
Composition	Yb 1.0 mol%	Yb 5.0 mol%	Yb 10.0 mol%
Eu 0.05 mol%	1.0 %	2.2 %	1.6 %
Eu 0.10 mol%	1.0 %	1.1 %	2.2 %

relationships that could have influenced the work reported in this paper.

## References

- Weber E. R. Photovoltaics moving into the terawatt age. In: *Proc. SPIE 10368, Next Generation Technologies for Solar Energy Conversion VIII*. 2017;10368: 1036803. DOI: <https://doi.org/10.1117/12.2277978>
- Seibt M., Kveder V. Gettering Processes and the Role of Extended Defects. In: *Advanced Silicon Materials for Photovoltaic Applications*. John Wiley & Sons, Ltd; 2012. pp. 127–188. DOI: <https://doi.org/10.1002/9781118312193.ch4>
- Turkevych I., et al. Strategic advantages of reactive polyiodide melts for scalable perovskite photovoltaics. *Nature Nanotechnology*. 2019;14(1): 57–63. DOI: <https://doi.org/10.1038/s41565-018-0304-y>
- Abdollahi Nejand B., et al. Vacuum-assisted growth of low-bandgap thin films (FA 0.8 MA 0.2 Sn 0.5 Pb 0.5 I3) for all-perovskite tandem solar cells. *Advanced Energy Materials*. 2020;10(5): 1902583. DOI: <https://doi.org/10.1002/aenm.201902583>
- Im J. H., et al. 6.5 % efficient perovskite quantum-dot-sensitized solar cell. *Nanoscale*. 2011;3(10): 4088–4093. DOI: <https://doi.org/>
- Huang X., Sanyang H., Wei H., Xiaogang L. Enhancing solar cell efficiency: the search for luminescent materials as spectral converters. *Chemical Society Reviews*. 2013;42(1): 173–201. DOI: <https://doi.org/>
- Trupke T., Green M. A., Würfel P. Improving solar cell efficiencies by down-conversion of high-energy photons. *Journal of Applied Physics*. 2002;92(3): 1668–1674. DOI: <https://doi.org/>
- Yao H., Shen H., Tang Q. Highly luminescent up/down conversion thin films prepared by a room temperature process. *Thin Solid Films*. 2019;683: 1–7. DOI: <https://doi.org/10.1016/j.tsf.2019.05.010>
- Loiko P. A., Khaidukov N. M., Mendez-Ramos J., Vilejshnikova E. V., Skoptsov N. A., Yumashev K. V. Up- and down-conversion emissions from Er<sup>3+</sup> doped K<sub>2</sub>YF<sub>5</sub> and K<sub>2</sub>YbF<sub>5</sub> crystals. *Journal of Luminescence*. 2016;170: 1–7. DOI: <https://doi.org/10.1016/j.jlumin.2015.10.016>
- Li L., Lou C., Cao H., Diao H., Karunakaran S. K. Enhancing concentrator monocrystalline Si solar cells by down conversion Ce<sup>3+</sup>-Yb<sup>3+</sup> co-doped YAG phosphors. *Applied Physics Letters*. 2018;113(10): 101905. DOI: <https://doi.org/10.1063/1.5043221>
- Serrano D., Braud A., Doualan J.-L., Camy P., Benayad A., Menard V., Moncorge R. Ytterbium sensitization in KY<sub>3</sub>F<sub>10</sub>: Pr<sup>3+</sup>, Yb<sup>3+</sup> for silicon solar cells efficiency enhancement. *Optical Materials*. 2011;33(7): 1028–1031. DOI: <https://doi.org/10.1016/j.optmat.2010.07.023>
- Fischer S., Ivaturi A., Jakob P., Krämer K. W., Martin-Rodriguez R., Meijerink A., Goldschmidt J. C. Upconversion solar cell measurements under real sunlight. *Optical Materials*. 2018;84: 389–395. DOI: <https://doi.org/10.1016/j.optmat.2018.05.072>
- Kuznetsov S., Ermakova Y., Voronov V., Fedorov P., Busko D., Howard I. A., Turshatov A. Up-conversion quantum yields of SrF<sub>2</sub>:Yb<sup>3+</sup>, Er<sup>3+</sup> sub-micron particles prepared by precipitation from aqueous solution. *Journal of Materials Chemistry C*. 2018;6(3): 598–604. DOI: <https://doi.org/10.1039/C7TC04913G>
- Fischer S., Ivaturi A., Jakob P., Krämer K. W., Martin-Rodriguez R., Meijerink A., Richards B., Goldschmidt J. C. Upconversion solar cell measurements under real sunlight. *Optical Materials*. 2018;84: 389–395. DOI: <https://doi.org/10.1016/j.optmat.2018.05.072>
- Lyapin A. A., Gushchin S. V., Kuznetsov S. V., Ryabochkina P. A., Ermakov A. S., Proydakova V. Yu., Voronov V. V., Fedorov P. P., Artemov S. A., Yaprntsev A. D., Ivanov V. K. Infrared-to-visible upconversion luminescence in SrF<sub>2</sub>:Er powders upon excitation of the <sup>4</sup>I<sub>13/2</sub> level. *Optical Materials Express*. 2018;8(7): 1863–1869. DOI: <https://doi.org/10.1364/OME.8.001863>
- Rozhnova Yu. A., Kuznetsov S. V., Fedorov P. P., Voronov V. V. Synthesis of up-conversion Ho<sup>3+</sup> and Er<sup>3+</sup> doped strontium fluoride luminophores for visualiser of two-micron radiation. *Kondensirovannye sredy i mezhfaznye granitsy = Condensed Matter and Interphases*. 2016;18(3): 408–413. Available at: <https://journals.vsu.ru/kcmf/article/view/150/107> (In Russ., abstract in Eng.)
- Alexandrov A. A., Mayakova M. N., Voronov V. V., Pominova D. V., Kuznetsov S. V., Baranchikov A. E., Ivanov V. K., Lysakova E. I., Fedorov P. P. Synthesis of upconversion luminophores based on calcium fluoride. *Kondensirovannye sredy i mezhfaznye granitsy = Condensed Matter and Interphases*. 2020;22(1): 3–10. DOI: <https://doi.org/10.17308/kcmf.2020.22/2524>
- Van Der Ende B. M., Aarts L., Meijerink A. Near-infrared quantum cutting for photovoltaics. *Advanced Materials*. 2009;21(30): 3073–3077. DOI: <https://doi.org/10.1002/adma.200802220>
- Piper W. W., DeLuca J. A., Ham F. S. Cascade fluorescent decay in Pr<sup>3+</sup>-doped fluorides: Achievement of a quantum yield greater than unity for emission of visible light. *Journal of Luminescence*. 1974;8(4): 344–348. DOI: [https://doi.org/10.1016/0022-2313\(74\)90007-6](https://doi.org/10.1016/0022-2313(74)90007-6)
- Yasyrkina D. S., Kuznetsov S. V., Ryabova A. V., Pominova D. V., Voronov V. V., Ermakov R. P., Fedorov P. P. Dependence of quantum yield of up-conversion luminescence on the composition of fluorite-type solid solution NaY<sub>1-x-y</sub>Yb<sub>x</sub>Er<sub>y</sub>F<sub>4</sub>. *Nanosystems: Physics, Chemistry, Mathematics*.

2013;4(5): 648–656. Available at: <http://nanojournal.ifmo.ru/en/articles-2/volume4/4-5/physics/paper07/>

21. Ding M., Lu C., Cao L., Song J., Ni Y., Xu Z. Facile synthesis of  $\beta$ - $\text{NaYF}_4:\text{Ln}^{3+}$  (Ln = Eu, Tb, Yb/Er, Yb/Tm) microcrystals with down- and up-conversion luminescence. *Journal of Materials Science*. 2013;48(14): 4989–4998. DOI: <https://doi.org/10.1007/s10853-013-7285-x>

22. Tao F., Wang Z., Yao L., Weili C., Li X. Synthesis and photoluminescence properties of truncated octahedral Eu-Doped  $\text{YF}_3$  submicrocrystals or nanocrystals. *The Journal of Physical Chemistry C*. 2007;111(8): 3241–3245. DOI: <https://doi.org/10.1021/jp065905z>

23. Sveshnikov B. Ya., Shirokov V. V. On the dependence of measurements of the average duration and yield of luminescence during quenching on the law of interaction of molecules. *Optika i spektroskopiya* [Opt. Spectrosc. (USSR)]. 1962;12(5): 320.

24. Kuznetsov S. V., Nizamutdinov A. S., Proydakova V. Yu., Madirov E. I., Voronov V. V., Yapryntsev A. D., Ivanov V. K., Gorieva V. G., Marisov M. A., Semashko V. V., Fedorov P. P. Synthesis and luminescence of  $\text{Sr}_{1-x-y}\text{Yb}_x\text{Eu}_y\text{F}_{2+x+y}$  solid solutions for photonics. *Inorganic Materials*. 2019;55(10): 1031–1038. DOI: <https://doi.org/10.1134/S002016851910008X>

### Information about the authors

*Sergey V. Kuznetsov*, PhD in Chemistry, Leading Researcher, Prokhorov General Physics Institute of the Russian Academy of Sciences, Moscow, Russian Federation; e-mail: [kouznetzovsv@gmail.com](mailto:kouznetzovsv@gmail.com). ORCID iD: <https://orcid.org/0000-0002-7669-1106>.

*Aleksei S. Nizamutdinov*, PhD in Physics and Mathematics, Associate Professor, Kazan Federal University; Kazan, Russian Federation; e-mail: [anizamutdinov@mail.ru](mailto:anizamutdinov@mail.ru). ORCID iD: <https://orcid.org/0000-0003-1559-6671>.

*Eduard I. Madirov*, Postgraduate student, Kazan Federal University, Kazan, Russian Federation; e-mail:

[ed.madirov@gmail.com](mailto:ed.madirov@gmail.com). ORCID iD: <https://orcid.org/0000-0001-7092-8523>.

*Vasilii A. Konyushkin*, PhD in Technical Sciences, Head of Laboratory, Prokhorov General Physics Institute of the Russian Academy of Sciences, Moscow, Russian Federation; ORCID iD: <https://orcid.org/0000-0002-6028-8937>.

*Andrei N. Nakladov*, Research Fellow, Prokhorov General Physics Institute of the Russian Academy of Sciences, Moscow, Russian Federation; ORCID iD <https://orcid.org/0000-0002-4060-8091>.

*Valery V. Voronov*, PhD in Physics and Mathematics, Head of Laboratory, Prokhorov General Physics Institute of the Russian Academy of Sciences, Moscow, Russian Federation; e-mail: [voronov@lst.gpi.ru](mailto:voronov@lst.gpi.ru). ORCID iD: <https://orcid.org/0000-0001-5029-8560>.

*Aleksei D. Yapryntsev*, Postgraduate student, Kurnakov Institute of General and Inorganic Chemistry of the Russian Academy of Sciences, Moscow, Russian Federation; ORCID iD: <https://orcid.org/0000-0001-8166-2476>.

*Vladimir K. Ivanov*, DSc in Chemistry, Associate Member of the Russian Academy of Sciences, Director of the Kurnakov Institute of General and Inorganic Chemistry of the Russian Academy of Sciences, Moscow, Russian Federation; e-mail: [van@igic.ras.ru](mailto:van@igic.ras.ru). ORCID iD: <https://orcid.org/0000-0003-2343-2140>.

*Vadim V. Semashko*, DSc in Physics and Mathematics, Professor, Kazan Federal University, Kazan, Russian Federation; ORCID iD: <https://orcid.org/0000-0003-4967-1991>.

*Pavel P. Fedorov*, DSc in Chemistry, Head of Department, Prokhorov General Physics Institute of the Russian Academy of Sciences, Moscow, Russian Federation; e-mail: [ppfedorov@yandex.ru](mailto:ppfedorov@yandex.ru). ORCID iD: <https://orcid.org/0000-0002-2918-3926>.

All authors have read and approved the final manuscript.

*Translated by Anastasiia Ananeva*

*Edited and proofread by Simon Cox*



# Condensed Matter and Interphases (Kondensirovannye sredy i mezhfaznye granitsy)

## Original articles

DOI: <https://doi.org/10.17308/kcmf.2020.22/2835>

Received 28 January 2020

Accepted 15 May 2020

Published online 25 June 2020

ISSN 1606-867X

eISSN 2687-0711

## The study of the quasi-triple system FeS–Ga<sub>2</sub>S<sub>3</sub>–Ag<sub>2</sub>S by a FeGa<sub>2</sub>S<sub>4</sub>–AgGaS<sub>2</sub> section

©2020 Sh. H. Mammadov

*Institute of Catalysis and Inorganic Chemistry named after Academician M. F. Nagiyev  
of the National Academy of Sciences of Azerbaijan,  
113 G. Javid pr., Baku Az1143, Azerbaijan*

### Abstract

The interest in the study of systems containing sulphides with the formula A<sup>I</sup>B<sup>III</sup>C<sup>VI</sup><sub>2</sub> is generated in particular by emerging opportunities for their practical use in the production of non-linear optical devices, detectors, solar cells, photodiodes, luminophors, etc. Therefore, taking into account the search for new promising materials based on silver and iron thiogallates, the goal of this work is to study the quasi-binary section FeGa<sub>2</sub>S<sub>4</sub>–AgGaS<sub>2</sub> of the quaternary system Fe–Ag–Ga–S.

The alloys of the AgGaS<sub>2</sub>–FeGa<sub>2</sub>S<sub>4</sub> system were synthesised from high-purity base metals: iron – 99.995 %, gallium – 99.999 %, silver – 99.99 %, and sulphur – 99.99 %. The alloys were studied using differential thermal analysis, X-ray phase analysis, and microstructural analysis as well as microhardness measurement and density determination.

Using the methods of physicochemical analysis, a *T*-*x* phase diagram of the AgGaS<sub>2</sub>–FeGa<sub>2</sub>S<sub>4</sub> section, which is the internal section of the quasi-triple FeS–Ga<sub>2</sub>S<sub>3</sub>–Ag<sub>2</sub>S system, was studied and constructed for the first time. It was established that this system is of the simple eutectic type. The composition of the eutectic point is 56 mol% FeGa<sub>2</sub>S<sub>4</sub> and *T* = 1100 K. The solid solution ranges were determined on the basis of the source components. Based on FeGa<sub>2</sub>S<sub>4</sub> and AgGaS<sub>2</sub> at the eutectic temperature the solubility stretches to 10 and 16 mol% respectively. With decreasing temperature, the solid solutions narrow and, at room temperature, comprise 4 mol% AgGaS<sub>2</sub> based on iron thiogallate (FeGa<sub>2</sub>S<sub>4</sub>) and 11 mol% FeGa<sub>2</sub>S<sub>4</sub> based on silver thiogallate (AgGaS<sub>2</sub>).

**Keywords:** phase diagram, solid solution, FeGa<sub>2</sub>S<sub>4</sub>, AgGaS<sub>2</sub>, quasi-triple system, eutectic, X-ray analysis, FeS–Ga<sub>2</sub>S<sub>3</sub>–Ag<sub>2</sub>S.

**For citation:** Mammadov Sh. H. The study of the quasi-triple system FeS–Ga<sub>2</sub>S<sub>3</sub>–Ag<sub>2</sub>S by a FeGa<sub>2</sub>S<sub>4</sub>–AgGaS<sub>2</sub> section. *Kondensirovannye sredy i mezhfaznye granitsy = Condensed Matter and Interphases*. 2020;22(2): 232–237. DOI: <https://doi.org/10.17308/kcmf.2020.22/2835>

## 1. Introduction

The interest in the study of systems containing sulphides with the formula A<sup>I</sup>B<sup>III</sup>C<sup>VI</sup><sub>2</sub> is generated in particular by emerging opportunities for their practical use in the production of non-linear optical devices, detectors, solar cells, photodiodes, luminophors, etc. [1–17].

The reported data shows that multicomponent sulphide compounds, especially those containing magnetic (FeGa<sub>2</sub>S<sub>4</sub>, Fe<sub>2</sub>Ga<sub>2</sub>S<sub>5</sub>, FeIn<sub>2</sub>S<sub>4</sub>, etc.) ions, are functional materials and are used in the production of magneto-optical devices, photodetectors, lasers, light modulators, etc. [18–25].

The source components comprising the quaternary system Ag–Fe–Ga–S were thoroughly studied in [26–42]. Compositions AgGaS<sub>2</sub>, Ag<sub>9</sub>GaS<sub>6</sub>, and Ag<sub>2</sub>Ga<sub>20</sub>S<sub>31</sub> were established during the study of the Ag<sub>2</sub>S–Ga<sub>2</sub>S<sub>3</sub> binary system [26, 30, 31]. Ag<sub>2</sub>Ga<sub>20</sub>S<sub>31</sub> is formed from them by a peritectic reaction at 1268 K while AgGaS<sub>2</sub> and Ag<sub>9</sub>GaS<sub>6</sub> melt congruently at 1270 and 1063 K respectively. AgGaS<sub>2</sub> crystallises within the chalcopyrite-type structure (*a* = 5.7544, *c* = 10.299 Å space group I42d) [27] and is a *p*-type semiconductor with a band gap of Δ*E* = 2.75 eV [32].

The phase diagram of the section Ga<sub>2</sub>S<sub>3</sub>–FeS was studied in [33–42]. The authors established

✉ Sharafat Hajiaga Mammadov, e-mail: [azxim@mail.ru](mailto:azxim@mail.ru)



The content is available under Creative Commons Attribution 4.0 License.

that triple compounds  $\text{FeGa}_2\text{S}_4$  and  $\text{Fe}_2\text{Ga}_2\text{S}_5$  are formed in the system  $\text{Ga}_2\text{S}_3\text{-FeS}$  [38, 42].

The microhardness of the  $\text{FeGa}_2\text{S}_4$  and  $\text{Fe}_2\text{Ga}_2\text{S}_5$  compounds are  $4000 \pm 5$  and  $3500 \pm 5$  MPa respectively [42].

The  $\text{FeGa}_2\text{S}_4$  compound melts congruently at 1418 K [38], although, according to [39],  $\text{FeGa}_2\text{S}_4$  is formed by a peritectic reaction at 1343 K and undergoes polymorphous transformation at 1283 K.  $\text{FeGa}_2\text{S}_4$  crystallises in a rhombic crystal system of the  $\text{ZnAl}_2\text{S}_4$  type with the following parameters:  $a = 1.289$  nm,  $b = 0.751$ ,  $c = 0.609$  nm [40]. According to [41], this compound has two crystalline modifications: low-temperature trigonal P3ml:  $a = 0.3654$  nm,  $c = 1.2056$  nm; and high-temperature rhombic:  $a = 1.289$ ,  $b = 0.751$ ,  $c = 0.609$  nm.

The goal of this work is to study the quasi-binary section  $\text{FeGa}_2\text{S}_4\text{-AgGaS}_2$  of the quaternary system  $\text{Fe-Ag-Ga-S}$ .

## 2. Experimental

Synthesis of the alloys of the  $\text{AgGaS}_2\text{-FeGa}_2\text{S}_4$  system were conducted from base metals. The base metals ( $\text{AgGaS}_2$  and  $\text{FeGa}_2\text{S}_4$ ) were synthesised using high-purity: iron – 99.995 %, gallium – 99.999 %, silver – 99.99 %, and sulphur – 99.99 %. Stoichiometric mixtures of the elements were placed in vacuum quartz ampoules (17 cm long and 1.5 cm in diameter) with residual pressure  $\sim 0.133$  Pa [43]. Then the ampoule was placed in a two-zone furnace. The furnace was slowly heated from room temperature to the fusion temperature of the compound  $\text{FeGa}_2\text{S}_4$ . Sulphur becomes condensed in the cold region and returns to the interaction zone. The alloys in a liquid state were stirred at regular intervals. The outer part of the ampoule was cooled with water. After 1.5–2 hours in the cold region, the mass of the sulphur decreased. After that, the whole ampoule was placed in the furnace and held at a temperature of 1450 K for 2.5 hours. The process of synthesis lasted for at least 4 hours. Then the obtained samples were homogenised at a temperature of 800 K for 150 h. The alloys were studied using differential thermal analysis (DTA), X-ray phase analysis (XRD), and microstructural analysis (MSA) as well as microhardness measurement and density determination. XRD was performed on a D2 PHASER using Ni-filtered  $\text{CuK}_\alpha$  radiation.

DTA of the alloys of the system was conducted on an HTP-73 device with a heating rate of 10 degrees per minute. Calibrating chromel-alumel thermocouples were used with  $\text{Al}_2\text{O}_3$  as a reference standard. An etchant of the composition  $\text{NH}_4\text{NO}_3$  (3–8 wt%) +  $\text{K}_2\text{Cr}_2\text{O}_7$  (0.02–0.5 wt%) + conc.  $\text{H}_2\text{SO}_4$  was used during the study of the microstructure of the alloys with the etching time of 20 sec. The microhardness of the alloys was measured on a microhardness tester PMT-3 at the loads 0.01 and 0.02 N. MSA of the system alloys was performed on a MIM-8 metallographic microscope on preliminarily etched sections polished with the paste.

## 3. Results and discussion

Based on the results of physicochemical analysis (DTA, XRD, MSA, and density determination), a phase diagram of the system  $\text{AgGaS}_2\text{-FeGa}_2\text{S}_4$  was developed. The DTA results showed that all thermograms of the system alloys (90–10 mol%  $\text{AgGaS}_2$ ) have three endoeffects each, except for the alloy containing 56 mol%  $\text{FeGa}_2\text{S}_4$  while the alloys containing 90 and 10 mol%  $\text{AgGaS}_2$  demonstrate two and four endoeffects each respectively (Table 1). The effects at 905 K correspond to the phase transition  $\alpha\text{-FeGa}_2\text{S}_4 \leftrightarrow \beta\text{-FeGa}_2\text{S}_4$ .

As Fig. 1 shows, the phase diagram of the system  $\text{AgGaS}_2\text{-FeGa}_2\text{S}_4$  belongs to the eutectic type with limited component solubility in solid state. The solubility at 300 K based on  $\text{AgGaS}_2$  is

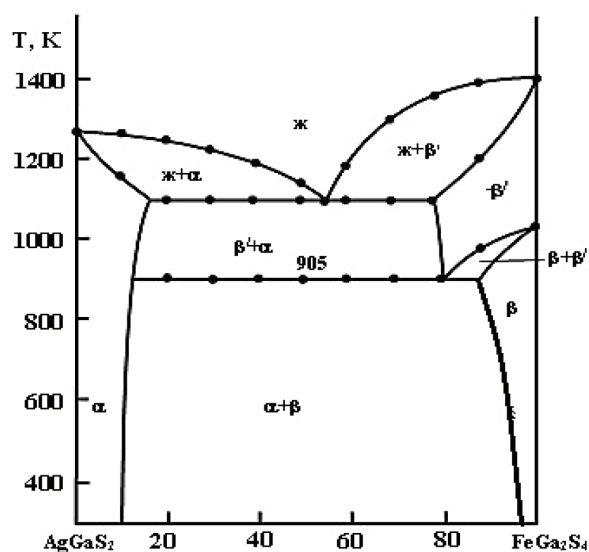


Fig. 1. Phase diagram of the  $\text{AgGaS}_2\text{-FeGa}_2\text{S}_4$  system



**Table 1.** Composition, results of the DTA of alloys of the AgGaS<sub>2</sub>–FeGa<sub>2</sub>S<sub>4</sub> system

Composition mol% FeGa <sub>2</sub> S <sub>4</sub>	Thermal effects, K
100	1420
90	905, 980, 1235, 1405
80	905, 1100, 1375
70	905, 1100, 1310
60	905, 1100, 1175
56	1100 (eutectic)
50	905, 1100, 1145
40	905, 1100, 1195
30	905, 1100, 1230
20	905, 1100, 1250
10	1175, 1260
0.0	1270

11 mol% FeGa<sub>2</sub>S<sub>4</sub> and 4 mol% AgGaS<sub>2</sub> based on FeGa<sub>2</sub>S<sub>4</sub>. The solubility at the eutectic temperature stretches to 16 and 10 mol% respectively. The eutectic has a composition of 56 mol% FeGa<sub>2</sub>S<sub>4</sub> and crystallises at 1100 K.

The liquidus of the system AgGaS<sub>2</sub>–FeGa<sub>2</sub>S<sub>4</sub> consists of the primary crystallisation branches  $\alpha$  and  $\beta$  solid solutions crossing at 56 mol% FeGa<sub>2</sub>S<sub>4</sub> and  $T = 1100$  K. The temperature of the phase transition  $\beta(\text{FeGa}_2\text{S}_4) \leftrightarrow \beta'(\text{FeGa}_2\text{S}_4)$  is reduced to 905 K under the influence of the second component. MSA of the annealed alloys showed that the alloys of the system AgGaS<sub>2</sub>–FeGa<sub>2</sub>S<sub>4</sub> are single-phase except for the alloys containing 11–96 mol% FeGa<sub>2</sub>S<sub>4</sub>.

Below solidus,  $\alpha$  and  $\beta$  solid solutions co-crystallise. The solubility regions based on source components are narrow: 11 mol% FeGa<sub>2</sub>S<sub>4</sub> based on AgGaS<sub>2</sub> and 4 mol% AgGaS<sub>2</sub> based on the second component. Solubility limits were determined using the XRD and MSA of the alloys annealed and quenched at the temperature 700 K.

To determine the limits of the regions of solid solutions of the source components (AgGaS<sub>2</sub> and FeGa<sub>2</sub>S<sub>4</sub>), 98, 96, 95, 93, 91, 90, 89, 88 mol% were additionally synthesised from both sides. These alloys were annealed at 650 and 800 K with the annealing duration of 1 month (Table 2).

After the annealing, a microstructural analysis of the alloys was conducted that showed that there are limited solubility regions near AgGaS<sub>2</sub> and FeGa<sub>2</sub>S<sub>4</sub>. Solid solutions based on AgGaS<sub>2</sub> belong to the Ag<sub>2</sub>GeS<sub>3</sub> structural type and

**Table 2.** Annealing of the alloys of the AgGaS<sub>2</sub>–FeGa<sub>2</sub>S<sub>4</sub> system at temperatures of 650 and 800 K

Composition mol%		650 K phase count	800 K, phase count
AgGaS <sub>2</sub>	FeGa <sub>2</sub> S <sub>4</sub>		
0.0	100	$\alpha$	$\alpha$
2.0	98	$\alpha$	$\alpha$
4.0	96	$\alpha+\beta$	$\alpha$
5.0	95	$\alpha+\beta$	$\alpha+\beta$
7.0	93	$\alpha+\beta$	$\alpha+\beta$
9.0	91	$\alpha+\beta$	$\alpha+\beta$
10	90	$\alpha+\beta$	$\alpha+\beta$
11	89	$\alpha+\beta$	$\alpha+\beta$
12	88	$\alpha+\beta$	$\alpha+\beta$
100	0.0	$\beta$	$\beta$
98	2.0	$\beta$	$\beta$
96	4.0	$\beta$	$\beta$
95	5.0	$\beta$	$\beta$
93	7.0	$\beta$	$\beta$
91	9.0	$\beta$	$\beta$
90	10	$\alpha+\beta$	$\beta$
89	11	$\alpha+\beta$	$\beta$
88	12	$\alpha+\beta$	$\alpha+\beta$

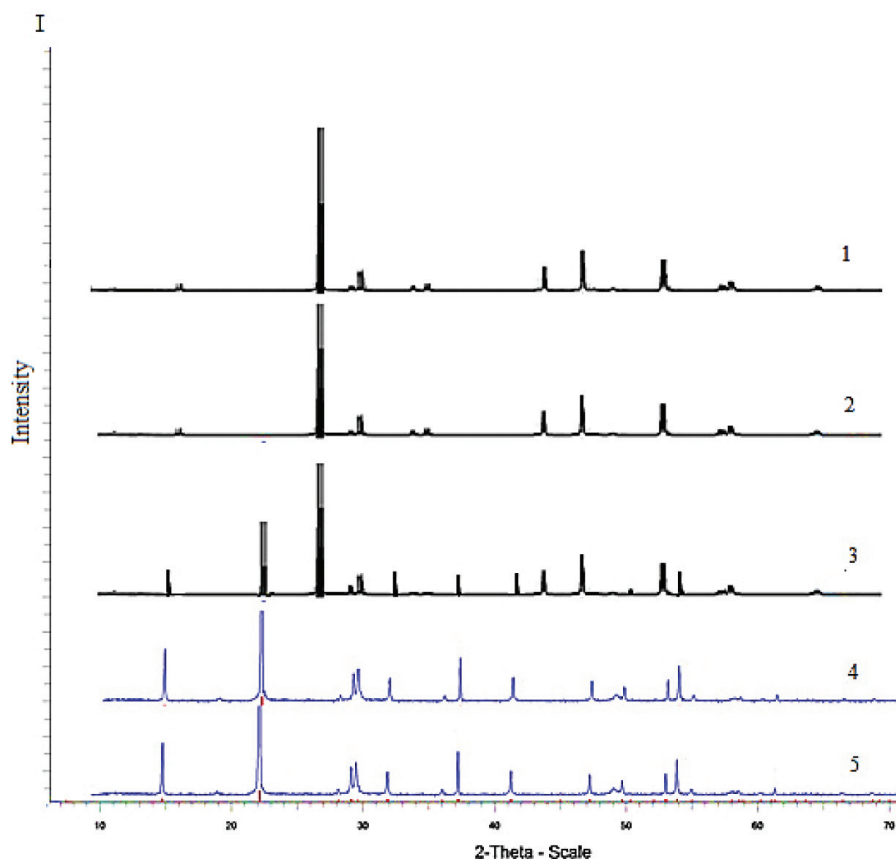
crystallise in the monoclinic syngony. Within the solubility limits, the parameters of the crystal lattice increase:  $a = 0.627 \div 0.748$ ,  $b = 0.580 \div 0.664$ ,  $c = 1.318 \div 1.386$  nm,  $\beta = 93.27 \div 93^\circ 61$ .

The results of the X-ray phase analysis are in good agreement with the data of the microstructural analysis and confirm the formation of solid solutions based on the source components in the system AgGaS<sub>2</sub>–FeGa<sub>2</sub>S<sub>4</sub>.

The data of the X-ray powder patterns of the alloys of the system AgGaS<sub>2</sub>–FeGa<sub>2</sub>S<sub>4</sub> showed that the samples of the compositions 0–11 and 95–100 mol% FeGa<sub>2</sub>S<sub>4</sub> are single-phase. Their diffraction lines are identical to the diffraction patterns of the source components (silver thiogallate and iron thiogallate). The diffraction pattern of the alloys containing 11–96 mol% FeGa<sub>2</sub>S<sub>4</sub> is two-phase (Fig. 2).

#### 4. Conclusions

1. Using the methods of physicochemical analysis (XRD, DTA, MSA), a phase diagram of the system AgGaS<sub>2</sub>–FeGa<sub>2</sub>S<sub>4</sub> was studied and constructed for the first time. It was established that the system is a quasi-binary cross-section of the FeS–Ga<sub>2</sub>S<sub>3</sub>–Ag<sub>2</sub>S quasi-triple system and belongs to the simple eutectic type.



**Fig. 2.** Diffraction pattern of the alloys of the  $\text{AgGaS}_2\text{-FeGa}_2\text{S}_4$  system: 1 –  $\text{AgGaS}_2$ ; 2 – 11 mol%  $\text{FeGa}_2\text{S}_4$ ; 3 – 40 mol%  $\text{FeGa}_2\text{S}_4$ ; 4 – 96 mol%  $\text{FeGa}_2\text{S}_4$ ; 5 –  $\text{FeGa}_2\text{S}_4$

2. The formation of solid solutions based on their source components was found in the  $\text{AgGaS}_2\text{-FeGa}_2\text{S}_4$  system. The solubility based on iron thiogallate at room temperature is 4 mol%  $\text{AgGaS}_2$  and the solubility based on silver thiogallate is 11 mol%  $\text{FeGa}_2\text{S}_4$ .

### Conflict of interests

The author declares that they have no known competing financial interests or personal relationships that could have appeared to influence the work reported in this paper.

### References

1. Zhao B., Zhu S., Li Z., Yu F., Zhu X., Gao D. Growth of  $\text{AgGaS}_2$  single crystal by descending crucible with rotation method and observation of properties. *Chinese Sci. Bull.* 2001;46(23): 2009–2013. DOI:
2. Goryunova N. A. Slozhnyealmazopodobnye poluprovodniki [Complex diamond-like semiconductors]. Moscow: Sov. radio. Publ.; 1968. 215 c. (In Russ.)
3. Abrikosov N. Kh., Shelimova L. E. Poluprovodnikovye materialy na osnove soedinenii

$\text{A}^{\text{IV}}\text{B}^{\text{VI}}$  [Semiconductor materials based on compounds  $\text{A}^{\text{IV}}\text{B}^{\text{VI}}$ ]. Moscow: Nauka Publ.; 1975. 195 p. (In Russ.)

4. Kushwaha A. K., Khenata R., Bouhemadou A., Bin-Omran S., Haddadi K. Lattice dynamical properties and elastic constants of the ternary chalcopyrite compounds  $\text{CuAlS}_2$ ,  $\text{CuGaS}_2$ ,  $\text{CuInS}_2$ , and  $\text{AgGaS}_2$ . *Journal of Electronic Materials.* 2017;46(7): 4109–4118. DOI: <https://doi.org/10.1007/s11664-017-5290-6>

5. Uematsu T., Doi T., Torimoto T., Kuwabata S. Preparation of luminescent  $\text{AgInS}_2\text{-AgGaS}_2$  solid solution nanoparticles and their optical properties. *The Journal of Physical Chemistry Letters.* 2010;1(22): 3283–3287. DOI: <https://doi.org/10.1021/jz101295w>

6. Karaagac H., Parlak M. The investigation of structural, electrical, and optical properties of thermal evaporated  $\text{AgGaS}_2$  thin films. *J. Thin Solid Films.* 2011;519(7): 2055–2061. DOI: <https://doi.org/10.1016/j.tsf.2010.10.027>

7. Karunakaran N., Ramasamy P. Synthesis, growth and physical properties of silver gallium sulfide single crystals. *Materials Science in Semiconductor Processing.* 2016;41: 54–58. DOI: <https://doi.org/10.1016/j.mssp.2015.08.012>

8. Zhou H., Xiong L., Chen L., Wu L. Dislocations that decrease size mismatch within the lattice leading to ultrawide band gap, large second-order susceptibility,

and high nonlinear optical performance of AgGaS<sub>2</sub>. *Angewandte Chemie International Edition*. 2019;58(29): 9979–9983. DOI: <https://doi.org/10.1002/anie.201903976>

9. Li G., Chu Y., Zhou Z. From AgGaS<sub>2</sub> to Li<sub>2</sub>ZnSiS<sub>4</sub>: Realizing impressive high laser damage threshold together with large second-harmonic generation response. *Journal Chemistry of Materials*. 2018;30(3): 602–606. DOI: <https://doi.org/10.1021/acs.chemmater.7b05350>

10. Yang J., Fan Q., Yu Y., Zhang W. Pressure effect of the vibrational and thermodynamic properties of chalcopyrite-type compound AgGaS<sub>2</sub>: A first-principles investigation. *Journal Materials*. 2018;11(12): 2370. DOI: <https://doi.org/10.3390/ma11122370>

11. Paderick S., Kessler M., Hurlburt T. J., Hughes S. M. Synthesis and characterization of AgGaS<sub>2</sub> nanoparticles: a study of growth and fluorescence. *Journal Chemical Communications*. 2018;54(1): 62–65. DOI: <https://doi.org/10.1039/C7CC08070K>

12. Kato K., Okamoto T., Grechin S., Umemura N. New Sellmeier and thermo-optic dispersion formulas for AgGaS<sub>2</sub>. *Journal Crystals*. 2019;9(3): 129–135. DOI: <https://doi.org/10.3390/cryst9030129>

13. Li W., Li Y., Xu Y., Lu J., Wang P., Du J., Leng Y. Measurements of nonlinear refraction in the mid-infrared materials ZnGeP<sub>2</sub> and AgGaS<sub>2</sub>. *Journal Applied Physics B*. 2017;123(3). DOI: 10.1007/s00340-017-6643-9

14. Jahangirova S. K., Mammadov Sh. H., Ajdarova D. S., Aliyev O. M., Gurbanov G. R. Investigation of the AgGaS<sub>2</sub>–PbS and some properties of phases of variable composition. *Russian Journal of Inorganic Chemistry*. 2019;64(9): 1169–1171. DOI: <https://doi.org/10.1134/S0036023619090092>

15. Asadov S. M., Mustafaeva S. N., Guseinov D. T. X-ray dosimetric characteristics of AgGaS<sub>2</sub> single crystals grown by chemical vapor transport. *Inorganic Materials*. 2017;53(5): 457–461. DOI: <https://doi.org/10.1134/S0020168517050028>

16. Mys O., Adamenko D., Skab I., Vlokh R. Anisotropy of acousto-optic figure of merit for the collinear diffraction of circularly polarized optical waves at the wavelength of isotropic point in AgGaS<sub>2</sub> crystals. *Ukrainian Journal of Physical Optics*. 2019;20(2): 73–80. DOI: <https://doi.org/10.3116/16091833/20/2/73/2019>

17. Karunagaran N., Ramasamy P. Investigation on synthesis, growth, structure and physical properties of AgGa<sub>0.5</sub>In<sub>0.5</sub>S<sub>2</sub> single crystals for Mid-IR application. *Journal of Crystal Growth*. 2018;483: 169–174. DOI: <https://doi.org/10.1016/j.jcrysgro.2017.11.030>

18. Ranmohotti K. G. S., Djieutedjeu H., Lopez J., Page A., Haldolaarachchige N., Chi H., Sahoo P., Uher C., Young D., Poudeu P. F. P. Coexistence of high-T<sub>c</sub> ferromagnetism and n-type electrical conductivity in FeBi<sub>2</sub>Se<sub>4</sub>. *J. of the American Chemical Society*.

2015;137(2): 691–698. DOI: <https://doi.org/10.1021/ja5084255>

19. Karthikeyan N., Aravindsamy G., Balamurugan P., Sivakumar K. Thermoelectric properties of layered type FeIn<sub>2</sub>Se<sub>4</sub> chalcogenide compound. *Materials Research Innovations*. 2018;22(5): 278–281. DOI: <https://doi.org/10.1080/14328917.2017.1314882>

20. Nakafsuji S., Tonomura H., Onuma K., Nambu Y., Sakai O., Maeno Y., Macaluso R. T., Chan J. Y. Spin disorder and order in quasi-2D triangular Heisenberg antiferromagnets: comparative study of FeGa<sub>2</sub>S<sub>4</sub>, Fe<sub>2</sub>Ga<sub>2</sub>S<sub>5</sub> and NiGa<sub>2</sub>S<sub>4</sub>. *Phys. Rev. Letters*. 2007;99(1–4): 157–203. DOI: <https://doi.org/10.1103/PhysRevLett.99.157203>

21. Rushchanskii K. Z., Haeuseler H., Bercha D. M. Band structure calculations on the layered compounds FeGa<sub>2</sub>S<sub>4</sub> and NiGa<sub>2</sub>S<sub>4</sub>. *J. Phys. Chem. Solids*. 2002;63(11): 2019–2028. DOI: [https://doi.org/10.1016/S0022-3697\(02\)00188-9](https://doi.org/10.1016/S0022-3697(02)00188-9)

22. Dalmas de Reotier P., Yaouanc A., MacLaughlin D. E., Songrui Zhao. Evidence for an exotic magnetic transition in the triangular spin system FeGa<sub>2</sub>S<sub>4</sub>. *J. Phys. Rev. B*. 2012;85(14): 140407.1–140407.5. DOI: <https://doi.org/10.1103/physrevb.85.140407>

23. Myoung B. R., Lim J. T., Kim C. S. Investigation of magnetic properties on spin-ordering effects of FeGa<sub>2</sub>S<sub>4</sub> and FeIn<sub>2</sub>S<sub>4</sub>. *Journal of Magnetism and Magnetic Materials*. 2017;438: 121–125. DOI: <https://doi.org/10.1016/j.jmmm.2017.04.056>

24. Asadov M. M., Mustafaeva S. N., Hasanova U. A., Mamedov F. M., Aliyev O. M., Yanushkevich K. I., Nikitov S. A., Kuli-Zade E. S. Thermodynamics of FeS–PbS–In<sub>2</sub>S<sub>3</sub> and properties of intermediate phases. *Journal Defect and Diffusion Forum*. 2018;385: 175–181. DOI: <https://doi.org/10.4028/www.scientific.net/DDF.385.175>

25. Li K., Yuan D., Shen S., Guo J. Crystal structures and property characterization of two magnetic frustration compounds. *Journal Powder Diffraction*. 2018;33(3): 190–194. DOI: <https://doi.org/10.1017/S0885715618000507>

26. Chen B., Zhu S., Zhao B., Lei Y., Wu X., Yuan Z., He Z. Differential thermal analysis and crystal growth of AgGaS<sub>2</sub>. *Journal of Crystal Growth*. 2008;310(3): 635–638. DOI: <https://doi.org/10.1016/j.jcrysgro.2007.10.067>

27. Sinyakova E. F., Kosyakov V. I., Kokh K. A. Oriented crystallization of AgGaS<sub>2</sub> from the melt system Ag–Ga–S. *J. Inorganic Materials*. 2009;45(11): 1217–1221. DOI: <https://doi.org/10.1134/S0020168509110041>

28. Chykhrij S. I., Parasyuk O. V., Halka V. O. Crystal structure of the new quaternary phase AgCd<sub>2</sub>GaS<sub>4</sub> and phase diagram of the quasibinary system AgGaS<sub>2</sub>–CdS. *Journal of Alloys and Compounds*. 2000;312(1–2): 189–195. DOI: [https://doi.org/10.1016/S0925-8388\(00\)01145-2](https://doi.org/10.1016/S0925-8388(00)01145-2)

29. Olekseyuk I. D., Parasyuk O. V., Halka V. O., Piskach L. V. F., Pankevych V. Z., Romanyuk Ya. E. Phase equilibria in the quasi-ternary system  $\text{Ag}_2\text{S}-\text{CdS}-\text{Ga}_2\text{S}_3$ . *J. Alloys and compounds*. 2001;325(10): 167–179. DOI: [https://doi.org/10.1016/S0925-8388\(01\)01361-5](https://doi.org/10.1016/S0925-8388(01)01361-5)
30. Brand G., Kramer V. Phase equilibrium in the quasi-binary system  $\text{Ag}_2\text{S}-\text{Ga}_2\text{S}_3$ . *Mater. Res. Bull.* 1976;11(11): 1381–1388. DOI: [https://doi.org/10.1016/0025-5408\(76\)90049-0](https://doi.org/10.1016/0025-5408(76)90049-0)
31. Lazarev V. B., Kish Z. Z., Peresh E. Yu., Semrad E. E. *Slozhnye khal'kogenidy v sisteme  $A^3-B^{3+}-C^{VI}$*  [Complex chalcogenides in the  $A^3-B^{3+}-C^{VI}$  system]. Moscow: Metallurgiya Publ; 1993. 229 p. (In Russ.)
32. Ugay Ya. A. *Vvedenie v khimiyu poluprovodnikov* [Introduction to the chemistry of semiconductors]. Moscow: Vysshaya shkola Publ.; 1975. 302 p. (In Russ.)
33. Pardo M. E., Dogguy-Smiri L., Flahaut J., Nguyen H. D. System  $\text{Ga}_2\text{S}_3-\text{FeS}$  Diagramme de phase – etude cristallographique. *Mater. Res. Bull.* 1981;16(11): 1375–1384. DOI: [https://doi.org/10.1016/0025-5408\(81\)90056-8](https://doi.org/10.1016/0025-5408(81)90056-8)
34. Wintenberger M. About the unit cells and crystal structures of  $\sim\text{M}\text{Ga}_2\text{X}_4$  ( $\text{M} = \text{Mn}, \text{Fe}, \text{Co}$ ;  $\text{X} = \text{S}, \text{Se}$ ) and  $\text{ZnAl}_2\text{S}_4$  Type. In: *Proc. VII Int. Conf. on Solid Compounds of Transition Elements, CNRS*. Grenoble, France: IA 14/1-3, 1983.
35. Rustamov P. G., Babaeva P. K., Azhdarova D. S., Askerova N. A., Ailazov M. R. Nature of interaction in  $\text{Mn}(\text{Fe}, \text{Co}, \text{Ni})-\text{Ga}(\text{In})-\text{S}(\text{Se})$  ternary systems. *Azerb. Khim. Zh.* 1984;15: 101–103.
36. Raghavan V.  $\text{Fe}-\text{Ga}-\text{S}$  (Iron-Gallium-Sulfur). *J. Phase Equil.* 1998;19: 267–268. DOI: <https://doi.org/10.1361/105497198770342319>
37. Ueno T., Scott S. D. Phase relations in the  $\text{Ga}-\text{Fe}-\text{S}$  system at 900 and 800 C. *The Canadian Mineralogist*. 2002;40(2): 568–570. DOI: <https://doi.org/10.2113/gscanmin.40.2.563>
38. Allazov M. R. The system of  $\text{FeS}-\text{GaS}-\text{S}$ . *Bulletin of Baku State University*. 2009;(2): 42–47. Available at: <http://static.bsu.az/w8/Xeberler%20Jurnali/Tebiet%202009%203/42-47.pdf>
39. Dogguy-Smiri L., Dung Nguyen Huy, Pardo M. P. Structure cristalline du polytype  $\text{FeGa}_2\text{S}_4 \alpha 1\text{T}$ . *Mater. Res. Bull.* 1980;15(7): 861–866. DOI: [https://doi.org/10.1016/0025-5408\(80\)90208-1](https://doi.org/10.1016/0025-5408(80)90208-1)
40. Hahn H., Klingler W. Unter such ungen uber ternare chalkogenide. I. Uber die, kristall structure iniger ternaerer sulfide, die sich vom  $\text{In}_2\text{S}_3$  ableiten. *Zeitschrift fur Anorganische und Allgemeine Chemie*. 1950;263(4): 177–190. DOI: <https://doi.org/10.1002/zaac.19502630406>
41. Dogguy-Smiri L., Pardo M. P. Etude cristallographique du systeme  $\text{FeS}-\text{Ga}_2\text{S}_3$ . *Compt. Rend. Acad. Sci.* 1978;287: 415–418.
42. Allazov M. R., Musaeva S. S., Abbasova R. F., Huseynova A. G. Phase crystallization regions along isothermal sections of  $\text{Fe}-\text{Ga}-\text{S}$  systems. *Bulletin of the Baku State University*. 2013; (3):11–14. Available at: <http://static.bsu.az/w8/Xeberler%20Jurnali/Tebiet%20202013%20203/11-15.pdf> (In Russ., abstract in Eng.)
43. Rzaguluev V. A., Kerimli O. Sh., Azhdarova D. S., Mammadov Sh. H., Aliev O. M. Phase equilibria in the  $\text{Ag}_8\text{SnS}_6-\text{Cu}_2\text{SnS}_3$  and  $\text{Ag}_2\text{SnS}_3-\text{Cu}_2\text{Sn}_4\text{S}_9$  systems. *Kondensirovannye sredyi mezhfaznye granitsy=Condensed Matter and Interphases*. 2019;21(4): 544–551. DOI: <https://doi.org/10.17308/kcmf.2019.21/2365> (In Russ., abstract in Eng.)

### Information about the authors

Sharafat H. Mammadov, PhD in Chemistry, Associate Professor, Senior Researcher, Institute of Catalysis and Inorganic Chemistry n.a. Academician M. F. Nagiyev of the Azerbaijan National Academy of Sciences, Baku, Azerbaijan; e-mail: [azxim@mail.ru](mailto:azxim@mail.ru). ORCID iD: <https://orcid.org/0000-0002-1624-7345>.

Author have read and approved the final manuscript.

Translated by Marina Strepetova  
Edited and proofread by Simon Cox



# Condensed Matter and Interphases (Kondensirovannye sredy i mezhfaznye granitsy)

## Original article

DOI: <https://doi.org/10.17308/kcmf.2020.22/2837>

Received 27 January 2020

Accepted 15 April 2020

Published online 25 June 2020

ISSN 1606-867X

eISSN 2687-0711

## Spectral analysis of heat fluctuations in KI transient premelting states

©2020 E. S. Mashkina

Voronezh State University,  
1 Universitetskaya pl., Voronezh 394018, Russian Federation

### Abstract

Nonequilibrium fluctuations, which are of nonlinear Brownian noise by type, occur in different systems near the phase transition points. As a rule, such nonequilibrium processes are the precursors of materials fracture and degradation. Observation of the transient premelting states near the melting point  $T_m$  and anomalous temperature behaviour of some physical parameters indicate changes in the structure and properties of a solid body as it approaches the melting point. As a rule, the changes are nonlinearly dependent on heating rate. It is necessary to calculate the index of the shape of the fluctuation spectrum to characterise the state of complex dynamic systems. The index has information about the processes in the system and the interrelations between different subsystems. Changes in the spectral characteristics of fluctuation processes may indicate the state of the system and also help us to develop the methods to predict its evolution. The aim of this study is parametrisation of heat fluctuations in the premelting states of KI ionic crystals and the study of the dependence of spectral parameters on kinetic modes of heating.

Wavelet-analysis has been used to determine the spectral characteristics of thermal fluctuations in the KI premelting states in various kinetic modes. Wavelet-analysis combines the capabilities of classical spectral Fourier-analysis with the capabilities of a local study of various fluctuation and oscillating processes in frequency and time domains. It makes it possible to determine the features of the processes at various times and scales of the evolution of the system.

Wavelet transform of oscillating processes allowed obtaining information about the dynamics of the development of complex systems under various nonequilibrium conditions. It was shown that heat fluctuations in the KI premelting states are nonlinear Brownian noise with the coefficient of selfsimilarity of  $\beta \sim 2$ . Using the Hurst parameter, the type of fluctuation process was defined. It was shown that in dynamic heating modes ( $\nu = 5, 10$  K/min) the fluctuation process is characterised by oscillating nature of evolution of the “stable-unstable” type (the property of antipersistence). In quasistatic modes ( $\nu = 1$  K/min) the initial tendency of the evolution of the system is maintained (the property of persistence).

**Keywords:** potassium iodide, premelting, melting point, fluctuation, wavelet-analysis, index of selfsimilarity, nonlinear Brownian noise, Hurst parameter, structural reconstruction.

**For citation:** Mashkina E. S. Spectral analysis of heat fluctuations in KI transient premelting states. *Kondensirovannye sredy i mezhfaznye granitsy = Condensed Matter and Interphases*. 2020;22(2): 238–244. DOI: <https://doi.org/10.17308/kcmf.2020.22/2837>

✉ Ekaterina S. Mashkina, e-mail: [me22-1@phys.vsu.ru](mailto:me22-1@phys.vsu.ru)



The content is available under Creative Commons Attribution 4.0 License.

## 1. Introduction

Fluctuation processes with  $1/f^\beta$  spectrum ( $\beta$  – the index of the shape of the spectrum) occur in different physical, chemical, and biological systems [1–4]. The study of such processes is one of the most important issues in material science. In the context of deformation and fracture of materials and various phase transitions far from thermodynamic equilibrium, unstable dynamic states arise. They are the precursors of structural changes in the system [5–9].

The study of fluctuation processes at critical points in order to obtain new materials and systems with unique properties is of great practical importance. In this case, new technological approaches are required, which are based on the concept of nonlinear phenomena, when the choice of a specific development path of the system at a critical point can be carried out under the influence of a small control action.

Dynamic methods of analysis can be effectively used in the study of the precursors of various phase transitions [10,11]. An analysis of the evolution of complex excited systems with determination of the low-frequency spectral dependences of dynamic variables allows us to come closer to understanding of the features of the formation of spatio-temporal structures during such evolution.

To characterise the state of complex fluctuating systems, spectral parameters are introduced that carry information about the dynamic processes taking place in the system and the interrelations of various subsystems. A change in these spectral parameters at different hierarchy levels indicates a change in the state of the system. Based on this information, it is possible to develop methods for predicting the evolution of complex dynamic systems.

The aim of this work is to study, using the wavelet-analysis method, the spectral characteristics of fluctuation processes of KI premelting phases in various kinetic heating modes.

## 2. Experimental

Previously, our studies of the melting of substances with various types of chemical bonds showed that the fluctuation transient states occur near the melting point in certain temperature-

time intervals [12, 13]. It is particularly interesting to observe thermal fluctuations (fluctuations in the dissipation heat) in the vicinity of a first-order phase transition in this context, since the presence of such processes cannot be unambiguously associated with the existence of a continuous relaxation time spectrum in the system.

Along with the traditional spectral analysis methods, the method of wavelet-analysis [14–17] of nonequilibrium oscillating processes is applied to study the dynamics of complex systems to determine their interrelations and certain possible development paths under various external influences.

A wavelet transform is one of the methods of analysis and processing of nonstationary (in time) or heterogeneous (in space) signals of different types. Such an analysis is used when it is necessary to obtain not only a simple enumeration of the characteristic frequencies of the studied fluctuation signal, but also to obtain information at certain local points at which these frequencies appear.

For the spectral analysis of fluctuations of the dissipation heat and parameterisation of the KI premelting phases in various kinetic modes, the obtained database was used. It includes the records of the readings of the differential thermocouple in the dynamic mode at heating rates  $v = 5, 10$  K/min and in the quasistatic mode ( $v = 1$  K/min). The constant recording sample speed is 1 s. The length of the record in the files ranged from 500 to 1500 samples.

DTA-curves of KI premelting in different kinetic modes are shown in Fig. 1. As can be seen from the above figure, on the DTA-curves in dynamic and quasistatic modes, the dynamic states arising at the premelting stage have clear temperature boundaries.

The premelting effects are characterised by the system of experimentally defined nonequilibrium thermodynamic parameters: the temperature of the beginning and end of the premelting effect ( $T'_{pre-m}$ ,  $T''_{pre-m}$ ), the premelting temperature range ( $\delta T_{pre-m}$ ), the premelting dissipation temperature ( $\Delta Q_{pre-m}$ ) [12]. Each heating mode has its own values of thermodynamic parameters of the transient states. Depending on the heating mode, different states are formed which characterise the premelting effects. Thus, in contrast with

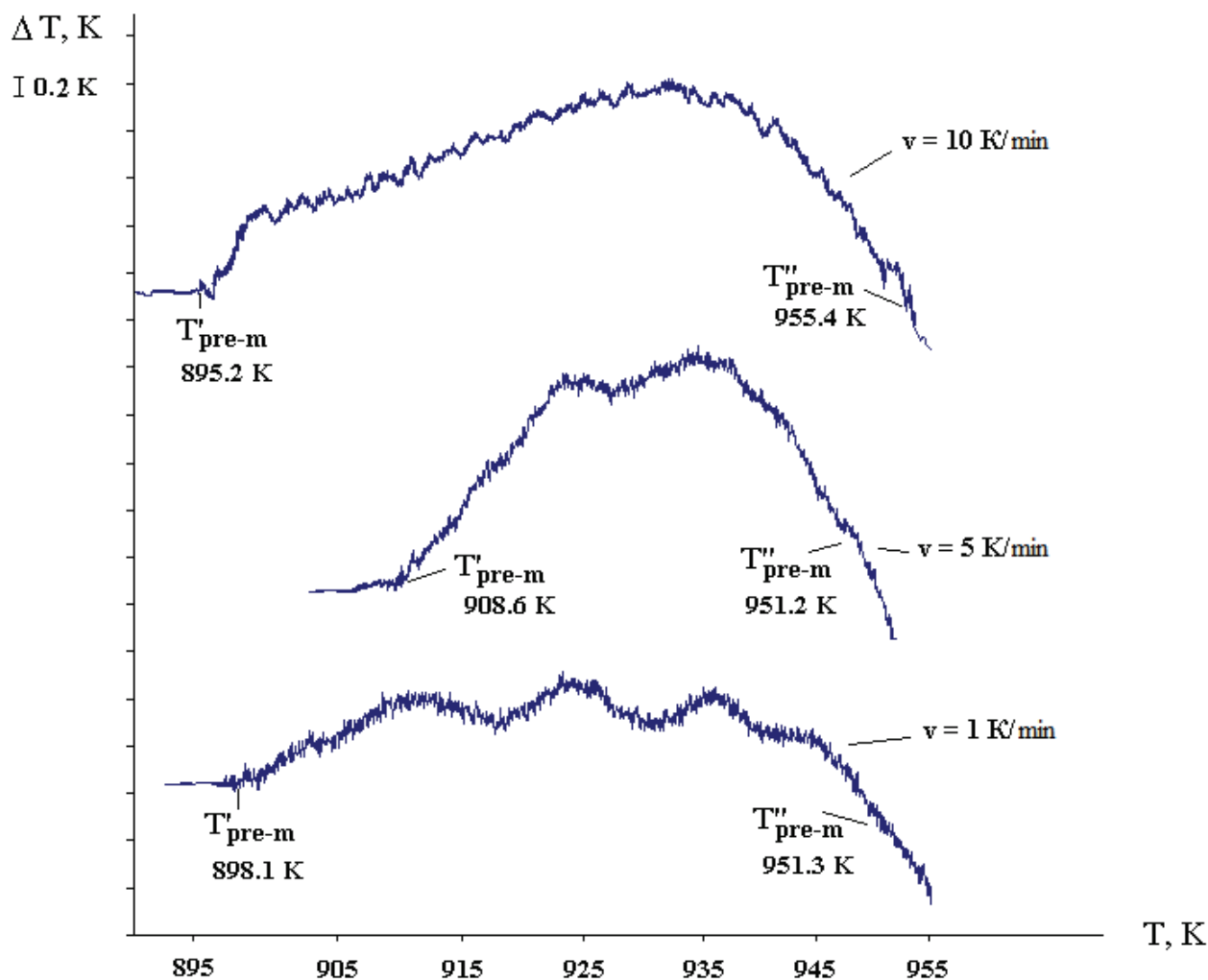


Fig. 1. DTA-curve of the KI premelting effect in different kinetic modes

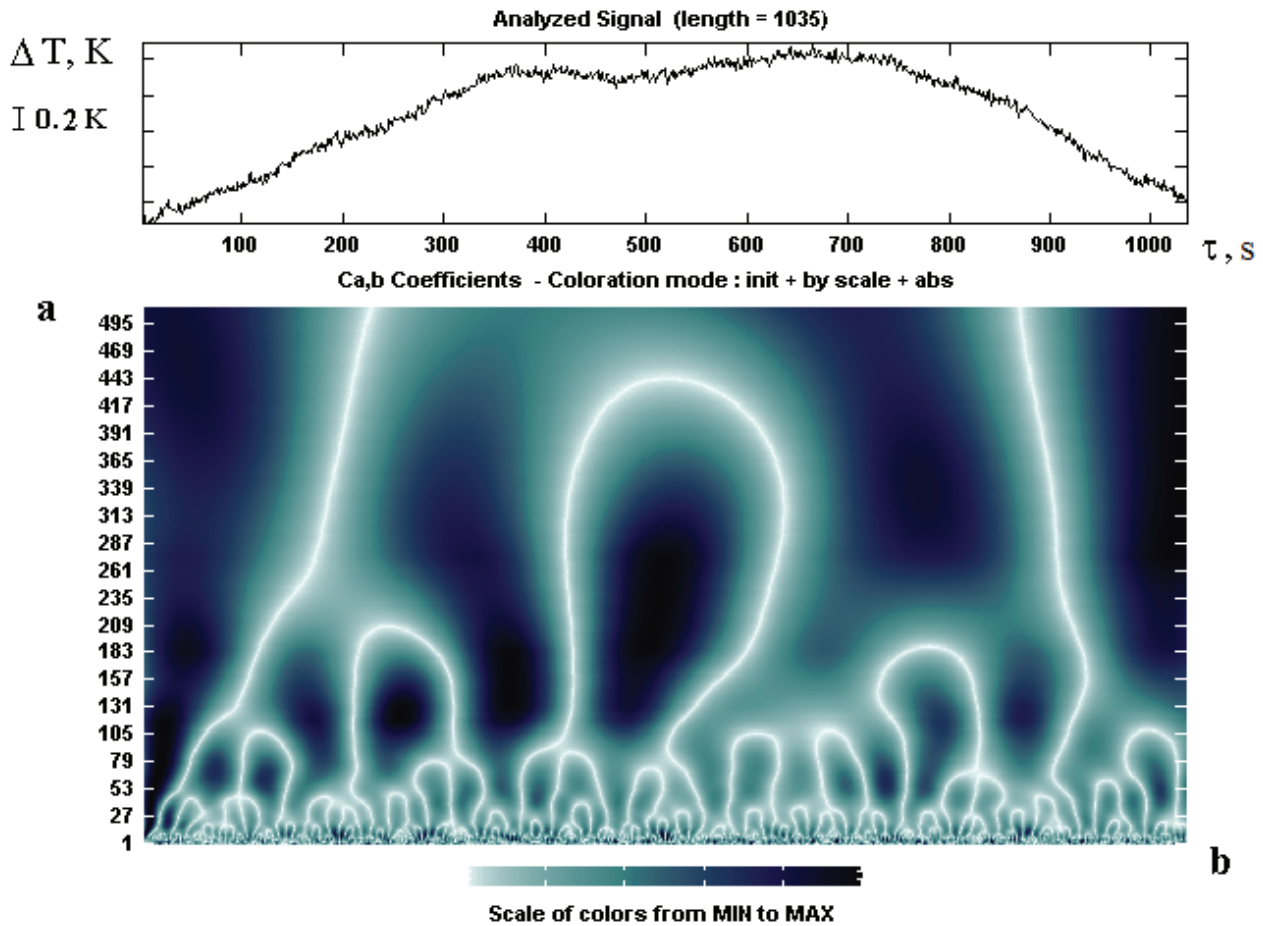
the dynamic heating mode ( $v = 5, 10$  K/min), the amplitude of the heating impulse of KI premelting in the quasistatic heating mode ( $v = 1$  K/min) decreases, and the thermal fluctuations become oscillating.

The spectral analysis of fluctuation processes of KI premelting was carried out in the MatLab software using the continuous wavelet transform method with the basis function Symlet8. The continuous wavelet transform allows for a more explicit and clear interpretation of the results of the signal analysis, and information about changes in characteristic frequencies of fluctuation processes and their interaction is easier to analyse. Moreover, when studying the fluctuation process, it is possible to consider the group of phases of this process corresponding to various independent spectral components.

### 3. Results and discussion

The wavelet-diagram of the KI premelting effect in the dynamic mode at a heating rate of 5 K/min is shown in Fig. 2. Time  $\tau$  (or the shift parameter  $b$ ) is plotted along the abscissa and the wavelet time scale  $a$ . Dark areas of the diagram correspond to the positive values of the  $W(a,b)$  coefficients and its bright areas correspond to the negative values. The  $W(a,b)$  value ranges are marked with different intensities of colour. The hierarchical arch structure of local extrema of the  $W(a,b)$  coefficients, reproduced at different scales, is clearly visible in the given wavelet-diagram. It demonstrates a scaled self-similarity of dissipation heat fluctuations of KI premelting.

A scalogram is used to define the self-similarity coefficient  $\beta$  or the index of the shape of the spectrum. It is given as a mean square of wavelet coefficients  $E_w \sim W^2(a,b)$  with a given scale



**Fig. 2.** DTA-curve of dissipation heat fluctuation and wavelet-diagram of the KI premelting effect (dynamic mode,  $\nu = 5$  K/min)

*a.* The scalogram represents the same information as the Fourier power spectral density that is the function of frequency, i.e., it corresponds to the smoothed power spectrum of the Fourier transform. The self-similarity coefficient  $\beta$  is defined as the angle of the dependence of  $\lg E_w$  on  $\lg a$  (Fig. 3) and it indicates the degree of correlation of the frequency components of the fluctuation signal.

Scalogram analysis of the thermal fluctuations of KI premelting in the dynamic mode ( $\nu = 5, 10$  K/min) showed that the coefficient is  $\beta \sim 2$ , and in the quasistatic mode ( $\nu = 1$  K/min) the self-similarity coefficient slightly decreases. The values of the self-similarity coefficients  $\beta$  and frequency intervals of dissipation heat fluctuations in transient states of KI premelting in different kinetic modes are provided in the Table. 1.

This kind of wavelet transform pattern and the value of the self-similarity coefficient indicate

that the fluctuation processes in KI premelting states are nonlinear Brownian noise ( $1/f^2$  type noise), i.e., they are a random process with independent increments.

The linear display of scalograms revealed the difference in the intensity of dissipation processes of KI premelting in different kinetic modes (Fig. 4). Based on this analysis, it can be seen that with a decrease in the heating rate during the transition from dynamic to quasistatic mode, the intensity of thermal fluctuations decreases. A decrease in the intensity of thermal fluctuations in the KI premelting states in the quasistatic

**Table 1.** Fluctuation of dissipation heat parameters of transient processes during the melting of KI

$\nu$ , K/min	$\beta$	$\Delta f_{pre-m}$ , Hz	$H$
1	1.9	0.007–0.03	0.58
5	2.2	0.01–0.07	0.42
10	2.1	0.02–0.18	0.4



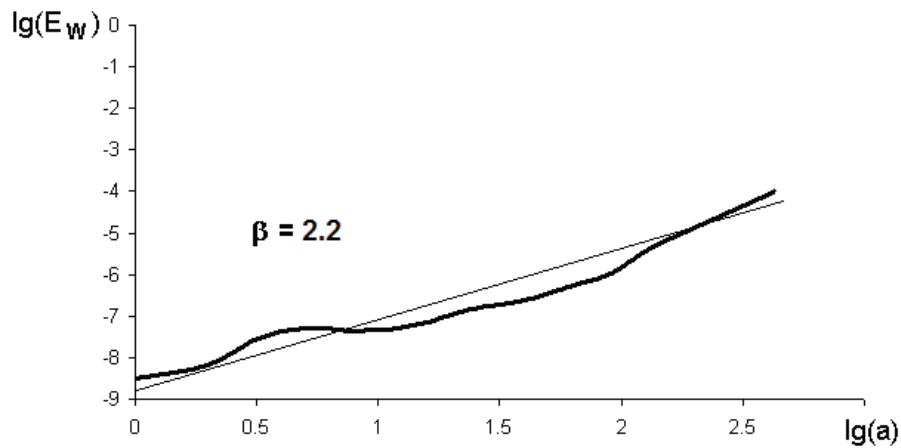


Fig. 3. Scalogram of the KI premelting effect (dynamic mode,  $v = 5$  K/min)

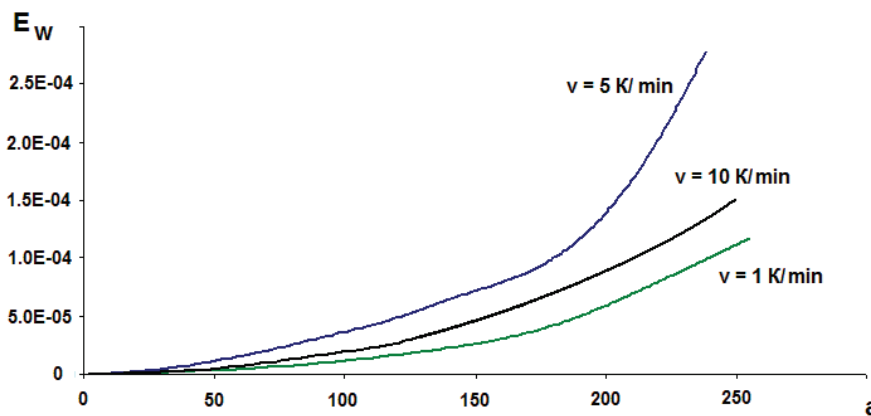


Fig. 4. Evolution of heat fluctuation intensity of the KI premelting effect in different kinetic modes

mode leads to a weakening of correlations in the system, which is also indicated by a decrease in the self-similarity coefficient  $\beta$ .

When analysing complex fluctuation signals, it is possible to evaluate the degree of their randomness using such a stochastic characteristic as the Hurst parameter ( $H$ ) [18, 19]. The Hurst parameter is the measure of the tendency of the process towards trend (in contrast to the usual Brownian motion). A value of  $H > 0.5$  indicates that the dynamics of the process in the past, heading in a certain direction, and is likely to continue its development in the same direction. If  $H < 0.5$ , the process is predicted to change its direction, while in the case of  $H = 0.5$  it indicates uncertainty.

Evaluation of the Hurst parameter of heat fluctuations of the KI premelting states in the dynamic heating modes provides the values

of  $H < 0.5$  (Table 1). This indicates a system which is more prone to reconstructions when its development tendency changes. Such fluctuation signals are characterized by a lack of stability (antipersistence). Their growth in the past means a decrease in the future, and a tendency to decrease in the past makes an increase in the future likely. Evaluation of the Hurst parameter in the dynamic heating mode gives the value of  $H \sim 0.58$ . This value of  $H$  indicates that this time dependence has a stable tendency to change (persistence). In other words, the presence of  $1/f^2$  type fluctuations in the system indicate structural changes in it. In such cases, as a rule, an oscillatory change of the “stability-instability-stability” type occurs.

If far from a critical point, the system will be quite stable, and the fluctuations will not have a noticeable effect on its behaviour. But if the

system is near a critical point (phase transition point  $T_m$ ), then an intensification of fluctuations will be a consequence of its sensitivity to small changes in the initial conditions. The intensification of fluctuations may lead to the formation of the ordered or so-called dissipative structures. This important phenomenon is known as ordering through fluctuations [20]. When the system approaches a phase transition point  $T_m$ , characteristic features appear that are the precursors of nonlinear instabilities.

#### 4. Conclusions

Therefore, the wavelet transform allows us to identify a complex hierarchy of scales in the process of energy redistribution of the fluctuation process. The energy represented by a large-scale “plateau” is redistributed between several “ridges” in a certain range of scales. Energy maxima can also be found between them. A similar process is observed with smaller scales. Therefore, a certain combination of ordering and chaos in the case of nonlinear Brownian noise, revealed during wavelet processing, reflects the presence of correlations in the system with a fluctuating dynamic variable.

Based on the wavelet-analysis, it was found that the transient fluctuation processes of KI premelting in various kinetic modes are nonlinear Brownian noise and are characterized by such features as the frequency interval, self-similarity coefficient of thermal fluctuations of the premelting, and Hurst parameter. In quasistatic modes, at heating rates of  $v \sim 1$  K/min, states with a weaker correlation arise in the KI premelting states. The fluctuation process in this case is characterized by a long-term memory effect with a tendency to follow trends. With dynamic modes of thermal fluctuations in the KI premelting states the correlations in the system intensify, and the resulting reconstructions in the system lead to a qualitative change in the structure. As a result, it is possible to not only describe the behaviour of the investigated fluctuation process, but also to predict its dynamics. In this case, it becomes possible to get an idea of the properties of fluctuating systems and distinguish noise (random process) from a certain deterministic behaviour.

#### Conflict of interests

The author declares that they have no known competing financial interests or personal relationships that could have influenced the work reported in this paper.

#### References

1. Bityutskaya L. A., Selezvev G. D. Thermal flicker noise in dissipative processes of pre-melting of crystalline materials. *Physics of the Solid State*. 1999;41(9): 1537–1540. DOI: <https://doi.org/10.1134/1.1131018>
2. Gerashchenko O. V., Matveev V. A., Pleshonov N. K., Bairamukov V. Yu. Electrical resistance and  $1/f$  fluctuations in thin titanium films. *Physics of the Solid State*. 2014;56(7): 1443–1448. DOI: <https://doi.org/10.1134/S1063783414070130>
3. Klochikhin V. L., Lakeev S. G., Timashev S. F. Flicker-noise in chemical kinetics (Microscopic kinetics and fluctuations in stationary chemical processes). *Russian Journal of Physical Chemistry A*. 1999;73(2): 172–178. Available at: <https://elibrary.ru/item.asp?id=13313799>
4. Pavlov A. N., Hramov A. E., Koronovskii A. A., Sitnikova E. Yu, Makarov V. A., Ovchinnikov A. A. Wavelet analysis in neurodynamics. *Phys. Usp.* 2012;55: 845–875. DOI: <https://doi.org/10.3367/UFNe.0182.201209a.0905>
5. Kosopov G. D., Bardyug D. Yu. Analysis of ice premelting in water-containing disperse media *Technical Physics Letters*. 2007;33(7): 622–624. DOI: <https://doi.org/10.1134/S1063785007070243>
6. Shibkov A. A. Gasanov M. F., Zolotov A. E., Zheltov M. A., Denisov A. A., Koltsov R. Yu., Kochegarov S. S. Elektrokhimicheskaya emissiya pri deformirovani i razrushenii alyumini-magnievogo splava v vodnoi srede [Electrochemical emission at deformation and fracture of aluminium-magnesium alloy in water medium]. *Technical Physics*. 2020;90(1): 85–93. DOI: <https://doi.org/10.21883/JTF.2020.01.48666.151-19> (In Russ.)
7. Feychuk P., Bityutskaya L., Mashkina E., Shcherbak L. Heat processes oscillations in the molten and solid CdTe. *J. Cryst. Growth*. 2005;275 (1–2): e1827–e1833. DOI: <https://doi.org/10.1016/j.jcrysgro.2004.11.256>
8. Umeno Y., Shimada T., Kitamura T. Dislocation nucleation in a thin Cu film from molecular dynamics simulations: Instability activation by thermal fluctuations. *Phys. Rev. B*. 2010;82(10): 104108/1–104108/11. DOI: <https://doi.org/10.1103/PhysRevB.82.104108>
9. Urakaev F. Kh., Massalimov I. A. Energy fluctuations and particle emission in a crack mouth. *Physics of the Solid State*. 2005;47(9): 1675–1680. DOI: <https://doi.org/10.1134/1.2045350>

10. Koverda V. P., Terekhov V. N. Scaling of  $1/f$  noise in nonequilibrium phase transitions. *Technical Physics*. 2004; 49(9):1104–1109. DOI: <https://doi.org/10.1134/1.1800229>
11. Zhigalskii G. P. Fluktuacii i shumi v elektronnykh tverdotel'nykh priborah [Fluctuation and noises in electronic solid state devices]. Moscow: Fizmatlit Publ.; 2012. 512 p. (in Russ.)
12. Bityutskaya L. A., Mashkina E. S. System of kinetic parameters of the transition processes under melting of crystalline substances. *Phase Transition*. 2000;71: 317–330. DOI: <https://doi.org/10.1080/01411590008209312>
13. Mashkina E. S. An anion influence on transient states during ionic crystals melting. *Kondensirovannyye sredy i mezhfaznye granitsy = Condensed Matter and Interphases*. 2011;13(3): 309–314. Available at: [http://www.kcmf.vsu.ru/resources/t\\_13\\_3\\_2011\\_010.pdf](http://www.kcmf.vsu.ru/resources/t_13_3_2011_010.pdf) (In Russ.)
14. Astaf'eva N. M. Wavelet analysis: basic theory and some applications. *Phys. Usp.* 1996;39(11): 1085–1108. DOI: <https://doi.org/10.1070/PU1996v039n11ABEH000177>
15. Dremin I. M., Ivanov O. V., Nechitailo V. A. Wavelets and their uses. *Phys. Usp.* 2001;44(5): 447–478. DOI: <https://doi.org/10.1070/PU2001v044n05ABEH000918>
16. Arby P., Goncalves P., Vehel J. L. *Scaling, fractals and wavelets*. London: John Wiley & Sons; 2009. 464 p.
17. Smolentsev N. K. *Osnovi teorii waveletov. Waveleti v MATLAB* [Fundamentals of wavelet theory. Wavelets in MATLAB]. Moscow: DMK Press; 2014. 628 p. (In Russ.)
18. Hurst H. E., Black R. P., Simaika Y. M. *Long-term storage: An experimental study*. London: Constable; 1965. 145 p.
19. Chen B. B., Imashev S. A. Evaluation of Hurst parameter on energetic spectrum based on wavelet transform. *Vestnik KRSU*. 2007;7(8): 65–75. Available at: <https://www.elibrary.ru/item.asp?id=13519890> (In Russ., abstract in Eng.)
20. Zulpukarov M.-G. M., Malinetsky G. G., Podlazov A. V. Bifurcation theory inverse problem in a noisy dynamical system. Example solution. *Izvestiya VUZ. Applied Nonlinear Dynamics*. 2005;13(5–6): 3–23. Available at: <file:///C:/Users/%D0%BF%D0%BE%D0%BB%D1%8C%D0%B7%D0%BE%D0%B2%D0%B0%D1%82%D0%B5%D0%BB%D1%8C/Downloads/2005no5-6p003.pdf> (In Russ., abstract in Eng.)

#### Information about the author

*Ekaterina S. Mashkina*, PhD in Physics and Mathematics, Associate Professor, Voronezh State University, Voronezh, Russian Federation; e-mail: [me22-1@phys.vsu.ru](mailto:me22-1@phys.vsu.ru). ORCID iD: <https://orcid.org/0000-0002-9911-5208>.

Author have read and approved the final manuscript.

*Translated by Anastasiia Ananeva  
Edited and proofread by Simon Cox*



# Condensed Matter and Interphases (Kondensirovannye sredy i mezhfaznye granitsy)

DOI: <https://doi.org/10.17308/kcmf.2020.22/2851>

Received 29 April 2020

Accepted 15 May 2020

Published online 25 June 2020

ISSN 1606-867X

eISSN 2687-0711

## The Effect of Certain Complex Chemostimulators and Modifiers on InP Thermal Oxidation

© 2020 I. Ya. Mittova<sup>✉,a</sup>, B. V. Sladkoptsev<sup>a</sup>, N. A. Ilyasova<sup>a</sup>, E. V. Tomina<sup>a</sup>, A. I. Dontsov<sup>a,b</sup>, O. S. Tarasova<sup>a</sup>

<sup>a</sup>Voronezh State University,  
1 Universitetskaya pl., Voronezh 394018, Russian Federation

<sup>b</sup>Voronezh State Technical University,  
14, Moskovskij pr., Voronezh 394026, Russian Federation

### Abstract

It is advisable to control characteristics and rate of formation of nanoscale films on InP by introducing chemostimulators, modifiers, or both simultaneously during the thermal oxidation of semiconductors. The chemostimulating effect of the compounds is determined by their transit role as oxygen transmitters or their catalytic function. Modifiers can affect the composition, surface morphology, structure, and properties of the film without changing the film growth rate. The effect of chemostimulators and modifiers on a single process of film synthesis with the desired properties was assumed to be productive.

**Purpose:** Establishment of the effect of certain complex chemostimulators and modifiers on the kinetics, growth mechanism, and properties of complex oxide films on InP in the nanoscale thickness range.

The object of the study was indium phosphide FIE-1A orientation (100).  $\text{SnO}_2/\text{InP}$  and (40 %  $\text{Co}_3\text{O}_4$ +60 %  $\text{MnO}_2$ )/InP heterostructures with a layer thickness of ~ 30 nm were formed by magnetron sputtering. Sulphate was deposited through the aerosol phase, followed by air drying and annealing at 200 °C for 30 min for the formation of the  $\text{Bi}_2(\text{SO}_4)_3/\text{InP}$  heterostructures.  $\text{SnO}_2/\text{InP}$  and InP samples were thermally oxidized under the influence of  $\text{AlPO}_4$  and  $\text{Bi}_2(\text{SO}_4)_3$ , respectively, introduced into the gas phase in the temperature range 490-570 °C in an oxygen stream for 60 min. The thickness of the films was controlled by laser and spectral ellipsometry and their phase and elemental composition were established by XRD and Auger electron spectroscopy, respectively. For the determination of the electrophysical properties of the films, the contacts were sprayed with aluminium and the resistivity was determined.

The fundamental role of the physicochemical nature of the chemostimulator, its ability to transit interactions and the renewability of oxide forms in the process of InP thermal oxidation was established. The introduction of phosphate groups from  $\text{AlPO}_4$  into thermal oxide films, with or without the deposition of  $\text{SnO}_2$  on the surface, led to the film resistance similar to that for the oxidation of  $\text{SnO}_2/\text{InP}$  heterostructures without the additional introduction of phosphates and was  $8.5 \cdot 10^7$  Ohm-cm.  $\text{Bi}_2(\text{SO}_4)_3$ , being a modifier of the composition and properties of the films, did not have a significant chemostimulating effect. Films grown under its influence had a semiconductor characteristics ( $\rho \sim 10^6$  Ohm-cm). The most effective was a 40 %  $\text{Co}_3\text{O}_4$ +60 %  $\text{MnO}_2$  complex chemostimulator, which determined the accelerated (up to 70 %) formation of film by the catalytic-transit mechanism (up to 70 %), being a part of the synthesized films and capable of purposefully modifying their properties by varying the content of components in it (XRD, SE).

**Keywords:** indium phosphide, nanoscale films, chemostimulated oxidation, chemostimulator, modifier, modification of composition and properties.

**Funding:** The study was financially supported by the Russian Foundation for Basic Research (Grant no. 18-03-00354a).

**For citation:** Mittova I. Ya., Sladkoptsev B. V., Ilyasova N. A., Tomina E. V., Dontsov A. I., Tarasova O. S. The effect of certain complex chemostimulators and modifiers on InP thermal oxidation. *Kondensirovannye sredy i mezhfaznye granitsy = Condensed Matter and Interphases*. 2020;22(2): 245–256. DOI: <https://doi.org/10.17308/kcmf.2020.22/2851>

✉ Irina Ya. Mittova, e-mail: [imittova@mail.ru](mailto:imittova@mail.ru).



The content is available under Creative Commons Attribution 4.0 License.

## 1. Introduction

Indium phosphide is one of the most important materials of modern semiconductor micro-, nano- and optoelectronics [1,2]. It is used in the production of super high frequency integrated circuits, InP heterostructures are used as photodetectors, in field effect transistors based on Gate stack technology, memory cells, optoelectronic devices, in solar cells, and laser diodes [3–7]. Films grown by InP thermal oxidation could be used in the development of highly efficient and cheap photoconverters of natural and linearly polarized InP-based radiation [8]. However, the InP interface with intrinsic oxide is usually characterized by a rather high density of states, low thermodynamics, and the temporal stability of parameters [9, 10]. It is advisable to control the rate of formation and characteristics of films of the nanoscale thickness range on InP by introducing chemostimulators, modifiers, or both at the same time during the thermal oxidation of these semiconductors [11]. Chemostimulators increase the growth rate of films during thermal oxidation, while suppressing negative reactions and surface degradation [12, 13]; modifiers change the composition, structure, and properties of films [14, 15]. The chemostimulating effect of purposefully selected and introduced compounds is due to their transit role as active oxygen transmitters to semiconductor components or a catalytic function [12]. Modifiers can, without changing the rate of increase in film thickness compared to intrinsic oxidation, affect the film composition, surface morphology, and grain structure, and hence their properties. It is logical to assume that the effect of chemostimulators and modifiers in a single process of film synthesis with the desired properties should be the most productive; however, to control the latter, it is necessary to isolate and separately study the role of such compounds in the InP thermal oxidation process.

The purpose of this study was establishment of the effect of certain binary and complex chemostimulators and modifiers on the kinetics, growth mechanism, and properties of complex oxide films on InP in the nanoscale thickness range.

## 2. Experimental

The objects of the study were thin nanoscale films formed on two-sided polished single-crystal indium phosphide samples FIE-1A orientation (100), doped with tin; the concentration of the main charge carriers at 300 K was not less than  $5 \cdot 10^{16} \text{ cm}^{-3}$ , intrinsic n-type conductivity. The substrates were pre-treated with an etchant of composition  $\text{H}_2\text{SO}_4$  (reagent grade, Russian Federation Purity Standard GOST 4204-77, 92.80 %) :  $\text{H}_2\text{O}_2$  (special purity grade, Russian Federation Purity Standard TU 6-02-570-750, 56 %) :  $\text{H}_2\text{O} = 2:1:1$  for 10 min, then repeatedly washed in distilled water and dried in air.

For the introduction of chemostimulators and modifiers, several approaches were used.  $\text{SnO}_2/\text{InP}$  and (40 %  $\text{Co}_3\text{O}_4$ +60 %  $\text{MnO}_2$ )/InP (molar %) heterostructures with a layer thickness of ~ 30 nm were formed by magnetron sputtering. The deposition was performed in a Covap II vacuum ion sputter, the initial vacuum was  $2 \cdot 10^{-5}$ , and sputtering was carried out in an atmosphere of  $\text{O}_2$ +Ar (purity 99.99 %) at a pressure of  $10^{-3}$  mm Hg. Sn with a purity of 99.99 %, Co with a purity of 99.9 %, and Mn with a purity of 99.9 % were used as the starting material. For the creation of the composition (40 %  $\text{Co}_3\text{O}_4$ +60 %  $\text{MnO}_2$ ) on InP by the magnetron sputtering method, a composite cobalt-manganese target was produced. The composition was selected experimentally taking into account the ratio of areas and sputtering coefficients of the corresponding metals, as well as differences in saturated vapour pressures above the metal surface for cobalt and manganese. Semiconductor substrate during magnetron sputtering was heated to 200 °C for the production of  $\text{SnO}_2$  crystal structure on the InP surface [16].

For the modification of the surface of the semiconductor with bismuth (III) sulphate layers, deposition through the aerosol phase in the established optimal (in terms of modifier layer thickness and reproducibility of results) mode was carried out. The sputtering of the  $\text{Bi}_2(\text{SO}_4)_3$  solution (concentration 0.44 mol/l) was carried out at room temperature substrates using a compressor dispersant, providing an aerosol with a droplet size of the solution up to 4-5  $\mu\text{m}$ . After deposition, the samples were dried in air and annealed in an SNOL muffle furnace at a

temperature of 200 °C for 30 min, thus forming  $\text{Bi}_2(\text{SO}_4)_3/\text{InP}$  heterostructures.

Another approach was the introduction of a chemostimulator or modifier through the gas phase during the oxidation process.  $\text{SnO}_2/\text{InP}$  and  $\text{InP}$  samples were oxidized by  $\text{AlPO}_4$  and  $\text{Bi}_2(\text{SO}_4)_3$  introduced into the gas phase.

Thermal oxidation of all samples was carried out in a MTP-2M-50-500 resistive heating furnace. Temperature adjustment ( $\pm 1^\circ$ ) was carried out using a TPM-10 meter/controller. Thermal oxidation was carried at an oxygen flow rate of 30 l/h. (linear gas flow rate in the reactor was 10 cm/min) for 60 min. In this case,  $\text{SnO}_2/\text{InP}$  heterostructures were oxidized at 530 °C similarly to [16], 40 %  $\text{Co}_3\text{O}_4$ +60 %  $\text{MnO}_2$ )/ $\text{InP}$  heterostructures were oxidized in the temperature range 490-570 °C, and  $\text{Bi}_2(\text{SO}_4)_3/\text{InP}$  – heterostructures were oxidized at 500–550 °C. Samples synthesized by magnetron sputtering were located perpendicular to the oxygen flow. When the oxidation was performed under the action of substances introduced through the gas phase,  $\text{AlPO}_4$  (m ~ 0.3 g) and  $\text{Bi}_2(\text{SO}_4)_3$  (m ~ 1 g) samples were placed in a cylindrical quartz container, covered with the oxidized  $\text{InP}$  sample (at a distance of 10 cm from the surface of the modifiers). Every 10 min, the samples were removed from the reactor and the thickness of the formed films was determined by laser (LE, LEF-754,  $\lambda = 632.8$  nm, absolute error

$\pm 1$  nm) and spectral (SE, Ellipse-1891 spectral ellipsometer, static circuit, range wavelengths of 250–1100 nm) ellipsometry, after oxidation was continued until the process time limit of 60 min was reached.  $\text{AlPO}_4$  powder was synthesized in a similar manner [17]. XRD results showed that all reflections in the diffractogram corresponded to that of an  $\text{AlPO}_4$  powder sample (Fig. 1).

The composition of the films grown by thermal oxidation was determined by the method of X-ray diffraction analysis (XRD) using ARL X'TRA X-ray diffractometer (copper anode, start angle –  $2^\circ$ , final –  $70^\circ$ , step –  $0.05^\circ$ ). X-ray diffraction patterns were recorded in the geometry of a grazing beam (with a fixed position of the arm of the X-ray tube).

The elemental composition of  $\text{Bi}_2(\text{SO}_4)_3/\text{InP}$  oxide films (500 and 525 °C) and thickness distribution of the components were studied by Auger electron spectroscopy (AES) using an ESO-3 spectrometer with a DESA-100 analyser, accuracy  $\pm 10\%$ , using the layer-by-layer etching of films with argon ions.

For the determination of the electrophysical properties, aluminium contacts were magnetronically sputtered on the surface of the synthesized samples through a mask with openings of  $5 \cdot 10^{-3} \text{ cm}^2$  in vacuum and the resistivity  $\rho$  (Ohm cm) of the formed structures was determined using an Agilent 344 10A universal multimeter. The thickness of the formed

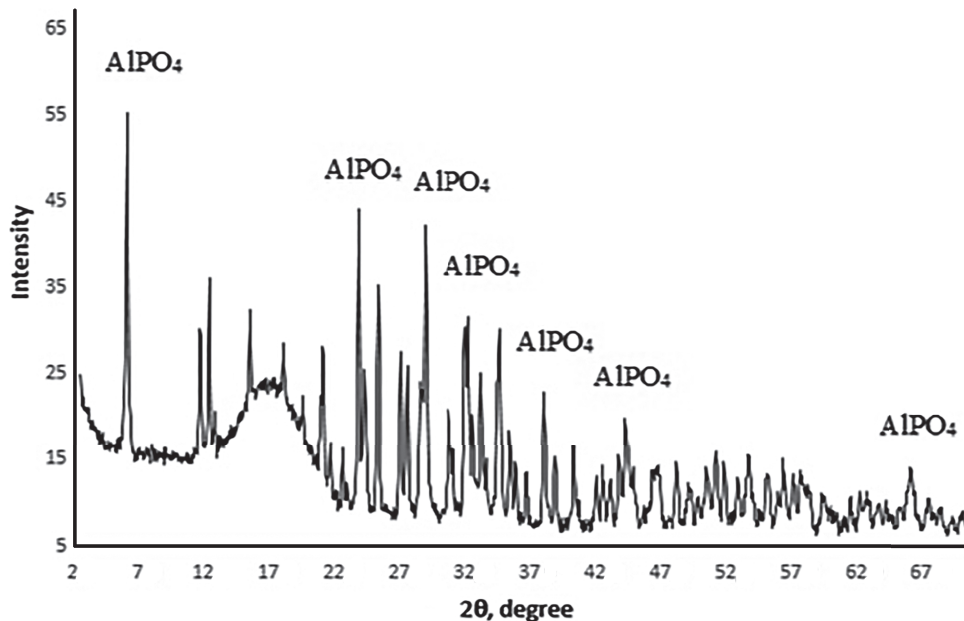


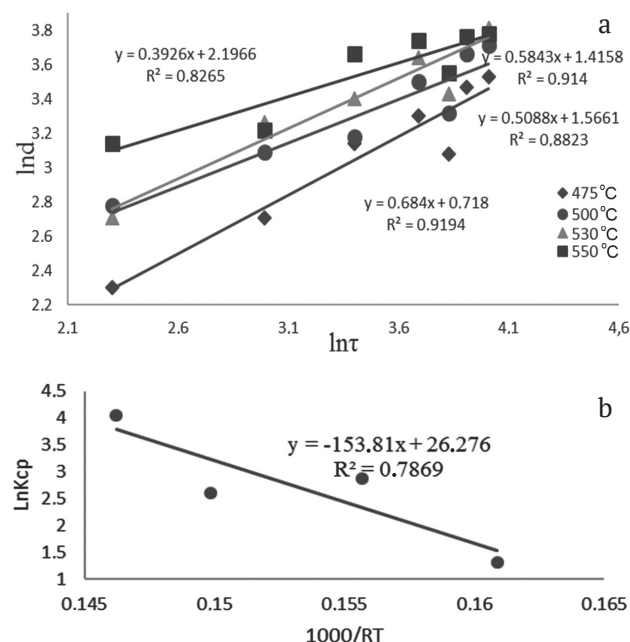
Fig. 1. X-ray diffraction pattern of  $\text{AlPO}_4$

film was taken into account in the process of measuring  $\rho$ .

### 3. Results and discussion

In [16], it was found that the oxide of the p-element of IVA group,  $\text{SnO}_2$ , thermodynamically capable of the transit of oxygen to InP components, in the process of thermal oxidation of this semiconductor plays only a modifying role. Thermal oxidation of  $\text{SnO}_2/\text{InP}$  heterostructures resulted in the formation of nanoscale films, with a higher electrical resistivity ( $\rho = 9 \cdot 10^6 \text{ Ohm}\cdot\text{cm}$ ) than the intrinsic oxide on InP, possessing ohmic conductivity. The achieved semiconductor properties in [16] were explained by the fact that metallic indium is not released during the oxidation of  $\text{SnO}_2/\text{InP}$  heterostructures,  $\text{SnO}_2$  promotes its chemical binding with phosphorus, as a result of which, based on the XRD data, the formation of the corresponding phosphates occurs.

$\text{AlPO}_4$  can serve as a compound playing only a modifying role in the considered process. It contains an “inert” cation, which does not cause either transit or catalytic effects, and a phosphate anion, an increase in the concentration of which in the films on InP, as was shown in [12], improves the electrophysical characteristics of films.



**Fig. 2.** Log plots of kinetic isotherms (a) and Arrhenius plot of the kinetic constant (b) of the process of thermal oxidation of InP with the gas phase of  $\text{AlPO}_4$  at 475–550 °C over 60 min

The kinetic curves of InP thermal oxidation under the influence of  $\text{AlPO}_4$  introduced through the gas phase are shown in Fig. 2a. The kinetic parameters of the process, calculated based on the exponential kinetic equation similarly to [15], and the value of the effective activation energy (EAE), determined using the corresponding Arrhenius equation (Fig. 2b) are shown in Table 1.

The values of the relative change in the film thickness over 60 min at temperatures of 475–550 °C as a result of the InP thermal oxidation process with the introduction of  $\text{AlPO}_4$  from the gas phase in comparison with the reference intrinsic oxidation of InP calculated according

to the equation  $b = \frac{\Delta d_{\text{InP}+\text{AlPO}_4}}{\Delta d_{\text{InP}}}$ , did not exceed

1.23, i.e.  $\text{AlPO}_4$  was not a chemostimulator of the InP thermal oxidation process. However, being part of the growing film,  $\text{AlPO}_4$  could modify its properties. Since, as noted above, the modifying role of the deposited  $\text{SnO}_2$  film was previously established in the thermal oxidation process of InP, the next step was to establish a possible synergy of the action of two modifiers simultaneously introduced by various methods. For this,  $\text{SnO}_2/\text{InP}$  heterostructures, which were formed similarly to [16], were oxidized under the influence of  $\text{AlPO}_4$  instead of a pure InP surface.

The kinetic curves of the oxidation of  $\text{SnO}_2/\text{InP}+\text{AlPO}_4$  and  $\text{SnO}_2/\text{InP}$  samples at a temperature of 530 °C as the most clearly reflecting the process regularities are shown in Fig. 3.

As can be seen from Fig. 3, the effect of  $\text{AlPO}_4$  leads to higher film thickness at the developed stage of the oxidation process due to additional phosphate groups coming from  $\text{AlPO}_4$ , which in turn act as the polyphosphate skeleton of the forming films.

According to the XRD data in Table 2, the introduced aluminium phosphate is included in the film, e.g. the addition of phosphate groups can possess a modifying effect.

However, such a change in composition practically did not change the properties of the films. Electrical resistivity of the  $\text{SnO}_2/\text{InP}+\text{AlPO}_4$ , oxidized at 530 °C for 60 min was  $8.5 \cdot 10^7 \text{ Ohm}\cdot\text{cm}$ , approaching that for  $\text{SnO}_2/\text{InP}$  heterostructure without oxidation –  $7.3 \cdot 10^7 \text{ Ohm}\cdot\text{cm}$  and slightly exceeding the value for  $\text{SnO}_2/\text{InP}$  heterostructure after thermal oxidation in the same mode –

**Table 1.** Kinetic parameters of the thermal oxidation of InP under the influence of various chemostimulators and modifiers

Kinetic parameters			$n \pm \Delta n, \text{nm}^{1/n} \text{min}^{-1}$	EAE, kJ/mol
	$T, ^\circ\text{C}$	$\ln k_{cp}$		
InP+AlPO <sub>4</sub> <sup>(g)</sup>	475	1.32	0.68±0.142	153
	500	2.88	0.51±0.034	
	530	2.61	0.58±0.042	
	550	4.04	0.39±0.149	
	$n_{av}$		0.54±0.092	
InP+Bi <sub>2</sub> (SO <sub>4</sub> ) <sub>3</sub> <sup>(g)</sup>	450	2.89	0.44±0.001	187
	475	4.06	0.43±0.001	
	500	5.95	0.36±0.003	
	530	10.51	0.20±0.001	
	550	11.51	0.13±0.001	
	$n_{av}$		0.31±0.002	
Bi <sub>2</sub> (SO <sub>4</sub> ) <sub>3</sub> /InP	500	38.23	0.11±0.002	459
	530	41.53	0.09±0.001	
	550	42.49	0.09±0.001	
	$n_{av}$		0.09±0.001	
(40 % Co <sub>3</sub> O <sub>4</sub> +60 % MnO <sub>2</sub> )/InP	490	11.09	0.30±0.031	50
	510	11.39	0.25±0.020	
	530	11.89	0.25±0.018	
	550	12.38	0.28±0.005	
	570	12.75	0.27±0.002	
	$n_{av}$		0.27±0.028	

**Table 2.** The identified phases: SnO<sub>2</sub>/InP without thermal oxidation, SnO<sub>2</sub>/InP at 530 °C and SnO<sub>2</sub>/InP with the gas phase of AlPO<sub>4</sub> at 530 °C

Samples	Interplane distance, $d_{hkl}$	The identified phase
SnO <sub>2</sub> /InP	5.5010; 3.2985	InP
	2.9092; 2.2040; 1.9599	SnO <sub>2</sub>
SnO <sub>2</sub> /InP (530 °C) [6]	5.5524	Sn <sub>3</sub> (PO <sub>4</sub> ) <sub>2</sub>
	2.9321	In(PO <sub>3</sub> ) <sub>3</sub>
	1.5074	InPO <sub>4</sub>
SnO <sub>2</sub> /InP+AlPO <sub>4</sub> <sup>(g)</sup>	5.3777; 2.5246; 2.9145;	Sn <sub>3</sub> (PO <sub>4</sub> ) <sub>2</sub>
	3.3849	InP
	1.5798; 1.5570	InPO <sub>4</sub>
	1.5483; 1.5258	AlPO <sub>4</sub>

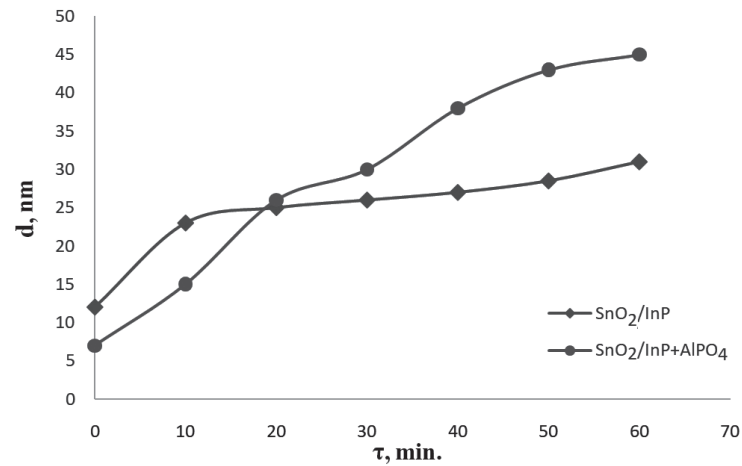
9.0·10<sup>6</sup> Ohm·cm. Thus, in the absence of a chemostimulating effect, synergistic effects of the studied modifiers have not been achieved.

Bi<sub>2</sub>(SO<sub>4</sub>)<sub>3</sub> can act as a compound simultaneously providing both a chemostimulating and a modifying effect on the InP thermal oxidation process. Bismuth sulphate contains a transition cation former, the action of which was established for the thermal oxidation of Si, GaAs, and InP [12,18], and the anionic sulphate group, similar in structure to phosphate group [17] and is barely

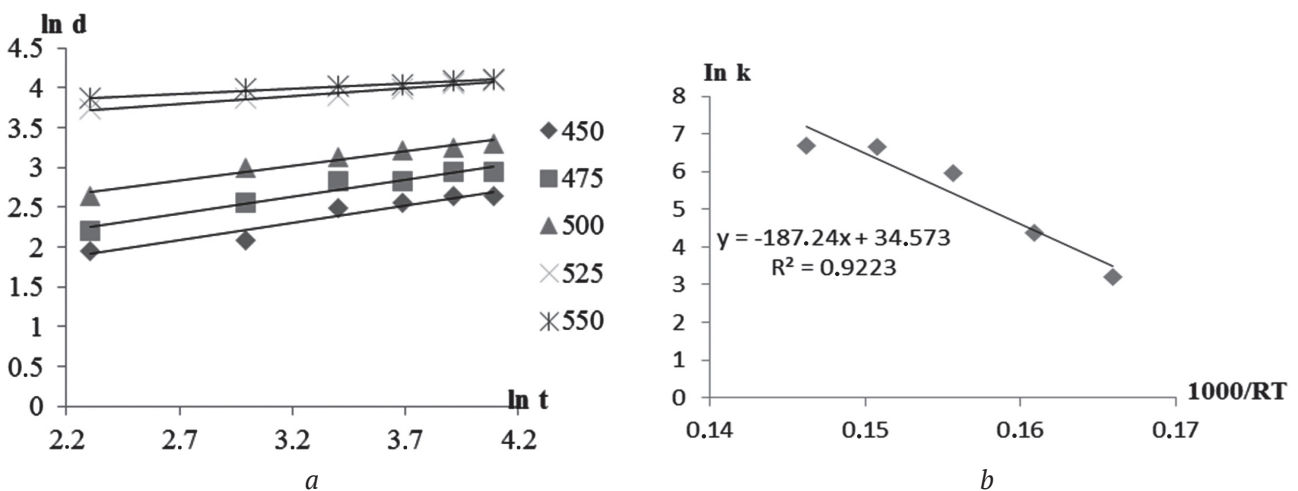
distinguishable from it by IR spectroscopy [19]. It is known that at InP oxidation temperatures, this compound only partially releases sulphur oxides, mainly preserving the bismuth oxide and sulphate fragments required for our process.

Kinetic isotherms of InP thermal oxidation under the influence of Bi<sub>2</sub>(SO<sub>4</sub>)<sub>3</sub> introduced through the gas phase in a process similar to the introduction of AlPO<sub>4</sub> are shown in Fig. 4a, the corresponding Arrhenius plot is demonstrated in Fig. 4b. The kinetic parameters of the process,





**Fig. 3.** Kinetic curves of SnO<sub>2</sub>/InP heterostructures with thermal oxidation with and without the gas phase of AlPO<sub>4</sub> at 530 °C over 60 min



**Fig. 4.** Log plots of kinetic isotherms (a) and Arrhenius plot of the kinetic constant  $\ln k_{av} = f(10^3/RT)$  (b) of the process of thermal oxidation of InP with the gas phase of Bi<sub>2</sub>(SO<sub>4</sub>)<sub>3</sub>

calculated according to the aforementioned exponential equation [15], indicate an increase in the contribution of the diffusion component with increasing film thickness (a regular decrease in the exponent  $n$  with increasing process parameters) and demonstrate the fact that the solid-phase reaction limited by diffusion in the solid phase is a determining process for InP + Bi<sub>2</sub>(SO<sub>4</sub>)<sub>3</sub> in the investigated temperature range of 450–550 °C. The value of EAE was 187 kJ/mol, which, taking into account the error of this calculation (about 10%), can be considered equal to the EAE of the intrinsic oxidation process of indium phosphide, which we determined for InP samples of the same batch (170 kJ/mol) and coinciding with the value obtained previously for intrinsic oxidation of indium phosphide [12].

Based on the values of the acceleration of process calculated using the formula  $b = \frac{\Delta d_{\text{InP+Bi}_2(\text{SO}_4)_3}}{\Delta d_{\text{InP}}}$ ,

the highest effectiveness of the action of the chemostimulator modifier (1.50–1.76 times) occurs at 525 and 550 °C during the first 20 min of the process. With an increase in the oxidation time, the relative increase in the film thickness decreases monotonically, which is typical for a determining diffusion-controlled solid-state process. Under these conditions, the studied process was already approaching the oxidation of the reference sample. The maximum acceleration at the highest temperatures was associated with the increased evaporation of the modifier chemostimulator and an increase in its concentration in the gas phase, which is usually observed in similar processes [14].

For the determination of the dependence of the peculiarities of the action of the chemostimulator modifier on the InP thermal oxidation depending on the way it was introduced into a system, at the next stage InP was thermally oxidized in the presence of  $\text{Bi}_2(\text{SO}_4)_3$  introduced through the aerosol phase, similarly to [11] forming  $\text{Bi}_2(\text{SO}_4)_3/\text{InP}$  heterostructures. Analysis of kinetics of the process (Fig. 5, Table 1) shows the dependence of the revealed patterns on the way chemostimulator-modifier was introduced into the system.

For  $\text{Bi}_2(\text{SO}_4)_3/\text{InP}$  heterostructures very low values  $n$  ( $n_{\text{av}} = 0.09$ ) indicate that diffusion was so significantly decreased that the film thickness remains virtually unchanged. Formally, we can assume that and in this case, the solid-state reaction limited by diffusion in the solid phase was determining, however, a very high EAE value of 459 kJ/mol, indicated a significant contribution of bismuth diffusion into the substrate, which is typical for some chemically stimulated processes with a limited source [12]. Moreover, a value many times higher than the EAE of the intrinsic oxidation of indium phosphide and thermal oxidation of InP in the presence of a chemostimulator modifier  $\text{Bi}_2(\text{SO}_4)_3$  introduced into the system through the gas phase, indicated that the process was constrained in this temperature range. However, it should be noted, that this value is still estimative and preliminary, since it was determined only based on three points. The values of the acceleration process in comparison with the standard were

approximately the same as in the previous case, with the same dynamics of change.

The Auger distribution profiles of components in films synthesized by InP thermal oxidation under the influence of bismuth (III) sulphate introduced through the gas phase in the mode of 500 °C, 60 min (Fig. 6a), showed the presence of bismuth in an amount of about 25 at % over the entire depth of the film. For films synthesized by thermal oxidation of InP under the influence of  $\text{Bi}_2(\text{SO}_4)_3$  introduced through the aerosol phase at 525 °C, 60 min (Fig. 6b), the bismuth content after 5 min of etching was 20 at%. The bismuth content in the film decreased with increasing etching time.

The surface of films formed by thermal oxidation of InP under the influence of  $\text{Bi}_2(\text{SO}_4)_3$ , introduced through the gas and aerosol phases was depleted in the volatile component (phosphorus), however, a second component of the substrate (indium) was present in the surface layer. This confirms the well-known fact of partial evaporation of  $\text{P}_2\text{O}_5$  during the growth of films, the slow formation (although, it was accelerated by a chemostimulator-modifier) of a phosphate skeleton and a high content of  $\text{In}_2\text{O}_3$  in films corresponding to non-strong oxidation conditions [12, 20, 21]. In films synthesized by thermal oxidation of InP under the influence of  $\text{Bi}_2(\text{SO}_4)_3$  introduced through the gas phase (see Fig. 6a), after 20 min of etching, the almost complete disappearance of oxygen and sulphur and a noticeable increase in the phosphorus content was revealed. However, the amount of bismuth remained quite high, which was largely determined

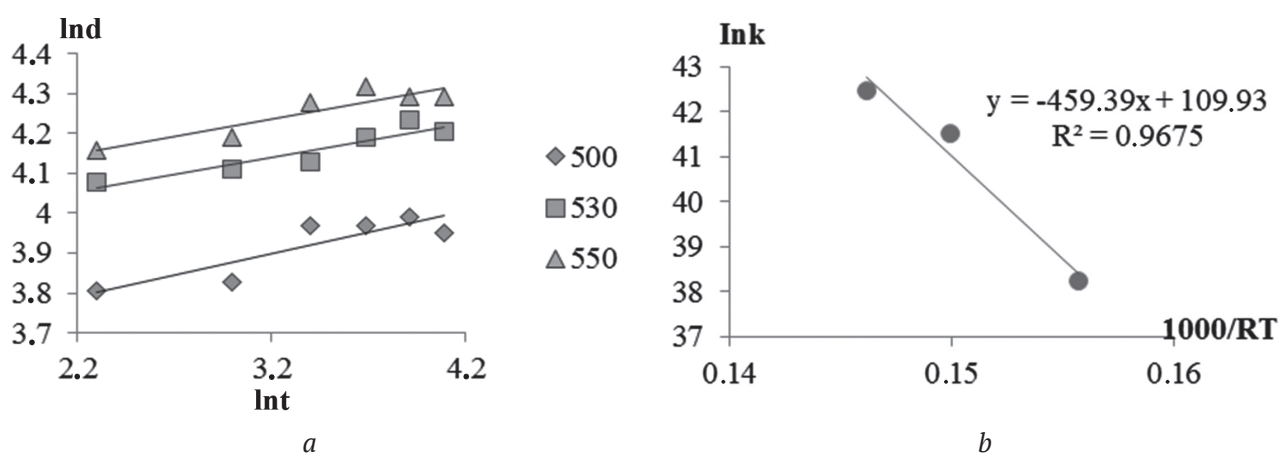
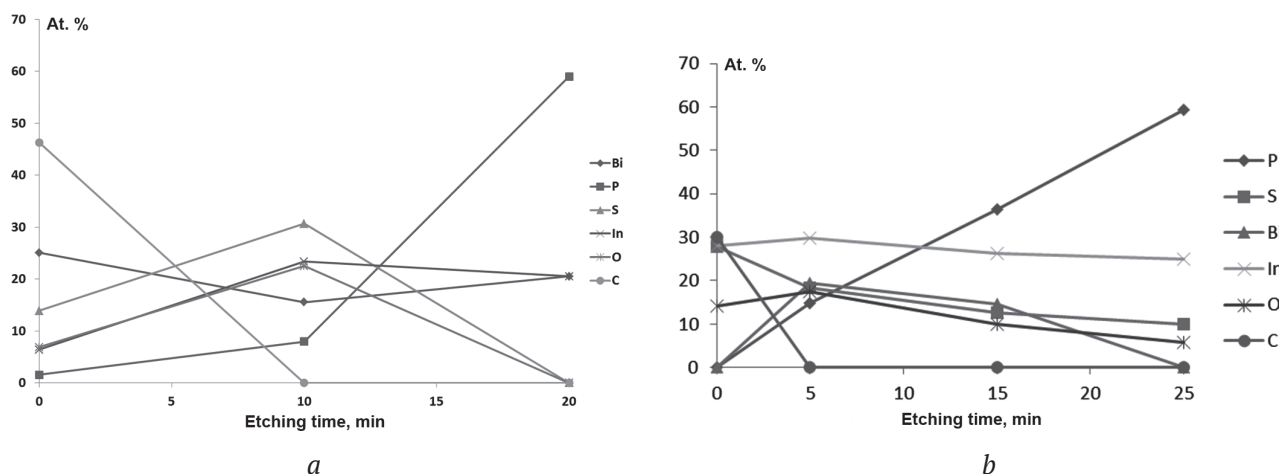


Fig. 5. Log plots of kinetic isotherms (a) and Arrhenius plot of the kinetic constant  $\ln k_{\text{av}} = f(10^5/RT)$  (b) of the process of thermal oxidation of  $\text{Bi}_2(\text{SO}_4)_3/\text{InP}$  heterostructures



**Fig. 6.** Auger profile of thermal oxidation of InP with the  $\text{Bi}_2(\text{SO}_4)_3$  gas phase (at 500 °C during 60 min.) (a) and thermal oxidation of  $\text{Bi}_2(\text{SO}_4)_3/\text{InP}$  heterostructures (at 525 °C, 60 min) (b)

by the constant replenishment of the concentration of the modifier chemostimulator from an endless source in the absence of evaporation of bismuth-containing fragments, in contrast to sulphur-containing fragments. For films, grown by thermal oxidation of  $\text{Bi}_2(\text{SO}_4)_3/\text{InP}$  heterostructures (see Fig. 6b), after 25 min of etching, a noticeable increase in the phosphorus content was observed, bismuth disappeared almost completely, indicating its consumption without replenishment in the case of the final source of the modifier chemostimulator. The amount of sulphur and oxygen was ~ 10 and 6 at%, respectively. The similarity of the distribution profiles of oxygen and sulphur (see Figs. 6a and 6b) indicates that the indium and phosphorus of the substrate can be coordinated not only with oxygen, but also with sulphur. The possibility of such coordination for InP thermal oxidation processes with deposited sulphide layers, sulphur transit, similar to oxygen transit, was demonstrated by us in [12]. Thus, despite the small chemostimulating effect, probably caused by the strength of the binding of bismuth to the sulphate group and a sharp decrease in its capacity as an oxygen transmitter, the role of  $\text{Bi}_2(\text{SO}_4)_3$  as a modifier was obvious. The films grown by both of the above methods had semiconductor properties ( $\rho \sim 10^6 \text{ Ohm}\cdot\text{cm}$ ), in contrast to intrinsic oxide on InP, which is characterized by ohmic conductivity [12, 21].

From all that has been said it follows that the physicochemical nature of the chemostimulator, its ability to transit interactions, and the

renewability of oxide forms play dominant roles. From this point of view, both  $\text{SnO}_2$  and  $\text{Bi}_2(\text{SO}_4)_3$ , being modifiers of the composition and properties of the films, practically do not possess a chemostimulating effect, or the effect was noticeable, but was not very significant. The value of the acceleration of the process compared to the intrinsic oxidation did not even reach two times.

From the point of view of achieving a significant chemostimulating effect while simultaneously modifying the composition and properties of the synthesized films, the use of combinations of oxides with the possibility of synergistic effects was effective. For experimental verification of this position, a composition of 40 %  $\text{Co}_3\text{O}_4$ +60 %  $\text{MnO}_2$  was chosen and magnetronically (see Experimental) deposited on the surface of InP. In terms of its qualitative composition, the sprayed layer corresponded to the specified one (XRD, Fig. 7).

The course of oxidation isotherms of (40 %  $\text{Co}_3\text{O}_4$ +60 %  $\text{MnO}_2$ )/InP heterostructures in the temperature range from 490 to 570 °C is shown in Fig. 8.

The results of processing kinetic data of the oxidation process of heterostructures (40 %  $\text{Co}_3\text{O}_4$ +60 %  $\text{MnO}_2$ )/InP using the formal kinetic equation [15] are presented in Table 1. From the table it follows that  $n_{\text{av}}$  was 0.27, and the EAE was 50 kJ/mol, which was much lower than the EAE of the “reference” systems ( $\text{Co}_3\text{O}_4/\text{InP}$  – 103 kJ/mol,  $\text{MnO}_2/\text{InP}$  – 180 kJ/mol, native InP oxidation was

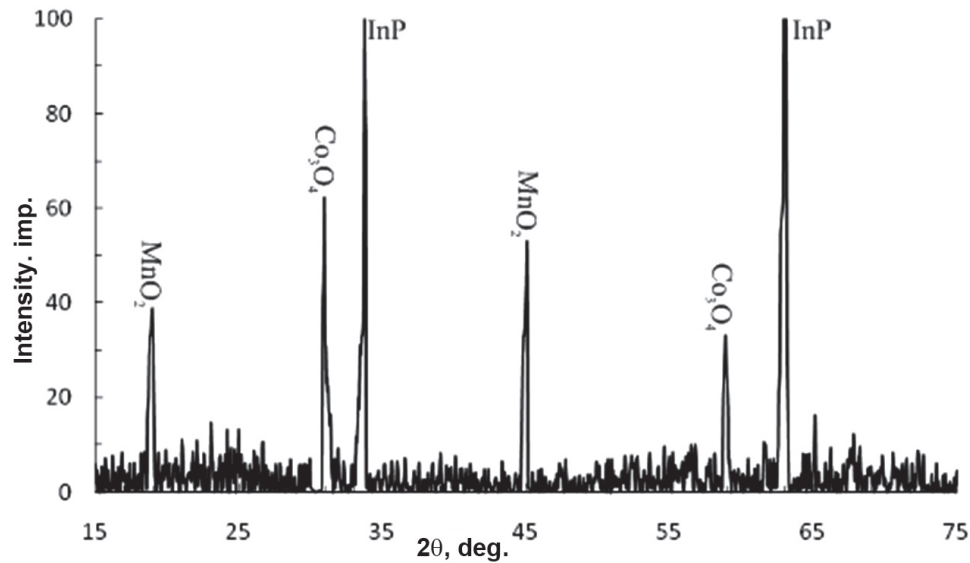


Fig. 7. X-ray diffraction pattern of (40 %  $\text{Co}_3\text{O}_4$ +60 %  $\text{MnO}_2$ )/InP heterostructure without thermal oxidation

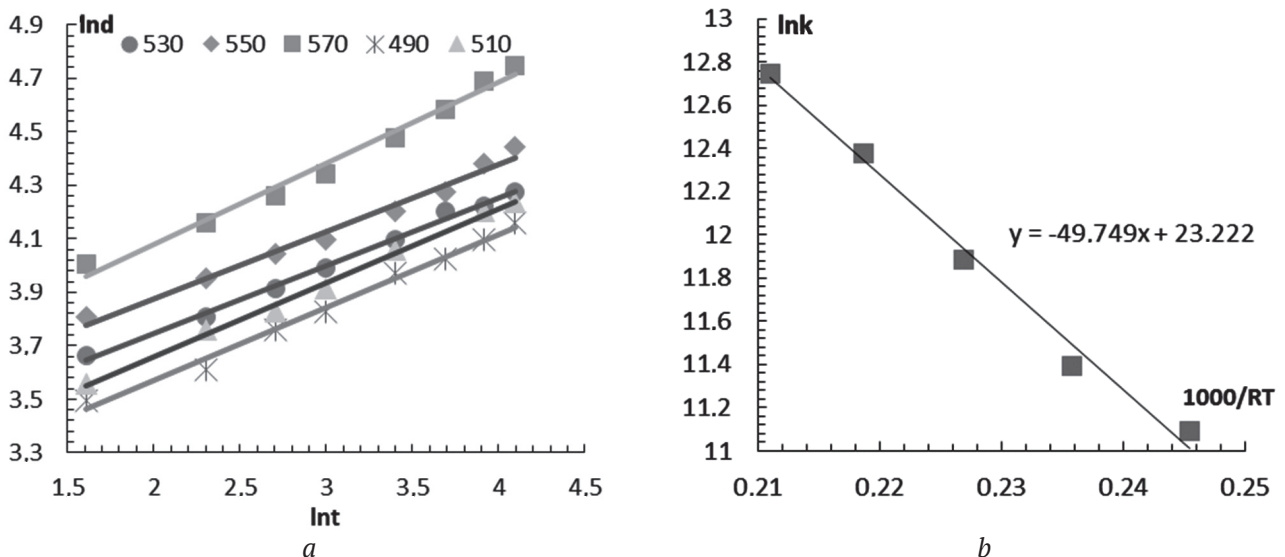


Fig. 8. Log plots of kinetic isotherms (a) and Arrhenius plot of the kinetic constant  $\ln k_{av} = f(10^5/RT)$  (b) of the process of thermal oxidation of (40 %  $\text{Co}_3\text{O}_4$ +60 %  $\text{MnO}_2$ )/InP at 490-570 °C (a)

170 kJ/mol). The determining solid-phase stage was limited by diffusion in the solid phase, but the mechanism of action of the selected complex chemostimulator was close to the catalytic and close to that for  $\text{V}_2\text{O}_5$ /InP heterostructures [12].

The thickness of the formed oxide films turned out to be much higher than expected under the assumption of an independent parallel effect of  $\text{Co}_3\text{O}_4$  and  $\text{MnO}_2$  on the thermal oxidation of InP, which proves the synergy of the combined effects of the chemostimulators of the applied composition.

The relative increase in film thickness compared to intrinsic oxide on indium phosphide

for  $\text{MnO}_2$ /InP,  $\text{Co}_3\text{O}_4$ /InP and (40 %  $\text{Co}_3\text{O}_4$ +60 %  $\text{MnO}_2$ )/InP heterostructures, calculated using

$$b = \frac{\Delta d_{\text{Me}_x\text{O}_y/\text{InP}} - \Delta d_{\text{InP}}}{\Delta d_{\text{InP}}} \cdot 100\%, \quad [13]$$

gradually increased to 60 min, its maximum value was 70 %. Data allowing evaluating the effectiveness of the composition in comparison with individual oxides are shown in Table 3.

$\text{MnO}_2$ /InP heterostructures were characterized by the maximum value of the relative increase in film thickness at the initial stage of the process, in the first 10 min. For  $\text{Co}_3\text{O}_4$ /InP heterostructures the maximum relative increase in film thickness was observed at 30 min. It must be emphasized

**Table 3.** The values of the relative change of the film thickness formed in the process of thermal oxidation of MnO<sub>2</sub>/InP, Co<sub>3</sub>O<sub>4</sub>/InP and (40 % Co<sub>3</sub>O<sub>4</sub>+60 % MnO<sub>2</sub>)/InP in comparison with the thermal oxidation of InP

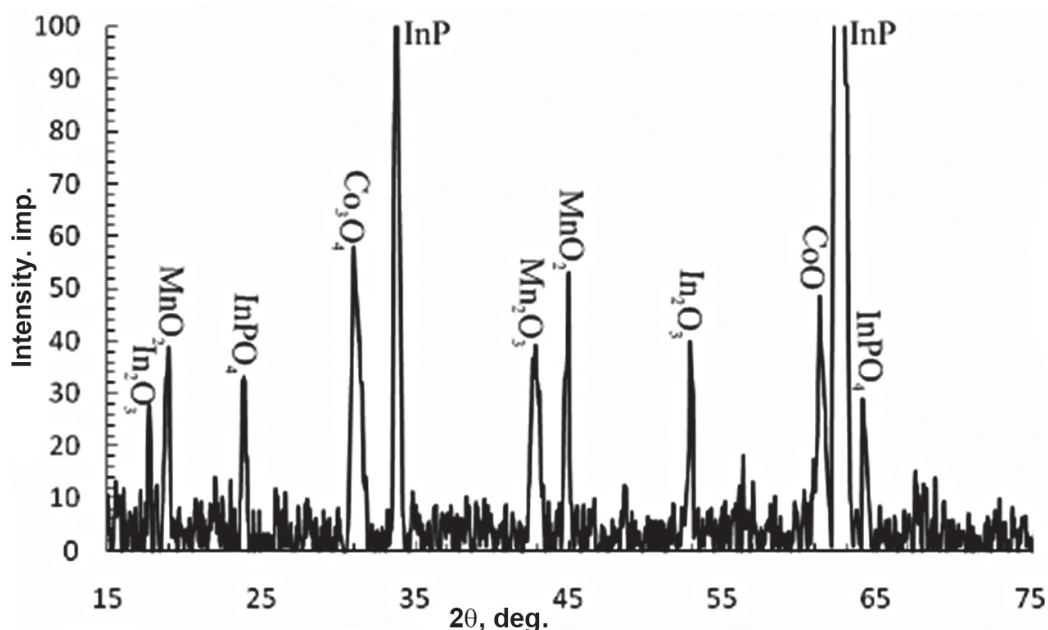
Heterostructure	T, °C	The values of the relative change of the film thickness formed in the process of thermal oxidation, %					
		10, min	20, min	30, min	40, min	50, min	60, min
MnO <sub>2</sub> /InP	530	67	60	56	25	17	11
Co <sub>3</sub> O <sub>4</sub> /InP		37	42	61	50	47	30
(40 % Co <sub>3</sub> O <sub>4</sub> +60 % MnO <sub>2</sub> )/InP		50	25	31	43	56	70

that for the transit mechanism of chemically stimulated oxidation of A<sup>III</sup>B<sup>V</sup> the values of the relative increase in the film thickness decreased during the developed stage of the process passing through the maximum. The relative increase in film thickness during the thermal oxidation of (40 % Co<sub>3</sub>O<sub>4</sub>+60 % MnO<sub>2</sub>)/InP heterostructures had a different dynamics, which, in addition to the low EAE, indicates the large contribution of the catalytic component to transit, e.g. the transit-catalytic mechanism of the process.

According to XRD data, films formed by the oxidation of (40 % Co<sub>3</sub>O<sub>4</sub>+60 % MnO<sub>2</sub>)/InP heterostructures, contained cobalt oxides Co<sub>3</sub>O<sub>4</sub> and CoO, manganese oxides in various oxidation states (MnO<sub>2</sub>; Mn<sub>2</sub>O<sub>3</sub>), In<sub>2</sub>O<sub>3</sub> and InPO<sub>4</sub> (Fig. 9).

From these data it follows that, in addition to chemostimulation, which is reflected in the increase in the rate of film formation (see Table

3), a modification was made by changing their composition. This modification, first, achieved a very low content of unoxidised indium in the films of ~ 0.5 %, according to spectral ellipsometry, while the volume fraction of inclusions of unoxidised indium in films did not exceed 1 %. This means that the intrinsic films on InP, possessing ohmic conductivity, were replaced by semiconductor ones, which is consistent with our previously obtained data [15]. Secondly, there is the possibility to control of the contribution of the catalytic component into the process mechanism and fine adjustment of the properties of semiconductor films by changing the composition of the deposited oxides and taking into account the synergism of their combined effect. Such control is necessary, for example, for target regulation of their sensory response [22]. Third, the additional introduction of an anion



**Fig. 9.** X-ray diffraction pattern of (40 % Co<sub>3</sub>O<sub>4</sub>+60 % MnO<sub>2</sub>)/InP after thermal oxidation at 530 °C over 60 min

former modifier associated with an effective chemostimulator (for example, manganese or cobalt phosphates, or both) to this system will ensure, as we showed in [14], a transition to high-quality dielectric films characterized by high growth rate and acceptable, fairly smooth, surface morphology.

#### 4. Conclusion

Thus, in this study, the fundamental role of the physicochemical nature of the chemostimulator, its ability to transit interaction and the renewability of oxide forms in the process of InP thermal oxidation was established. The introduction of modifying phosphate groups from  $\text{AlPO}_4$  in the thermal oxide films, together with the deposition of  $\text{SnO}_2$  on the surface of without it, led to the resistance of the films, similar to that for the oxidation of  $\text{SnO}_2/\text{InP}$  heterostructures, without additional administration of phosphates. The sophisticated chemostimulator modifier  $\text{Bi}_2(\text{SO}_4)_3$  introduced in the oxidation process both through the gas phase and onto the InP surface, being a modifier of the composition and properties of the films, did not possess a significant chemostimulating effect, which is explained by the limited capabilities of the cation former as a transmitter. The complex 40 %  $\text{Co}_3\text{O}_4$  + 60 %  $\text{MnO}_2$  chemostimulator deposited on the InP surface, determining the accelerated formation of films in comparison with intrinsic oxidation by the transition-catalytic mechanism was the most effective out of the studied chemostimulators. This chemostimulator was the part of the synthesized films, capable of purposefully modifying their properties by varying the content of components in it.

#### Acknowledgements

The research results were partially obtained were obtained using the equipment of Shared Scientific Equipment Centre of Voronezh State University. URL: <http://ckp.vsu.ru>

#### Conflict of interests

The authors declare that they have no known competing financial interests or personal relationships that could have influenced the work reported in this paper.

#### References

1. Lutz J., Schlangenotto H., Scheuermann U., De Doncker R. *Semiconductor Power Devices. Physics, Characteristics, Reliability*. Springer-Verlag Berlin Heidelberg; 2018. 714 p. DOI: <https://doi.org/10.1007/978-3-319-70917-8>
2. Mikhailova M. P., Moiseev K. D., Yakovlev Y. P. Discovery of III–V semiconductors: Physical properties and application semiconductors. *Semiconductors*. 2019;53(3): 273–290. DOI: <https://doi.org/10.1134/S1063782619030126>
3. Sychikova Ya. A. *Nanorazmernye struktury na poverhnosti fosfida indiya* [Nanoscale structures on the surface of indium phosphide]. LAP Lambert Academic Publishing; 2014. 127 p. (In Russ.)
4. Chistokhin I. B., Zhuravlev K. S. SVCH-fotodetektory dlya analogovoi optovolokonnoi svyazi [Microwave photodetectors for analog fiber optic communications]. *Uspekhi prikladnoj fiziki*. [Advances in Applied Physics]. 2015;3(1): 85–94. Available at: <https://elibrary.ru/item.asp?id=22968188> (In Russ.)
5. Arbiol J., Xiong Q. *Semiconductor Nanowires: Materials, Synthesis, Characterization and Applications*. Elsevier Ltd; 2015. 554 p.
6. Eichler H. J., Eichler J., Lux O. *Semiconductor lasers*. In: *Lasers. Springer Series in Optical Sciences*. Vol. 220. Springer, Cham.; 2018. p. 165–203. DOI: [https://doi.org/10.1007/978-3-319-99895-4\\_10](https://doi.org/10.1007/978-3-319-99895-4_10)
7. Kabanov V. F., Pereverzev Y. E., Hassoon O. A., Glukhovskoy E. G. Study properties of monolayers with quantum dots of semiconductors  $\text{A}_2\text{B}_6$  and  $\text{A}_3\text{B}_5$ . *Materials Today: Proceedings*. 2018;5(5): 13735–13738. DOI: <https://doi.org/10.1016/j.matpr.2018.02.012>
8. Nikolaev Yu. A., Rud' Yu. V., Terukov E. I., Rud' V. Yu. Photosensitivity of heterojunctions obtained using thermal oxidation of indium phosphide. *Technical Physics Letters*. 2007;33(4): 313–315. DOI: <https://doi.org/10.1134/S1063785007040128>
9. Punkkinen M. P. J., Laukkanen P., Leng J., Kuzmin M., Tuominen M., Tuominen V., Dahl J., Pessa M., Guina M., Kokko K., Sadowski J., Johansson B., Väyrynen I. J., Vitos L. Oxidized In-containing III–V(100) surfaces: formation of crystalline oxide films and semiconductor-oxide interfaces. *Physical Review B*. 2011;83: 195329. DOI: <https://doi.org/10.1103/PhysRevB.83.195329>
10. Nelson A., Geib K., Wilmsen W. C. Composition and structure of thermal oxides of indium phosphide. *Journal of Applied Physics*. 1983; 54(7): 4134–4140. DOI: <https://doi.org/10.1063/1.332547>
11. Tomina E. V., Mittova I. Ya., Sladkopezhev B. V., Kostryukov V. F., Samsonov A. A., Tretyakov N. N. Thermal oxidation as a method of formation of nanoscale functional films on  $\text{A}^{\text{III}}\text{B}^{\text{V}}$  semiconductors: influence of deposited oxide metal layers. Overview. *Kondensirovannyye sredy i mezhfaznyye granitsy* =

*Condensed Matter and Interphases*. 2018; 20(2): 184–203. DOI: <https://doi.org/10.17308/kcmf.2018.20/472> (In Russ., abstract in Eng.)

12. Mittova I. Ya. Influence of physical-chemical nature of chemostimulator, method and method of its introduction into system on mechanism of thermal oxidation of GaAs and InP. *Inorganic Materials*. 2014;50(9): 874–881. DOI: <https://doi.org/10.1134/S0020168514090088>

13. Sladkoptsev B. V., Lapenko A. A., Samsonov A. A., Tomina E. V., Mittova I. Ya. Transit and catalytic oxidation of semiconductors A<sup>III</sup>B<sup>V</sup> with deposited nanoscale layers of cobalt and vanadium oxides of different thicknesses. *Kondensirovannye sredy i mezhfaznye granitsy = Condensed Matter and Interphases*. 2010;12(3): 268–275. Available at: <https://journals.vsu.ru/kcmf/article/view/1124/1206> (In Russ.)

14. Mittova I. Ya., Sladkoptsev B. V., Samsonov A. A., Tomina E. V., Andreenko S. Y., Kostenko P. V. Growth and properties of nanofilms produced by the thermal oxidation of MnO<sub>2</sub>/InP under the effect of Mn<sub>3</sub>(PO<sub>4</sub>)<sub>2</sub>. *Inorganic Materials*. 2019;55(9): 915–919. DOI: <https://doi.org/10.1134/S0020168519090073>

15. Tretiakov N. N., Mittova I. Ya., Sladkoptsev B. V., Samsonov A. A., Andreenko S. U. Effect of magnetron sprayed layer of MnO<sub>2</sub> on InP thermal oxidation kinetics, composition and morphology of synthesized films. *Inorganic Materials*. 2017;53(1): 65–71. DOI: <https://doi.org/10.1134/S0020168517010174>

16. Mittova I. Ya., Kostryukov V. F., Ilyasova N. A., Sladkoptsev B. V., Samsonov A. A. Modification of nanoscale thermal oxide films formed on indium phosphide under the influence of tin dioxide. *Nanosystems: Physics, Chemistry, Mathematics*. 2020;11(1): 110–116. DOI: <https://doi.org/10.17586/2220-8054-2020-11-1-110-116>

17. Tretyakov Yu. D. *Neorganicheskaya himiya* [Inorganic Chemistry]. Moscow: Academy, 2007, 352 p. (In Russ.)

18. Mittova I. Ya., Lavrushina S. S., Pinyaeva O. A., Lopatin S. I., Tibilova E. K. GaAs thermal oxidation in the presence of titanium sulfate. *Russian Journal of Inorganic Chemistry*. 2005;50(5): 685–688.

19. *Atlas IK spektrov ortofosfatov* [Atlas of IR spectrums of ortho-phosphates]. Moscow: Nauka Publ.; 1985. 235 p. (In Russ.)

20. Hollinger G., Hughes G., Himpfel F. J., Jordan J. L., Morar J. F. Early stages in the formation of the oxide-InP (100) interface. *Surface Science*. 1986;168: 617–625. DOI: [https://doi.org/10.1016/0039-6028\(86\)90892-7](https://doi.org/10.1016/0039-6028(86)90892-7)

21. Wilmsen C. W., Kee R. W. The improvement of grown oxides for the surface protection of A<sup>III</sup>B<sup>V</sup> compounds. *Thin Solid Films*. 1978;51(1): 93–98. DOI: [https://doi.org/10.1016/0040-6090\(78\)90217-1](https://doi.org/10.1016/0040-6090(78)90217-1)

22. Kostryukov V. F., Mittova I. Ya., Sladkoptsev B. V., Parshina A. S., Balasheva D. S. The role of BiPO<sub>4</sub> introduced through the gas phase in the process of creating thin films on the surface of InP. *Kondensirovannye sredy i mezhfaznye granitsy = Condensed Matter and Interphases*. 2019;21(2): 215–224. Available at: <https://journals.vsu.ru/kcmf/article/view/759> DOI: <https://doi.org/10.17308/kcmf.2019.21/759> (In Russ., abstract in Eng.)

### Information about the authors

*Irina Ya. Mittova*, DSc in Chemistry, Professor, Professor of Department of Materials Science and Industry of Nanosystems, Voronezh State University, Voronezh, Russian Federation; e-mail: [imittova@mail.ru](mailto:imittova@mail.ru). ORCID iD: <https://orcid.org/0000-0001-6919-1683>.

*Boris V. Sladkoptsev*, PhD in Chemistry, Associate Professor of Department of Materials Science and Industry of Nanosystems, Voronezh State University, Voronezh, Russian Federation; e-mail: [dp-kmins@yandex.ru](mailto:dp-kmins@yandex.ru). ORCID iD: <https://orcid.org/0000-0002-0372-1941>.

*Natalya A. Ilyasova*, MSc student of the Department of Materials Science and Industry of Nanosystems, Voronezh State University, Voronezh, Russian Federation; e-mail: [Ilyasova\\_1997@mail.ru](mailto:Ilyasova_1997@mail.ru).

*Elena V. Tomina*, DSc in Chemistry, Associate Professor, Associate Professor of Department of Materials Science and Industry of Nanosystems, Voronezh State University, Voronezh, Russian Federation; e-mail: [tomina-ev@yandex.ru](mailto:tomina-ev@yandex.ru). ORCID iD: <https://orcid.org/0000-0002-5222-0756>.

*Aleksey I. Dontsov*, PhD in Physics and Mathematics, Associate Professor of the Department of Materials Science and Industry of Nanosystems, Voronezh State University, Associate Professor of the Department of Physics, Voronezh State Technical University, Voronezh, Russian Federation; e-mail: [dontalex@mail.ru](mailto:dontalex@mail.ru). ORCID iD 0000-0002-3645-1626.

*Olga S. Tarasova*, MSc student of the Department of Materials Science and Industry of Nanosystems, Voronezh State University, Voronezh, Russian Federation; e-mail: [tarasova\\_os96@mail.ru](mailto:tarasova_os96@mail.ru). ORCID iD 0000-0003-1619-8755.

All authors have read and approved the final manuscript.

*Translated by Valentina Mittova*  
*Edited and proofread by Simon Cox*



# Condensed Matter and Interphases (Kondensirovannye sredy i mezhfaznye granitsy)

## Original articles

DOI: <https://doi.org/10.17308/kcmf.2020.22/2852>

Received 10 April 2020 eISSN

Accepted 15 May 2020

Published online 25 June 2020

ISSN 1606-867X

2687-0711

## Glauconite-Based Sorbents for Skimming Oil and Oil Products

© 2020 Yu. S. Peregudov, R. Mejri, E. M. Gorbunova, S. I. Niftaliev

Voronezh State University of Engineering Technologies,  
19 Revolyutsii prospect, Voronezh 394036, Russian Federation

### Abstract

Natural glauconite-based sorbents were obtained for skimming oil and oil products from different surfaces. Glauconite is an aluminosilicate mineral and is widely used for cleaning various pollutants from water and soil. The classification allowed selecting a glauconite fraction with a particle size of 0.045-0.1 mm, which is the most effective for the sorption of oil products. For this, the sorbent was thermally activated and modified using organic compounds. The glauconite samples were thermally treated at temperatures of 100, 600, and 1000 °C. To provide glauconite with hydrophobic properties, it was modified with stearic acid.

When the sorbents came into contact with water (duration 92 hours), it was found that with the mass fraction of stearic acid of 5 wt% the lowest weight loss was observed in all the three samples. The contact angle of wetting for sorbents is greater than 90°, which led to a change in the state of its surface. The obtained samples were not wetted with water and could remain on its surface for a long time. The interaction of oil and a hydrophobic sorbent showed that after seven minutes the particles of the sorbent penetrated the oil that also has a hydrophobic surface and can sorb a surfactant applied on the sorbent, which indicates the affinity of stearic acid to oil. A granular sorbent, thermally activated at a temperature of 1000 °C and modified with a cellulose-containing component, sorbed the oil for 2 minutes. The use of this modifier increased the sorbent porosity, which affected the sorption rate.

**Keywords:** glauconite, sorbent modification methods, hydrophobicity, oil spill clean-up.

**For citation:** Peregudov Yu. S., Mejri R., Gorbunova E. M., Niftaliev S. I. Glauconite-Based Sorbents for Skimming Oil and Oil Products. *Kondensirovannye sredy i mezhfaznye granitsy = Condensed Matter and Interphases*. 2020; 22(2): 257–265. DOI: <https://doi.org/10.17308/kcmf.2020.22/2852>.

### 1. Introduction

Oil production, transportation, and refining are sometimes accompanied by emergency situations. To eliminate the spills of oil products on water or soil, natural sorbents (mineral and organic), as well as waste from various industries and waste composition are used [1–4].

A sawdust-based sorbent was treated with ethanol, sodium hydroxide, and hydrochloric acid to increase the efficiency of oil absorption. It was shown that the treated sawdust had a higher sorption capacity, even after 90 minutes of sorption with four-fold recurrence [5].

✉ Sabukhi I. Niftaliev, e-mail: [sabukhi@gmail.com](mailto:sabukhi@gmail.com)

The effectiveness of wetting and sorption of oil by natural fibres (kapok, cattail, cotton), which possess natural hydrophobicity and oleophilicity, was evaluated and compared. Water on the surface of the fibres forms contact angles of wetting between 120 and 145°. A drop of oil was quickly absorbed by the surface of the fibres within several seconds. Kapok fibre has the highest sorption and oil retention ability as compared with other samples [6].

Artificial organic sorbents based on glycerol propoxylate were obtained for oil sorption by volume polymerisation method with various amounts of a cross-linking agent. The synthesised gels were used as absorbents



The content is available under Creative Commons Attribution 4.0 License.



for various organic solvents, petroleum, and oils [7].

A sorbent with high hydrophobic and oleophilic properties for the separation of oil-water mixtures and oil-water emulsions was obtained based on kapoka fibre with a ZnO nano-needle coating. For this, a one-stage hydrothermal method followed by hydrophobic modification with dodecylalcohol was used [8].

An effective sorbent with high oil sorption was obtained by the inclusion of crushed rice straw into a polyurethane matrix. The oil absorption rate was high in the first 15–30 minutes, then it decreased, and a complete saturation of the sorbent was observed after 2 hours [9].

Sorbents based on natural minerals are widely used in sorption technologies, for example, samples with high mesoporosity (oxides of silicon, aluminium, zirconium, carbon materials, aluminosilicates) are recommended for clean-up of oil spills on land [10]. Capillary condensation is observed in materials with pores of this size (2–50 nm).

Good sorption results for petroleum products are typical for diatomites, sepiolite, and zeolites obtained from ash. Adsorption of petroleum substances on the porous surface of such minerals proceeds according to the capillary mechanism associated with the filling of existing pores and the formation of a layer of oil products on the outer surface of the adsorbent particles. Oil substances cannot penetrate into narrow micropores of the mineral; there is a correlation between the viscosity and density of the oil: viscous and thick oils were adsorbed by the same material in larger amounts than light oils.

Hydrophobic silica aerogels, zeolites, organoclays, and other natural minerals demonstrated high oil absorption [11].

The modification of silica clay results in the increase of hydrophobicity, specific surface area, and porosity of the sorbent, as well as its ability to absorb oil. It was established that the modified silicate clay is a highly effective sorbent with respect to emulsified oil products. The optimal sorption parameters were determined that allow achieving a degree of oily wastewater treatment of more than 99 % [12].

A group of sorbents based on cellulose-containing materials is also of interest [13–15].

A new physicochemical method for obtaining a sorbent based on cellulose was proposed that includes foaming, plasma treatment, and modification with a hydrophobic agent [15].

Aerogels based on nanocellulose can be obtained that combine such properties as high porosity, large surface area, low density, high sorption, biodegradability, and easy surface modification [16].

A sorbent in the form of a hydrophobic nanostructured aerogel was obtained based on cotton cellulose, which had high oil absorption and retention ability, excellent selectivity with respect to oil and water, good mechanical strength, and recycling ability [17].

Using biological delignification, cellulose was extracted from raw rice husk and acetylated to make it hydrophobic. The obtained sorbents showed a high oil absorption rate, and saturation capacity was achieved after 5 minutes of contact with oil [18].

Nanofibrillation and hydrophobic modification of spent cellulose fibres allowed obtaining nanofibre sponges with ultra-low density and high porosity. They demonstrated excellent absorption characteristics for various oils and organic solvents and can be reused multiple times. Nanofibre aerogels showed selectivity in the absorption of marine diesel fuel from a water-oil mixture [19].

Hydrophobic sponge materials, in particular melamine sponges, can be used as potential oil sorbents [20, 21, 22]. Fluorinated kaolin was used to transfer the sponge from a hydrophilic to a hydrophobic state, which increased the adsorption capacity for various oils and organic solvents [20]. Hydrophobic sponges based on commercial melamine sponges can also be obtained through the adsorption of silica nanoparticles and coating silanization [21] or by N-acylation with fatty acid derivatives [22].

It seems relevant to use glauconite, a widespread natural eco-friendly aluminosilicate, as a sorbent of oil products. Its important property is the ability to improve sorption properties as a result of applying various activation and modification methods.

Almost all sorbents based on natural minerals are hydrophilic; therefore, to reduce water absorption and wettability of the mineral sorbent

surface, they are modified with hydrophobic agents [23, 24, 25].

A hydrophobic modification of the sodium alginate foam was obtained by simple freeze-drying and subsequent cross-linking with zirconium ions. They showed excellent adsorption capacity for various oils and organic solvents [26].

When treating vermiculite, an aluminosilicate mineral, with a hydrophobic agent, a sorbent was obtained that has high water resistance values and can remain on water surface for a long time. The immobilisation of bacterial cells of oil degraders of the genus *Pseudomonas* on the surface of a hydrophobic sorbent allows intensifying metabolic processes and achieving a high degree of purifying water from oil products [27].

Various forms of sorbents, including powdered, granular, briquetted, fibrous, canvas, etc., are used for oil sorption [28–32]. It is more convenient to use different types of sorbents for different purposes, such as skimming oil from a water surface, from a solid surface, or for treating wastewater containing oil products. These sorbents should be different in their operational properties.

Sorbent oil-spill booms are used to contain the spread of oil and minimise the effects of oil spills [33].

The reviewed technologies and materials used to create sorbents for oil and oil products are sometimes expensive. In some cases, unsustainable substances are used. Most of the proposed sorbents are combustible and require specific storage conditions. Therefore, developing inexpensive, effective, and eco-friendly sorbent materials for oil and its derivatives remains an important task. This problem can be solved by using natural aluminosilicate mineral materials.

The aim of this work was to obtain powdered hydrophobic and granular oil sorbents based on an eco-friendly mineral glauconite.

## 2. Experimental

The chemical, oxide, and phase compositions of glauconite from the Karinsky deposit in the Chelyabinsk Region are well-known [34]. It was found that the best results for the sorption of oil

products were shown by the glauconite fraction with a particle size of 0.045–0.1 mm. It was chosen as the basis for creating the oil sorbents.

The technique for obtaining hydrophobic sorbents was implemented as follows. The first glauconite sample was heated in an electric furnace at 100 °C, the second and the third ones were heated at 600 and 1000 °C, respectively. They were thermally treated for 2 hours. The second and the third samples were cooled to 90–100 °C. All the three sorbents were transferred to a laboratory mixer and mixed with the added crystalline stearic acid (melting temperature above 69.6 °C). During this process, the glauconite particles were coated with stearic acid. The hydrophobic agent was added in an amount of 2, 3, 4, and 5 wt% to determine the effect of its amount on the buoyancy of sorbents.

The preparation of granular sorbents was different from the hydrophobic ones, as instead of stearic acid, 5 wt% of cellulose-containing component was added at 25 °C and mixed in a mixer. Then, a small amount of distilled water was added to the obtained sorbents and mixed thoroughly. The mixture was extruded through a spinneret with a hole diameter of 3 mm. The obtained granules with a length of 0.5–1.0 mm were dried in air for 24 hours.

The buoyancy of the sorbents was determined as follows. A weighed portion of the sorbent weighing 3 g was placed in a glass with a volume of 50 ml that was half-filled with water. The contact time of the sorbent with water was: series 1 – 6 hours; series 2 – 12 hours; series 3 – 24 hours; series 4 – 36 hours; series 5 – 48 hours; series 6 – 92 hours. After this, the sorbent remaining afloat was removed, dried to a constant mass, and the amount of the drowned sorbent was determined by the difference in the weights.

Oil absorption ( $A$ , %) was calculated by the formula:

$$A = \frac{P_T - P_0}{P_0} \times 100 \%,$$

where  $P_T$  is the weight of the sorbent after its immersion in oil, g;  $P_0$  is the initial weight of the sorbent, g.

### 3. Results and discussion

The results of the study for the buoyancy of the obtained hydrophobic sorbents after 92 hours of contact with water are presented in Fig. 1.

An increase in the fraction of hydrophobic agent contributes to an increase in the buoyancy of sorbents in the following series: glaucanite at  $100\text{ }^\circ\text{C}$  < glaucanite, thermally activated at  $1000\text{ }^\circ\text{C}$  < glaucanite, treated at a temperature of  $600\text{ }^\circ\text{C}$ . The smallest weight loss was observed for all three hydrophobic sorbents with a mass fraction of the hydrophobic agent of 5%. This value of 5% produced the best buoyancy for the sorbent that was thermally activated at  $600\text{ }^\circ\text{C}$ .

Using the *Statistica Neural Networks* programme, a three-dimensional graph of the dependence of the buoyancy of glaucanite-based sorbents on the mass fraction of the hydrophobisator and temperature was constructed (Fig. 2).

It is clear that with an increase in the mass fraction of stearic acid from 2 to 5%, the buoyancy increases. The activation temperature of glaucanite does not greatly affect the buoyancy. When stearic acid is added to glaucanite in an amount of more than 4%, a sorbent with the buoyancy of more than 90% can be obtained in the entire range of burning temperatures.

To determine the hydrophobicity, the sorbents modified with a 5 wt% stearic acid with maximum buoyancy were chosen. When a drop of water is applied to the surface of the obtained sorbents, the liquid does not spread over the surface and retains the shape of a drop (Fig. 3).

The contact angle of wetting is a characteristic of the ability of water to wet a solid surface. The sorbent surface, on which the water forms an obtuse contact angle, is hydrophobic, and the water on such surface is in the form of balls. The images show that the contact angle for all sorbents is greater than  $90^\circ$ . This prevents the interaction of water molecules with the sorbent surface. A change in the state of surface due to the modification with a hydrophobic agent provides sorbents with such new properties as water non-wettability, the ability to remain on the water surface for a long time, and a change in the mechanism of interaction with oil compared to the initial mineral.

The first stage of the study involved testing the interaction of oil with the surface of sorbents. Fig. 4 presents images of the interaction of a hydrophobic sorbent with oil on a solid surface (as exemplified by glaucanite treated at a temperature of  $1000\text{ }^\circ\text{C}$ ).

Hydrophobic powdered sorbents were placed on glass plates, and a drop of oil was applied to them, which did not spread as compared to the initial mineral. After 2 minutes, the shape of the drop of oil changed; it became flat, and after 7 minutes it turned into a film containing a hydrophobic sorbent. Oil particles also have a hydrophobic surface on which they can sorb a surfactant deposited on the sorbent. This indicates the affinity of stearic acid to oil.

The obtained sorbents were tested for the absorption of oil and oil products from a solid

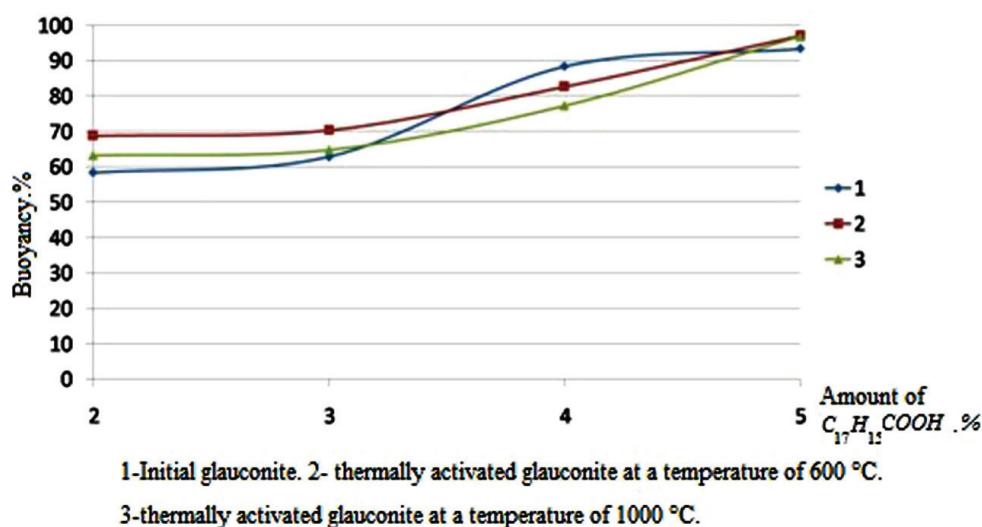
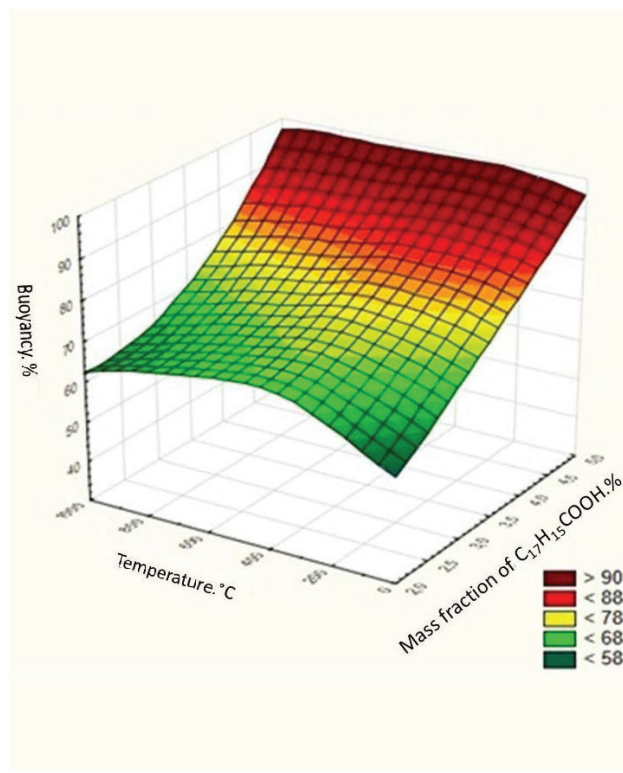


Fig. 1. Buoyancy of glaucanite-based sorbents depending on the mass fraction of water repellent

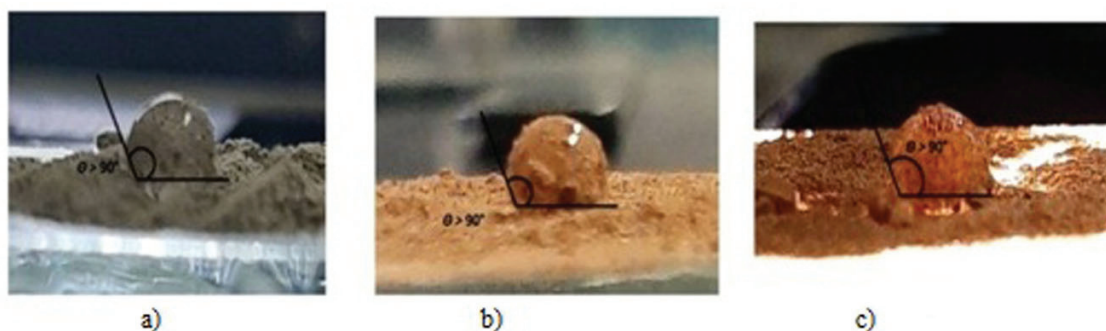
surface. The sorption capacity of powdered sorbents after hydrophobisation decreases by an average of 40 % due to the changes in the state of the glauconite surface. The sorbent pores are sealed with a layer of hydrophobisator, which leads to a decrease in sorption (Fig. 5).

The results of sorption for oil and oil products by granular sorbents are presented in Fig. 6.

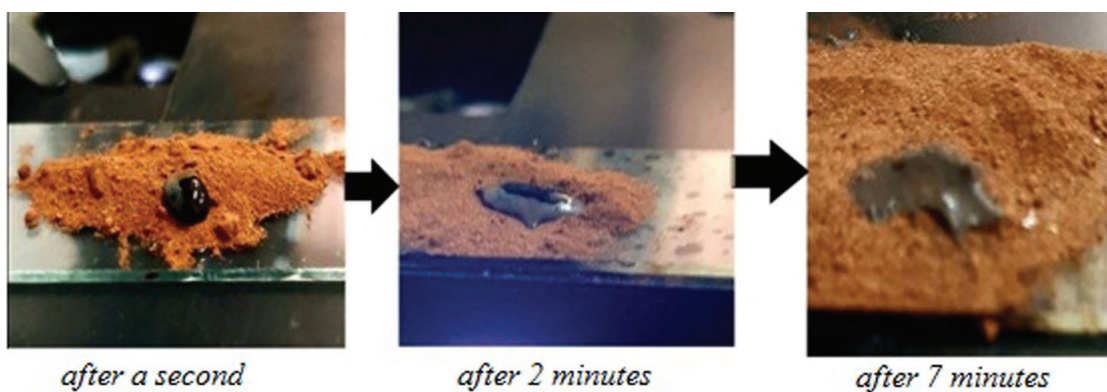
According to the presented diagrams, the modification of glauconite-based sorbents with a cellulose-containing component increases their sorption capacity. For the initial glauconite, the sorption capacity for oil and oil products increases by 1.2–1.3 times, for the glauconite thermally activated at a temperature of 1000 °C by 1.3–1.5 times, and for the glauconite treated at a temperature of 600 °C by 1.0–1.2 times. The best values of sorption for oil and oil products were shown by a sorbent thermally activated at a temperature of 1000 °C. This is due to the fact that the activation results in the formation of a large number of defects on the glauconite surface in the form of pores and cracks [34]. When glauconite is modified, a cellulose-containing component gets into these defects, and it absorbs and retains oil



**Fig. 2.** The response surface of the output parameter (buoyancy) and the contour line of its cross sections depending on the temperature and mass fraction of stearic acid



**Fig. 3.** Images of water wetting of the hydrophobic sorbent surface: a) glauconite at 100 °C; b) glauconite treated at 600 °C; c) glauconite treated at 1000 °C



**Fig. 4.** The interaction of petroleum with a hydrophobic sorbent

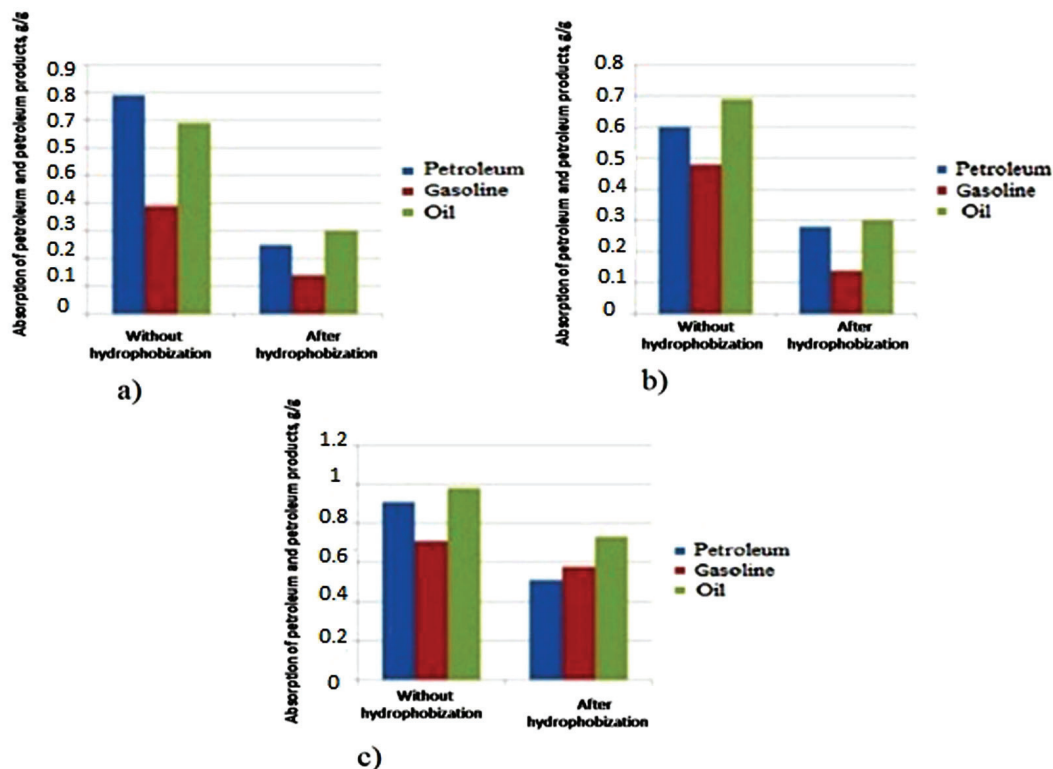


Fig. 5. The effect of a hydrophobic agent on the sorption capacity of sorbents: a) glaucanite at 100 °C; b) glaucanite, thermally activated at a temperature of 600 °C; c) glaucanite, thermally activated at a temperature of 1000 °C

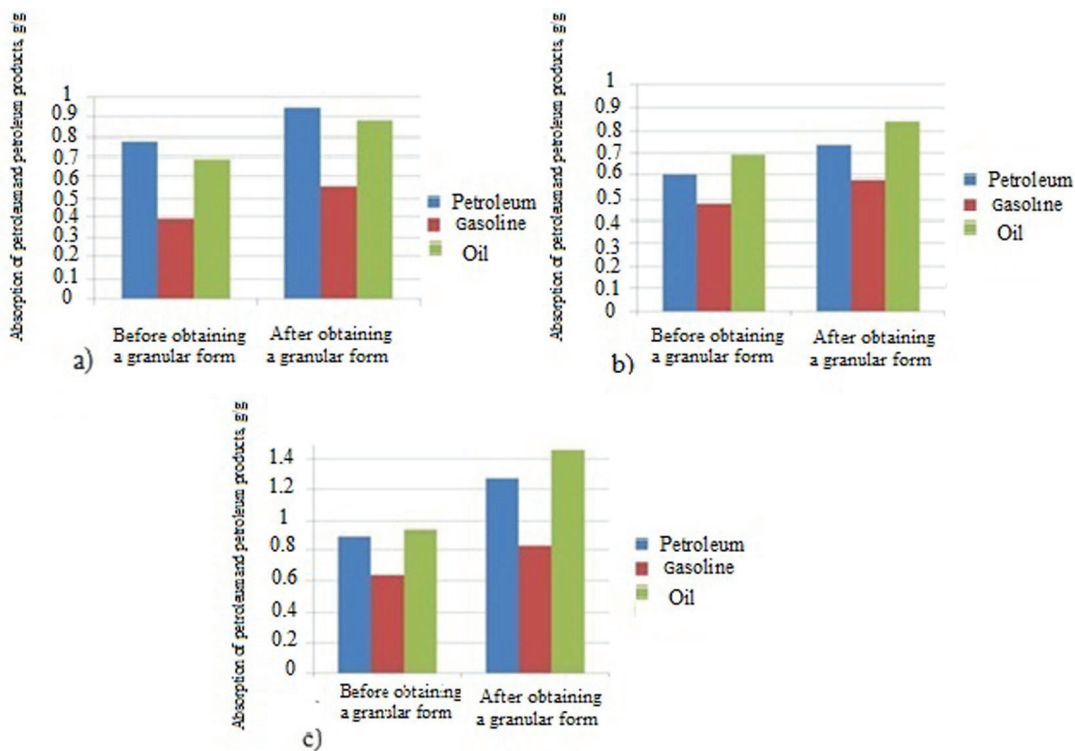


Fig. 6. Absorption of oil and oil products by granular sorbents: a) glaucanite; b) glaucanite, thermally activated at a temperature of 600 °C; c) glaucanite treated at a temperature of 1000 °C

and oil products in a larger amount than other samples.

Let us determine the time of oil absorption by a granular sorbent treated at a temperature of 1000 °C. After applying a drop of oil to the sorbent, it is completely absorbed within 2 minutes with stirring (Fig. 7), while for a hydrophobic sorbent, the interaction time with the oil is 7 minutes.

The studies of the obtained sorbents based on glauconite (hydrophobic powdered and granular) showed a decrease and an increase in the sorption of oil and oil products on a solid surface, respectively. A granular sorbent absorbs oil 3.5 times faster than a hydrophobic one, which indicates different sorption mechanisms. The modification with a cellulose-containing component had a positive effect due to obtaining a more porous structure of the sorbent in comparison with the initial glauconite. Taking into account the short time of oil absorption, it can be used to eliminate oil spills on solid surfaces and for the treatment of oily wastewater.

#### 4. Conclusions

To prepare the sorbents for oil and oil products, a natural eco-friendly mineral was used. A hydrophobic powdered glauconite-based sorbent is characterised by low sorption of oil and oil products, but it can remain on the water surface for a long time and has affinity to oil. While distributing in the oil phase, this sorbent aggregates and thickens it, forming dense conglomerates. This prevents the oil from

spreading and increases its viscosity, which will increase the degree of extraction of the formation-bound oil. Therefore, it can be used to remove oil films from water surfaces.

The granular glauconite sorbent showed its effectiveness as it absorbs oil 3.5 times faster. Timely use of this sorbent in case of emergency spills of oil and its derivatives can minimise hazardous effects on the human environment.

#### Conflict of interests

The authors declare that they have no known competing financial interests or personal relationships that could have influenced the work reported in this paper.

#### References

1. Carmody O., Frost R., Xi Y., Kokot S. Surface characterisation of selected sorbent materials for common hydrocarbon fuels. *Surface Science*. 2007;601: 2066–2076. DOI: <https://doi.org/10.1016/j.susc.2007.03.004>
2. Anh Q. T. Q., Fazylova D. I., Nazirova A. A., Zenitova L. A., Yanov V. V. Polyurethane foam filled with chitosan – sorbent for elimination of oil pollution. *Ecology and Industry of Russia*. 2019;23(5): 37–41. DOI: <https://doi.org/10.18412/1816-0395-2019-5-37-41>
3. Kalinina E. V., Glushankova I. S., Rudakova L. V., Sabirov D. O. Obtaining a modified sorbent based on soda production sludge for liquidation of oil and oil products spills from the water Surface. *Ecology and Industry of Russia*. 2018;22(5): 30–35. DOI: <https://doi.org/10.18412/1816-0395-2018-5-30-35>
4. Domracheva V., Trusova V., Ostapchuk D. Waste water treatment from petroleum products using carbon sorbents and wastes of foam polymers. *Ecology*

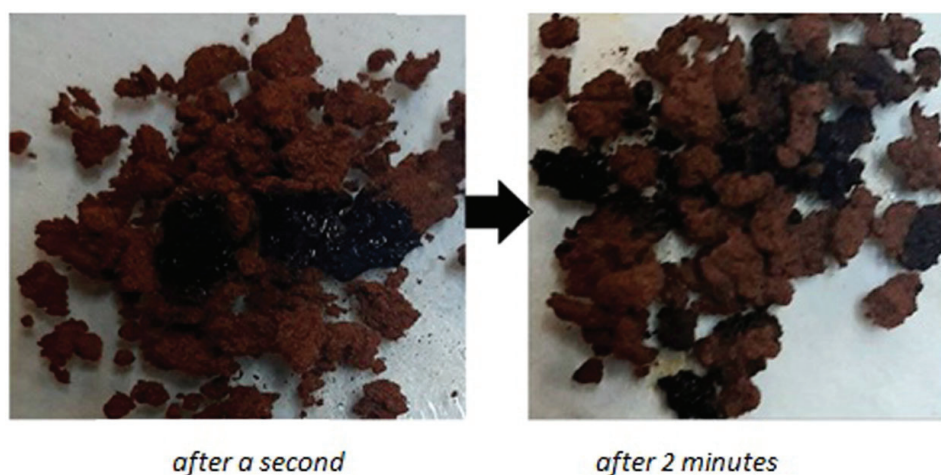


Fig. 7. The interaction of petroleum with a granular sorbent, thermally activated at a temperature of 1000 °C

- and Industry of Russia*. 2017;21(11): 25–29. DOI: <https://doi.org/10.18412/1816-0395-2017-11-25-29>
5. Nurliyana Che Mohamed Hussein S., Hidayati Othman N., Dollah A., Nazihah Che Abdul Rahim A., Shuhadah Japperi N., Syamimi Mohd Asymawi Ramakrishnan N. Study of acid treated mixed sawdust as natural oil sorbent for oil spill. *Materials Today: Proceedings*. 2019;19(4): 1382–1389. DOI: <https://doi.org/10.1016/j.matpr.2019.11.156>
  6. Cao S., Dong T., Xu G., Wang F. Oil spill cleanup by hydrophobic natural fibers. *Journal of Natural Fibers*. 2017;14(5): 727–735. DOI: <https://doi.org/10.1080/15440478.2016.1277820>
  7. Kizil S., Bulbul Sonmez H. Oil loving hydrophobic gels made from glycerol propoxylate: Efficient and reusable sorbents for oil spill clean-up. *Journal of Environmental Management*. 2017;196: 330–339. DOI: <https://doi.org/10.1016/j.jenvman.2017.02.016>
  8. Wang J., Wang A., Wang W. Robustly superhydrophobic/superoleophilic kapok fiber with ZnO nanoneedles coating: Highly efficient separation of oil layer in water and capture of oil droplets in oil-in-water emulsions. *Industrial Crops and Products*. 2017;108: 303–311. DOI: <https://doi.org/10.1016/j.indcrop.2017.06.059>
  9. Hoang P. H., Hoang A. T., Chung N. H., Dien L. Q., Nguyen X. P., Pham X. D. The efficient lignocellulose-based sorbent for oil spill treatment from polyurethane and agricultural residue of Vietnam. *Energy Sources, Part A: Recovery, Utilization, and Environmental Effects*. 2018;40(3): 312–319. DOI: <https://doi.org/10.1080/15567036.2017.1415397>
  10. Bandura L., Wozuk A., Kołodzinska D. Franus W. Application of mineral sorbents for removal of petroleum substances: a review. *Minerals*. 2017;7(3): 37. DOI: <https://doi.org/10.3390/min7030037>
  11. Adebajo M. O., Frost R. L., Klopogge J. T., Carmody O., Kokot S. Porous materials for oil spill cleanup. A review of synthesis and absorbing properties. *Journal of Porous Materials*. 2003;10(3): 159–170. DOI: <https://doi.org/10.1023/A:1027484117065>
  12. Gracheva N. V., Zheltobryukhov V. F., Selezneva N. A. Sorption of petroleum products by modified silica clay. *Vestnik Volgogradskogo Gosudarstvennogo Arkhitekturno-Stroitel'nogo Universiteta. Ser.: Stroitel'stvo i arkhitektura* [Bulletin of Volgograd State University of Architecture and Civil Engineering Series: Civil Engineering and Architecture]. 2019;74: 80–87. Available at: [http://vgasu.ru/attachments/1\\_74\\_.pdf](http://vgasu.ru/attachments/1_74_.pdf)
  13. Hubbe M. A. New horizons for use of cellulose-based materials to adsorb pollutants from aqueous solutions. *Lignocellulose*. 2013;2(2): 386–411. Available at: [http://lignocellulose.sbu.ac.ir/Issue%2005/Ligno100\\_Hubbe\\_Cellulose-Based%20Materials%20o%20Adsorb%20Pollutants\\_386-411\\_PDF.pdf](http://lignocellulose.sbu.ac.ir/Issue%2005/Ligno100_Hubbe_Cellulose-Based%20Materials%20o%20Adsorb%20Pollutants_386-411_PDF.pdf)
  14. Prathap A., Sureshan K. M. Organogelator-cellulose composite for practical and eco-friendly marine oil-spill recovery. *Angewandte Chemie*. 2017;129(32): 9405–9409. DOI: <https://doi.org/10.1002/ange.201704699>
  15. Zhang H., Li Y., Xu Y., Lu Z., Chen L., Huang L., Fan M. Versatile fabrication of superhydrophobic and ultralight cellulose based aerogel for oil spillage cleanup. *Physical Chemistry Chemical Physics*. 2016;18(40): 28297–28306. DOI: <https://doi.org/10.1039/C6CP04932J>
  16. Liu H., Geng B., Chen Y., Wang H. Review on the aerogel-type oil sorbents derived from nanocellulose. *ACS Sustainable Chem. Eng.* 2017;5(1): 49–66. DOI: <https://doi.org/10.1021/acssuschemeng.6b02301>
  17. Bidgoli H., Mortazavi Y., Khodadadi A. A. A functionalized nano-structured cellulosic sorbent aerogel for oil spill cleanup: Synthesis and characterization. *Journal of Hazardous Materials*. 2019;366: 229–239. DOI: <https://doi.org/10.1016/j.jhazmat.2018.11.084>
  18. Wang Z., Saleem J., Barford J. P., McKay G. Preparation and characterization of modified rice husks by biological delignification and acetylation for oil spill cleanup. *Environmental Technology*. 2018;41(15): 1980–1991. DOI: <https://doi.org/10.1080/09593330.2018.1552725>
  19. Laitinen O., Suopajärvi T., Isterberg M., Liimatainen H. Hydrophobic, superabsorbing aerogels from choline chloride-based deep eutectic solvent pretreated and silylated cellulose nanofibrils for selective oil removal. *ACS Appl. Interfaces*. 2017;9(29): 25029–25037. DOI: <https://doi.org/10.1021/acsami.7b06304>
  20. Wang Y., Chen A., Peng M., Tan D., Liu X., Shang C., Luo S., Peng L. Preparation and characterization of a fluorinated kaolin-modified melamine sponge as an absorbent for efficient and rapid oil/water separation. *Journal of Cleaner Production*. 2019;217: 308–316. DOI: <https://doi.org/10.1016/j.jclepro.2019.01.253>
  21. Gao H., Sun P., Zhang Y., Zeng X., Wang D., Zhang Y., Wang W. A two-step hydrophobic fabrication of melamine sponge for oil absorption and oil/water separation. *Surface and Coatings Technology*. 2018;339: 147–154. DOI: <https://doi.org/10.1016/j.surfcoat.2018.02.022>
  22. Oribayo O., Pan Q., Feng X., Rempel G. L. Hydrophobic surface modification of FMSS and its application as effective sorbents for oil spill clean-ups and recovery. *AIChE Journal*. 2017;63(9): 4090–4102. DOI: <https://doi.org/10.1002/aic.15767>
  23. Anuzyte E., Vaisis V. Natural oil sorbents modification methods for hydrophobicity improvement. *Energy Procedia*. 2018;147: 295–300. DOI: <https://doi.org/10.1016/j.egypro.2018.07.095>

24. Patowary M., Pathak K., Ananthkrishnan R. A facile preparation of superhydrophobic and oleophilic precipitated calcium carbonate sorbent powder for oil spill clean-ups from water and land surfaces. *RSC Advances*. 2015;5(97): 79852–79859. DOI: <https://doi.org/10.1039/C5RA13847G>

25. Yudakov A. A., Ksenik T. V., Perfilyev A. V., Molchanov V. P. Hydrophobically-modified sorbents for the purification of oily waters. *Vestnik DVO RAN [Vestnik of Far Eastern Branch of Russian Academy of Sciences]*. 2009;(2): 59–63. Available at: <https://socionet.ru/d/spz:cyberleninka:1540:14725834/http://cyberleninka.ru/article/n/gidrofobno-modifitsirovannye-sorbenty-dlya-ochistki-neftesoderzhaschih-vod>

26. Wang Y., Feng Y., Yao J. Construction of hydrophobic alginate-based foams induced by zirconium ions for oil and organic solvent cleanup. *Journal of Colloid and Interface Science*. 2019;533: 182–189. DOI: <https://doi.org/10.1016/j.jcis.2018.08.073>

27. Fokina N. V. Prospects for the use of sorbents of various modifications in the purification of natural environments from petroleum products in the conditions of the Kola North. *Vestnik MGTU*. 2019;22(1): 101–108. DOI: <https://doi.org/10.21443/1560-9278-2019-22-1-101-108>

28. Prokof'ev V. Yu., Razgovorov P. B., Zakharov O. N., Gordina N. E. Study of pore texture of sorbents based on kaolin clay. *Russian Journal of Applied Chemistry*. 2011;84(11): 1866–1870. DOI: <https://doi.org/10.1134/S107042721111005X>

29. Wahi R., Chuah L. A., Choong T. S. Y., Ngaini Z., Nourouzi M. M. Oil removal from aqueous state by natural fibrous sorbent: An overview. *Separation and Purification Technology*. 2013;113: 51–63. DOI: <https://doi.org/10.1016/j.seppur.2013.04.015>

30. Bhardwaj N., Bhaskarwar A. N. A review on sorbent devices for oil-spill control. *Environmental Pollution*. 2018;243: 1758–1771. DOI: <https://doi.org/10.1016/j.envpol.2018.09.141>

31. Moazed H., Viraraghavan T. Coalescence / filtration of an oil-in-water emulsion in a granular organo-clay / anthracite mixture bed. *Water, Air, and Soil Pollution*. 2002;138: 253–270. DOI: <https://doi.org/10.1023/A:1015581011172>

32. Wei Q. F., Mather R. R., Fotheringham A. F., Yang R. D. Evaluation of nonwoven polypropylene oil sorbents in marine oil-spill recovery. *Marine Pollution Bulletin*. 2003;46(6): 780–783. DOI: [https://doi.org/10.1016/S0025-326X\(03\)00042-0](https://doi.org/10.1016/S0025-326X(03)00042-0)

33. Pagnucco R., Phillips M. L. Comparative effectiveness of natural by-products and synthetic sorbents in oil spill booms. *Journal of Environmental Management*. 2018;225: 10–16. DOI: <https://doi.org/10.1016/j.jenvman.2018.07.094>

34. Niftaliev S. I., Peregudov Yu. S., Mokshina N. Ya., Mezhi R., Saranov I. A. The effect of thermal activation of glauconite on its water-retaining and oil capacity. *Ecology and Industry of Russia*. 2019;23(7): 42–47. DOI: <https://doi.org/10.18412/1816-0395-2019-7-42-47>

### Information about the authors

*Yurii S. Peregudov*, PhD in Chemistry, Associate Professor at the Department of Inorganic Chemistry and Chemical Technology, Voronezh State University of Engineering Technologies, Voronezh, Russian Federation; e-mail: [inorganic\\_033@mail.ru](mailto:inorganic_033@mail.ru). ORCID iD: <https://orcid.org/0000-0003-2129-3191>.

*Rami Mejri*, Postgraduate Student at the Department of Inorganic Chemistry and Chemical Technology, Voronezh State University of Engineering Technologies, Voronezh, Russian Federation, e-mail: [mezhi@inbox.ru](mailto:mezhi@inbox.ru). ORCID iD: <https://orcid.org/0000-0002-4165-687X>.

*Elena M. Gorbunova*, PhD in Chemistry, Associate Professor at the Department of Inorganic Chemistry and Chemical Technology, Voronezh State University of Engineering Technologies, Voronezh, Russian Federation; e-mail: [lobanova8686@gmail.com](mailto:lobanova8686@gmail.com). ORCID iD: <https://orcid.org/0000-0002-3550-0115>.

*Sabukhi I. Niftaliev*, DSc in Chemistry, Professor, Head of Department of Inorganic Chemistry and Chemical Technology, Voronezh State University of Engineering Technologies, Voronezh, Russian Federation; e-mail: [sabukhi@gmail.com](mailto:sabukhi@gmail.com). ORCID iD: <https://orcid.org/0000-0001-7887-3061>.

All authors have read and approved the final manuscript.

*Translated by Lyubov Kats*

*Edited and proofread by Marina Strepetova*





# Condensed Matter and Interphases (Kondensirovannye sredy i mezhfaznye granitsy)

DOI: <https://doi.org/10.17308/kcmf.2020.22/2853>

Received 27 January 2020

Accepted 15 April 2020

Published online 25 June 2020

ISSN 1606-867X

eISSN 2687-0711

## Kinetics of Atomic Hydrogen Evolution and Hydrogen Permeability of Ag–Pd Alloys in an Alkaline Medium

© 2020 N. D. Rodina, N. B. Morozova✉, A. V. Vvedenskii

Voronezh State University,  
1 Universitetskaya pl., Voronezh 394018, Russian Federation

### Abstract

Homogeneous Ag–Pd alloys are effective catalysts for the cathodic evolution of hydrogen. They are characterised by high mechanical strength and are less susceptible to hydrogen embrittlement than metallic palladium. The aim of this study was to determine the kinetics of hydrogen evolution on palladium and its homogeneous alloys with silver in an alkaline aqueous solution, and to investigate their hydrogen permeability.

The behaviour of Pd and Ag–Pd alloys ( $X_{Pd} = 15–80$  at%) in a deaerated 0.1 M KOH aqueous solution was studied using cyclic voltammetry and double step anodic-cathodic chronoamperometry. Cyclic voltammograms for Pd and Ag80Pd were similar. However, when a small amount of silver ( $\leq 20$  at%) was introduced into palladium, the ionization rate of hydrogen decreased. A further increase in the concentration of silver in the alloy resulted in a complete suppression of the ionisation process. For Ag–Pd alloys with palladium concentrations below 30 at%, the voltammograms did not show any hydrogen ionization peaks. The dependencies of the peak ionisation current on the potential scan rate for all the studied alloys were linear and were extrapolated to the origin of the coordinates, which indicated that the process was complicated by solid-phase diffusion. The slopes of the lines for Ag60Pd and Ag50Pd alloys were higher than the slope for the Ag80Pd alloy, which indicated the presence of silver oxides on the surface. For all the studied electrodes the dependence of the peak current potential on the potential scan rate log linearly increased, which means that the electrochemical stage of atomic hydrogen ionization, which is complicated by solid-phase diffusion, is irreversible. The hydrogen permeability parameters of the alloys were calculated using potentiostatic cathodic and anodic current transients at different time intervals (1–10 sec.). The longer the hydrogenation time, the lower the current amplitudes on cathodic and anodic branches of the chronoamperograms. The hydrogen permeability parameters were calculated based on cathodic and anodic current transients linearised in the corresponding criteria coordinates, using the results of theoretical modelling of hydrogen injection and extraction for semi-infinite thickness electrodes. The phase-boundary exchange constant and the ionisation rate constant of atomic hydrogen were maximum for the alloy with the concentration of palladium of 80 at%. The hydrogen extraction rate constant changed linearly with the decrease in the concentration of palladium. The study determined that the values of hydrogen permeability for Ag–Pd alloys in alkaline solutions are lower than in acidic ones.

The determining stage of the hydrogen evolution reaction on Ag–Pd alloys ( $X_{Pd} \leq 40$  at%) in a 0.1M KOH solution is the electrochemical stage of atomic hydrogen ionization complicated by its diffusion in the solid phase. The hydrogen permeability parameters in Ag–Pd alloys are maximum, when the concentration of palladium is  $\sim 80$  at%. Therefore, such alloys can be used as materials for efficient hydrogen purification and storage.

**Keywords:** homogeneous Ag–Pd alloys; atomic hydrogen injection and extraction; hydrogen permeability; aqueous alkaline medium.

**For citation:** Rodina N. D., Morozova N. B., Vvedenskii A. V. Kinetics of Atomic Hydrogen Evolution and Hydrogen Permeability of Ag–Pd Alloys in an Alkaline Medium. *Kondensirovannye sredy i mezhfaznye granitsy = Condensed Matter and Interphases*. 2020; 22(2): 266–274. DOI: <https://doi.org/10.17308/kcmf.2020.22/2853>

✉ Natalia B. Morozova, e-mail: [mnb@chem.vsu.ru](mailto:mnb@chem.vsu.ru)



The content is available under Creative Commons Attribution 4.0 License.

## 1. Introduction

Although there are electrocatalysts for hydrogen evolution reaction (HER) highly efficient in acidic media, their application is still rather problematic. Most importantly, their application is limited due to the high corrosion susceptibility of the electrolytic cell and the fact that the obtained hydrogen gas is contaminated by acidic fog. On the contrary, an advantage of alkaline electrolytes is that they produce less vapour operating at high temperatures and have lower vapour pressure. Furthermore, non-noble electrodes are also more stable and do not corrode after a reaction [1].

In alkaline electrolytes, the kinetics and rate of HER is determined by the following factors: water adsorption and dissociation, the energy of hydrogen adsorption and desorption, and the affinity of hydroxyl ions to the catalyst's surface [2]. This means that for a catalyst to be efficient for HER in an alkaline medium, it should be able to dissociate water molecules adsorbed on its surface, and aggregate the resulting particles.

The most common catalyst with these properties is crystalline palladium. An advantage of palladium membranes is their increased ability to transport hydrogen through the metal. This happens because palladium has high hydrogen solubility at a wide range of temperatures [3]. The disadvantage that hinders the application of palladium membranes is that they are susceptible to hydrogen embrittlement, both at high concentrations of  $H_2$  and after multiple cycles of hydrogen adsorption and desorption.

Hydrogen embrittlement comes in the form of microstructural changes caused by a significant shrinkage and expansion of the metal's crystal lattice. During the adsorption process, hydrogen atoms randomly occupy octahedral interstitial sites of the palladium crystal lattice. It was noted that with a low H/Pd atomic ratio (of about 0.06), the  $\alpha$ -phase of Pd-H remains dominant [4]. This phase is an ideal dilute palladium-hydrogen solid solution [5]. With larger quantities of the adsorbed hydrogen the  $\beta$ -phase of Pd-H, also called palladium hydride, begins to form. This phase is a saturated palladium-hydrogen solid solution and coexists with the  $\alpha$ -phase at low temperatures [5]. Nucleation and the growth of palladium hydride in the  $\alpha$  matrix of the

Pd-H solid solution sets up severe strains in the material resulting in the deformation of the crystal lattice and dislocation multiplication and hardening [6].

To reduce hydrogen embrittlement, palladium is doped with transition metals, such as Ag, Cu, Fe, Ni, Pt, and Y [3]. Of particular interest are Ag-Pd alloys. These alloys are highly selective and permeable enough towards hydrogen at room temperature, which makes them a promising material for the production of diffusion membranes [7]. It is also vital that silver and palladium form a continuous series of substitutional solid solutions within the whole concentration range with no miscibility gaps [8].

According to [9], Ag-Pd alloys with the concentrations of Ag of up to 60 % can efficiently absorb hydrogen. The hydrogen absorbed by these alloys exists in two basic phases,  $\alpha$  and  $\beta$ , analogous to pure palladium. The results of the X-ray diffraction analysis in [10] demonstrated that the lattice parameters of  $\alpha$  and  $\beta$  phases are the least different for the Ag77Pd alloy. This happens because the crystal lattice of palladium is already extended by the silver atoms and hence is less susceptible to hydrogen embrittlement. Consequently, the mechanical strength of the diffusion membranes produced from Ag-Pd alloys increases significantly [11]. It is therefore important to study the mechanism of hydrogen permeation through the alloy's electrodes in more detail. The aim of this study was to determine the kinetics of hydrogen evolution on palladium, and to investigate hydrogen permeability of palladium and its homogeneous alloys with silver in an alkaline aqueous solution.

## 2. Experimental

The object of the study were close-packed Ag-Pd electrodes with  $X_{Pd} = 15, 30, 40, 50, 60,$  and 80 at% in a 0.1M KOH (chemically pure) bidistilled aqueous solution. The surface of the electrodes was preliminary polished using MgO aqueous suspension and suede leather, degreased with ethanol, and washed in distilled water.

The experiments were conducted in a three-electrode glass cell. The auxiliary electrode was a platinized platinum electrode, and the reference electrode was a silver chloride electrode. Prior

to polarization measurements, the solution was deaerated by sparging with chemically pure argon for 30 minutes. Electrochemical measurements were performed using a computer-aided IPC-Compact potentiostat. All the potentials are given here relative to the standard hydrogen electrode, and the current values are given per single unit of the real surface area of the alloys [12].

In order to remove the trace amounts of oxides from the surface of the electrodes, the studied electrodes were held in the solution at the initial potential  $E_p = -0.60$  V for 500 seconds before obtaining cyclic voltammograms. Cyclic voltammograms were obtained in potentiodynamic mode (at a scan rate of  $v = 5$  mV/s) starting at  $E_p$  and sweeping to the cathode region. It was then swept back in the anode direction, switching potentials. Dependencies  $i, E$ -were limited by the peak currents of hydrogen and oxygen evolution.

To obtain voltammograms at different potential scan rates, the electrodes were preliminary hydrogenated with the potential being  $E_c = -0.90$  V for  $t_c = 3$  sec. and  $t_c = 5$  sec. The potential scan rate varied within the range of 0.5–100 mV/s.

To determine the parameters of extraction and injection of atomic hydrogen, double step anodic-cathodic chronoamperometry was used. Before obtaining the chronoamperograms, the working electrode was held at the potential  $E_p = -0.60$  V for 500 seconds. To standardise the state of the surface, the curve corresponding to the cathode current drop was obtained at the cathode hydrogenation potential  $E_c = -0.90$  V. The hydrogenation time  $t_c$  varied within the range of 1–10 seconds. The potential was then switched to the peak anodic potential of hydrogen ionization  $E_m^a$ , whose values were determined using the preliminary obtained  $i, E$ -dependencies. The current drop was registered before it reached its steady state value. After that, still holding the working electrode in the solution, we once more set the initial potential  $E_p$  and repeated the whole sequence for a different value  $t_c$ .

### 3. Results and discussion

The kinetics of hydrogen evolution in a 0.1M KOH hydrogen solution was determined using cyclic voltammetry. The results are presented

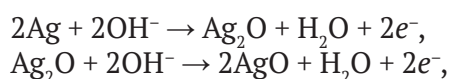
in Fig. 1. The anodic branches of the cyclic voltammograms obtained for Pd and Ag-Pd alloys with  $X_{Pd} \geq 50$  at%, show a characteristic current peak corresponding to the atomic hydrogen ionization from the electrode's surface in the potential region from  $-0.30$  to  $0.20$  V. Lower ionization rate of atomic hydrogen on pure palladium as compared to its alloys is demonstrated by a lower anodic peak amplitude. The latter can be accounted for by adsorption of hydroxide ions on the electrode's surface, or by the formation of silver compounds on the surface which block the active regions of the surface and cause anodic passivation [13]. It should be noted, that at  $X_{Pd} = 50$  at% the ionisation peak is already less prominent, and its form is distorted by the competing process of silver oxidation. For Ag–Pd alloys with low palladium concentrations ( $X_{Pd} \leq 30$  at%) no hydrogen ionization peak is observed.

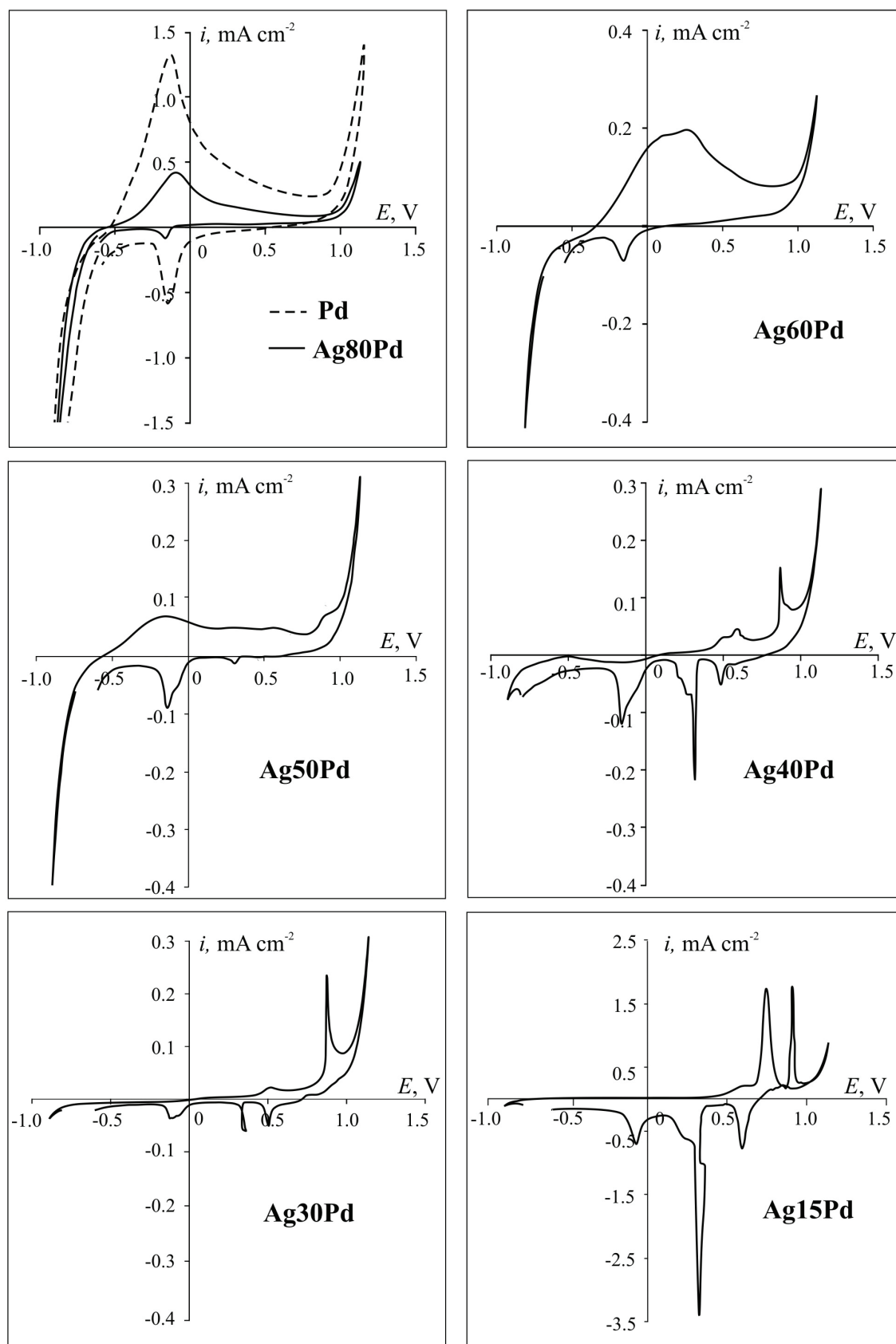
When the potential sweeps to more positive values, the region of palladium oxidation, observed at  $0.20$ – $0.80$  V, is barely visible on Pd and the Ag80Pd alloy. For alloys with  $X_{Pd} \leq 50$  at% this region is practically absent, since the process is suppressed by silver oxidation. As the potential sweeps to the cathode, both pure palladium and its alloys show a cathodic peak of reduction of PdO. For Pd, this peak is registered at  $E = -0.22$  V. However, with the decrease in the concentration of palladium, it shifts towards more positive potentials of up to  $-0.07$  V. According to [14], the formation of palladium oxide at  $pH \sim 13$  is described by the equation:



with the value of the equilibrium potential of the electrode being  $0.13$  V.

For electrodes with  $X_{Pd} \leq 40$  at%, two indistinct anodic peaks are observed in the potential ranges of  $0.43$ – $0.74$  V and  $0.89$ – $0.91$  V. These peaks correspond to the oxidation of metallic silver to  $Ag_2O$  and its subsequent postoxidation to AgO. The amplitudes of both peaks increase with larger concentrations of silver in the alloy. The equilibrium potentials  $E_{eq}$  of formation of  $Ag_2O$  and AgO on silver in the studied solution were determined by the half-reaction on the anode:

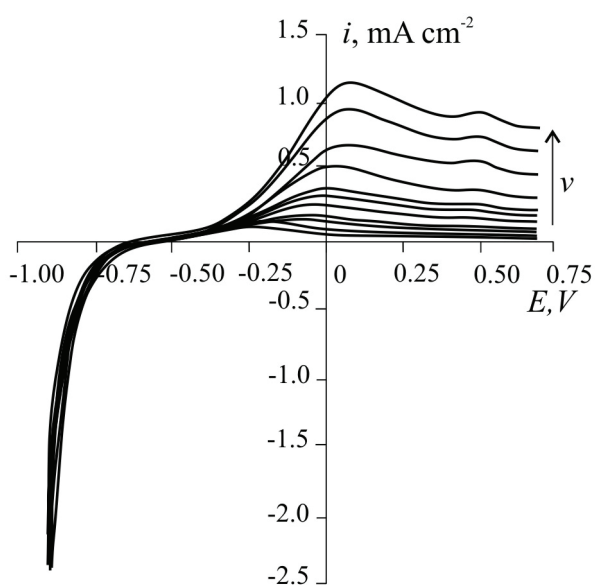




**Fig. 1.** Cyclic voltammograms obtained with a potential scan rate of 5 mV/s on Pd and Ag-Pd alloys in a 0.1 M KOH solution

and equalled to 0.40 and 0.67 V (standard hydrogen electrode) [14]. Based on the obtained data we can say that  $E_{\text{eq}}$  for silver oxidation processes are modified as compared to the calculated potentials. For 0.1M KOH they are 0.55 and 0.90 V, which was determined in [15]. Furthermore, Ag-40Pd and Ag15Pd alloys demonstrated characteristic prepeaks at 0.52 and 0.61 V respectively, which we assume to be connected with adsorption followed by AgOH oxidation [15]. The cathodic branches of the voltammograms showed peaks corresponding to the reduction of AgO (~ 0.50 V) and Ag<sub>2</sub>O (~ 0.32 V). Potentials of cathodic and anodic peaks determined for the Ag15Pd alloy are almost fully compatible with the potentials of the same peaks for pure silver [13]. The voltammogram of the Ag30Pd alloy shows a hysteresis at the potential 0.30 V, which may mean that the electrode's surface is underoxidised.

To determine the kinetics of hydrogen evolution on Ag-Pd alloys voltammograms were obtained for various potential scan rates and the hydrogenation time  $t_c = 3$  sec. (Fig. 2). The results show that for all the studied samples the ionisation peak increases with higher potential scan rates and shifts towards more positive values. Furthermore, the splitting of the main anodic peak into a number of smaller ones is observed, which may indicate the adsorptive



**Fig. 2.** Dependencies of the current density of hydrogen ionization on the potential scan rate on Pd and Ag-Pd alloys in a 0.1 M KOH solution obtained at  $t_c = 3$  s

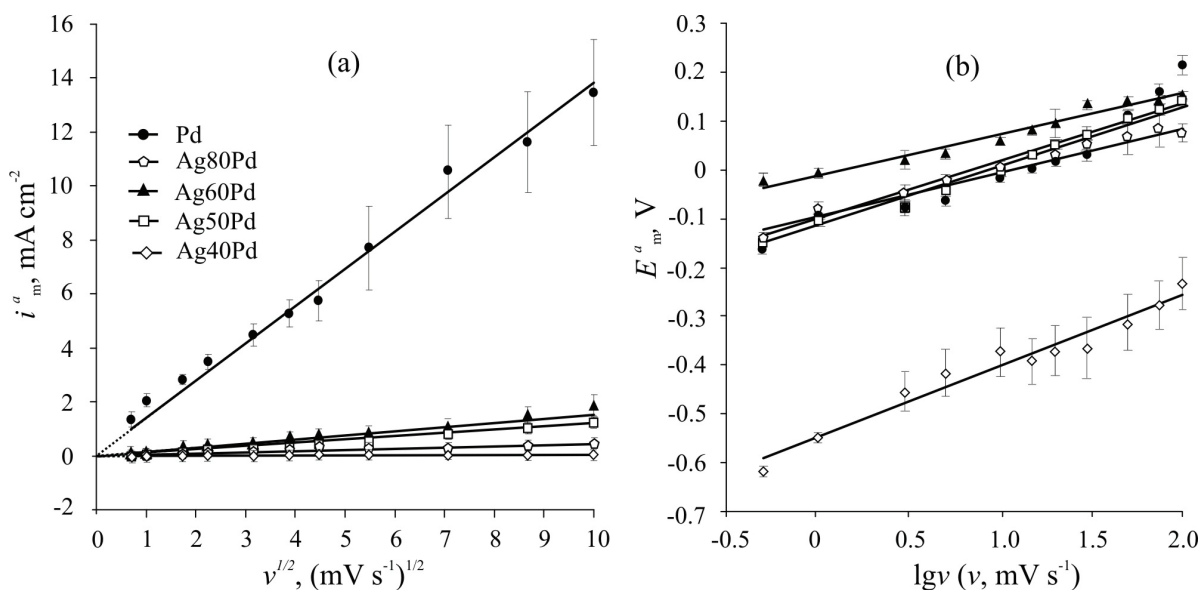
accumulation of various forms of oxygen-containing particles [16, 17]. The experimental data was processed based on the first anodic peak whose potential corresponded to the ionisation of atomic hydrogen.

The characteristic parameters of the experimental  $i, E$ -curves were replotted with some criterion coordinates. Thus, the obtained dependencies  $i_m^a - v^{1/2}$  (Fig. 3a) are easily linearized and extrapolated to the origin of the coordinates, which means that ionisation of hydrogen is complicated by solid-phase diffusion. The slopes of the graphs  $di_m^a / dv^{1/2}$  for Ag60Pd and Ag50Pd alloys are higher than that for the Ag80Pd alloy, which is most likely to be caused by silver oxidation.

The dependencies of the potential of the ionisation peak  $E_m^a$  on  $\lg v$  (Fig. 3b) are also linear for all the studied systems, which means that the electrochemical stage of atomic hydrogen ionization is irreversible. The slopes  $dE_m^a / d \lg v$ , obtained for palladium and the Ag–Pd alloy with the concentration of palladium of 80 at%, are similar, 0.049 and 0.042 V respectively, which corresponds to the single-electron charge transfer process. However, the values  $dE_m^a / d \lg v$  for the alloys with  $X_{\text{Pd}} \leq 60$  % vary within the range of 0.091–0.122 V. It is possible that in this case the kinetics of charge transfer is complicated by the formation of silver oxides. Similar dependencies are observed when the hydrogenation time is  $t_c = 5$  sec.

Using the results obtained previously on Ag–Pd electrodes in an acidic medium [18], we can assume that the kinetics of injection and ionisation of atomic hydrogen does not generally depend on the nature or the medium of the electrolyte. The complications observed in the alkaline medium are caused by silver oxidation during its dissolution from the alloys. Furthermore, as opposed to the acidic medium, in the alkaline solution atomic hydrogen is formed from the molecules of H<sub>2</sub>O. Therefore, the process of injection and ionisation of atomic hydrogen on a metal in an alkaline medium can be modelled as shown in Fig.4.

The study of injection and extraction of atomic hydrogen, as well as calculation of the hydrogen permeability parameters was performed by processing double step anodic-cathodic



**Fig. 3.** Values of the current ( $i_m^a$ ) and potential ( $E_m^a$ ) of the anodic peak on voltammograms for Pd and Ag–Pd alloys in a 0.1 M KOH solution obtained at various potential scan rates; ( $t_c = 3$  s).

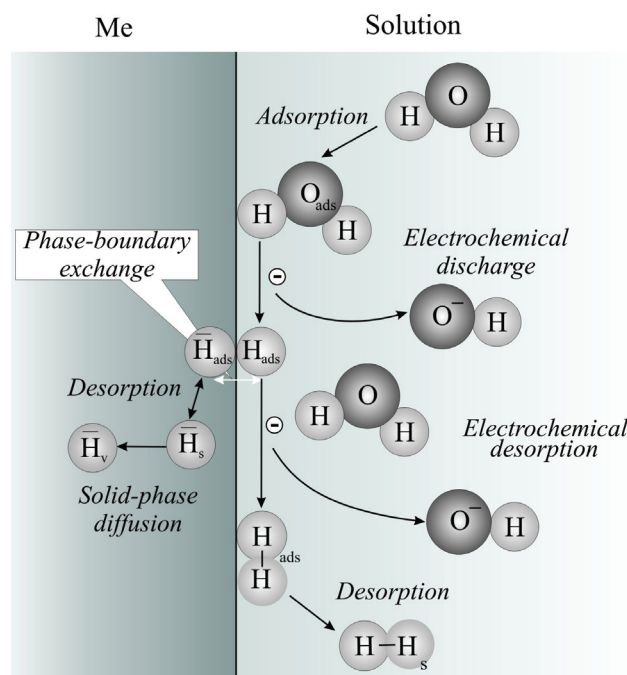
chronoamperograms obtained on palladium and its alloys. Thus, with longer hydrogenation time,  $i, t$ -dependencies (Fig. 5) show an expected decrease in the amplitudes of the cathodic and anodic branches of the chronoamperograms. This may be caused by the adsorption of oxygen-containing particles, primarily OH, which hinder the ionisation of atomic hydrogen from the surface. Indeed, while obtaining a series of chronoamperograms for different hydrogenation time, we did not polish the electrode surface between the cycles. This must have caused the accumulation of adsorbed particles and hence slowed down the ionisation process and hydrogen injection.

To see whether this assumption was correct, we obtained double step anodic-cathodic chronoamperograms only for  $t_c = 10$  sec. Cathodic and anodic current amplitudes were significantly higher than those obtained during subsequent registration (Fig. 5b). Larger concentrations of silver in the alloy result in expected decrease in the rate of ionisation of atomic hydrogen both in the cathodic and anodic region, which complies with the voltammetric dependencies.

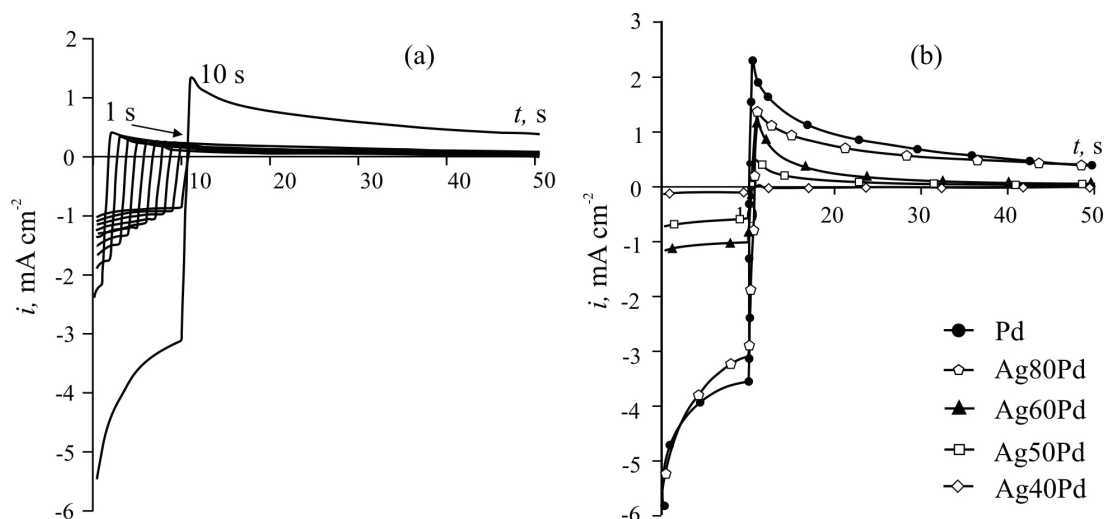
Cathodic chronoamperograms obtained for hydrogenation time  $t_c = 10$  sec., were rectified to the coordinates  $i_c-t_c^{-1/2}$  and  $i_c-t_c^{1/2}$ . For all the studied systems these dependencies are linear, but are not extrapolated to the origin of the

coordinates. This means that the registered cathodic current consists of at least two elements: the water discharge current and the maximum current of diffusion of H atoms inside the metallic phase.

Using the theoretical model for semi-infinite thickness electrodes described in [19], we performed the mathematical processing of



**Fig. 4.** Model of hydrogen evolution in an alkaline solution



**Fig. 5.** Double step chronoamperograms obtained in a 0.1 M KOH solution on the Ag80Pd alloy, with  $t_c = 1-10$  s (a), and for Pd and Ag–Pd alloys; the hydrogenation time  $t_c = 10$  s (b)

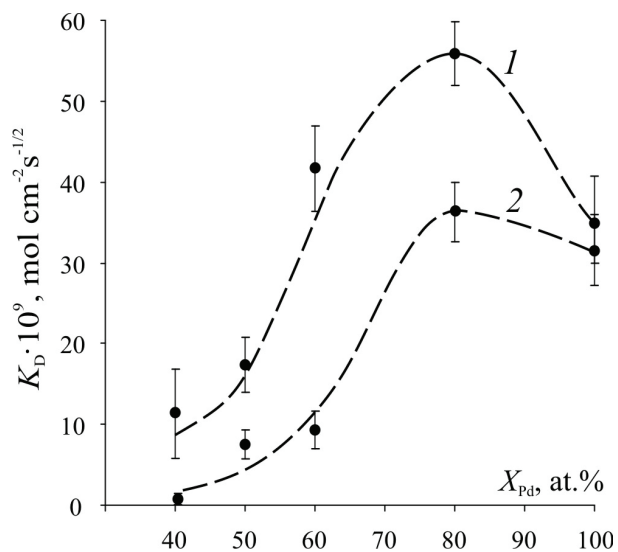
the cathodic chronoamperograms in order to determine the kinetic and diffusion parameters of the process of injection of atomic hydrogen. Mathematical modelling was used to calculate the following parameters:  $i_c(0)$  and  $i_c^\infty$  – initial and stationary cathodic current respectively, rate constants  $\bar{k}$  and  $\bar{k}$  of the reaction of injection and ionisation, and the equilibrium constant of this process  $K = k/k$ . The parameter characterising solid-phase diffusion, i.e. hydrogen permeability coefficient  $K_D = D^{1/2} \Delta c_{\bar{H}}$ , is integral; it is impossible to determine the diffusion coefficient  $D$  and the

magnitude of the change in the concentration  $\Delta c_{\bar{H}}$  of atomic hydrogen in the alloy separately. Hydrogen permeability parameters for Pd and Ag–Pd alloys calculated using the cathodic current transients, are given in Table 1.

All the parameters determined during our experiments, except for the hydrogen permeability coefficient  $K_D$ , decrease steadily with larger concentrations of silver in the alloy. The hydrogen permeability coefficient reaches its maximum on the Ag80Pd alloy. This can be accounted for by the maximum hydrogen permeability and hydrogen solubility in the crystal lattice of the Ag77Pd alloy determined in [10].

Comparison of the results obtained for Ag–Pd alloys in acidic [18] and alkaline media allowed us to conclude that hydrogen permeability of such alloys is lower in alkaline media than in acidic media. The dependency of hydrogen permeability coefficient  $K_D$  on the concentration of palladium is the same for the considered media. The coefficient reaches its maximum, when  $X_{Pd} = 80$  at% (Fig. 6). The hydrogen permeability coefficient for Pd and Ag–Pd alloys with  $X_{Pd} \geq 50$  at% in the alkaline medium is 1.5–4.5 times lower than in the acidic medium. For the Ag40Pd alloy the difference is even more significant.

The analysis of the results allowed us to conclude that upon transition from acidic to alkaline medium, hydrogen permeability is suppressed on all the studied alloys of the Ag–Pd system.



**Fig. 6.** Dependence of the hydrogen permeability coefficient on the alloy composition in a 0.1 M  $H_2SO_4$  solution (1) and a 0.1 M KOH solution (2)

**Table 1.** Characteristics of the hydrogen injection in palladium and in Ag-Pd alloys in a 0.1 M KOH solution

$X_{Pd}$ , at %	$i_c^\infty$ , mA/cm <sup>2</sup>	$i_c(0)$ , mA/cm <sup>2</sup>	$K_D \cdot 10^9$ , МОЛЬ/CM <sup>2</sup> C <sup>1/2</sup>	$\bar{k} \cdot 10^8$ , mol/cm <sup>2</sup> S <sup>1/2</sup>	$\bar{k} \cdot 10^4$ , cm/s	$K \cdot 10^5$ , mol/cm <sup>3</sup>
100	2.39±0.32	4.95±1.21	32.17±10.05	3.84±1.21	3.82±0.05	11.87±4.64
80	1.91±0.15	3.65±0.12	36.19±3.67	2.99±0.47	2.65±0.30	10.40±1.41
60	1.17±0.35	1.36±0.31	9.31±2.40	0.76±0.22	0.93±0.06	2.51±0.65
50	0.63±0.10	0.96±0.14	7.54±1.77	0.58±0.12	0.26±0.03	2.23±0.32
40	0.07±0.01	0.13±0.02	0.75±0.10	0.07±0.03	0.14±0.01	0.19±0.05

The anodic current drops were analysed using the same theoretical model [19]. Hydrogen permeability coefficients calculated based on the slopes of the linear regions of anodic chronoamperograms –  $K_D(i_a)$  and chronocoulograms –  $K_D(q_a)$ , are also maximum for the Ag80Pd alloy (Table. 2). It should be noted that hydrogen permeability coefficients calculated using the anodic current transients are significantly higher than those calculated based on the cathodic current transients. This may be the result of the dilatation of the crystal lattices of the alloys [18].

We can thus state that the dependency of practically all the parameters of hydrogen permeability on the composition of Ag–Pd alloys passes through the extremum observed for the Ag80Pd alloy. We can therefore conclude that 80 at% concentration of palladium in the alloy is optimal with regard to hydrogen permeability, which means that this alloy can be effectively used for hydrogen purification and storage.

#### 4. Conclusions

1. The behaviour of Ag-Pd alloys during hydrogen evolution in an alkaline solution was studied. Introduction of small quantities (up to 20 at%) of silver into the crystal lattice of palladium results in the increase in the rate of ionisation of atomic hydrogen. When  $X_{Ag} > 20$  at% the process is suppressed by silver oxidation.

2. When palladium alloys with concentrations of Ag of up to 60 at% are used, the kinetics of hydrogen evolution remains the same. The determining stage of the hydrogen evolution

reaction on Ag-Pd alloys in a 0.1M KOH solution is the electrochemical stage of atomic hydrogen ionization, which is complicated by its diffusion in the solid phase.

3. The dependency of the ionisation peak  $E_m^a$  on the potential scan rate indicates that the electrochemical stage is irreversible. For alloys with  $X_{Pd} \leq 60$  at% the kinetics of charge transfer is complicated by silver oxidation.

4. The parameters of hydrogen permeability are optimal, when the concentration of palladium in the alloy is ~80 at%. These alloys can be used as efficient materials for hydrogen purification and storage.

#### Conflict of interests

The authors declare that they have no known competing financial interests or personal relationships that could have influenced the work reported in this paper.

#### References

1. Mahmood N., Yao Y., Zhang J.-W., Pan L., Zhang X., Zou, J.-J. Electrocatalysts for hydrogen evolution in alkaline electrolytes: mechanisms, challenges, and prospective solutions. *Adv. Sci.* 2017;5(2): 1700464. DOI: <https://doi.org/10.1002/advs.201700464>
2. Zhang W., Lai W., Cao R. Energy-related small molecule activation reactions: oxygen reduction and hydrogen and oxygen evolution reactions catalyzed by porphyrin- and corrole-Based Systems. *Chem. Rev.* 2016;117(4): 3717–3797. DOI: <https://doi.org/10.1021/acs.chemrev.6b00299>
3. Yun S., Ted Oyama S. Correlations in palladium membranes for hydrogen separation: A review. *J. Membr. Sci.* 2011;375(1–2): 28–45. DOI: <https://doi.org/10.1016/j.memsci.2011.03.057>

**Table 2.** Values of  $K_D$  for Pd and its alloys obtained using anodic current transients in a 0.1M KOH solution

$X_{Pd}$ , at%	100	80	60	50	40
$K_D(i_a) \cdot 10^8$ , mol/cm <sup>2</sup> S <sup>1/2</sup>	28.03±2.40	35.35±3.29	6.50±1.09	6.13±0.99	0.23±0.04
$K_D(q_a) \cdot 10^{10}$ , mol/cm <sup>2</sup> S <sup>1/2</sup>	15.21±2.23	19.05±1.62	4.61±1.02	3.02±0.39	0.12±0.04



4. Bugaev A. L., Guda A. A., Dmitriev V. P., Lomachenko K. A., Pankin I. A., Smolencev N. Ju., Soldatov M. A., Soldatov A. V. Dinamika nanorazmernoj atomnoj i elektronnoj struktury materialov vodorodnoj energetiki pri realistichnyh tekhnologicheskikh usloviyah [Operando dynamics of the nanoscale atomic and electronic structure of materials for hydrogen storage]. *Engineering Journal of Don*. 2012;4-1(22): 89–90. Available at: <https://elibrary.ru/item.asp?id=18640138&> (in Russ., abstract in Eng.)
5. Goltsova M. V., Zhirov G. I. Gidridnye prevrashcheniya v sisteme Pd-H. Struktura i svoystva palladiya i ego gidrida [Hydride transformations in the Pd-H system. The structure and properties of palladium and its hydride]. In: *The interaction of hydrogen isotopes with structural materials, Proceedings of the X International school of young scientists and specialists, 28 June – 4 July 2015*. Moscow: Research centre “Kurchatov institute” Publ.; 2015. p. 171–189. Available at: <http://book.sarov.ru/wp-content/uploads/2017/12/IHISM-15.pdf> (in Russ., abstract in Eng.)
6. Knapton A. G. Palladium alloys for hydrogen diffusion membranes. *Platinum Met. Rev.* 1977;21(2): 44–50. Available at: <https://www.technology.matthey.com/article/21/2/44-50>
7. Sharma B., Kim J.-S. Pd/Ag alloy as an application for hydrogen sensing. *Int. J. Hydrog. Energy*. 2017;42(40): 25446–25452. DOI: <https://doi.org/10.1016/j.ijhydene.2017.08.142>
8. Ghosh G., Kantner C., Olson G. B. Thermodynamic modeling of the Pd-X (X=Ag, Co, Fe, Ni) systems. *J. Phase Equilib.* 1999;20(3): 295–308. DOI: <https://doi.org/10.1361/105497199770335811>
9. Lukaszewski M., Klimek K., Czerwinski A. Microscopic, spectroscopic and electrochemical characterization of the surface of Pd–Ag alloys. *J. Electroanal. Chem.* 2009;637(1–2): 13–20. DOI: <https://doi.org/10.1016/j.jelechem.2009.09.024>
10. Wise M. L. H., Farr J. P. G., Harris I. R. X-ray studies of the  $\alpha/\beta$  miscibility gaps of some palladium solid solution-hydrogen systems. *J. Less Common Met.* 1975;41(1): 115–127. DOI: [https://doi.org/10.1016/0022-5088\(75\)90099-5](https://doi.org/10.1016/0022-5088(75)90099-5)
11. Amandusson H., Ekedahl L.-G., Dannetun H. Hydrogen permeation through surface modified Pd and PdAg membranes. *J. Membr. Sci.* 2001;193(1): 35–47. DOI: [https://doi.org/10.1016/S0376-7388\(01\)00414-8](https://doi.org/10.1016/S0376-7388(01)00414-8)
12. Shcheblykina G. E., Bobrinskaya E. V., Vvedenskii A. V. Determination of real surface area of metals and alloys by a combined electrochemical method. *Protection of Metals*. 1998;34(1): 11–14. Available at: <https://elibrary.ru/item.asp?id=23725216>.
13. Lesnykh N. N., Tutukina N. M., Marshakov I. K. The effect of sulfate and nitrate ions on the passivation and activation of silver in alkaline solutions. *Protection of Metals*. 2008;44(5): 472–477. Available at: <https://elibrary.ru/item.asp?id=11154994>
14. Nikolskii B. P., Rabinovich V. A. *Spravochnik khimika*. V. 3. [Chemist’s handbook. V. 3.]. Moscow: Khimiya Publ.; 1965. 1008 p. (in Russ.)
15. Kudryashov D. A., Grushevskaya S. N., Ganzha S. V., Vvedenskii A. V. Effect of the crystal face orientation and alloying with gold on the properties of thin anodic films of Ag(I) oxide: I. Photocurrent. *Protection of Metals and Physical Chemistry of Surfaces*. 2009;45(5): 451–460. Available at: <https://elibrary.ru/item.asp?id=12901352>
16. Adzic R. R., Hciao M. W., Yeager E. B. Electrochemical oxidation of glucose on single-crystal gold surfaces. *J. Electroanal. Chem.* 1989;260(2): 475–485. DOI: [https://doi.org/10.1016/0022-0728\(89\)87164-5](https://doi.org/10.1016/0022-0728(89)87164-5)
17. Strobac S., Adzic R. R. The influence of OH-chemisorption on the catalytic properties of gold single crystal surfaces for oxygen reduction in alkaline solutions. *J. Electroanal. Chem.* 1996;403(1–2): 169–181. DOI: [https://doi.org/10.1016/0022-0728\(95\)04389-6](https://doi.org/10.1016/0022-0728(95)04389-6)
18. Morozova N. B., Vvedenskii A. V., Beredina I. P. Katodnaya inzhekciya, anodnaya ekstrakciya i diffuziya vodoroda v metallurgicheskikh Cu, Pd- i Ag, Pd-splavah. II. Eksperimental’nye dannye [Kathodic injection, anodic extraction and hydrogen diffusion in metallurgic Cu, Pd- and Ag, Pd-alloys. I. Theoretical model]. *Kondensirovannye sredy i mezhfaznye granitsy = Condensed Matter and Interphases*. 2014;16(2): 178–188. Available at: <https://journals.vsu.ru/kcmf/article/view/823> (in Russ., abstract in Eng.)
19. Morozova N. B., Vvedenskii A. V., Beredina I. P. The phase-boundary exchange and the non-steady-state diffusion of atomic hydrogen in Cu-Pd and Ag-Pd alloys. Part I. Analysis of the model. *Protection of Metals and Physical Chemistry of Surfaces*. 2014;50(6): 573–578. DOI: <https://doi.org/10.7868/S0044185614060138>

### Information about the authors

*Natalia D. Rodina*, 5th year student, Faculty of Chemistry, Voronezh State University, Voronezh, Russian Federation; e-mail: [mnb@chem.vsu.ru](mailto:mnb@chem.vsu.ru).

*Natalia B. Morozova*, PhD in Chemistry, Associate Professor, Department of Physical Chemistry, Voronezh State University, Voronezh, Russian Federation; e-mail: [mnb@chem.vsu.ru](mailto:mnb@chem.vsu.ru). ORCID iD: <https://orcid.org/0000-0003-4011-6510>.

*Aleksander V. Vvedenskii*, DSc in Chemistry, Professor, Department of Physical Chemistry, Voronezh State University, Voronezh, Russian Federation; e-mail: [alvved@chem.vsu.ru](mailto:alvved@chem.vsu.ru). ORCID iD: <https://orcid.org/0000-0003-2210-5543>.

All authors have read and approved the final manuscript.

*Translated by Yulia Dymant*

*Edited and proofread by Simon Cox*